

**GROWTH, CHARACTERIZATION, AND APPLICATIONS OF
LANTHANIDE MONOPNICTIDE NANOPARTICLES AND FILMS IN
AND ON III-V SEMICONDUCTORS**

by

Cory C. Bomberger

A dissertation submitted to the Faculty of the University of Delaware in partial fulfillment of the requirements for the degree of Doctor of Philosophy in Materials Science and Engineering

Fall 2016

© 2016 Cory C. Bomberger
All Rights Reserved

ProQuest Number: 10194425

All rights reserved

INFORMATION TO ALL USERS

The quality of this reproduction is dependent upon the quality of the copy submitted.

In the unlikely event that the author did not send a complete manuscript and there are missing pages, these will be noted. Also, if material had to be removed, a note will indicate the deletion.



ProQuest 10194425

Published by ProQuest LLC (2017). Copyright of the Dissertation is held by the Author.

All rights reserved.

This work is protected against unauthorized copying under Title 17, United States Code
Microform Edition © ProQuest LLC.

ProQuest LLC.
789 East Eisenhower Parkway
P.O. Box 1346
Ann Arbor, MI 48106 – 1346

**GROWTH, CHARACTERIZATION, AND APPLICATIONS OF
LANTHANIDE MONOPNICTIDE NANOPARTICLES AND FILMS IN
AND ON III-V SEMICONDUCTORS**

by

Cory C. Bomberger

Approved: _____
Darrin J. Pochan, Ph.D.
Chair of the Department of Materials Science and Engineering

Approved: _____
Babatunde A. Ogunnaike, Ph.D.
Dean of the College of Engineering

Approved: _____
Ann L. Ardis, Ph.D.
Senior Vice Provost for Graduate and Professional Education

I certify that I have read this dissertation and that in my opinion it meets the academic and professional standard required by the University as a dissertation for the degree of Doctor of Philosophy.

Signed: _____
Joshua M. O. Zide, Ph.D.
Professor in charge of dissertation

I certify that I have read this dissertation and that in my opinion it meets the academic and professional standard required by the University as a dissertation for the degree of Doctor of Philosophy.

Signed: _____
Matthew F. Doty, Ph.D.
Member of dissertation committee

I certify that I have read this dissertation and that in my opinion it meets the academic and professional standard required by the University as a dissertation for the degree of Doctor of Philosophy.

Signed: _____
Robert L. Opila, Ph.D.
Member of dissertation committee

I certify that I have read this dissertation and that in my opinion it meets the academic and professional standard required by the University as a dissertation for the degree of Doctor of Philosophy.

Signed: _____
Ajay K. Prasad, Ph.D.
Member of dissertation committee

I certify that I have read this dissertation and that in my opinion it meets the academic and professional standard required by the University as a dissertation for the degree of Doctor of Philosophy.

Signed: _____

Lars Gundlach, Ph.D.

Member of dissertation committee

ACKNOWLEDGEMENTS

This dissertation would not exist without help from many people. First and foremost I would like to thank my advisor, Professor Joshua M. O. Zide. I remember thinking as an undergraduate student that I never wanted to work on an molecular beam epitaxy (MBE) system; they seemed to break too easily, cost too much money, and produced material too slowly for most production processes. My view on MBE changed during my visit to the University of Delaware. Professor Zide pointed out that MBE provides the opportunity to perform truly exciting research that can have a massive impacts on future devices. At the end of the day, I came to the University of Delaware because of this enthusiasm for fundamental research and the care Professor Zide has for his students. While the MBE did break, and Professor Zide probably became tired of me explaining the problems we were facing with the MBE, I am extremely glad I had the opportunity to work for Professor Zide. I have learned a tremendous amount of information from him and I am sure it will prove to be invaluable in my future career. It has also been a pleasure to work for Professor Zide because of his desire to connect with his students on a personal level and his genuine care for their well-being and happiness. I have truly enjoyed my time working in his group.

I am also extremely thankful for my committee members: Professor Matthew F. Doty, Professor Robert L. Opila, Professor Ajay K. Prasad, and Professor Lars Gundlach. I have learned a lot from each of them, both in the classroom and through research projects. I have been pushed and challenged by each of them and have grown as a result. I am thankful for the help they have each provided in my research and dissertation.

I would also like to thank the past and present members of the EMERG group: John Petropoulos, Laura Clinger, Dr. Yujun Zhong, Dr. Pernell Dongmo, Matthew

Lewis, Bo Tew, Jing Zhang, Eric Chen, and Yuejing Wang. I would also like to thank the undergraduate students whom I have worked with: Peter Attia, Kelsi Skeens, Chelsea Shockey, Kevin Bichoupan, Ana Haddad, Isaac King, and Lisa Mwanza. It really is all of you who make this group so friendly. You have all played an instrumental role in my research and I am thankful for your help and friendship. I will truly cherish the time we spent together and I will miss working with each of you. While not technically members of the EMERG group, I must also thank Dongxia Wei and Professor Stephanie Law for their help in maintaining and repairing the MBE.

I would like to thank all of my collaborators, both those who have helped with my projects and those whom I had the pleasure to help. Without all of you, I would not have been able to complete all of this work. I have learned an enormous amount from each of you. In particular, I would like to thank Professor D. Bruce Chase. Nearly every project I have worked on involved optics and his help has been key in my ability to understand each measurement. Professor Chase also provided indispensable guidance on many of my presentations.

To the many friends I have made while in Delaware: friends from UD, friends from running group, and friends from church - thank you. You have made life here in Delaware truly enjoyable. You have each made a lasting impression on my life and I will cherish the memories we have made. And to the friends from outside of Delaware, thank you for your continued support and encouragement. I will always hold dear your friendship and the memories we have made.

I owe an enormous amount of gratitude to my family. You all have been extremely supportive, caring, and patient. Mom and Dad, you have always taught me to work hard and to always try my best; that has been essential in all of my success. Thank you. Cody, thank you for your support and friendship.

Finally, I want to dedicate this dissertation to my wife, Kasondra. Thank you for your endless support and love. Without you, none of this would have been possible.

TABLE OF CONTENTS

LIST OF TABLES	x
LIST OF FIGURES	xi
ABSTRACT	xxii

Chapter

1 REVIEW OF LANTHANIDE MONOPNICIDE MATERIALS	1
1.1 Introduction	1
1.2 Growth of LN-V Materials	2
1.2.1 MBE Growth of LN-V Nanostructures	3
1.2.1.1 Nanostructure Growth via Co-deposition	4
1.2.1.2 Nanoparticle Growth via Growth Interrupt	13
1.2.2 MBE LN-V Film Growth	19
1.2.3 Other Growth Methods	22
1.3 Electronic Band Structure and Carrier Dynamics	25
1.4 Optical Properties	31
1.5 Electrical Properties	35
1.6 Thermal Conductivity	44
1.7 Application of LN-V:III-V	47
1.8 Thesis Outline	56
2 GROWTH AND CHARACTERIZATION TECHNIQUES	57
2.1 Molecular Beam Epitaxy	57
2.2 X-ray Diffraction	62
2.2.1 ω - 2θ scans	62

2.2.2	Reciprocal Space Mapping	64
2.3	Rutherford Backscattering Spectroscopy	67
2.4	Hall Effect and Resistivity Measurements	68
2.5	Spectrophotometry	72
2.6	Transient Absorption Spectroscopy	73
3	ELECTRONIC STRUCTURE AND BAND ALIGNMENT OF TERBIUM ARSENIDE NANOPARTICLES IN GaAs AND In_{0.53}Ga_{0.47}As	76
3.1	Growth Conditions and Sample Properties	77
3.2	Carrier Dynamics in GaAs	78
3.2.1	Measurement and Data Analysis Details	80
3.2.2	Fluence Dependent Optical Pump Terahertz Probe Results . .	81
3.2.3	Temperature Dependent Optical Pump Terahertz Probe Results	86
3.3	Carrier Dynamics in In _{0.53} Ga _{0.47} As	86
3.4	Optical Absorption	91
3.5	Determining the Fermi Level	93
3.6	Proposing a Band Alignment	94
3.7	TbAs Nanoparticle Electronic Structure Conclusion	97
4	GROWTH AND CHARACTERIZATION OF TbAs FILMS . . .	99
4.1	Molecular Beam Epitaxy Growth of TbAs Films	100
4.2	Structural Properties of TbAs Films	101
4.3	TbAs Film's Optical Band Gap	105
4.4	Electrical Properties of TbAs Films	108
4.5	TbAs Drude Edge	112
4.6	Conclusion	114
5	GROWTH AND CHARACTERIZATION OF ErAs:GaBiAs . . .	116
5.1	Growth of ErAs:GaBiAs	118
5.2	Band Gap of ErAs:GaBiAs	122
5.3	Film Relaxation and Morphology	127
5.4	ErAs:GaBiAs Electronic Properties	133
5.5	Charge Carrier Lifetimes	136
5.6	Conclusion	143

6 CONCLUSION AND FUTURE WORK	144
6.1 Implications of the TbAs Nanoparticle Band Structure	144
6.2 TbAs Film Applications	148
6.3 Future Work on ErAs:GaBiAs	149
BIBLIOGRAPHY	150
Appendix	
A PASSIVE POWER GENERATION IN A TEMPORALLY-VARYING TEMPERATURE ENVIRONMENT VIA THERMOELECTRICS	167
A.1 Model Description	168
A.2 Simulation Results and Discussion	176
A.3 Experimental Verification	182
A.4 Optimization	184
A.5 Summary and Applications	188
B FIGURE REPRINT PERMISSIONS	190

LIST OF TABLES

1.1	Effect of substrate orientation on the nanostructure geometry. . . .	9
1.2	Possible Drude edge wavelengths of the LN-V films	35
5.1	The majority carrier type, carrier concentration, resistivity, and mobility of the ErAs:GaBiAs samples without droplets depend on the Er and Bi incorporation.	135
5.2	The majority carrier type, mobility, and resistivity of the ErAs:GaBiAs samples with droplets all depend on the bismuth and erbium incorporation as well as the presence of droplets on the surface.	137
A.1	Material properties of HE1 and HE2. [1, 2, 3, 4] Reprinted from [5] with permission from Elsevier.	170
A.2	Material properties of the air. [6] Reprinted from [5] with permission from Elsevier.	171
A.3	Fitting parameters for radiative exchange between HE2 and the sun, based on the angle of the sun as a function of time on July 10th, 11th, and 12th.[7, 8]Reprinted from [5] with permission from Elsevier.	174
A.4	Device specifications. Reprinted from [9] with permission from Elsevier.	183

LIST OF FIGURES

1.1	Cross-sectional transmission electron microscopy images comparing the random distribution of nanoparticles grown via co-deposition and the nanopartilces placed at specific locations grown via the growth interrupt method. The co-deposition sample (a) is ErAs in $\text{In}_{0.53}\text{Ga}_{0.47}\text{As}$, [10] and the growth interrupt sample (b) is LuAs in $\text{In}_{0.53}\text{Ga}_{0.47}\text{As}$. [11] (a) is adapted with permission from [10] Copyright 2008 American Chemical Society. (b) is reprinted from [11], with the permission of AIP Publishing.	3
1.2	The co-deposition of Er in $\text{In}_{0.53}\text{Ga}_{0.47}\text{As}$ with Er concentrations (a) below, (b) at, and (c) above the solid solubility limit. The nanoparticles are circled for ease of identification. [12] Reprinted with permission from [12]. Copyright 2011, American Vacuum Society. .	5
1.3	TEM images along the [110] and $\bar{1}\bar{1}0$ directions of ErSb co-deposited in GaSb showing (a,b) the formation of rods that (c,d) increase in density with increaed ErSb concentration. At higher concentrations the rods grow horizontally (e,f) and finally form lamellar nanosheets (g,h) at the highest ErSb compositions studied. [13] Reprinted with permission from [13]. Copyright 2013 American Chemical Society .	8
1.4	An atom probe tomography reconstruction of (a) one TbErAs nanoparticle indicating the 5 at.% Tb isosurface and the 5 at.% Er isosurface, suggesting a core-shell structure. A zoomed out reconstruction (b) shows that all the Er rich regions are surrounded by Tb rich regions. A concentration profile (c) shows the the concentration of Tb (red), Er (blue) and the Tb/Er ratio (black) in the nanoparticle, indicating a mixed TbErAs core and pure TbAs shell. [14]	11
1.5	Scanning tunneling microsocpy images showing the four types of ErSb that can form on GaSb. [15] Reprinted from [15], with the permission of AIP Publishing.	15

1.6	Cross sectional TEM images of a (a) LaAs film grown using the barrier layer and a (d) LaAs film grown without the barrier layer. Fast Fourier transform approximate the selective area diffraction patterns of the (b) LaAs/LuAs/GaAs interface and the (c) LaAs/GaAs interface.[16] Reprinted from [16], with the permission of AIP Publishing.	20
1.7	Cross-section TEM image of (a) conventionally grown and (b) nanoparticle seeded ErAs layers capped with GaAs.[17] Reprinted from [17], with the permission of AIP Publishing.	23
1.8	HAADF STEM image showing the clean and atomically abrupt ErAs GaAs interface. The overlay represents the atomic column positions with blue circles representing As, red circles representing Er, and yellow circles representing Ga.[18] Reprinted from [18], with the permission of AIP Publishing.	24
1.9	LDA+U calculated band structure and density of states for ErAs. In the density of states diagram the total, Er 5d, Er 4f, and As 4p states are indicated by black, red, green, and blue lines, respectively.[19] Reprinted figure with permission from [19] Copyright 2009 by the American Physical Society.	26
1.10	(a) Averaged differential conductance curves of ErAs nanoparticles, red line, protruding from the GaAs matrix, black line obtained with cross-sectional scanning tunneling spectroscopy. (b)Individual differential conductance curves at different locations ontop of the ErAs nanoparticle and GaAs matrix.[20] Reprinted figure with permission from [20] Copyright 2011 by the American Physical Society.	28
1.11	The absorption feature in ErAs/GaAs superlattices increases in wavelength with increased ErAs deposition amount per layer.[21] Reprinted from [21], with the permission of AIP Publishing.	32
1.12	The normalized temperature dependent resistivity for films of ErAs, LuAs, and LaAs; consistent with the films being metallic or semimetallic.[16] Reprinted from [16], with the permission of AIP Publishing.	36
1.13	The (a) conductivity, (b) mobility, and (c) electron concentration all depend on the amount of ErAs (red) and ScAs (blue) co-deposited in $\text{In}_{0.53}\text{Ga}_{0.47}\text{As}$.[22] Reprinted from [22], with permission from Elsevier	39

1.14	The room temperature carrier concentration of ErAs:(In _{0.52} Al _{0.48} As) _x (In _{0.53} Ga _{0.47} As) _{1-x} as a function of the amount of In _{0.52} Al _{0.48} As. The black circles represent the measured values, the line represents the carrier concentration predicted by the Fermi-Dirac integral where the energy difference between the Fermi level and conduction band edge changes linearly with composition.[23] Reprinted from [23], with the permission of AIP Publishing.	41
1.15	The activation energy, which is related to the Fermi level, depends on the lanthanide type and LN-V deposition amount.[11] Reprinted from [11], with the permission of AIP Publishing.	42
1.16	The Seebeck coefficient and electrical conductivity both increase with temperature for 0.6% ErAs co-deposited in (In _{0.53} Ga _{0.47} As) _{0.8} (In _{0.52} Al _{0.48} As) _{0.2} , suggesting electron filtering.[24] Reprinted from [24], with the permission of AIP Publishing.	45
1.17	The reduction in thermal conductivity with increasing ErAs amount in In _{0.53} Ga _{0.47} As.[10] Addapted with permission from [10] Copyright 2008 American Chemical Society	46
1.18	The power output of a segmented thermoelectric power generator made from 50 μ m 0.6% ErAs co-depostied in (In _{0.53} Ga _{0.47} As) _{1-x} (In _{0.52} Al _{0.48} As) _x and 0.8 mm Bi ₂ Te ₃ , showing a power output of 6.3 W.[24] Reprinted from [24], with the permission of AIP Publishing.	49
1.19	The ZT of 0.6% ErAs co-depostied in In _{0.53} Ga _{0.47-x} Al _x As as a function of temperature, showing a ZT of 1.3 at 800 K.[23] Reprinted from [23], with the permission of AIP Publishing.	50
1.20	A room temperature J-V curve for a conventional tunnel junction (dashed line) and an ErAs enhanced tunnel junction (solid line and inset). Depicting the drastically reduced bias required to achieve the same tunneling current.[25] Reprinted from [25], with the permission of AIP Publishing.	53
2.1	Schematic of a general molecular beam epitaxy system. Schematic from http://lase.ece.utexas.edu/mbe.php , reprinted with permission from Professor Seth Bank.	58
2.2	Schematic of the X-ray diffraction geometry.	63

2.3	Schematic showing (a) a lattice matched film (black circles) on a substrate (open circles), (b) a compressively strained film on a substrate, and (c) a relaxed film on a substrate.	66
2.4	A randomly oriented and simulated RBS spectrum of ErAs:GaAs with 1.4% ErAs.	68
2.5	A schematic showing the van der Pauw geometry used for resistivity and Hall effect measurements. The black triangles represent the contacts, the squiggly lines represent the probes, and the circle with the X represents the direction of the magnetic field.	69
3.1	Schematic showing TbAs nanoparticles dispersed throughout a III-V matrix as a result of co-depositing Tb with the III-V materials. Reprinted figure with permission from [26]. Copyright 2014 by the American Physical Society.	79
3.2	Long delay times (a) cannot be fit by a single exponential decay (solid black line) and short delay times (b) cannot be fit by a double exponential decay (red dashed lines). To fit the entirety of the data a triple exponential decay is required (green dot-dashed line).[26] Reprinted figure with permission from [26]. Copyright 2014 by the American Physical Society.	82
3.3	The relaxation of carriers into the TbAs nanoparticle (a) does not show a dependence on optical pump fluence while the fraction of carriers relaxing into the nanoparticles (b) decreases with increasing pump fluence. The recombination lifetime of carriers in the TbAs nanoparticle (c) increases with increasing pump fluence while the fraction of carriers recombining in or leaving the TbAs nanoparticles (d) decreases with increasing pump fluence. The relaxation time across the bulk band gap (e) approaches the lifetime of bulk GaAs and the fraction of carriers relaxing across the bulk band gap (f) approaches one with increasing pump fluence. This suggests that TbAs nanoparticles are indirect semiconductors.[26] Reprinted figure with permission from [26]. Copyright 2014 by the American Physical Society.	85
3.4	The fraction of carriers relaxing into the TbAs nanoparticle states (black squares) and the fraction of carriers recombining or leaving the TbAs nanoparticles (red circles) does not statistically depend on temperature.[26] Reprinted figure with permission from [26]. Copyright 2014 by the American Physical Society.	87

3.5	The exponential decay in THz absorption for the TbAs:In _{0.53} Ga _{0.47} As sample as a function of time, depicting the need for triple (red), double (blue), and single (black) exponential fits. Reprinted from [27], with the permission of AIP Publishing.	88
3.6	(a) The relaxation time of each of the three processes (relaxation into the nanoparticles shown as black squares, emptying or recombining in the nanoparticles shown as red circles, and relaxation across the matrix's band gap shown as blue triangles) as a function of pump fluence is shown for the TbAs:In _{0.53} Ga _{0.47} As sample (solid symbols) and the TbAs:GaAs sample (hollow symbols). (b) The fraction of carriers participating in each relaxation process as a function of pump fluence is shown for both the TbAs:In _{0.53} Ga _{0.47} As sample and the TbAs:GaAs sample. Reprinted from [27], with the permission of AIP Publishing.	89
3.7	A Tauc Plot for an indirect absorption with the linear fits (dashed lines) was used to calculate an absorption energy of 0.63 ± 0.01 eV for the TbAs:GaAs system (black) and 0.43 ± 0.01 eV for the TbAs:In _{0.53} Ga _{0.47} As (red) system. Note that the detector cuts out for energies below 0.5 eV.[27] Adapted from [27], with the permission of AIP Publishing.	92
3.8	Free electron concentration of the TbAs:GaAs (black dots) strongly depends on temperature, until unintentional doping (green dashed line) dominates, allowing an exponential fit (red line) to estimate a Fermi level. The degenerate TbAs:In _{0.53} Ga _{0.47} As (blue dots) has little temperature dependence.[27] Reprinted from [27], with the permission of AIP Publishing.	94
3.9	Schematic showing the proposed band alignments of TbAs nanoparticles (red) in In _{0.53} Ga _{0.47} As (yellow) and GaAs (blue). Energy offsets are shown with green arrows, dashed lines represent the nanocomposites' estimated Fermi level, thin lines represent the first energy level within the nanoparticle, thick lines represent band edges, and dotted lines represent exaggerated band bending at the nanoparticle matrix interface. Note that all energies involving the TbAs nanoparticle are relative to the first energy level; the conduction and valence band edges of TbAs are only included as an estimate.[27] Adapted from [27], with the permission of AIP Publishing.	96

4.1	RHEED pattern observed ~ 150 nm into the thick TbAs sample (a) shows a clear, streaky 1×1 RHEED pattern with (b) rotated 90° showing a slight degradation in morphology. These represent the RHEED patterns observed throughout the growth of both samples.[28]	101
4.2	004 ω -2 Θ scan of the thick (black) and thin (red) TbAs samples. The peak corresponding to the TbAs films is broad with a low intensity, indicating defects likely introduced from exceeding the critical thickness of TbAs.[28]	102
4.3	224 RSM scan of the thin TbAs sample. The green dashed line represents the direction in which a fully strained film peak would be located and the red dashed line represents the direction in which a fully relaxed film peak would be located. The broadening of the TbAs film peak indicates that the film has some mosaic character. [28] . .	103
4.4	224 RSM scan of the thick TbAs sample. Again, the green dashed line represents the direction in which a fully strained film peak would be located and the red dashed line represents the direction in which a fully relaxed film peak would be located. The broadening of the TbAs film peak indicates that the film has some mosaic character.	104
4.5	Cross-section EDS maps of Tb, Ga, and As, showing a clear TbAs layer on top of GaAs.[28]	105
4.6	Cross-section TEM images of the (a) thicker TbAs sample, (b) zoomed-in on the TbAs-GaAs buffer layer interface, and (c) an electron diffraction pattern of the TbAs film.[28]	106
4.7	Cross-section TEM images of the thinner TbAs samples showing a film thickness of 68 nm. Note that during the FIB process, much of film was thinned too much, resulting in the film being removed. . .	107
4.8	Indirect Tauc plot for the TbAs thick and thin samples, revealing an optical absorption of 435 meV and 517 meV, respectively. The solid lines show the measured data, dashed line show the linear fits used to obtain the optical band gap.	109
4.9	The resistivity (top) and free electron concentration (bottom) of both the thick and thin TbAs samples does not change significantly over the temperature range measured.[28]	111

4.10	The mobility of both the thick and thin TbAs samples is ~ 25 cm ² /V-s and does not change significantly over the temperature range measured.	112
4.11	A schematic showing that group III atoms want to donate electrons while group V atoms want to accept the electrons. In the rock salt crystal structure, this results in planes of group III atoms giving electrons to the planes above and below of group V atoms. The LN-V film has mixed planes of LN and group V atoms. Thus, the extra atoms from the interfacial group III atoms adds carriers to the LN-V film.	113
4.12	Reflection (solid lines) and transmission (dashed lines) measurements of the thick and thin TbAs samples show a possible Drude edge at $\sim 2.75 \mu\text{m}$. [28]	115
5.1	Graph showing the Bi and Er growth conditions, samples are identified by relative amounts of Er and Bi in the samples without Ga droplets. ErAs and bismuth concentrations are determined by characterization methods discussed below. [29]	119
5.2	$\omega - 2\Theta$ scans of the <i>No Er Low Bi</i> and <i>No Er High Bi</i> samples show Bi concentrations of 2.6% and 5.3%, respectively.	120
5.3	The growth conditions for each droplet sample are shown as a combination of Bi beam equivalent pressures of 0, 1.02×10^{-8} , and 1.75×10^{-8} Torr and ErAs concentrations of 0%, 1.14%, and 2.6%. Note that the ErAs:GaAs samples were measured with RBS to calibrate the amount of ErAs in all of the films.	122
5.4	The band gap obtained from the Tauc plot (inset) and bismuth concentration (calculated using a previously developed model [30]) for the samples without droplets. The dashed lines represent Bi concentrations obtained from XRD. The inset is the direct gap Tauc plot where the symbols show the measured data and the dashed lines are the linear fits used to extrapolate the band gaps. [29]	124

5.5	Tauc plots of the ErAs:GaBiAs samples with droplets, as-grown (a) and mechanically polished (b). The solid lines represent the measured data while the dashed lines represent the linear fit used to extrapolate the band gap. Note that samples <i>Droplet, Low Er No Bi</i> and <i>Droplet, High Er No Bi</i> did not have Ga droplets and thus were not mechanically polished. The peaks present in samples <i>Droplet, Low Er No Bi</i> and <i>Droplet, High Er No Bi</i> have previously been attributed to surface plasmon resonances from the ErAs nanoparticle.[31, 21] The samples containing Bi do not exhibit this peak as the resonance is likely to have been suppressed from absorption in the GaBiAs layer or shifted to energies outside our detection range.	125
5.6	Bar chart showing the band gap of the ErAs:GaBiAs samples with droplets, as-grown (a) and mechanically polished (b) samples. . . .	126
5.7	Select cross sectional transmission electron microscopy (TEM) images of the ErAs:GaBiAs samples without droplets, (a) is a selection from sample <i>Low Er No Bi</i> with (b) zoomed in, (c) shows a selection from <i>Low Er Low Bi</i> with (d) being further zoomed in. The insets in (b) and (d) are the diffraction patterns for the <i>Low Er No Bi</i> and <i>Low Er Low Bi</i> samples, respectively. It is unclear from the images whether or not ErAs nanoparticles formed, but both the micrographs and diffraction patterns suggest that the Bi containing samples have a lower density of twin boundaries.	129
5.8	Reciprocal space maps (RSM) of samples (a) <i>High Er No Bi</i> (b) <i>No Er Low Bi</i> (c) <i>High Er Low Bi</i> and (d) <i>High Er High Bi</i> with the vertical dashed line showing the strained line and the angled dashed line showing the relaxation line.[29]	130

5.9	A selection of scanning electron microscope (SEM) and energy dispersive spectroscopy (EDS) maps of the ErAs:GaBiAs samples with droplets, both as grown and post polish. SEM images of the as grown (a) <i>Droplet, No Er High Bi</i> , (b) <i>Droplet, Low Er High Bi</i> , and (c) <i>Droplet, High Er High Bi</i> show that increasing the Er amount results in more and larger Ga droplets. The GaAs pillars present after droplet removal are shown for sample <i>Droplet, Low Er High Bi, Polished</i> (d). Mixed color EDS map (e) of the <i>Droplet, High Er High Bi</i> shows that the droplets are mostly (h) Ga, shown as blue, and lack (g) As, shown as green. Bi and Er are depicted as red and white, respectively. A mixed color EDS map (f) of sample <i>Droplet, Low Er High Bi, Polished</i> shows that the pillars are of the same material at the matrix. In (f) white is As, also shown in (i), red is Ga, also shown in (j), Bi is white, and Er is light blue. The inability of the EDS maps to distinguish the pillars from the matrix suggests that the pillars are the start of droplet epitaxial growth.	132
5.10	Reciprocal space maps (RSM) of samples (a) <i>Droplet, No Er High Bi</i> and (b) <i>Droplet, High Er High Bi</i> show that the ErAs:GaBiAs samples with droplets remain strained but have significantly less Bi incorporation than predicted by spectrophotometry.	134
5.11	Transient absorption optical pump optical probe measurements showing the change in the probes absorption as a function of time after the pump laser. Note that transients have been vertically offset. The insets are a zoomed-in view of the first few picoseconds of each measurement.[29]	139

5.12	Schematic showing the proposed processes that change the change in absorption. Two relaxation processes are present in the ErAs:GaAs samples (a), relaxation across the bulk band gap (90.0 ps) and relaxation of carriers into the ErAs nanoparticles (1.3 ps). Two processes are present in the GaBiAs samples (b), relaxation across the bulk band gap (90.0 ps) and recovery of the bleached Bi E+ valence band to defect transition (89.8 and 28.6 ps). The ErAs:GaBiAs samples have up to four processes (c), relaxation across the bulk band gap (90.0 ps), relaxation of carriers into the ErAs nanoparticles (1.3 ps), recovery of the bleached Bi E+ valence band to defect transition (89.8 and 28.6 ps), and recovery of the bleached Bi E+ valence band to defect transition with the aid of semimetallic ErAs nanoparticles (1.2 ps). In this schematic the recovery of the bleached Bi E+ valence band to defect transition is shown as filling the emptied Bi E+ valence band states by carriers relaxing out of the defect states or carriers relaxing out of the ErAs nanoparticle. Alternatively, the recovery of the bleached Bi E+ valence band to defect transition could occur by filling the emptied Bi E+ valence band states from the conduction band or by emptying the electrons in the defect states within the band gap into the ErAs nanoparticle. Note that a dashed line is used for the E+ valence band in (b) and (c) to show that the E+ valence band may not form a complete band at the Bi concentrations studied here. [29]	141
6.1	The temperature dependent (a) electrical conductivity, (b) Seebeck coefficient, and (c) thermoelectric power factor of TbAs:In _{0.53} Ga _{0.47} As compared to ErAs:In _{0.53} Ga _{0.47} As and Si:In _{0.53} Ga _{0.47} As.	146
6.2	The simple model's prediction of (a) electrical conductivity, (b) Seebeck coefficient, and (c) thermoelectric power factor improvement provided by a barrier that perfectly scatters electrons with energy lower than the barrier height. The red dashed box highlights the estimated barrier height that TbAs provides.	147
A.1	A schematic of the device setup. Heat exchanger 1 is the sphere below the thermoelectric plate, with a temperature of Tb. Heat exchanger 2 is the rod array and copper plate assembly mounted to the top of the thermoelectric plate, with a temperature of Tt. The inset shows the array of thermoelectric elements that make up the thermoelectric module. [5] Reprinted from [5] with permission from Elsevier.	169

A.2	(a) Temperature profiles for HE1, HE2, and the surrounding fluid; (b) resulting temperature difference ($T_t - T_b$) across the thermoelectric; (c) instantaneous and time-averaged power density generated by the thermoelectric device. [5] Reprinted from [5] with permission from Elsevier.	178
A.3	Average power density produced by the thermoelectric module as a function of the thermoelectric modules surface area. Inset shows that power increases with size at small sizes. [5] Reprinted from [5] with permission from Elsevier.	181
A.4	Picture of the devices tested, labels indicate the quartz sphere's diameter. [9] Reprinted from [9] with permission from Elsevier. . .	182
A.5	Experimental and theoretical power profiles for the 110 mm device and the corresponding environments temperature profile, indicating good agreement between theory and experiment.[9] Reprinted from [9] with permission from Elsevier.	184
A.6	Experimental and theoretical average power output as a function of K_{rapid}/K_{slow} indicating increased device sizes result in increased power output.[9] Reprinted from [9] with permission from Elsevier.	186
A.7	(a) Theoretical prediction of the average power as a function of the heat exchangers' heat transfer coefficients for the 22 mm device with a 1 hour period of temperature oscillation. (b) Experimental average power as a function of layer of insulation of the 22 mm devices, effectively decreasing the heat transfer coefficient of the slow heat exchanger. Measurements were performed with a 1 hour period of temperature oscillation.[9] Reprinted from [9] with permission from Elsevier.	187

ABSTRACT

Lanthanide monopnictides have properties that makes them interesting for many applications including thermoelectrics and photoconductive switches. Despite their usefulness, many of their fundamental properties remain unknown. This dissertation explores the fundamental properties of TbAs, both as nanoparticles and films. This dissertation also presents a novel lanthanide monopnictide nanocomposite as a possible candidate material for photoconductive switches.

To study the electronic structure of TbAs we used fluence dependent optical pump terahertz probe measurements, revealing that TbAs nanoparticles saturate and are likely semiconductors. Spectrophotometry shows a large blue shift in the optical absorption energy when the matrix is changed from $\text{In}_{0.53}\text{Ga}_{0.47}\text{As}$ to GaAs. To explore these differences, temperature dependent Hall effect measurements are utilized, revealing that TbAs: $\text{In}_{0.53}\text{Ga}_{0.47}\text{As}$ is degenerately doped while TbAs:GaAs has the Fermi level located near the center of the GaAs band gap. These combined measurements indicate that TbAs forms a type I (straddled) heterojunction with GaAs and a type II (staggered) heterojunction with $\text{In}_{0.53}\text{Ga}_{0.47}\text{As}$.

The study of TbAs nanoparticles revealed that TbAs is a semiconductor, but the band gap energy remains unknown. Films of TbAs were grown in an attempt to determine the band gap. Spectrophotometry reveals the optical band gap is dependent upon film thickness. Additionally, Hall effect measurements show that the films are degenerately doped with the carrier concentration also depending on thickness. Degenerately doping causes a Burstein-Moss shift in the optical absorption where the magnitude of the shift depends on carrier concentration, and thus thickness.

In addition to studying the fundamental properties of TbAs, this dissertation explores ErAs:GaBiAs as a novel candidate material for photoconductive switches.

Spectrophotometry measurements reveal that bismuth reduces the band gap, as expected, allowing these materials to be pumped with fiber-coupled lasers. Hall effect measurements reveal that ErAs pins the Fermi level within the band gap; resulting in a high dark resistance while maintaining a high mobility. The ErAs nanoparticles also provide a carrier recombination pathway that results in a short carrier lifetime, shown by transient absorption optical pump optical probe measurements. These measured properties show that ErAs:GaBiAs is a promising choice for fiber-couple photoconductive switches.

Chapter 1

REVIEW OF LANTHANIDE MONOPNICTIDE MATERIALS

1.1 Introduction

Lanthanide pnictides (LN-V), also commonly referred to as rare-earth pnictides (RE-V), have become of great interest in recent years for a wide range of applications including: thermoelectrics, tunnel junctions, photoconductive switches, and ohmic contacts.[32] Much of the early work on LN-V materials focused on molecular beam epitaxy (MBE) grown ErAs and ErSb nanoparticles embedded in III-As and III-Sb semiconductors. The MBE growth, properties, and applications of ErAs and ErSb was previously reviewed by Hanson et al.[32] Duan et al. also provided a review on the electronic, magnetic, and transport properties of rare-earth monopnictides including: progress in theoretical advancements in electronic structure calculations; the electronic, magnetic, and transport properties of Gd-V, Eu-V, and Er-V; half-metallicity, metal-insulator transitions, and magnetic orderings; and possible ways to improve the magnetic and electronic properties for spintronic applications.[33]

Since those reviews, the field of LN-V materials has expanded. In the past decade, ErAs and ErSb have been studied more thoroughly, and other LN-V systems such as TbAs, LuAs, LaAs, GdAs, and GdN have become of interest. In this chapter I will focus on the growth, properties, and applications of LN-V materials, highlighting the commonalities and differences among them and how the work presented in this dissertation fits into the general field of LN-V materials. Section 1.2 will discuss the various growth mechanisms for LN-V materials including nanoparticle and film growth. Section 1.3 discusses the band structure of the various LN-V materials. The optical properties, electrical properties, and thermal conductivity are presented in Sections 1.4, 1.5, 1.6, respectively. Section 1.7 will discuss some of the recent advancements

in device applications as a result of LN-V materials. Finally, section 1.8 outlines the remainder of this thesis. Note that Natali et al. recently provided a review on the rare-earth mononitrides, and thus our discussion on rare-earth mononitrides will be limited.[34] Also, while Sc is not technically a lanthanide, we will discuss the progress made in Sc-V particles and films as they provide a nice comparison to many of the other LN-V material systems.

The high quality growth of LN-V nanoparticles and films, and subsequently their properties, are possible because of the crystal structure of LN-V materials. Thus, before delving into the growth and resulting properties of LN-V based materials I will highlight some of the important structural properties of the LN-V films. Many of the LN-V materials including, but not limited to, ErAs, LuAs, GdAs, TbAs, LaAs, GdN, and ErSb have the rocksalt crystal structure. This allows for a continuous group V sublattice between the zincblende III-V and rocksalt LN-V materials.[32, 11, 35, 36, 37, 16, 38, 39, 40, 13] Note that LaAs can form multiple stable crystal phases, including LaAs, LaAs₂, and La₄As₃, and multiple stable orientations. This is likely part of the reason that it is difficult to grow LaAs films and difficult to grow high-quality III-V on top of LaAs nanoparticles and films; this will be discussed in more detail below.[11, 16, 38, 39]

1.2 Growth of LN-V Materials

To date, most of the LN-V work has been done on materials grown via molecular beam epitaxy (MBE), either as LN-V nanoparticles co-deposited within the III-V matrix, LN-V nanoparticles deposited during a III-V matrix growth interrupt, or LN-V grown as complete films. In addition to the MBE growth of LN-V, a few other techniques used for bulk and thin film growth of LN-V materials that are worth mentioning include: vapor-solid reaction in ampoules, metal organic vapor phase epitaxy, pulsed-laser deposition, and reactive ion sputtering. Additionally, inert gas condensation has been utilized to grow LN-V nanoparticles absent of a host material.[41]

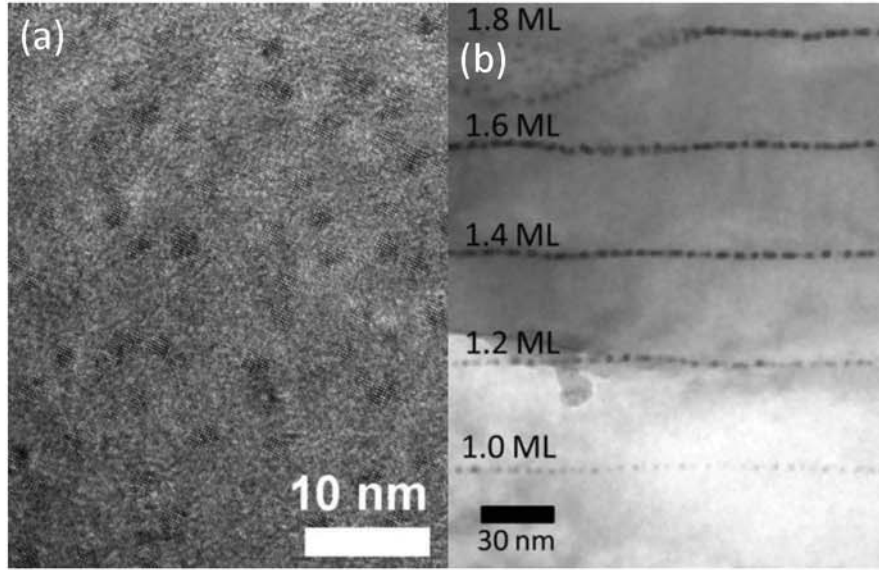


Figure 1.1: Cross-sectional transmission electron microscopy images comparing the random distribution of nanoparticles grown via co-deposition and the nanoparticles placed at specific locations grown via the growth interrupt method. The co-deposition sample (a) is ErAs in $\text{In}_{0.53}\text{Ga}_{0.47}\text{As}$, [10] and the growth interrupt sample (b) is LuAs in $\text{In}_{0.53}\text{Ga}_{0.47}\text{As}$. [11] (a) is adapted with permission from [10] Copyright 2008 American Chemical Society. (b) is reprinted from [11], with the permission of AIP Publishing.

1.2.1 MBE Growth of LN-V Nanostructures

In recent years much of the interest in LN-V materials has been in the form of nanostructures epitaxially deposited in LN-V films. As mentioned above, there are two MBE growth methods to incorporate LN-V nanostructures in III-V matrices: co-deposition and growth interrupt. Co-deposition is used to randomly, albeit evenly, disperse the nanostructures throughout the film, example shown in Fig. 1.1(a). Alternatively, the growth interrupt method is used to grow superlattices of LN-V nanostructures or to place the nanostructures at a particular location within the film, such as in a p/n junction, example shown in Fig. 1.1(b). In this section we will discuss these growth mechanisms and the effects of changing the growth parameters on the geometry of the nanostructures.

1.2.1.1 Nanostructure Growth via Co-deposition

The general co-deposition growth mechanism holds true for most of the LN-V:III-V systems, with each system having minor differences. Typically, as LN atoms impinge on the surface they displace the group III atoms and bond with the group V atoms already on the surface. As the amount of LN atoms incorporating increases above the solid solubility limit, the LN-V form nanostructures. This results in nanostructures randomly distributed throughout the film, Fig. 1.1(a). The co-deposition growth method has a few potential advantages over the growth interrupt method, discussed in detail below, including shorter growth times and reduced nanoparticle spacing.[42] While this growth mechanism is true for most of the LN-V:III-V systems, each system has minor differences such as the solid solubility limit and how the growth conditions may alter the final nanostructure shape and density. Below, I discuss these differences.

As mentioned above, LN-V form nanostructures if the concentration of LN exceeds the solid solubility limit of the III-V matrix. If the solid solubility limit is not exceeded, the LN atoms can dope the III-V matrix. Modeling shows that the LN-Ga substitution is the most favorable defect with the LN ion taking the isoelectronic trivalent configuration, resulting in some of the LN atoms being electrically inactive and not acting as dopants.[43] Doping with LN atoms can be achieved by incorporating low amounts of LN atoms. An alternative method to dope, and not form nanostructures, is to grow at colder temperatures. [44] Burke et al. observed that while nanoparticles may form for 0.2% and 0.4% Er in $\text{In}_{0.53}\text{Ga}_{0.47}\text{As}$ grown at 490°C, nanoparticles were not observed for 0.6% Er grown at 430°C.[44, 45] Under normal $\text{In}_{0.53}\text{Ga}_{0.47}\text{As}$ growth temperatures, 490°C, the Er solubility limit appears to be $\sim 0.08\%$, below which Er acts as a dopant.[12] Additionally, when growing at a temperature of 490°C with more than 0.2% Er, ErAs nanoparticles start to form in $\text{In}_{0.53}\text{Ga}_{0.47}\text{As}$, growing above and below the solubility limit is demonstrated in Fig. 1.2.[12, 22] Er has also been observed to dope InAs and GaAs, although the solubility limit in GaAs is much lower.[45]

An extensive study on the solubility limits has not been completed for all of

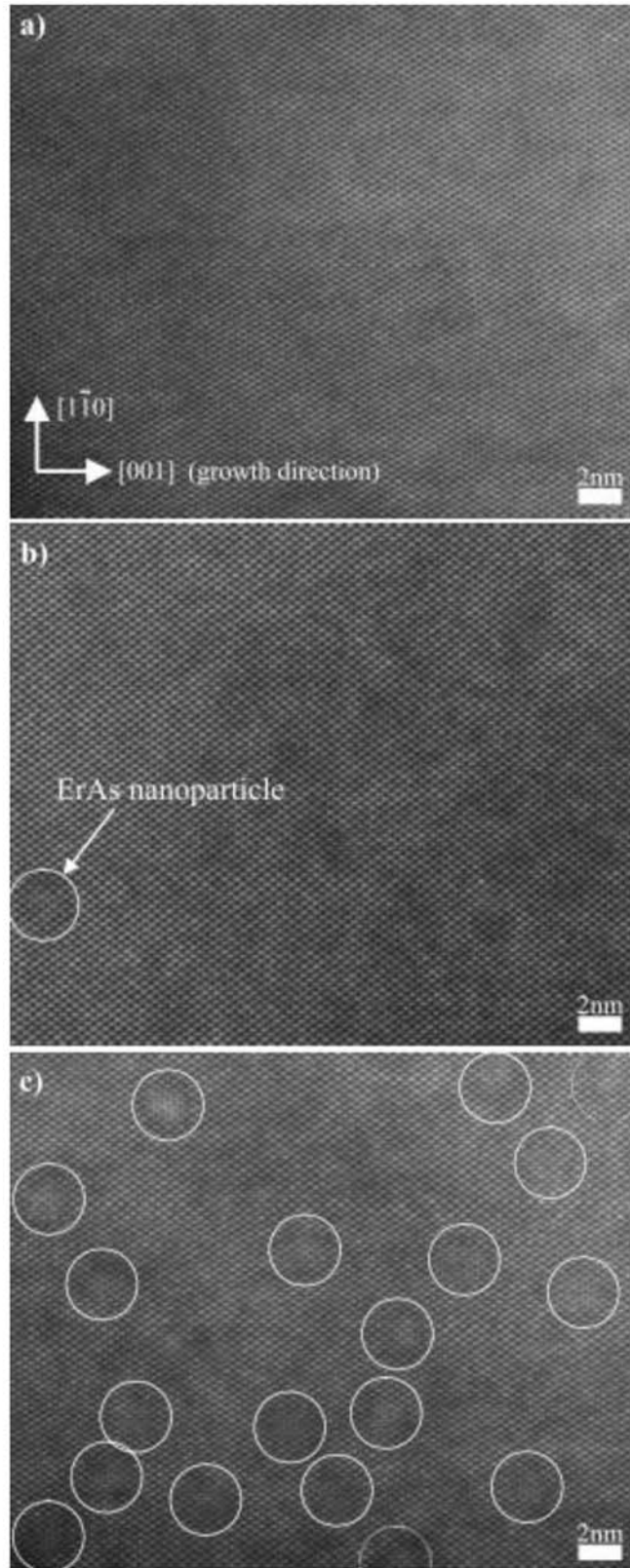


Figure 1.2: The co-deposition of Er in $\text{In}_{0.53}\text{Ga}_{0.47}\text{As}$ with Er concentrations (a) below, (b) at, and (c) above the solid solubility limit. The nanoparticles are circled for ease of identification.[12] Reprinted with permission from [12]. Copyright 2011, American Vacuum Society.

the RE:III-V combinations, but nanoparticles have been formed in many of the systems. The solubility of Tb in $\text{In}_{0.53}\text{Ga}_{0.47}\text{As}$ appears to be between 0.1 and 0.4% Tb; nanoparticles have not been observed for 0.2% TbAs in $\text{In}_{0.53}\text{Ga}_{0.47}\text{As}$ while particles have been observed for 0.8% TbAs in $\text{In}_{0.53}\text{Ga}_{0.47}\text{As}$. [37] HAADF-STEM plan-view images show that 1.8% TbAs co-deposited in GaAs at a growth temperature of 490°C results in nanoparticles. Nanoparticles likely form at lower concentrations but to-date they have not been confirmed with microscopy. [36] The co-deposition of $\geq 0.66\%$ ScAs in $\text{In}_{0.53}\text{Ga}_{0.47}\text{As}$ at a growth temperature of 460°C results in nanoparticles, again nanoparticles may form at lower concentrations. [22] ErAs nanoparticles have been observed in an $(\text{In}_{0.52}\text{Al}_{0.48}\text{As})_x(\text{In}_{0.53}\text{Ga}_{0.47}\text{As})_{1-x}$ digital alloy grown at 490°C with an ErAs concentration of 0.6%. [23] Additionally, ErSb nanoparticles form in InGaSb and GaSb with Er concentration as low as 0.4% and 0.1-5% Er, respectively. [46, 13] While, many of the LN elements appear to have relatively low solid solubility limits in III-As and III-Sb, the solid solubility limit of LN atoms in III-N can be significantly higher. Eu^{3+} doped GaN films have been reported with Eu^{3+} concentrations on the order of a few percent. [47, 48]

Adjusting the amount of LN incorporated not only determines the formation of nanoparticles, but also determines the nanostructure's shape. The co-deposition of Er in GaSb at concentrations just above the solubility limit (0.1-5%Er) results in the formation of spherical ErSb nanoparticles. Increasing the amount of Er in $\text{Ga}_{1-x}\text{Er}_x\text{Sb}$ from $x=0.001$ to $x=0.55$ changes the ErSb nanostructure's shape from: spherical nanoparticles, to rod-shaped structures aligned along the growth direction, to nanowires forming in the growth direction, to horizontally aligned nanorods, and finally to lamellar nanosheets oriented along the $\langle 1\bar{1}0 \rangle$ direction. [13, 49] Figure 1.3 shows the transition from vertical nanorods to lamellar nanosheets. [13] Note that ErSb nanorods form because GaSb does not wet the exposed ErSb islands, resulting in pits that are filled with ErSb. The number of nanorods is determined by the number of initial islands and thus the initial Er concentration. [13] Similarly, the ErAs nanostructure's shape in $\text{In}_{0.53}\text{Ga}_{0.47}\text{As}$ depends on the amount of Er deposition. At 3% Er, the

particles are slightly ($\sim 28\%$) elongated along the $\langle 110 \rangle$ direction and at 6% Er the elongated particles are preferentially located on the $\{114\}$ $\text{In}_{0.53}\text{Ga}_{0.47}\text{As}$ planes at an angle of $\sim \pm 19^\circ$ with the (001) surface and an average 4 nm spacing between planes of particles. This ordering is likely due to either interactions between nanoparticles or surface instability driven by the Er atoms.[50]

The shape of nanostructures can also be tuned by changing the growth temperature. Increasing the growth temperature from 400°C to 540°C changes ErSb from squares with in-plane dimensions of 3×3 nm to rectangular with in-plane dimensions of 8×17 nm with the elongation along the $[\bar{1}10]$ direction. Each growth temperature results in a similar surface coverage, indicating that the ErSb nanoparticles maintain a 4 monolayer (ML) (1.2 nm) thickness.[13] The observed changes in the nanoparticle shape with temperature is mostly due to changes in the adatom mobility on the growth surface.[51] The nanostructure shape depending on the growth temperature is also observed for ErSb nanorods grown at a temperature of 540°C , resulting in the ErSb nanorods branching into trees at periodic locations. This suggests that a reproducible instability at the growth surface exists where the balance between filling surface pits with ErSb and GaSb switches.[13] Similarly, a change in nanoinclusion shape is seen in ErAs: $\text{In}_{0.53}\text{Ga}_{0.47}\text{As}$, where ErAs nanoparticles co-deposited in $\text{In}_{0.53}\text{Ga}_{0.47}\text{As}$ at growth temperatures of 460 and 490°C tend to be randomly distributed and spherical; however, a growth temperature of 525°C results in ErAs nanoparticles that are either aligned or elongated in the $[1\bar{1}0]$ crystal direction.[45] Increasing the ErAs: $\text{In}_{0.53}\text{Ga}_{0.47}\text{As}$ growth temperature also results in an increased nanoparticle density.[44] These shape changes with growth temperature do not appear to be universal; for example, ErAs in GaAs does not appear to change shape with growth temperature, however increasing the growth temperature from 500 to 605°C does increase the nanoparticles size.[52, 32]

In addition to controlling the shape of nanoparticles with the amount of LN deposition and growth temperature, changing the substrate orientation can change the nanostructure shape. Growth of co-deposited ErAs nanoparticles on (001) GaAs substrates typically results in spherical ErAs nanoparticles. The co-deposition of ErAs and

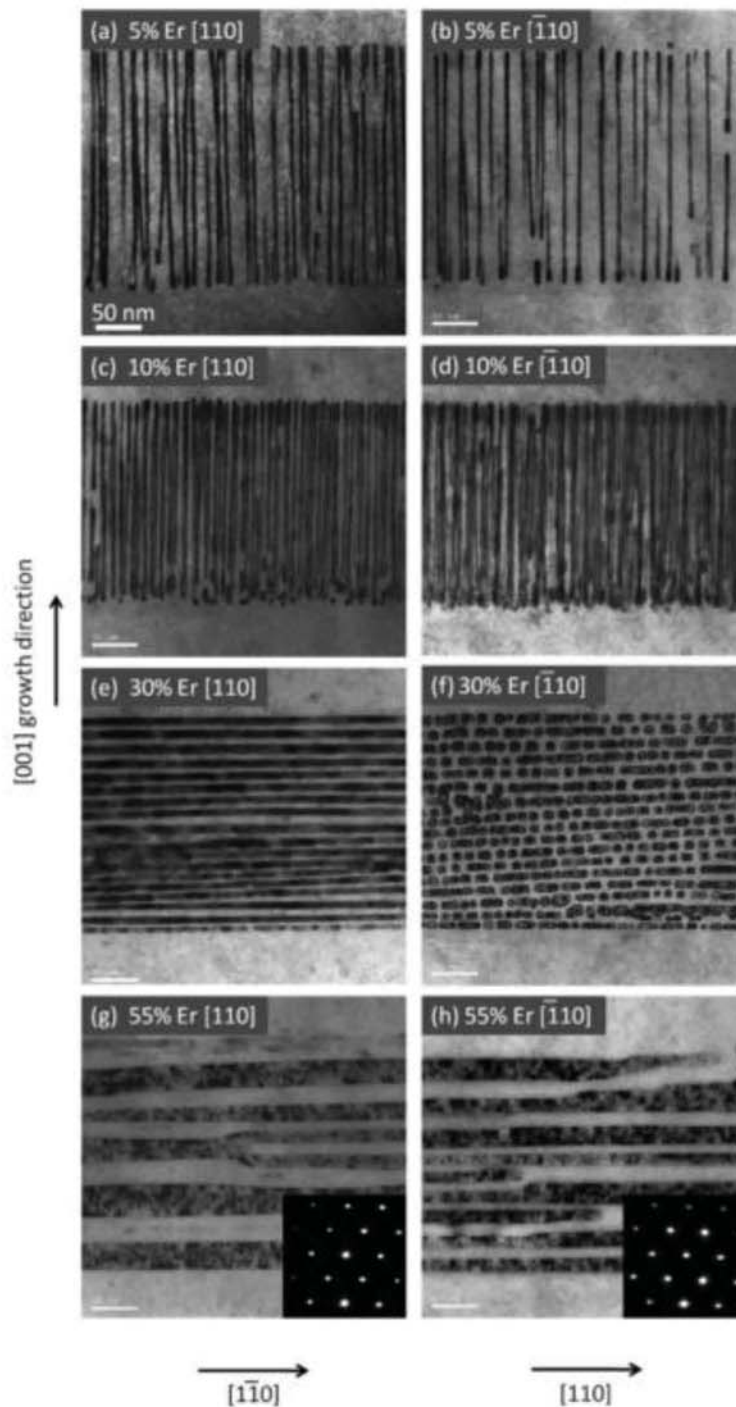


Figure 1.3: TEM images along the $[110]$ and $\bar{[110]}$ directions of ErSb co-deposited in GaSb showing (a,b) the formation of rods that (c,d) increase in density with increased ErSb concentration. At higher concentrations the rods grow horizontally (e,f) and finally form lamellar nanosheets (g,h) at the highest ErSb compositions studied.[13] Reprinted with permission from [13]. Copyright 2013 American Chemical Society

GaAs at 580°C on oriented substrates: (111)A, (211)A, (311)A, (511)A, and (114)A, shows that increasing the diffusion rate of Er adatoms on the surface changes the nanostructure. High diffusion rates result in nanorods while low diffusion rates favor small nanoparticles.[53, 54, 55] Table 1.1 shows the specific results from each substrate orientation, all samples were co-deposited and grown at 580°C. While most ErAs:GaAs co-deposition results in either nanoparticles or vertical nanorods, the growth on select substrate orientations results in nanorods tilted relative to the substrate. The tilt is likely due to how displaced Ga atoms and impinging Er atoms incorporate on the surface. The displaced Ga atoms cause additional GaAs to form at step edges while the ErAs forms primarily on the terraces. As ErAs continues to grow, GaAs continues to grow at the step edges, causing the observed tilt in the nanorod growth.[55, 54]

Substrate Orientation	Amount ErAs (%)	Nanostructure Type	Nanostructure Geometry	Nanostructure Spacing	Elongation Direction
(111)A[54]	6%	Rods	2 nm diameter	~6 nm	[111] (normal to surface)
(211)A[54]	6%	Rods	2 nm diameter	~5 nm	[211] (normal to surface)
(311)A[54]	10%	Rods	2 nm diameter	~4 nm	[211]
(411)A[55, 53]	6%	Rods	~2-3 nm diameter	~7 nm	[211]
(411)B[55]	6%	Nanoparticles	~2 nm diameter	~3 nm	-
(511)A[54]	10%	Elliptical Nanoparticles	2.7±0.5 nm wide 6.3±0.7 nm long	~3 nm	On (311) planes

Table 1.1: Effect of substrate orientation on the nanostructure geometry.

While the geometry of nanoinclusions depends on the amount of LN deposited, growth temperatures, and substrate orientation, in general the size of the nanoinclusion does not depend on the amount of LN deposited. Instead the amount of LN tends

to change the nanoparticles density.[50, 10] This allows us to state typical nanoparticle sizes. ErAs co-deposited in GaAs results in nanoparticles with diameters of 1.2-3 nm, higher growth temperatures result in larger particles.[32, 20] ErAs nanoparticles in $\text{In}_{0.53}\text{Ga}_{0.47}\text{As}$ typically have diameters of 1-3 nm.[22, 10] TbAs co-deposited in GaAs, grown at 490°C, results in nanoparticles with a diameter of 1.5 nm.[36, 50]. Additionally, cubic TbAs nanoparticles are observed with HAADF STEM in $\text{In}_{0.53}\text{Ga}_{0.47}\text{As}$ at concentrations of 0.8% TbAs with dimensions of ~ 1 nm.[37] ScAs nanoparticle are not easily distinguished from $\text{In}_{0.53}\text{Ga}_{0.47}\text{As}$ in TEM and they appear dark in STEM which easily overlaps with ion-milling damage during sample preparation. However, carrier concentration comparisons to ErAs: $\text{In}_{0.53}\text{Ga}_{0.47}\text{As}$ and atom probe tomography lead to an expectation that ScAs form nanoparticles larger than ErAs in $\text{In}_{0.53}\text{Ga}_{0.47}\text{As}$. [22, 56] It is also expected that ScErAs: $\text{In}_{0.53}\text{Ga}_{0.47}\text{As}$ form alloy nanoparticles with sizes between that of ScAs and ErAs.[56] This is contrary to the core-shell nanoparticles formed by TbErAs, discussed in more detail below.[14]

Above I mentioned that ScErAs nanoparticles are expected to form an alloy but TbErAs appears to form core-shell nanoparticles. Atom probe tomography, Fig. 1.4, shows that the co-deposition of 0.8% Tb and 0.4% Er into $\text{In}_{0.53}\text{Ga}_{0.47}\text{As}$ at 490°C results in nanoparticles with a pure TbAs shell and a mixed TbErAs core; STEM shows that the nanoparticles are coherent with the matrix and have a diameter of 2.4 nm.[14] A thermodynamic model that predicts the type of nanoparticle, core-shell vs mixed, based on metastable and kinetically limited states shows that it is practically impossible to have a "pure" ErAs core. The model also shows that at the nanoparticle sizes studied by Dongmo et al., it is thermodynamically favorable to have a "pure" TbAs shell. Note, at larger sizes it would be favorable to have a completely mixed particle.[14] Based upon the model, it is expected that co-depositing 0.8% Er and 0.4% Tb in GaAs should result in a ErAs shell and a mixed ErTbAs core; this is currently being studied with atom probe tomography.

It is worth noting that most of the LN amounts discussed in this paper have been calibrated with Rutherford backscattering spectroscopy (RBS) measurement due to the

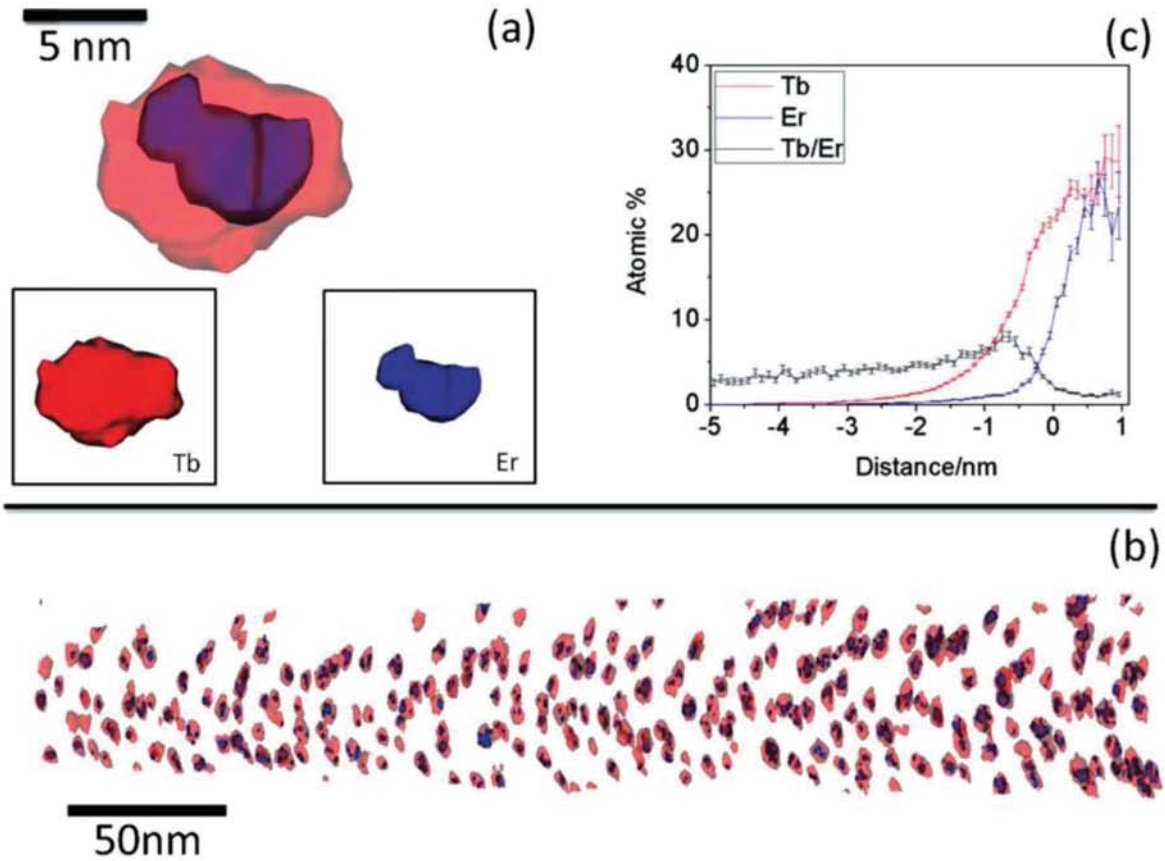


Figure 1.4: An atom probe tomography reconstruction of (a) one TbErAs nanoparticle indicating the 5 at.% Tb isosurface and the 5 at.% Er isosurface, suggesting a core-shell structure. A zoomed out reconstruction (b) shows that all the Er rich regions are surrounded by Tb rich regions. A concentration profile (c) shows the the concentration of Tb (red), Er (blue) and the Tb/Er ratio (black) in the nanoparticle, indicating a mixed TbErAs core and pure TbAs shell.[14]

challenges associated with determining RE amounts from x-ray diffraction (XRD) and secondary ion mass spectroscopy (SIMS). The LN atoms often cause a superdilation of the lattice, observed as the bonding length at the nanoparticle matrix interface expanding or contracting. Superdilation makes it difficult to determine LN amounts with XRD using Vegard's law. This has been observed for ErAs, ScAs, $\text{Sc}_{0.32}\text{Er}_{0.68}\text{As}$, and TbAs in GaAs, as well as TbAs in $\text{In}_{0.53}\text{Ga}_{0.47}\text{As}$. [57, 36, 37] Additionally, superdilation of the matrix makes lattice matching the LN-V nanoparticle to the III-V matrix difficult. For example, $\text{Sc}_{0.32}\text{Er}_{0.68}\text{As}$ has the same lattice constant as GaAs, but $\text{Sc}_{0.32}\text{Er}_{0.68}\text{As}$ nanoparticles in GaAs result a nanocomposite with a lattice constant larger than GaAs. Increasing the Sc amount to 0.5, resulting in $\text{Sc}_{0.5}\text{Er}_{0.5}\text{As}$, reduces the lattice-mismatch of the nanocomposite system, but does not completely eliminate it. [57] Additionally, RBS should be used instead of SIMS to determine the LN concentration because changing the growth parameters, such as growth temperature, changes the relative LN amounts that form nanoparticles and the amounts that dope the III-V matrix. This changes the bonding environment, and ultimately the amount of LN incorporated as measured by SIMS. RBS does not suffer from this problem. This discrepancy between SIMS and RBS measurements has been observed for Er in $\text{In}_{0.53}\text{Ga}_{0.47}\text{As}$. [44] Note that for many LN elements, the amount of LN is measured by RBS and calibrated to a flux measurement or the effusion cell temperature. Due to the low vapor pressure of Tb at the temperature of the ion gauge's filament, Tb sticks to the ion gauge's filament. This prevents an accurate flux measurements and can alter subsequent flux measurements. Thus, Tb growth rates must be calibrated via effusion cell temperature and not beam equivalent pressures. [36]

Another point worth noting is that standard wet chemical processes used on $\text{In}_{0.53}\text{Ga}_{0.47}\text{As}$ devices may be detrimental to the properties provided by LN-V nanoparticles co-deposited in $\text{In}_{0.53}\text{Ga}_{0.47}\text{As}$. This was observed for samples of TbAs co-deposited in $\text{In}_{0.53}\text{Ga}_{0.47}\text{As}$ where samples processed using the standard $\text{In}_{0.53}\text{Ga}_{0.47}\text{As}$ wet chemical processes show different room temperature electrical properties than unprocessed samples measured with indium contacts. One of the main causes for the

discrepancies is the buffered hydrofluoric acid etch of the encapsulation layers; the remaining discrepancies are possibly due to reactions with constituents of the photoresist, UV light exposure, and damage to contact pads due to reactions with the photoresist developing solutions and hydrofluoric acid. To avoid these discrepancies, dry chemical etches, instead of buffered hydrofluoric acid etch, should be used to pattern encapsulation layers. The use of shadow-mask evaporation would remove the remaining discrepancies caused by the photolithography process.[58]

1.2.1.2 Nanoparticle Growth via Growth Interrupt

The growth interrupt method has a few possible advantages over the co-deposition method discussed above, including the easier control of the size, shape, and density of the nanoparticles.[59, 60, 61, 32] In general the growth interrupt method is achieved by stopping the III-V film growth by closing the group III and group V shutters and opening the LN shutter. Typically, the LN atoms bond with group V atoms already in the film and nucleate in the III-V film as nanoparticles. Note, this requires displacing group III atoms. Many of the LN atoms are able to displace the group III atoms from the surface because the enthalpy of formation of the LN-V is significantly more negative than that of the III-V. For example, the enthalpy of formation of ErAs is over $4\times$ more negative than that of GaAs. The difference in enthalpy of formations indicates a strong thermodynamic driving force to replace the group III atoms with LN atoms, this replacement is aided by the fact that the group V atoms occupy the same face centered sublattice sites in the rocksalt LN-V systems and the zincblende III-V systems, and thus only requires a change in localized bonding.[62] Once the nanoparticles reach a height of ~ 4 ML, required to stabilize the LN-V crystal structure,[62] the nanoparticles expand laterally. The lateral expansion is caused by the ~ 4 ML of LN-V acting as a diffusion barrier for the LN species and the nanoparticles are forced to grow laterally.[15] The nanoparticle growth is then terminated by closing the LN shutter and III-V overgrowth is started by opening the group III and group V shutters. This allows for the overgrowth of a III-V film to seed from the uncovered III-V

layer. This technique has been used to grow a wide range of LN-V:III-V combinations including: LaAs, LuAs, GdAs, and ErAs in $\text{In}_{0.53}\text{Ga}_{0.47}\text{As}$, LuAs and ErAs in GaAs, and ErSb in GaSb.[11, 35, 63, 15]

The LN-V nanostructures form due to a surface-mediated growth mechanism where new growth LN-V preferentially bonds to LN-V already in the film, and new III-V preferentially bonds to III-V already in the film. In the ErAs:GaAs system, the impinging Er atoms bond with As already in the film, displacing Ga atoms. The displaced Ga atoms bond with impinging As atoms to form new GaAs islands.[62] ErSb:GaSb has a similar growth mechanism, except the re-growth of the GaSb is dependent on the growth temperature. At growth temperatures $\geq 500^\circ\text{C}$, the displaced Ga atoms have sufficient mobility to diffuse to step edges and particle edges, preventing the formation of GaSb islands. This allows ErSb to form islands that are in-plane and raised above the plane. At 450°C , some of the Ga regrows along around the ErSb nanoparticles and at GaSb step edges while other Ga regrows GaSb islands on the surface. At colder temperatures yet, the displaced Ga primarily regrows GaSb islands.[51] The different GaSb regrowth mechanisms leads to the formation of four types of ErSb nanoparticles: type A which extend 1 atomic layer (3 \AA) above the surface of GaSb, type B which has a top most layer in the same plane as GaSb, type C which appear at GaSb step edges with a portion of the ErSb island surface higher than the surrounding GaSb and a portion of the island in the plane of GaSb, and type D which appear only for deposition above 1.0 ML and appear in the middle of GaSb terraces with part of the ErSb particle even with the GaSb surface and part above the surface. Figure 1.5 shows the four ErSb nanopartilce types. Note that type C and type D particles are only present at higher growth temperatures. The regrowth of GaSb by the displaced Ga can transform a type A ErSb nanoparticle into a type B particle by first converting it to a type C particle.[15]

As discussed above, nanoparticles grown via the growth interrupt method typically grow to a height of ~ 4 ML and then expand laterally. The lateral extent of

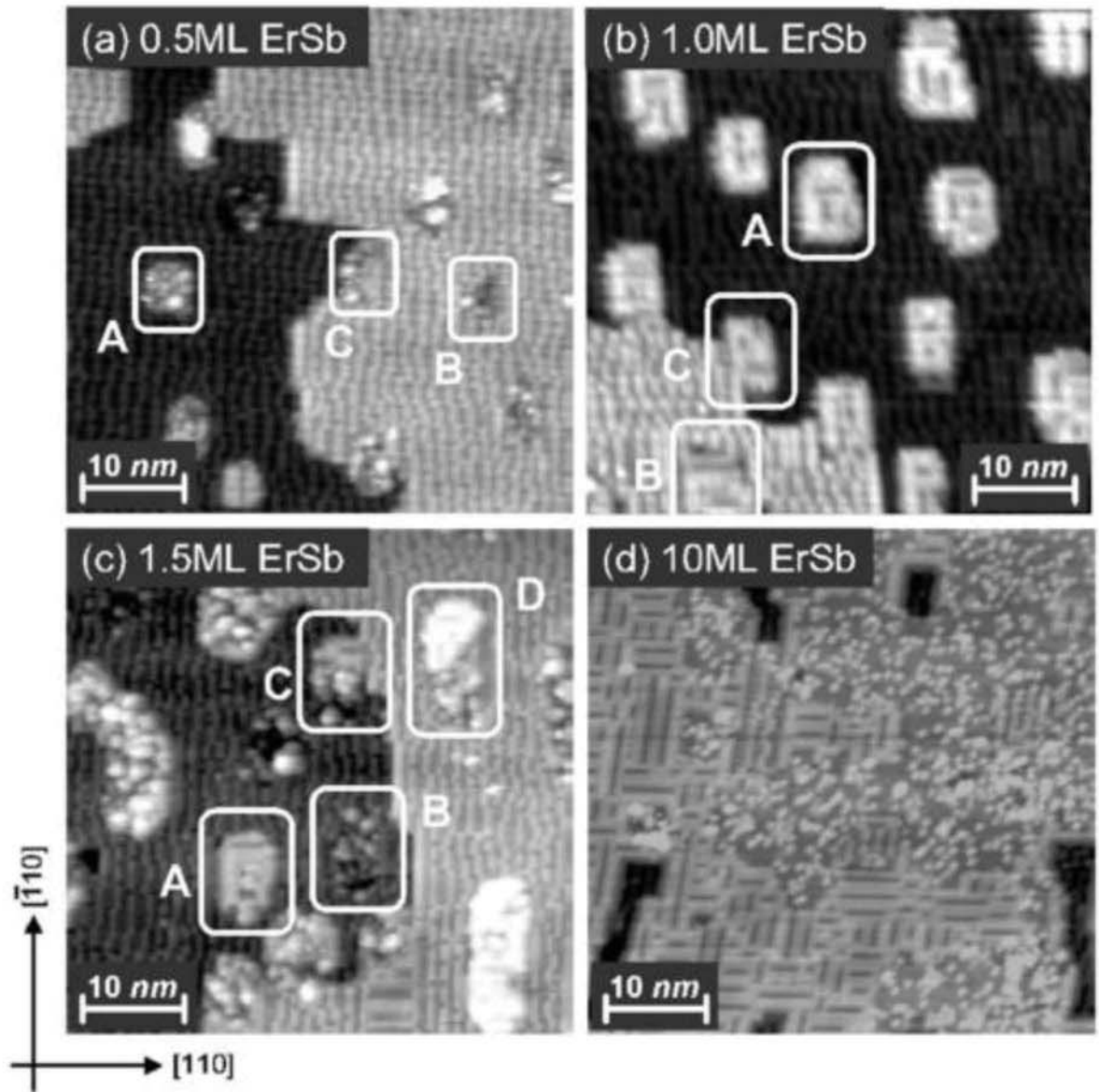


Figure 1.5: Scanning tunneling microscopy images showing the four types of ErSb that can form on GaSb.[15] Reprinted from [15], with the permission of AIP Publishing.

the nanostructure depends on both the amount of LN deposited and the growth temperature. The nanoparticle size depending on both the growth temperature and the lanthanide amount is seen in ErAs nanoparticle growth. Cross-sectional STEM shows that for 0.125 to 0.5 ML of ErAs deposition on GaAs (001) at 540°C results in nanoparticles with equal height and width and only differ in the density of nanoparticles, with higher ErAs amounts results in a higher density. For ErAs depositions above 0.5 ML ErAs, the nanoparticles either extend laterally, in the (001) plane, or increase in apparent size due to the coalescence of individual particles.[53] At a growth temperature of 450°C, 0.5 ML ErAs deposition results in nanoparticle diameters of ~ 3 nm and 1 ML ErAs deposited at 515°C resulted in nanoparticle diameters of 12-16 nm.[64, 65, 66] An increased lateral nanoparticle extent, with constant height, has also been observed in ErSb on GaSb and ErAs on GaAsSb.[21, 15] While LN-As nanoparticles tend to uniformly expand laterally with increasing deposition amounts, increased ErSb deposition results in elongated rectangles along the $[\bar{1}10]$ direction, likely due to anisotropic diffusion of Er and Ga on the GaSb surface.[15] An alternative way to increase the nanostructure's lateral dimension while maintaining a constant height is to decrease the LN-V growth rate.[21] Note that at high growth temperatures ErAs nanoparticles have a much greater vertical extent, and thus reduces the surface coverage. For example, atomic force microscopy measurements of 1.6 ML ErAs deposited at 570°C show nanoparticles with a 12 nm diameter and a height of ~ 10 -12 ML. [63]

LN-N nanoparticles grow on III-N materials in a similar method to the LN-As and LN-Sb on III-As and III-Sb, but with a few minor differences. For example, cubic GdN nanoparticles are grown on GaN with the nitrogen shutter remaining open during the nanoparticle growth. Additionally, low GdN depositions, $< \sim 1.2$ ML deposition, only results in heavily doped GdN, not nanoparticle formation. Note that one monolayer of deposited GdN is defined as the amount of GdN required to form one complete monolayer of GdN if 1 ML GdN could form a complete film. From 1.2 ML to 2.4 ML deposition, GdN nanoparticles form with a height of ~ 5.6 nm. Similar to the LN-As and LN-Sb, increasing the deposition amount results in nanoparticles with an increased

lateral growth.[67]

The lateral spacing between nanoparticles is important for the high quality overgrowth of zincblende III-V materials. At ~ 3 ML ErAs deposition on GaAs, the overgrowth with GaAs is degraded.[68] For LuAs on GaAs, the overgrowth starts to degrade at 2.5 ML LuAs deposition, as observed by reflection high energy electron diffraction (RHEED), and at a deposition of 3.0 ML LuAs the GaAs overgrowth is significantly degraded with planar defects evident in cross-section transmission electron microscopy (XTEM).[35] This is likely due to the LN-V atoms forming interconnected networks and at high concentrations due to LN-V forming films.[35, 61] The growth of films will be discussed more below. With low enough deposition amounts, the III-V overgrowth can be of high quality. This has been observed for up to 1.2ML of ErAs, LuAs, and GdAs nanoparticles in $\text{In}_{0.53}\text{Ga}_{0.47}\text{As}$ [11], and up to 2.0ML LuAs in GaAs.[35]

Most of the LN-V nanostructures grown via the growth interrupt method focus on a single LN species and a single group V species that is present in both the nanostructure and the film. Recent work shows that combining multiple group V atoms in a single nanoparticle and the growth of nanoparticles with a different group V species than the matrix proves to be difficult. Attempts to grow ErAsSb on GaAs result in nanoparticles with low amounts of Sb; the growth of ErAsSb on GaAs at 580°C with no As flux present during the nanoparticle growth and a 1 minute Sb soak prior to the nanoparticle growth results in a ErAsSb nanoparticle with less than 4% Sb. The low amounts of Sb is likely caused by Er diffusing throughout the Sb terminated surface and into the GaAs layer to form ErAs.[69] Note Zhang et al. found that depositing Er and Sb for one hour on GaAs after the growth of a GaAs layer still results in an ErAs film, results to be published.[69] TEM images of the ErAsSb nanoparticles show the particles have a dot shape with the same diameter in the $[110]$ direction as ErAs but are elongated in the $[1\bar{1}0]$ direction; the anisotropic dimensions increase with increasing Er deposition and growth temperature. The low incorporation of Sb in the nanoparticle, and the change in nanoparticle shape, suggests that the Sb is behaving as a surfactant

and the anisotropy in the nanoparticle shape is due to the anisotropic diffusion rate on the Sb terminated surface. [69, 13, 49]

One of the advantages of using the growth interrupt method is that the LN-V nanoparticles can be grown at designated and controllable heights within the film. This allows for the growth of non LN-V layers above and below a layer of LN-V nanoparticles. While initial studies of InGaAs/GaAs quantum wells grown above ErAs nanoparticles, with a carrier blocking layer, were found to be of comparable quality to those grown directly on a GaAs substrate,[70] it was later found that the growth of films with the Er source hot and the shutter closed results in unintentional Er-doping. This unintentional Er-doping can degrade the optical quality of the films grown. Thus, the parasitic Er flux prohibits the growth of the high optical quality III-V layers with the Er effusion cell hotter than 500°C. To overcome the parasitic Er doping, the Er effusion cells must be cool to below 500°C prior to the III-V film growth. Note that the photoluminescence intensity of films grown with the Er cell cooled to 500°C have a photoluminescence intensity 1000× higher than those grown with the Er cell hot.[71] This issue has also been observed with other LN-V material systems, such as LuAs, and that the effusion cell temperature at which this becomes an issue is LN species specific.[72]

Most of the MBE growths discussed in this chapter have been grown using pyrometry or band edge thermometry to measure the growth temperature, while the substrate temperature is controlled by a thermocouple located some distance away from the substrate. Eyink et al. noted that for a constant thermocouple temperature, the growth of ErAs nanoparticles changes the temperature of the growth measured by band edge thermometry. This is likely due to an increase in low energy photon absorption from the substrate heater. If uncorrected, the increase in growth temperature can significantly alter the growth of the remainder of the film, such as altering subsequently grown InAs quantum dots size/densities and can result in the formation of dislocations.[73]

1.2.2 MBE LN-V Film Growth

The growth mechanism of LN-V films is essentially an extension of the nanoparticle growth interrupt method with the exception that the group V shutter remains open during the growth. As in the growth interrupt method, the LN atoms impinging on the surface displace the group III atoms and bond with the group V atoms already in the film, forming LN-V nanoparticles. Once the nanoparticles reach a height of ~ 4 ML, the LN-V nanoparticles act as a nearly infinite barrier to LN atom diffusion, this forces the islands to grow laterally. As the nanoparticles continue to grow laterally, they coalesce into a complete film. Once formed, the film can continue to grow vertically in a layer-by-layer mode.[62] LN atoms displacing group III atoms near the surface and ErAs forming a diffusion barrier was confirmed by Schults et al. who grew ErAs on GaAs by only depositing Er, no As was deposited. After 5 ML deposition, RHEED and low energy electron diffraction (LEED) patterns changed, suggesting that Er could not diffuse through the already deposited ErAs layer to react with GaAs and the Ga displaced by the Er deposition is trapped on the surface as Ga metal.[62]

Many LN-As films have been grown on GaAs substrates with film thickness varying from a few nanometers to 600 nm including: ErAs, TbAs, LuAs, LaAs, and $\text{La}_x\text{Lu}_{1-x}\text{As}$ with $x = 5, 9, 15$, and 48%.[74, 18, 75, 35, 76, 16, 28] Most of these films are grown at lower temperatures, typically 430-460°C, with arsenic:lanthanide beam equivalent ratios ranging from 10:1 to 46:1. The lower substrate temperature, compared to normal GaAs growth temperatures, is often required to observe RHEED intensity oscillations.[75, 35] The LN-As films mentioned here were all grown with a capping layer, that is typically defective, to prevent oxidation of the film. Additionally, the La containing films were grown with a 10 ML top and bottom LuAs spacer layer to obtain high crystalline quality of the La containing layer, discussed in more detail below. It is worth noting that while most LN-V film growths have been on GaAs, it is possible to grow on other substrates, such as ErAs on $\text{In}_{0.53}\text{Ga}_{0.47}\text{As}$.[18]

Attempts to grow LaAs directly on GaAs and InAs over a wide range of growth parameters: 5-67 nm thick LaAs layers, substrate temperatures ranging from 390 to

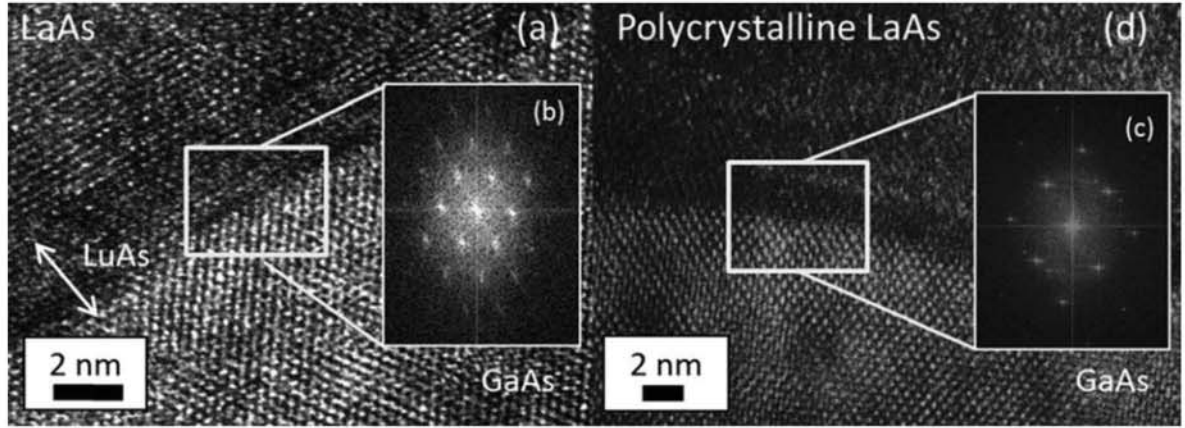


Figure 1.6: Cross sectional TEM images of a (a) LaAs film grown using the barrier layer and a (d) LaAs film grown without the barrier layer. Fast Fourier transform approximate the selective area diffraction patterns of the (b) LaAs/LuAs/GaAs interface and the (c) LaAs/GaAs interface.[16] Reprinted from [16], with the permission of AIP Publishing.

500°C, As beam equivalent pressures ranging from 15 to 50× that of La, and growth rates from 0.05 to 0.1ML/s, all resulted in polycrystalline films with poor surface morphology. The poor film quality was observed on both GaAs and InAs and thus strain relaxation is unlikely to be the cause of the poor film growth. Instead, the poor film quality may be due to instability of the LaAs/GaAs and LaAs/InAs interfaces caused by the similar enthalpies of formation between LaAs, LaGa, and LaIn and competing LaAs phase formations. With the use of thin LuAs barrier layers on the either side of the LaAs, high quality single crystal LaAs films can be grown, see Fig. 1.6. The LuAs layers may be acting as a barrier that prevents reactions between La and the group III atoms in the substrate as well as preventing the nucleation of other LaAs phases by acting as a template for rocksalt LaAs nucleation.[16] A Lu thin film acting as a barrier for additional RE adatom diffusion is similar to the previously discussed ErAs film preventing Er diffusion.[62]

While none of the binary LN-V systems are lattice matched to GaAs, alloying multiple LN elements or multiple group V elements allows LN-V films to be grown lattice matched to GaAs. This has been demonstrated with: 20 nm of $\text{Sc}_{0.32}\text{Er}_{0.68}\text{As}$

grown at 400°C,[77] 117 nm of $\text{Sc}_{0.2}\text{Yb}_{0.8}\text{As}$ grown at 400-450°C,[78] and 90 nm of $\text{ErP}_{0.6}\text{As}_{0.4}$ grown at 500°C.[79] Another option to grow lattice matched LN-V films is to grow a relaxed buffer layer and then grow the LN-V lattice matched to the relaxed buffer layer. For example 7 nm of PtLuAs has been grown lattice matched to an $\text{Al}_{0.1}\text{In}_{0.9}\text{Sb}$ buffer layer, which is relaxed on the GaAs substrate.[80]

In addition to LN-As films, LN-N films have been grown and studied including the rocksalt GdN (111) on GaN and GdN on Si with the use of an AlN buffer layer.[40, 81] Note that for the GdN films, a low growth temperature compared to normal nitride growth temperatures, 450°C, is required to obtain complete films. The RHEED patterns observed during the growth suggests that, similar to the other LN-V films mentioned earlier, GdN films form by first nucleating GdN island that expand laterally and coalesce into rough films.[40] As mentioned above, our discussion on the LN-N materials will be limited due to the recently published review article.[34]

As discussed above, the overgrowth of LN-V films with III-V materials results in a highly defective III-V capping layer. This is due to either wetting issues or a combination of island growth mode of III-V materials on LN-V films and the mismatch in rotational symmetry of the crystal structure.[74, 17] To overcome the poor overgrowth problem in ErAs:GaAs, Crook et al. have demonstrated a novel growth method that utilizes the ability of Er to diffuse through and embedded itself in GaAs. Instead of growing a complete ErAs layer only a partial ErAs seed layer is grown, essentially growing ErAs nanoparticles by the growth interrupt method discussed above. The incomplete ErAs film, or ErAs nanoparticles, are then overgrown with a thin GaAs spacer layer. The GaAs spacer layer is seeded from the exposed GaAs surface, preventing a mismatch in rotational symmetry and preserving a high quality zincblende GaAs layer. After the growth of the GaAs spacer layer, the growth temperature is raised to 600°C, to increase Er diffusion, and a low Er flux is resumed. The surface Er atoms diffuse through the GaAs spacer layer and incorporate at the subsurface ErAs nanoparticles, expanding the nanoparticles laterally until they coalesce into a film. Once an ErAs film growth is complete, a high quality zincblende GaAs capping layer without planar

defects can be grown from the already grown GaAs spacer layer. Figure 1.7 shows a comparison of a conventionally grown ErAs film and a nanoparticle seeded ErAs layer capped with GaAs. Note the GaAs spacer layer must be < 1 nm to allow Er to diffuse through the layer. [17] This growth method could extend to the other similar LN-V systems such as LuAs[35].

For specific applications, it is advantageous to be able to tune the interface roughness/geometry between the films. For example, the Schottky barrier height between ErAs and GaAs depends on the interface roughness. High angle annular dark field scanning transmission electron microscopy images show that typically the interface between ErAs and GaAs or $\text{In}_{0.53}\text{Ga}_{0.47}\text{As}$ are atomically abrupt, the GaAs surface is terminated by Ga, and no extended defects are observed, see Fig. 1.8.[18] This is consistent with modeling showing that the GaAs/ErAs interface consists of a polar GaAs with a zincblende structure and a nonpolar ErAs with a rocksalt structure. [82] Typically, the interface roughness/geometry can be controlled by wet etches which introduces the possibility of the semiconductor to oxidize. The GaAs/ErAs interface roughness/geometry can be controlled by repeatedly depositing only X ML of ErAs followed by $4-X$ ML GaAs, where $0 < X < 4$, and increasing X in each layer until a complete ErAs film is formed. Since ErAs preferentially incorporates on top of ErAs, increasing the amount of ErAs deposited in each layer quadratically from 0 to 4 ML results in a film of ErAs grown on top of inverted ErAs cones. This technique allows the Schottky barrier height to be engineered with growth conditions and a single epitaxial metal.[83]

1.2.3 Other Growth Methods

It is worth noting that molecular beam epitaxy is not the only way to grow LN-V materials. Much of the early work on LN-V materials was done on LN-V materials grown via vapor-solid reaction in ampoules.[84, 85, 86, 87]. Note that the vapor-solid reactions in ampoules allows for the formation, and thus the study, of non-stoichiometric LN-As.[87] Since the ampoule synthesis, other growth mechanisms have been explored. Organometallic vapor phase epitaxy has been used to form ErP.

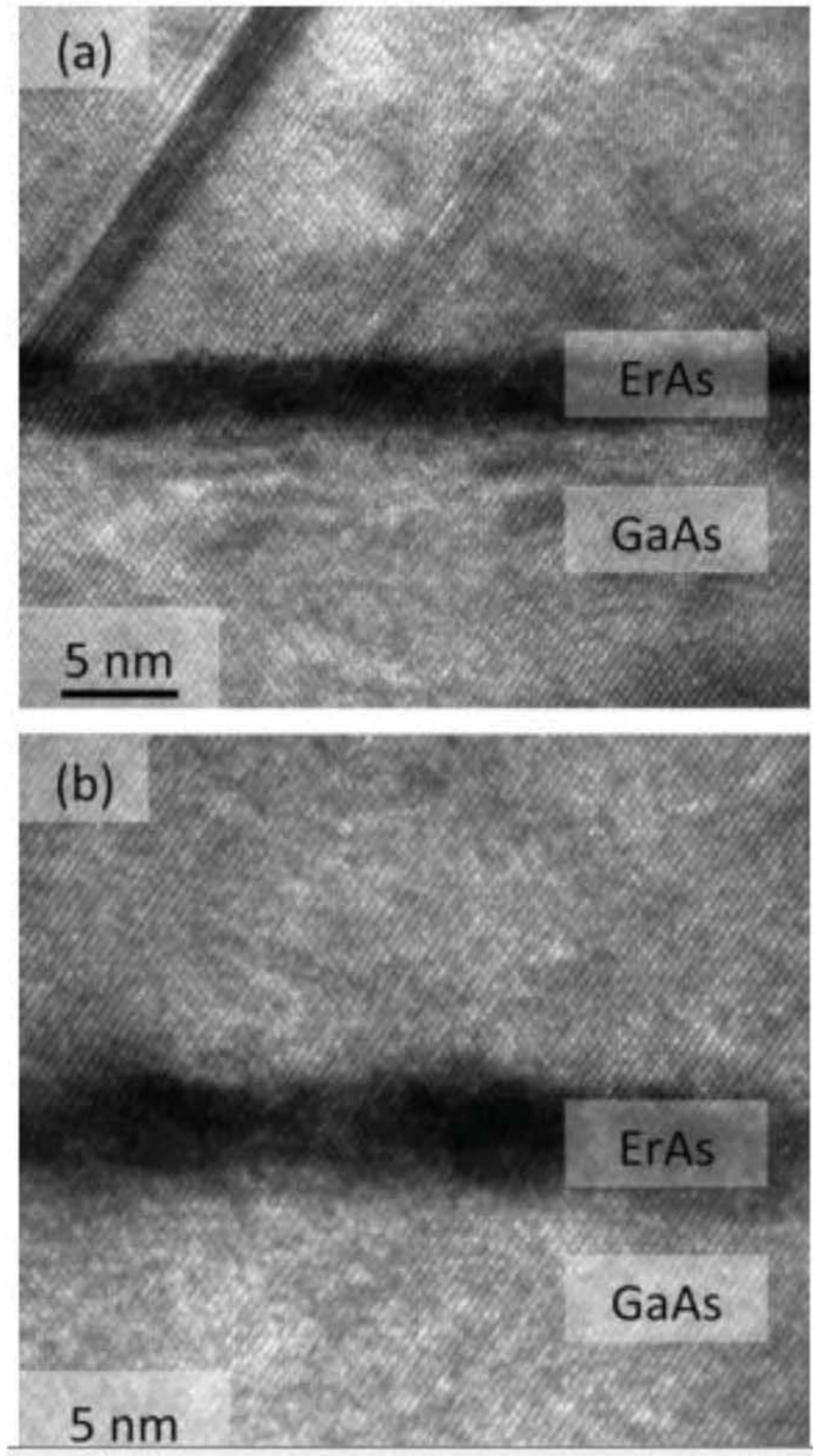


Figure 1.7: Cross-section TEM image of (a) conventionally grown and (b) nanoparticle seeded ErAs layers capped with GaAs.[17] Reprinted from [17], with the permission of AIP Publishing.

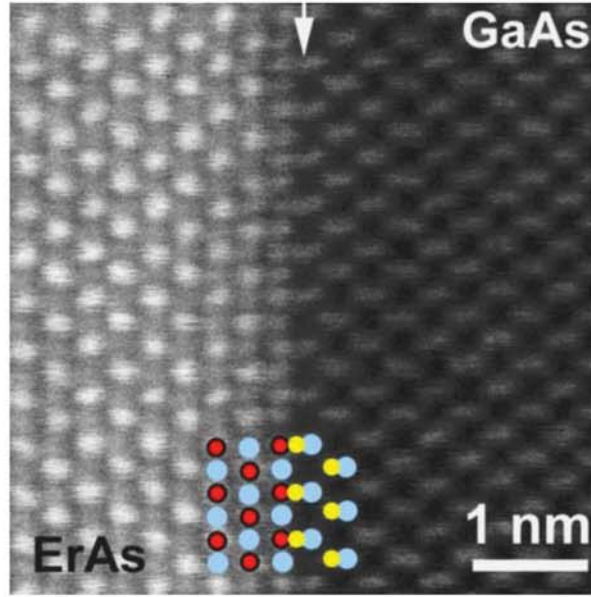


Figure 1.8: HAADF STEM image showing the clean and atomically abrupt ErAs/GaAs interface. The overlay represents the atomic column positions with blue circles representing As, red circles representing Er, and yellow circles representing Ga.[18] Reprinted from [18], with the permission of AIP Publishing.

Delta doping InP with Er via organometallic vapor phase epitaxy results in the formation of rocksalt ErP.[88] This growth technique was extended to form ErP islands on InP via organometallic vapor phase epitaxy where the island size can be controlled with growth temperature.[89] Some of the LN-N materials have also been grown via metalorganic chemical vapor deposition, but this is often limited by the availability of lanthanide precursors.[34] Many of the LN-N have also been grown by pulsed-laser deposition and reactive ion sputtering.[34, 90] Recently, Lewis et al. demonstrated an interesting new growth technique for ErAs nanoparticles absent of a host material via inert gas condensation. While this method was demonstrated for ErAs, it should be easily applicable to many of the other LN-V materials.[41]

1.3 Electronic Band Structure and Carrier Dynamics

One of the most important properties of a material system is the band structure as this often determines the other optoelectronic properties. Early work on LN-V materials often show a decrease in electrical resistivity with increasing temperature and optical absorptions, which suggests they are semiconductors.[84, 85, 86] These measurements matched the semiconductor prediction made by a simple empirical analysis based on a relationship between the band gap of III-V semiconductors and known covalent and ionic radii.[91] Much of the early work was done on materials prepared in ampules and at that time four and five nine purity lanthanide source materials were not readily available. This resulted in issues with material quality and made it difficult to produce large single crystal samples. The grain boundaries and impurities in the films could alter the measurements. Thus it is unsurprising that while early ampule growths of LN-V materials often show semiconducting behavior, the early MBE grown LN-V films often show metallic or semimetallic behavior.[74, 92, 79, 75, 93, 94] Note that while the simple empirical analysis predicting band gaps in LN-V works well for many III-V materials, it does not take into account the modeling challenges associated with the 4-f shell electrons in the lanthanide materials.[95, 82] More recent modeling, including density function theory, results in band diagrams showing that ErAs is semimetallic.[94] Additionally, with the proper treatment of the Er 4f shell electrons and accounting for the hybridization between the As p states and the upper Er f states; the band gap, Fermi surface pocket, carrier concentrations, and Shubnikov-de Hass frequencies can be correctly predicted for ErAs.[19] This modeling technique should transfer to other LN-V systems.[19] Figure 1.9 shows a theoretically calculated band diagram and density of states for ErAs.[19]

While measurements of ErAs films suggests that ErAs is semimetallic,[74, 75, 93] absorption measurements of ErAs nanoparticles epitaxially embedded in GaAs show an absorption peak at $\sim 2.5 \mu\text{m}$. This absorption peak, which is below the band gap of GaAs, increases in strength with increasing ErAs density. This absorption peak was originally attributed to surface plasmon resonances in the ErAs nanoparticles,

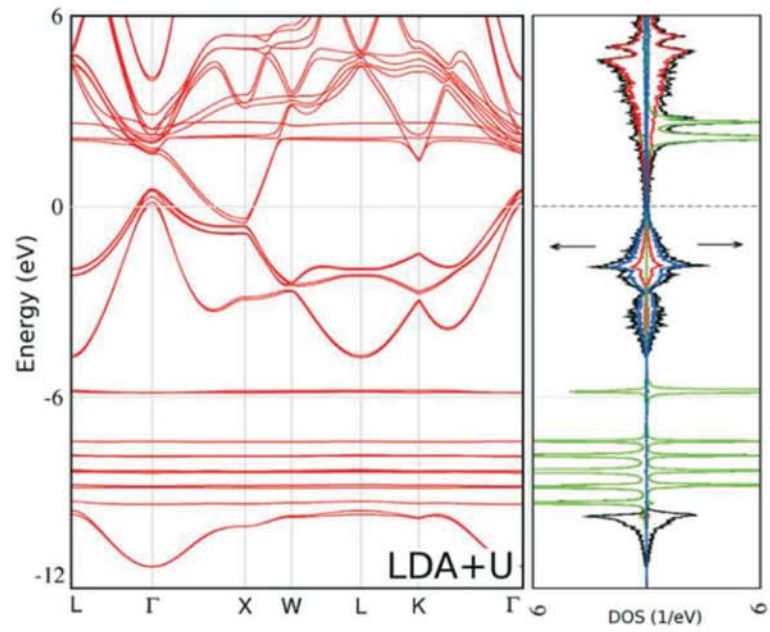


Figure 1.9: LDA+U calculated band structure and density of states for ErAs. In the density of states diagram the total, Er 5d, Er 4f, and As 4p states are indicated by black, red, green, and blue lines, respectively.[19] Reprinted figure with permission from [19] Copyright 2009 by the [American Physical Society](#).

consistent with ErAs being semimetallic.[31] It was later discovered that this absorption feature shifts to longer wavelengths with increased nanoparticle size.[21] The shift in the absorption feature's wavelength with changing nanoparticle size matched well with an effective mass model utilizing a spherical finite-step potential that predicted ErAs nanoparticles with diameters less than ~ 3 nm should have a quantum confined induced energy gap. This suggested that ErAs nanoparticles should be semiconductors with a quantum confined induced energy gap.[52] Subsequently, cross-sectional scanning tunneling spectroscopy (XSTS) measurements of ErAs:GaAs, cleaved in vacuum to expose a $\{110\}$ surface, show no evidence of a band gap in ErAs. Instead XSTS shows that the local density of states in ErAs has a sharp finite minimum at the Fermi-level, indicating that ErAs is in fact semimetallic, shown in Fig. 1.10.[20, 53] Additionally, the XSTS reveals an interface state 0.2 eV above the Fermi level that decays with distance away from the ErAs GaAs interface.[20] Including effects from the interface states and many-body effects into the simple finite-potential model mentioned above suggests that ErAs nanoparticles with a diameter of 2.3 nm will remain semimetallic and ErAs films should remain semimetallic down to 0.15 nm thick, which is much less than the 1 ML physical limit of 0.287 nm.[20] This indicates that the ErAs GaAs interface states and metallic screening prevents ErAs from transitioning into a semiconductor with a quantum confined induced energy gap. Additionally, modeling of the band overlap in ErAs as a function of hydrostatic strain suggests that a compression of the volume, such as that experienced by ErAs nanoparticles in GaAs, increases the band overlap of valence band maximum at the Γ point and conduction band minimum at the X point.[95]

Scanning tunneling spectroscopy (STS) has also been used to study the local density of states of several other LN-V materials. *In situ* STS of PtLuAs shows a steady decrease in the density of states approaching the Fermi level, with a non-zero density of states at the Fermi level. This indicates that PtLuAs does not have a bulk band gap and that the Fermi level is located in the valence band at the surface and throughout the bulk of the film. This matches the results from *ex situ* photoemission

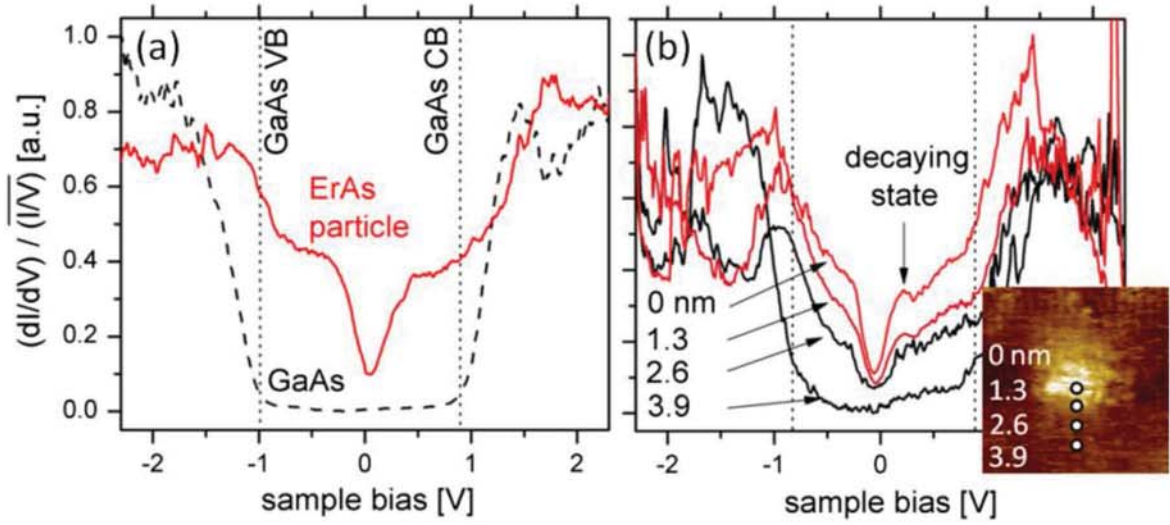


Figure 1.10: (a) Averaged differential conductance curves of ErAs nanoparticles, red line, protruding from the GaAs matrix, black line obtained with cross-sectional scanning tunneling spectroscopy. (b) Individual differential conductance curves at different locations ontop of the ErAs nanoparticle and GaAs matrix.[20] Reprinted figure with permission from [20] Copyright 2011 by the American Physical Society.

spectroscopy.[80] STS of ErP islands with lateral sizes of 20-50 nm and vertical heights ranging from 1-4 nm on InP shows that for ErP islands with heights greater than 3.4 nm are semimetallic while ErP islands with heights below 3.4 nm are semiconductors due to quantum size effects opening a band gap.[96] STS of ErSb nanoparticles grown on GaSb show that the conduction band and valence band of ErSb overlap, indicating that ErSb remains semimetallic down to the smallest size nanoparticle that could be nucleated on GaSb, 3.3×3.3 nm.[51] Additionally, the STS of ErSb on GaSb shows that ErSb, relative to GaSb, has a larger valence band density of states and a smaller conduction band density of states. Note, the GaSb has a band gap of ~ 0.6 eV with the Fermi level at $V=0$, contrary to the expected p-type character for Si:GaSb[51]

The XSTS measurements showing that ErAs nanoparticles are semimetallic, discussed above,[20] matches well with the band structure proposed by other measurement techniques such as carrier relaxation dynamics. For example, the large density of states in ErAs allows for the capacitance of GaAs p+/n+ junctions with ErAs nanoparticles

at the junction interface to be nearly independent of sample bias voltage while areas with low ErAs content show a bias-dependent voltage.[65] Additionally, photoluminescence (PL) lifetimes of InAs quantum dots located near ErAs nanoparticles is strongly dependent on the InAs quantum dot to ErAs nanoparticle separation, where small separation distances result in very quick PL decay times. This suggests that at short distances the carriers in the InAs quantum dots are escaping out of the InAs quantum dot and into the ErAs nanoparticles where they recombine non-radiatively. Additionally, the PL lifetime is independent of the pump fluence. These results are consistent with ErAs nanoparticles having a continuous density of states, supporting the notion that ErAs nanoparticles are semimetallic.[97] Similarly, optical pump terahertz (THz) probe measurements performed on ErAs co-deposited in $\text{In}_{0.53}\text{Ga}_{0.47}\text{As}$ with Be compensation doping shows that in the limit that the photocarrier density is less than the ErAs trap state density; the lifetime, ~ 3 ps, is independent of pump fluence.[42] Moreover, optical pump-probe measurements of ErAs superlattices in $\text{In}_{0.53}\text{Ga}_{0.47}\text{As}$ also show that nanoparticles are not becoming saturated and the trapping time depends on the amount of ErAs. Note that the optical pump-probe measurements show two carrier decay times, a fast one that is due to trapping by ErAs and a slow time that is due to the thermal activation of carriers already trapped by ErAs.[98] In ErAs: $\text{In}_{0.53}\text{Ga}_{0.47}\text{As}$ superlattices, compensated with Be delta-doping, the carrier lifetime is as short as 220 fs. Note this lifetime is dependent upon the superlattice period and the 220 fs lifetime was measured for a 5 nm period.[99] It is worth mentioning that faster relaxation rates can be achieved and the thermal activation reduced by compensation doping with carbon instead of beryllium.[98] The lifetime depending on superlattice spacing is similar to ErSb:GaSb superlattices where the carrier lifetime decreases with decreasing layer spacing.[32] Optical pump optical probe measurements of GdAs, ErAs, or LuAs superlattices in $\text{In}_{0.53}\text{Ga}_{0.47}\text{As}$ all have short lifetimes, with GdAs being the shortest, $1.3\times$ and $1.8\times$ shorter than ErAs and LuAs respectively. These differences suggests that it is possible to tune the carrier lifetime via strain.[11]

Unlike ErAs nanoparticles, optical-pump terahertz-probe measurements of 2.12%

TbAs co-deposited in GaAs show that the TbAs nanoparticles are saturable, implying that TbAs nanoparticles have a band gap. In the TbAs:GaAs system, a triple exponential decay function was required to model the decay in the THz probes absorption. This resulted in three carrier relaxation times corresponding to relaxation into the nanoparticles, carriers recombining within or leaving the TbAs nanoparticles, and bulk recombination. In this measurement, the pre-exponential amplitude coefficients provided information on the fraction of carriers participating in each relaxation process. By monitoring how the carrier relaxation times and the fraction of carriers participating in each relaxation process changes with increasing pump fluences, it was determined that the TbAs nanoparticles are saturable. The saturability of TbAs nanoparticles suggests that the nanoparticles have a finite density of states.[26] Combining the finite density of state in TbAs with the previous observation of TbAs nanoparticles quenching the photoluminescence of GaAs[36] suggests that that TbAs nanoparticles are indirect semiconductors.[26] A similar study on TbAs nanoparticles co-deposited in $\text{In}_{0.53}\text{Ga}_{0.47}\text{As}$ again revealed that TbAs nanoparticles can saturate and are likely indirect semiconductors.[27] Note, this study revealed that the TbAs nanoparticles in $\text{In}_{0.53}\text{Ga}_{0.47}\text{As}$ completely saturate at a lower pump fluence than in GaAs, likely due to differences in the band structure. By combining the fact that TbAs nanoparticles are saturable with the matrix dependent optical absorption features and Fermi level estimates obtained from Hall effect measurements, a type 1, straddled, heterojunction band alignment was proposed for TbAs:GaAs and a type 2, staggered, heterojunction band alignment was proposed for TbAs: $\text{In}_{0.53}\text{Ga}_{0.47}\text{As}$. [27] The determination that TbAs is a semiconductor and its band alignment with GaAs and $\text{In}_{0.53}\text{Ga}_{0.47}\text{As}$ is discussed in more detail in Chapter 3 and a schematic of this band alignment shown in Fig. 3.9.

The semiconducting nature of TbAs was later supported by absorption measurements of TbAs films, where a thickness dependent optical cutoff wavelength was observed. Electronic measurements reveal that the films are degenerately doped with the doping level depending on film thickness. This indicates that the optical cutoff wavelength is, in part, determined by degenerate doping level and the corresponding

Burstein-Moss shift. Note, in this system the Burstein-Moss shift depends on film thickness. The thickness dependent doping level also suggests that carriers come from interface states. These results show that TbAs is a degenerately doped semiconductor that has a band gap that is slightly less than 435 meV, the band gap measured for the film with the lowest carrier density.[28] The growth and characterization of TbAs films are discussed in more detail in Chapter 4.

It is worth noting that TbAs is not the only semiconducting LN-V material. Recent work, as summarized by Natali et al. on LN-N shows that most of the LN-N investigated so far are semiconductors, despite early theoretical work predicting semimetallic behavior. Advancements in handling the bands formed by the d-shell electrons and, more importantly, handling of the f-shell electrons in the theoretical models have led to improved band structure predictions.[34]

1.4 Optical Properties

The band structure of the LN-V materials, described above, determines many of the properties of the LN-V materials including their optical properties. While the band structure of some of the LN-V materials was determined with measurements such as scanning tunneling spectroscopy, many of the band structures were inferred from the measured electrical and optical properties. Below, I discuss the optical properties of the LN-V materials including nanoparticle absorption features, luminescence from LN doped III-V materials, and the optical properties of LN-V films.

As discussed above, superlattices of ErAs nanoparticles in GaAs show an absorption feature that can be shifted from ~ 1.3 to $2.5 \mu\text{m}$, which is below the GaAs band gap, by changing growth conditions. In the growth interrupt method, increasing the nanoparticle size by increasing the amount of ErAs deposited per layer moves the absorption feature to longer wavelengths, shown in Fig. 1.11. The absorption feature is also shifted to longer wavelengths with increased growth temperatures due to the increased lateral size of ErAs. Alternatively, faster ErAs growth rates result in shorter absorption wavelengths due to a higher density of smaller nanoparticles.[21] Note that

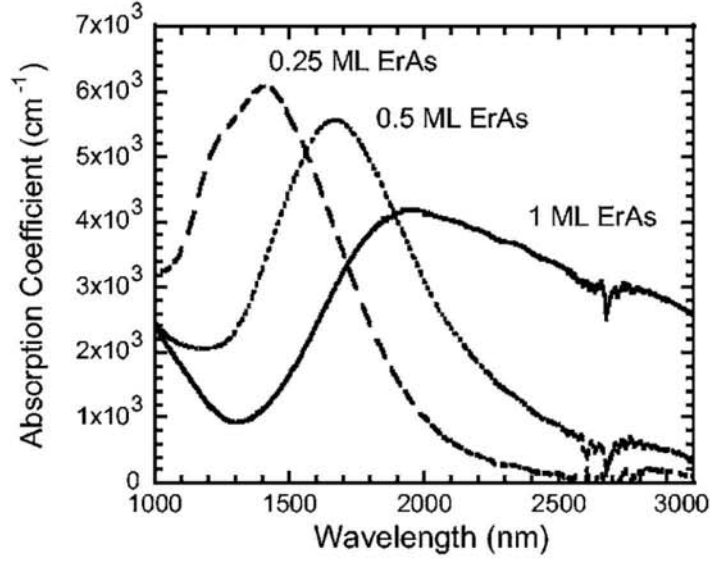


Figure 1.11: The absorption feature in ErAs/GaAs superlattices increases in wavelength with increased ErAs deposition amount per layer.[21] Reprinted from [21], with the permission of AIP Publishing.

increasing the total amount of ErAs nanoparticles in the film increases the absorption intensity. [21] Similarly, increasing the amount of ErAs nanoparticles co-deposited in GaAs also increases the absorption intensity. Similar to the growth interrupt method, increasing the growth temperature of the co-deposited ErAs nanoparticles results in a shift in the absorption feature to longer wavelengths, due to an increased particle size and possible flattening of the nanoparticle. [21] The exact cause of the absorption feature is difficult to determine and possible reasons for an absorption feature include quantum confined energy gaps[52] (disproved by the discussion above), measurements of the direct gap in a semimetal, or surface plasmon resonance of the semiconducting metal with the latter being the general consensus in the literature.[21, 31, 20]

In the nanoparticle co-deposition growth section I discussed how the geometry of ErAs nanostructures can be controlled with the choice of substrate orientation where growing on (411)A GaAs substrates results in ErAs nanorods. Similar to the ErAs nanoparticles discussed above, the ErAs nanorods also show an absorption feature. The ErAs nanorods show a ~ 0.05 eV shift in the absorption features energy when the

linear-polarization of the light is rotated 90° . This shift is likely due to the fact that the nanorods are inclined and the surface plasmon resonance will depend on the polarization of incident radiation. This shift is not detectable for ErAs nanostructures grown on (411)B or (100) GaAs, consistent with the formation of spherical nanoparticles.[55]

Similar to ErAs in GaAs, superlattices and co-deposited ErSb nanoparticles in GaSb show an optical absorption feature below the band gap of GaSb. The intensity of the absorption peak also increases with increasing nanoparticle density. Also, the absorption feature shifts to longer wavelengths with increasing nanoparticle size. Unlike ErAs nanoparticles, ErSb nanoparticles tend to elongate along the $[0\bar{1}1]$ direction with increased ErSb deposition. Thus, the absorption energy of ErSb particles occur at longer wavelengths when the light is polarized along the long axis when compared to polarized perpendicular to the long axis. This separation in absorption energy vs polarization angle increases with ErSb deposition, increasing the ErSb deposition to the point of nanowire formation results in the largest polarization dependence. Similar to ErAs, the optical absorption feature in the ErSb particles and wires are attributed to surface plasmon resonance in the semimetallic ErSb.[21, 49]

Superlattices of ErAs nanoparticles in $\text{GaAs}_{0.5}\text{Sb}_{0.5}$ show the optical absorption feature, attributed to a surface plasmon resonance, near the band edge of the $\text{GaAs}_{0.5}\text{Sb}_{0.5}$. While, nominally ErSb particles, actually $\text{ErAs}_x\text{Sb}_{1-x}$ particles with $x \ll 1$, in $\text{GaAs}_{0.5}\text{Sb}_{0.5}$ appears to have shifted the absorption feature into the $\text{GaAs}_{0.5}\text{Sb}_{0.5}$ band edge.[21] Alternatively, ErAsSb with low amounts of Sb grown via the growth interrupt mode on GaAs do show an optical absorption feature that is attributed to surface plasmon resonance. Similar to the ErSb particles, ErAsSb nanoparticles have an anisotropic shape, and thus the surface plasmon resonance strongly depends on the sample orientation. As with many of the other LN-V particles, the absorption features energy in ErAsSb can be tuned by adjusting the nanostructures geometry with growth parameters.[69]

LuAs nanoparticles in a superlattice with GaAs also show an absorption peak. Again this peak undergoes a red shift in absorption with increasing LuAs deposition.

The exact cause of the shift in the absorption energy is currently under investigation, but could be due to shifts in plasmon resonance or increased quantum confinement.[35].

Similar to many of the other LN-V materials, TbAs nanoparticles co-deposited in GaAs also exhibit an absorption peak at ~ 1 eV. To be consistent with the other LN-V materials, this absorption feature was originally attributed to a plasmon resonance.[36] As discussed above, it was recently discovered that TbAs nanoparticles are actually semiconductors.[26] This suggests that the absorption feature corresponds with the indirect gap transition within the semiconducting TbAs nanoparticles.[27] This is discussed in more detail in Chapter 3.

While many of the LN-As and LN-Sb nanoparticles are semimetals, which quench luminescence, LN doped III-V materials were originally of interest because of the atomic 4f optical transitions with the LN atom. In particular, the 4f optical transition within the Er atom occurs at $1.54 \mu\text{m}$, which is in the low-loss region of optical silica fibers. While Er doped GaAs shows this luminescence peak, Er has a low solubility limit in GaAs. Under typical MBE growth conditions ErAs nanoparticles form and quench the luminescence.[32, 100] Alternatively, LN have a significantly higher solubility limit in the III-N films, resulting in significant emission from the f-shell electrons in the LN ions. AlN and GaN based light emitting diodes doped with various LN elements have emission colors that depend on the LN species including: infrared and green with Er^{3+} , blue with Tm^{3+} , red with Eu^{3+} , and ultraviolet with Gd^{3+} . [101, 102, 103, 104]

In addition to LN-N nanoparticles and LN doped III-V materials having interesting optical properties, LN-V films also have interesting optical properties. For example the LN-V films are semimetallic or degenerately doped semiconductors that have a transparent window, defined as transmission greater than 20%. Note that while the transmission decreases with increasing film thickness, many of the films are transparent over some wavelength range with film thickness of several hundred nanometers. LuAs films show a broader transmission window with a higher peak transmission amount than that of ErAs films, both materials have their transmission window in the near

IR 1.3-1.55 μm range.[35, 105] LaAs has a much more broad transmission window than both LuAs and ErAs, but the window is shifted to the range of $\sim 3\text{-}8\ \mu\text{m}$. [16] In addition to a transmission window, many of the films possess a possible Drude edge; at wavelengths longer than the Drude edge the reflection trends toward 100% and transmission toward 0%. The possible Drude edge wavelengths for several of the Re-V films are summarized in Table 1.2. From Table 1.2 it is clear that the Drude edge of the LN-V materials varies with LN selection and is tunable by alloying LN-V materials. These differences could be due to multiple effects including differences in the band structure, as discussed above, or differences in charge carrier concentrations, discussed below. The differences in both transmission window and Drude edge of the LN-V films shows that the optical properties of LN-V can be tuned.

LN-V Material	Drude Edge (μm)
ErAs[35, 105]	~ 2.85
LuAs[35]	~ 3.1
LaAs[16]	~ 8.0
$\text{La}_{0.48}\text{Lu}_{0.52}\text{As}$ [106]	~ 4.5
TbAs[28]	~ 2.75

Table 1.2: Possible Drude edge wavelengths of the LN-V films

1.5 Electrical Properties

Similar to the optical properties, the electrical properties of the LN-V films have been used to infer the band structure for many of the LN-V material systems. For example, the resistivity of LuAs, LaAs and $\text{La}_x\text{Lu}_{1-x}\text{As}$ films show decreased resistivities with decreasing temperature, consistent with the films being metallic or semimetallic.[35, 16, 76] The normalized resistivity of ErAs, LuAs, and LaAs as a function of temperature is presented in Fig. 1.12.[16] The temperature dependent resistance shows that the dominant carrier scattering mechanism is from the lattice for temperature $> 80\ \text{K}$, carrier scattering for temperatures between 20 and 80 K, and impurity scattering for temperatures $< 20\ \text{K}$. [76] Alternatively, TbAs films show

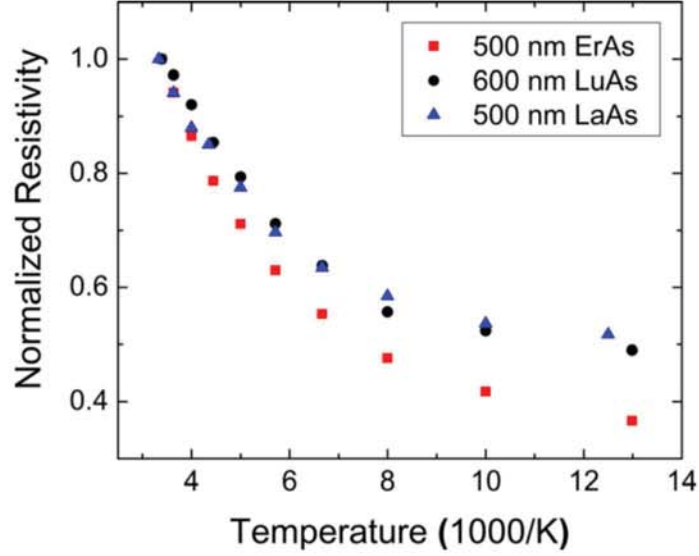


Figure 1.12: The normalized temperature dependent resistivity for films of ErAs, LuAs, and LaAs; consistent with the films being metallic or semimetallic.[16] Reprinted from [16], with the permission of AIP Publishing.

minimal temperature dependence on both the resistivity and carrier concentration from ~ 40 K to 500 K. Combining the electrical properties as a function of temperature with the observed optical transitions suggests that TbAs is a degenerately doped semiconductor.[28] Additionally, the carrier concentration depends on the film thickness, suggesting that the carriers come from interface states.[28] This is discussed in more detail in Chapter 4. Note that while the electronic properties of a film can help infer the band structure, they are not conclusive. For example, films of (111) GdN grown on (0001)GaN show metallic conductivity for temperatures down to 10 K. However, the carriers do not freeze out, and thus it cannot be determined from this measurement alone if GdN is a degenerately doped semiconductor, semimetallic, or half-metallic.[40]

For many applications it is desirable to be able to select and tune the electronic properties. The differences among the lanthanides provide this opportunity. For example, ErAs films have a reported resistivity of $60 \mu\Omega \text{ cm}$ and ErP have a reported resistivity of $150 \mu\Omega \text{ cm}$. By alloying ErAs and ErP, the sheet resistance can be tuned and a film of $\text{ErP}_{0.6}\text{As}_{0.4}$ has a resistivity of $80 \mu\Omega \text{ cm}$.[79] Note that the resistivity

of ErAs films increases by one or two orders of magnitude after being exposed to the atmosphere for one month, likely due to degradation of the films. Interestingly, films of ErP and $\text{ErP}_{0.6}\text{As}_{0.4}$ do not appear to degrade over time, and thus the resistance does not change. In addition to alloying the group V elements, the resistivity can be tuned by changing the LN elements.[79] This has been observed in films of $\text{La}_x\text{Lu}_{1-x}\text{As}$ which have an electrical resistivity between that of LaAs and LuAs.[76] LaAs films with 10 ML LuAs barrier layers have a room temperature resistivity of $\sim 593 \mu\Omega \text{ cm}$ while LuAs films have a room temperature resistivity of $90 \mu\Omega \text{ cm}$, closer to that of ErAs films.[16, 35]

Another way the electronic properties of a LN-V:III-V heterojunction can be controlled is with the film's orientation. First-principles modeling based on plane-wave density functional theory shows that the Schottky barrier height of a LN-V:III-V heterojunction changes with crystal orientation due to the change in bonding character across the interface. Note that the actual Schottky barrier heights calculated do not agree with experiment results, likely due to the Kohn-Sham band-gap problem. However, the modeling does predict the same trend previously seen in experiments,[107] where the p-type Schottky barrier height for the (011) and (001) ErAs:GaAs interfaces differ by 0.2 eV.[82] The Schottky barrier height can also be controlled with the LN-V:III-V interface roughness. As discussed above, the interface roughness can be controlled with the proper growth procedures, for example LN-V cones can be grown prior to the film. With the use of ErAs cones, the Schottky barrier height of ErAs on p-GaAs can be increased by 0.25 eV and the Schottky barrier height of ErAs on n-GaAs can be decreased by 0.29 eV. The amount the Schottky barrier height is changed depends on the pitch of the ErAs cone.[83]

In addition to the electrical properties of LN-V films, lanthanide dopants and nanoparticles also provide interesting electrical properties. First principles and hybrid density functional theory models show that interstitial Er doping in GaAs, InGaAs, and InAs is a donor while substitutional Er doping is electrically inactive; the formation energy of interstitial Er in InAs is significantly smaller than in GaAs and thus is more

electrically active.[45] Increasing the amount of Er doping in $\text{In}_{0.53}\text{Ga}_{0.47}\text{As}$ and InAs results in an increase in the carrier concentration and a decrease in the mobility; the doping efficiency is increased with increasing In content in the matrix.[12, 45] This results in a maximum conductivity at a Er doping level of $\sim 8 \times 10^{19} \text{ cm}^{-3}$. [12] The rate of carrier concentration increase and mobility decrease with Er doping levels changes for Er doping levels above $\sim 6 \times 10^{19} \text{ cm}^{-3}$, consistent with exceeding the saturation limit of Er in $\text{In}_{0.53}\text{Ga}_{0.47}\text{As}$ and the formation of ErAs nanoparticles.[12] The deposition of Er above the solubility limit in co-doped ErAs:III-V materials still results in atomic Er existing in the matrix and contributes to the electron concentration.[45] Similar to Er doping, Sc doping in $\text{In}_{0.53}\text{Ga}_{0.47}\text{As}$ results in a carrier concentration that increases with increasing Sc amounts; once the solubility limit is reached and ScAs nanoparticles form, the carrier concentration increases more slowly.[22] The conductivity, mobility, and carrier concentration as a function of amount of ErAs and ScAs co-deposited in $\text{In}_{0.53}\text{Ga}_{0.47}\text{As}$ is shown in Fig. 1.13.[22] As discussed above in the growth section, the solubility limit of Er in III-V materials is dependent upon temperature and is evident with electrical measurements. Increasing the growth temperature of Er doped $\text{In}_{0.53}\text{Ga}_{0.47}\text{As}$ results in a decreased carrier density, decreased electrical conductivity, and increased Seebeck coefficient, likely due to the formation of ErAs nanoparticles.[44] It is worth mentioning that in addition to changing the carrier concentration, mobility, and conductivity, increasing the amount of Er in $\text{In}_{0.53}\text{Ga}_{0.47}\text{As}$ changes the donor energy level. At low Er levels, $1.5 \times 10^{17} \text{ cm}^{-3}$, Er is a shallow donor in $\text{In}_{0.53}\text{Ga}_{0.47}\text{As}$ with activation energy of $\sim 25 \text{ meV}$. Increasing the Er doping level to just above only $4.4 \times 10^{17} \text{ cm}^{-3}$ results in the $\text{In}_{0.53}\text{Ga}_{0.47}\text{As}$ film being degenerately doped.[12]

As with doping $\text{In}_{0.53}\text{Ga}_{0.47}\text{As}$ with LN atoms, LN-As nanoparticles, including ErAs, ScAs, ScErAs, LuAs, LaAs, GdAs, and TbAs, act as a dopants in $\text{In}_{0.53}\text{Ga}_{0.47}\text{As}$ where increasing the LN amount often increases the doping level.[32, 11, 22, 56, 37, 27] In many of the nanoparticles, decreasing the nanoparticle size results in an increased doping level; indicating that the smaller nanoparticles cause the Fermi level to increase with respect to the band edge. While, many of the LN-As act as n-type dopants, ErSb

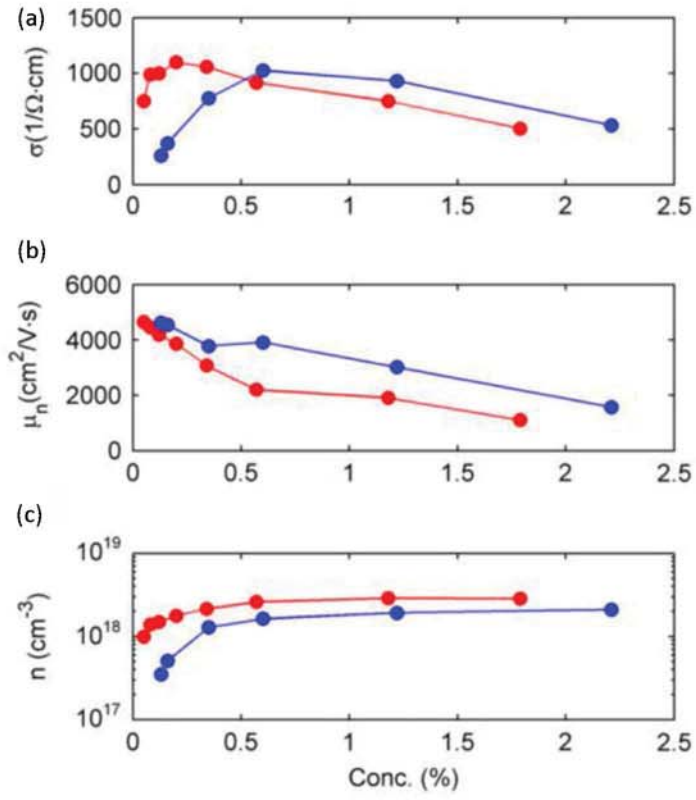


Figure 1.13: The (a) conductivity, (b) mobility, and (c) electron concentration all depend on the amount of ErAs (red) and ScAs (blue) co-deposited in $\text{In}_{0.53}\text{Ga}_{0.47}\text{As}$. [22] Reprinted from [22], with permission from Elsevier

reduces the carrier concentration in GaSb. Typically, GaSb is unintentionally p-type, and so incorporating ErSb, via the growth interrupt method, reduces the hole concentration. As with ErAs:In_{0.53}Ga_{0.47}As, smaller ErSb particles move the Fermi level farther up relative to the band edge. Since GaSb is p-type, incorporating smaller ErSb particles results in a larger reduction in hole concentration.[32] The LN-V nanoparticles moving the Fermi level of the matrix material was also observed in ErAs:GaBiAs where unintentionally doped GaBiAs is p-type but the incorporation of ErAs nanoparticles resulted in the nanocomposite changing to n-type.[29] This is discussed in more detail in Chapter 5.

There are multiple ways in which the Fermi level relative to the band edges, and subsequently carrier concentration, can be adjusted. For example the matrix material can change the energy difference between the band edge and the Fermi level. This has been observed in ErAs:(In_{0.52}Al_{0.48}As)_x(In_{0.53}Ga_{0.47}As)_{1-x} where the Fermi level was adjusted from within the conduction band for x=0 to near the middle of the band gap for x=1, shown in Fig. 1.14.[23] This is also observed when comparing the same lanthanide species in two different matrices; such as comparing TbAs:In_{0.53}Ga_{0.47}As to TbAs:GaAs where both systems are n-type but TbAs:In_{0.53}Ga_{0.47}As has a much higher carrier concentration.[27] Alternatively, the Fermi level location can be adjusted with the proper LN selection or LN alloying. Each of the LN-V nanoparticles pin the Fermi level at different locations. For example GdAs generally pins the Fermi level higher than ErAs and LuAs and all three pin the Fermi level higher than LaAs.[11] Figure 1.15 shows the activation energy, which is related to the Fermi level, as a function of some of the lanthanide species and deposition amounts.[11] Additionally, ScAs:In_{0.53}Ga_{0.47}As has a lower carrier concentration than ErAs:In_{0.53}Ga_{0.47}As, which indicates a lower Fermi level, and ScErAs:In_{0.53}Ga_{0.47}As has a carrier concentration in between the two. This indicates that is not only possible to tune the carrier concentration with LN amount and selection of LN, but also by alloying multiple LN species. Note, alloying to get a specific carrier concentration only works if the nanoparticle forms an alloy and not a core-shell structure, such as in TbErAs. The carrier concentration of TbErAs

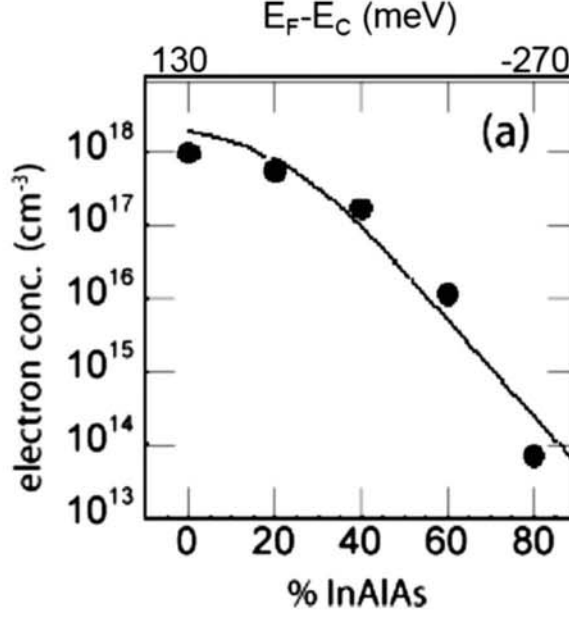


Figure 1.14: The room temperature carrier concentration of $\text{ErAs}:(\text{In}_{0.52}\text{Al}_{0.48}\text{As})_x(\text{In}_{0.53}\text{Ga}_{0.47}\text{As})_{1-x}$ as a function of the amount of $\text{In}_{0.52}\text{Al}_{0.48}\text{As}$. The black circles represent the measured values, the line represents the carrier concentration predicted by the Fermi-Dirac integral where the energy difference between the Fermi level and conduction band edge changes linearly with composition.[23] Reprinted from [23], with the permission of AIP Publishing.

core-shell nanoparticles in $\text{In}_{0.53}\text{Ga}_{0.47}\text{As}$ is lower than that of both $\text{ErAs}:\text{In}_{0.53}\text{Ga}_{0.47}\text{As}$ and $\text{TbAs}:\text{In}_{0.53}\text{Ga}_{0.47}\text{As}$. It is also worth noting that the carrier concentration in many of the LN-As:III-As nanocomposites can be reduced by compensation doping with beryllium, an acceptor in $\text{In}_{0.53}\text{Ga}_{0.47}\text{As}$. [108]

While the carrier concentration of the LN-V:III-V nanocomposites generally increases with increasing LN amounts, the mobility generally decreases with increasing LN amounts. This has been observed in both co-doped LN-V materials, including ErAs, ScAs, ScErAs, TbAs in $\text{In}_{0.53}\text{Ga}_{0.47}\text{As}$, and LN-V superlattices, including ErAs, LuAs, LaAs, and GdAs in $\text{In}_{0.53}\text{Ga}_{0.47}\text{As}$. [22, 56, 37, 11] It is worth noting that in the superlattice samples, both decreasing the spacing between the nanoparticle layers and increasing the amount of LN-V in each layer decreases the mobility. The decrease in mobility with increasing LN amount is likely due to the reduced III-V

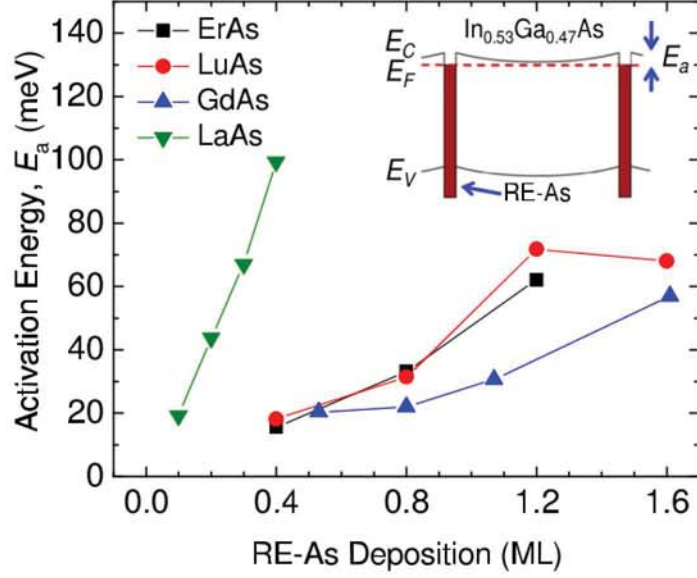


Figure 1.15: The activation energy, which is related to the Fermi level, depends on the lanthanide type and LN-V deposition amount.[11] Reprinted from [11], with the permission of AIP Publishing.

overgrowth at higher LN-V deposition amounts. It is worth noting that in general, the LN-V:III-V materials can have high mobilities. For example LuAs and GdAs superlattices with periods consisting of 40 nm $\text{In}_{0.53}\text{Ga}_{0.47}\text{As}$ and 1.6 ML LN-As have mobilities $>2400 \text{ cm}^2/\text{V-s}$, slightly higher than that of $\text{ErAs}:\text{In}_{0.53}\text{Ga}_{0.47}\text{As}$. Note that $\text{LaAs}:\text{In}_{0.53}\text{Ga}_{0.47}\text{As}$ superlattices have significantly lower mobilities, only 0.4 ML LaAs results in a mobility of $1600 \text{ cm}^2/\text{V-s}$. The reduced mobility in $\text{LaAs}:\text{In}_{0.53}\text{Ga}_{0.47}\text{As}$ is likely due to poor $\text{In}_{0.53}\text{Ga}_{0.47}\text{As}$ overgrowth quality as a result of multiple LaAs crystalline phases.[11] Additionally, the co-deposited LN-V materials can also have high mobilities. For example, 0.78% TbAs in $\text{In}_{0.53}\text{Ga}_{0.47}\text{As}$ has a mobility of $3494 \text{ cm}^2/\text{V-s}$, 0.3% ErAs in $\text{In}_{0.53}\text{Ga}_{0.47}\text{As}$ has a mobility of $\sim 3200 \text{ cm}^2/\text{V-s}$ and TbErAs nanoparticles, with 0.78% TbAs and 0.3% ErAs, co-deposited in $\text{In}_{0.53}\text{Ga}_{0.47}\text{As}$ has a mobility of $2497 \text{ cm}^2/\text{V-s}$. [37, 109]

Due to the increasing carrier concentration and decreasing mobility with increasing LN amounts, the conductivity initially increases and then decreases with LN amounts. The amount of LN required for the maximum conductivity, and the value

of the maximum conductivity, depends on LN-V species. For example, the conductivity of TbAs:In_{0.53}Ga_{0.47}As peaks with 1% TbAs, ScAs:In_{0.53}Ga_{0.47}As peaks with 0.6% ScAs, and ErAs:In_{0.53}Ga_{0.47}As peaks with 0.2% ErAs.[37, 56, 22] Note that the peak conductivities versus LN-As amounts are reported for room temperature values. The conductivity does depend on temperature, as observed in TbAs co-deposited in In_{0.53}Ga_{0.47}As where the conductivity increases with temperature due to an increased carrier concentration via nanoparticle doping at high temperatures. [110] Conductivity depending on LN-V species is also evident in the superlattice structures. For example, LuAs, ErAs, and GdAs nanoparticles in In_{0.53}Ga_{0.47}As all show a modest difference in conductivity. LaAs:In_{0.53}Ga_{0.47}As has a significantly lower conductivity for any given LN-V amount due to the lower mobility discussed above.[11] The dependence of conductivity on LN-V density is true for both the co-deposition method and the growth interrupt method. Note, in the growth interrupt method the LN-V density can be controlled with the amount of LN-V deposited each in layer and the spacing between the LN-V layers. For some applications, discussed below, it is desirable to reduce the conductivity or increase the dark resistance. In both the co-deposition and the growth interrupt methods the dark resistance can be increased with compensation doping.[42, 111, 108, 32] Note that in the growth interrupt method, compensation doping with beryllium via delta doping results in a dark current of at least one order of magnitude larger than step compensation doping provides.[99] An additional way to increase the resistance of superlattices of ErAs nanoparticles in In_{0.53}Ga_{0.47}As is with the use of thin In_{0.52}Al_{0.48}As barrier layers.[111] It is important to remember that the resistivity of the nanocomposite film is very dependent upon the matrix composition, for example the resistance of a TbAs:GaAs co-deposited sample is much higher than that of a TbAs:In_{0.53}Ga_{0.47}As co-doped sample.[36, 37, 27]

The Seebeck coefficient of materials typically tracks inversely with carrier concentration and conductivity. This is true for many of the LN-V nanoparticles in III-V including ErAs and ScAs co-deposited in In_{0.53}Ga_{0.47}As. As with many of the other electrical properties discussed above, the Seebeck coefficient depends on the

LN-V species, for example ErAs:In_{0.53}Ga_{0.47}As has a higher Seebeck coefficient than ScAs:In_{0.53}Ga_{0.47}As.[56] The Seebeck coefficient can be increased by electron filtering. For example, a super lattice of 20 nm ErAs:In_{0.53}Ga_{0.47}As and 10 nm In_{0.53}Ga_{0.28}Al_{0.19}As can increase the Seebeck coefficient 2 to 3 \times over ErAs:In_{0.53}Ga_{0.47}As.[112] This method primarily increases the Seebeck coefficient in the cross-plane direction.[113] The difference between the in-plane and cross-plan Seebeck coefficient is reduced at higher electron concentrations due to the Fermi level moving into the conduction band, reducing the InGaAlAs's barrier height and effectiveness as an electron filter.[114] Alternatively, the in-plane and cross-plane Seebeck coefficients can be increased by co-depositing ErAs directly in InGaAlAs. This results similar electron filter effects to the superlattice structure, shown by similar Seebeck coefficients.[115] The electron filtering effect allows for both the electrical conductivity and the Seebeck coefficient to increase with increasing temperature, shown in Fig. 1.16.[24] Interestingly, TbAs nanoparticles in In_{0.53}Ga_{0.47}As show both high Seebeck coefficients and high electrical conductivity; the Seebeck coefficient is more than twice that of Si-doped In_{0.53}Ga_{0.47}As while having an electrical conductivity on the same order of magnitude as conventionally doped semiconductors.[37] Additionally, both the Seebeck coefficient and the electrical conductivity increase at higher temperatures.[110] Presently, it is unknown why TbAs:In_{0.53}Ga_{0.47}As does not follow the general trend of the Seebeck coefficient tracking inversely with conductivity. However, I will speculate on this in Chapter 6

1.6 Thermal Conductivity

In addition to altering the optical and electrical properties, LN-V nanoparticles often significantly alter the thermal properties of a LN-V:III-V nanocomposite. For example, ErAs nanoparticles have three effects on the thermal conductivity: they donate electrons which increases the thermal conductivity, they increase the number of electrons which increases the electron phonon scattering and decreases the phonon contribution to thermal conductivity, and ErAs further reduces the phonon contribution to thermal conductivity by nanoparticle scattering. Only the nanoparticle scattering

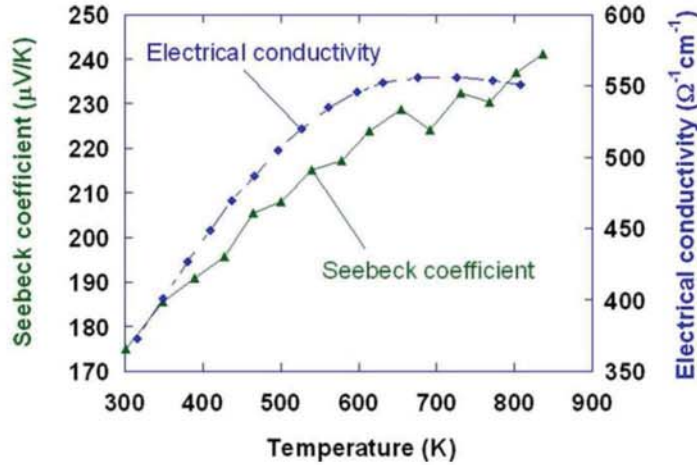


Figure 1.16: The Seebeck coefficient and electrical conductivity both increase with temperature for 0.6% ErAs co-deposited in $(\text{In}_{0.53}\text{Ga}_{0.47}\text{As})_{0.8}(\text{In}_{0.52}\text{Al}_{0.48}\text{As})_{0.2}$, suggesting electron filtering.[24] Reprinted from [24], with the permission of AIP Publishing.

significantly alters the thermal conductivity in the temperature ranges where ErAs nanoparticles have the largest effect.[116] Doping $\text{In}_{0.53}\text{Ga}_{0.47}\text{As}$ with Er also causes a decrease, albeit a small decrease, in the thermal conductivity. Growing the Er doped $\text{In}_{0.53}\text{Ga}_{0.47}\text{As}$ at increased temperatures results in a larger reduction in thermal conductivity, which is consistent with nanoparticle formation.[44]. While, the thermal conductivity of a III-V matrix can be reduced with LN doping, LN-V nanoparticles grown via the growth interrupt method, and LN-V nanoparticles grown via the co-deposition method, the co-deposition method results in the lowest thermal conductivity.[116]

As with the electronic and optical properties, the thermal conductivity strongly depends on LN-V concentrations and LN species. For low ErAs concentration, 0.3% ErAs, the largest reduction in thermal conductivity occurs between 150 and 450 K, with minimal reduction for temperatures above 600 K due to Umklapp phonon scattering dominating.[116] Increasing the ErAs amount to 3 or 6% lowers the thermal conductivity for temperature above 600 K due to the ErAs nanoparticles creating a mean free path that is shorter than the mean free path due to Umklapp scattering.[10] Note that increasing the amount of ErAs also results in a larger reduction in thermal conductivity for temperature below 600 K.[10] Figure 1.17 shows the decrease in

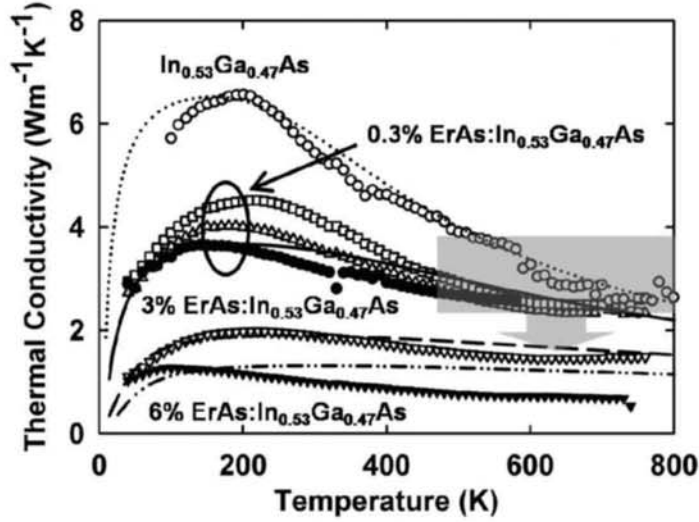


Figure 1.17: The reduction in thermal conductivity with increasing ErAs amount in $\text{In}_{0.53}\text{Ga}_{0.47}\text{As}$. [10] Adapted with permission from [10] Copyright 2008 American Chemical Society

thermal conductivity with increasing ErAs amount in $\text{In}_{0.53}\text{Ga}_{0.47}\text{As}$. The decrease in thermal conductivity with increasing LN-V amount has also been observed in ScAs and ScErAs with no strong dependence on the type of rare earth element. [56] Interestingly, significantly more TbAs, $>1.7\%$ TbAs, is required to reduce the thermal conductivity below that of $\text{In}_{0.53}\text{Ga}_{0.47}\text{As}$, again increasing the amount of TbAs results in a reduced thermal conductivity. [37, 110]

While the LN-V nanoparticles reducing the thermal conductivity of $\text{In}_{0.53}\text{Ga}_{0.47}\text{As}$ is the most studied, it is worth noting that the LN-V nanoparticles reduce the thermal conductivity of many other III-V matrices. For example, ErAs reduces the thermal conductivity of $(\text{In}_{0.53}\text{Ga}_{0.47}\text{As})_{0.8}(\text{In}_{0.52}\text{Al}_{0.48}\text{As})_{0.2}$, and increasing the amount of ErAs from 0.3 to 0.6% results in a $\sim 25\%$ reduction in thermal conductivity. ErSb nanocrystals reduce the thermal conductivity of $\text{In}_x\text{Ga}_{1-x}\text{Sb}$ due to the differences in stiffness and density between the nanoparticles and the matrix. [46] Note the ErSb: $\text{In}_x\text{Ga}_{1-x}\text{Sb}$ system is the p-type analog to the n-type ErAs: $\text{In}_{0.53}\text{Ga}_{0.47}\text{As}$ for applications such as thermoelectrics discussed below. Finally, ErAs nanoparticles and TbAs nanoparticles reduce the thermal conductivity of GaAs; in both cases the electrical conductivity is

low so the thermal conductivity is almost entirely due to phonons.[64, 117, 36]

1.7 Application of LN-V:III-V

Due to the electronic structure and properties discussed above, LN-V nanoparticles embedded within III-V films and LN-V films have become of interest for a wide range of applications. This includes thermoelectrics, terahertz detection and generation, tunnel junctions, and electrical contacts. Below I discuss some of the recent advances of using LN-V based materials for these applications. Note that LN-V review provided by Hanson et al. heavily focused on the applications of LN-V materials, and thus I will focus primarily on the progress made since that review.[32]

Thermoelectric power generators are one of the applications that have greatly benefited from LN-V nanoparticles. The effectiveness of a material is often characterized by the figure of merit ZT , which is determined by $ZT = \frac{S^2\sigma}{\kappa}T$ where S is the Seebeck coefficient, σ is the electrical conductivity, κ is the thermal conductivity, and $S^2\sigma$ is defined as the power factor. Typically, these properties are interrelated which prevents vast increases in the ZT . However, incorporating LN-V nanoparticles into III-V materials can improve the ZT by decoupling these parameters. For example ErAs nanoparticles in $\text{In}_{0.53}\text{Ga}_{0.47}\text{As}$ pin the Fermi level near the conduction band edge, donating electrons while maintaining a high carrier mobility which results in a high electrical conductivity. Additionally, the nanoparticles scatter phonons which reduces the thermal conductivity, leading to a net increase in the ZT . [32]

Recent work has focused on further improving the ZT . One way this can be done is with electron filtering to increase the Seebeck coefficient while keeping the thermal conductivity low with phonon scattering by ErAs nanoparticles. Superlattices consisting of ErAs co-deposited in $\text{Si}:\text{In}_{0.53}\text{Ga}_{0.47}\text{As}$ and $(\text{In}_{0.53}\text{Ga}_{0.47}\text{As})_{0.6}(\text{In}_{0.52}\text{Al}_{0.48}\text{As})_{0.41}$ results in a large improvement in ZT over bulk $\text{In}_{0.53}\text{Ga}_{0.47}\text{As}$. A large portion of that increase comes from electron filtering that improves the Seebeck coefficient. The remaining improvements coming from ErAs reducing the thermal conductivity.[112] Using this general idea, a 400 element thermoelectric module with each element being

200 $\mu\text{m} \times 200 \mu\text{m}$ in area and consisting of a 5 μm thick superlattice of 70 periods of 10 nm $(\text{In}_{0.53}\text{Ga}_{0.47}\text{As})_{0.6}(\text{In}_{0.52}\text{Al}_{0.48}\text{As}_{0.4})$ and 20nm ErAs:InGaAs with 0.3% ErAs output over 0.7 mW of power with a temperature difference of 30 K across the entire device.[113]

Typically, thermoelectric devices require thick films, and the numerous shutter operations for a superlattice growth are undesirable. Alternatively ErAs co-deposited in InGaAlAs can be used, eliminating the numerous shutter operations. The Schottky barriers formed between the randomly distributed ErAs nanoparticles and the matrix act as non-planer electron filters while the ErAs nanoparticles increase the conductivity by donating electrons and reduce the thermal conductivity by scattering long wavelength phonons.[118] The enhanced Seebeck coefficient and reduced thermal conductivity of ErAs: $(\text{In}_{0.53}\text{Ga}_{0.47}\text{As})_{0.8}(\text{In}_{0.52}\text{Al}_{0.48}\text{As})_{0.2}$ results in a ZT of 0.16 at 300 K and 1 at 600 K.[115] This resulted in a thermoelectric power generator made from 400 elements of 10 μm thick n-type ErAs: $(\text{In}_{0.53}\text{Ga}_{0.47}\text{As})_{0.8}(\text{In}_{0.52}\text{Al}_{0.48}\text{As})_{0.2}$ and p-type ErAs:In $_{0.53}$ Ga $_{0.47}$ As having an open circuit voltage of 2.1 V and output power of 1.12 W/cm 2 when a temperature difference of 120 K was applied across the device. Note that each element only experienced an average temperature difference ~ 24 K. The performance was further improved to an open circuit voltage of 3.5 V and output power of 2.5 W/cm 2 by increasing the element thickness to 20 μm and the temperature difference to 140 K, ~ 39 K average temperature difference across each element.[119] Further enhancements are possible with thicker elements and increased temperature differences. This was demonstrated by a segmented thermoelectric generators consisting 254 1 mm \times 1 mm elements made from 50 μm thick n-type ErAs: $(\text{In}_{0.53}\text{Ga}_{0.47}\text{As})_{0.8}(\text{In}_{0.52}\text{Al}_{0.48}\text{As})_{0.2}$ or p-type ErAs:In $_{0.53}$ Ga $_{0.47}$ As and 300 μm thick Bi $_2$ Te $_3$ producing an output power of 5.5 W with an open circuit voltage over 10 V when the Er containing side was maintained at 600 K and the cooled side was kept at ~ 285 K.[115] By increasing the amount of ErAs in the segmented thermoelectric generators, the power output of the thermoelectric power generator was further increased to 6.3 W, shown in Fig. 1.18.[24]

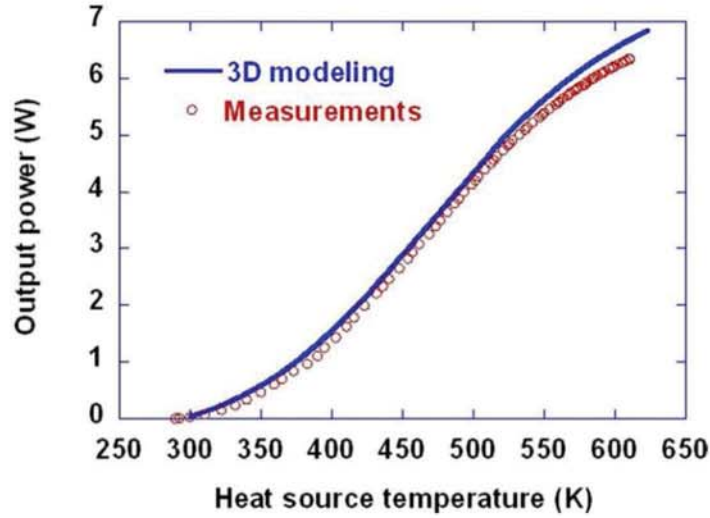


Figure 1.18: The power output of a segmented thermoelectric power generator made from 50 μm 0.6% ErAs co-deposited in $(\text{In}_{0.53}\text{Ga}_{0.47}\text{As})_{1-x}(\text{In}_{0.52}\text{Al}_{0.48}\text{As})_x$ and 0.8 mm Bi_2Te_3 , showing a power output of 6.3 W.[24] Reprinted from [24], with the permission of AIP Publishing.

Modeling suggests that the power factor could be increased, and ultimately the ZT increased, by optimizing the ErAs nanoparticle concentration, the barrier height between the particle and the matrix, and the electron concentration.[120] The barrier height between the particle and the matrix can be tuned by tuning the conduction band edge independently of the Fermi-level, which is possible by tuning the amount of Al in $\text{ErAs}:\text{In}_{0.53}\text{Ga}_{0.47-x}\text{Al}_x\text{As}$. This allows for the engineering of energy-dependent scattering of carriers by the nanoparticles and was observed by a simultaneous increase in both electrical conductivity and Seebeck coefficient with temperature for 0.6% ErAs co-deposited in $\text{In}_{0.53}\text{Ga}_{0.47-x}\text{Al}_x\text{As}$. At the same time a reduction in the thermal conductivity with increasing temperature was measured. This resulted in a ZT of 1.3 at 800 K, shown in Fig. 1.19.[23]

Thus far we have focused on improvements in ZT and thermoelectric generator output power by improving the n-type elements. It is important to note that there has been some recent work to improve the p-type element. For example, Be doped $\text{ErSb}:\text{GaSb}$ has a power factor three time higher than that of the best p-type

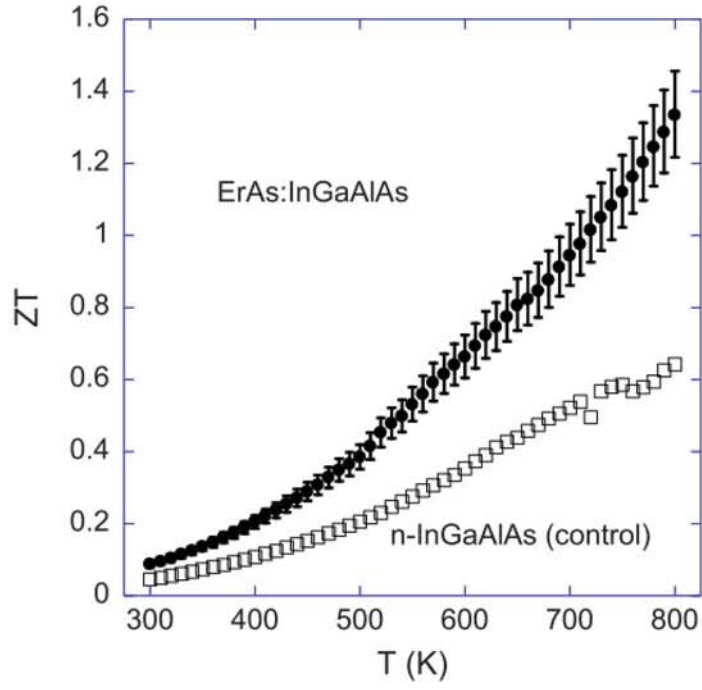


Figure 1.19: The ZT of 0.6% ErAs co-deposited in $\text{In}_{0.53}\text{Ga}_{0.47-x}\text{Al}_x\text{As}$ as a function of temperature, showing a ZT of 1.3 at 800 K.[23] Reprinted from [23], with the permission of AIP Publishing.

ErAs:In_{0.53}Ga_{0.47}As.[118] By alloying the ErSb:GaSb with In, the thermal conductivity can be reduced, resulting in an improved ZT for the p-type element. This has been observed in segmented thermoelectric modules of 8×8 elements of 54 μm n-type ErAs:In_{0.53}Ga_{0.47}As and p-type ErSb:In_{0.12}Ga_{0.88}Sb on 0.8 mm Bi₂Te₃. By maintaining the hot side, the Er containing segments, at ~ 600 K and the cold side, the Bi₂Te₃ segments, at ~ 285 K, the thermoelectric generator output over 1.4 W of power.[118]

This section has focused on ErAs and ErSb nanoparticles for thermoelectric devices and it should be noted that many other lanthanide based materials have been investigated for thermoelectric applications including Er doped In_{0.53}Ga_{0.47}As, and ScAs, ErAs, ScErAs, and TbAs co-deposited in In_{0.53}Ga_{0.47}As. Er doped In_{0.53}Ga_{0.47}As resulted in a room temperature power factor of ~ 9 W/m-K² and ZT of 0.06.[45] ScAs, ErAs, and ScErAs co-deposited in In_{0.53}Ga_{0.47}As all have a maximum room temperature ZT between 0.11 and 0.13 at rare earth concentrations less than 0.5%.[56] 0.2% TbAs co-deposited in In_{0.53}Ga_{0.47}As has a power factor of 2.38 W/m-K² and a ZT of 0.19 at room temperature. The improved room temperature ZT of TbAs:In_{0.53}Ga_{0.47}As is primarily due to the power factor improvement, and not due to a reduced thermal conductivity.[37] As a reference, unintentionally doped In_{0.53}Ga_{0.47}As without rare earth elements has a room temperature ZT of 0.0045.[56]

Another application that has seen benefits from lanthanide based materials is tunnel junctions. Semimetallic LN-V nanoparticles have previously been observed to increase the tunneling current through a p-n junction, because they allow for a two-step tunneling process.[32] The LN-V based tunnel junctions have been used in devices including multijunction solar cells and vertical-cavity surface emitting lasers.[25, 70]

As mentioned above, ErAs nanoparticles placed at the tunnel junctions of a multijunction solar cell increases the tunnel junctions performance. Incorporating 1.2 ML ErAs at the junction interface of an Al_{0.3}Ga_{0.7}As/GaAs multijunction solar cell only requires a ~ 0.3 mV bias, compared to the ~ 0.7 V bias required in the nonoptimized conventional tunnel junction. This results in efficiency of the multijunction solar cell with ErAs enhanced tunnel junctions being $\sim 2\times$ that of one with conventional tunnel

junctions.[25] Figure 1.20 shows the J-V curve for a conventional and ErAs enhanced tunnel junction; showing that the ErAs enhanced junction needs a significantly lower bias to achieve the same tunneling current.[25] The improvement in tunneling current density is dominated by the ErAs surface coverage of the junction.[63] As discussed in the growth section, the surface coverage of LN-V nanoparticles grown by the growth interrupt method is in part determined by the growth temperature. Thus, tunnel junctions with ErAs nanoparticles grown at temperatures from 485 to 545°C have similar surface coverages and tunneling current densities. However, increasing the growth temperature to $\geq 575^\circ\text{C}$ results in a lower tunneling current density due to lower surface coverage.[63, 121] The increased density of small nanoparticles at lower growth temperatures also changes the energy band alignment between the ErAs nanoparticle and III-V matrix, which enhances the tunneling conductivity.[70] Additionally, since the tunneling current density depends on surface coverage, a linear increase in the ErAs deposition results in a linear increase in current density.[63] At high deposition amounts, and thus for large nanoparticles, there is an increased resistance for tunneling into the nanoparticles, possibly due to the difficulty in overgrowth of larger nanoparticles or a morphological dependence of the Schottky barrier height between the ErAs nanoparticle and the GaAs film.[121] Recent work shows that for GaAs tunnel junctions only 0.7 ML ErAs grown at 530°C is required to get the maximum current enhancement without degrading the GaAs overgrowth.[66]

In addition to ErAs enhanced GaAs tunnel junction, LN-V materials have been shown to improve other III-V tunnel junctions. ErAs nanoparticles have also been shown to improve the tunneling current between highly n-doped and p-doped InAlGaAs and AlGaAs by reducing the total resistance and junction resistance compared to non-ErAs containing junctions. Note that a high acceptor density is essential for achieving the high current densities.[122] Similarly, GdN nanoislands also create midgap states in p-n GaN junctions, enhancing the interband tunneling by several orders of magnitude. Specifically, GdN nanoislands in GaN tunnel junctions provide very efficient hole tunneling into p-GaN layers and reduces the specific resistivity by two orders of

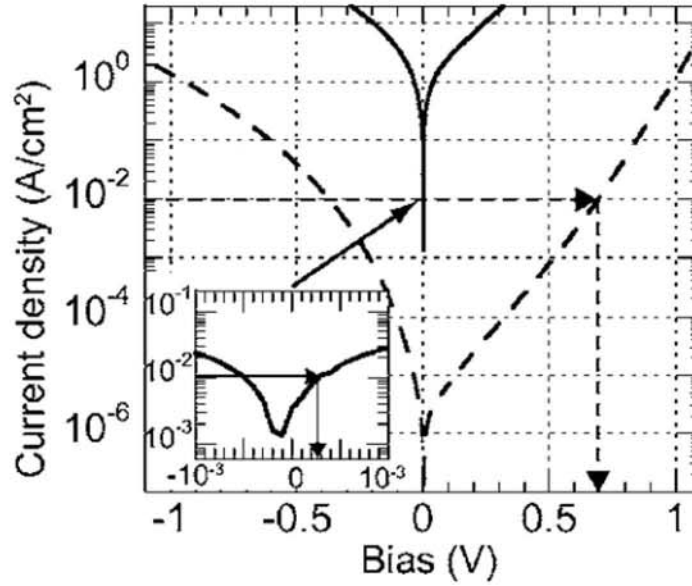


Figure 1.20: A room temperature J-V curve for a conventional tunnel junction (dashed line) and an ErAs enhanced tunnel junction (solid line and inset). Depicting the drastically reduced bias required to achieve the same tunneling current.[25] Reprinted from [25], with the permission of AIP Publishing.

magnitude, resulting in a reduced tunnel resistivity.[123]

Terahertz detection, generation, and modulation has also benefited from LN-V nanoparticles. Devices to detect, generate, and modulate THz radiation that have benefited from LN-V nanoparticles include photomixers and photoconductive switches, large area emitters, and split ring resonators.

The key properties of photoconductive switches include short carrier lifetimes, high dark resistance, high mobility, and a band gap that is compatible with the laser system driving the device.[32] Photoconductive switches made from ErAs:GaAs have up to $291\times$ and $157\times$ improved optical-to-terahertz power conversion than state of the art radiation damaged silicon on sapphire and low temperature grown GaAs, respectively. This is likely due to the carrier dynamics in ErAs:GaAs, and shows that ErAs:GaAs allows for uncompromised THz detection with enhanced optical efficiency.[124] Unfortunately, GaAs based photoconductive switches must be pumped with large and expensive Ti:sapphire lasers. To move to portable and inexpensive photoconductive

switches, devices that are able to be pumped with fiber coupled lasers are desired.

One method to make portable photoconductive switches is to change the host material to $\text{In}_{0.53}\text{Ga}_{0.47}\text{As}$, which can be pumped with a $1.55\ \mu\text{m}$ fiber coupled laser. However, as discussed above, co-deposited ErAs in $\text{In}_{0.53}\text{Ga}_{0.47}\text{As}$ results in a Fermi level pinned near the conduction band edge and, unfortunately, does not result in high dark resistances. One method to overcome this is to grow ErAs nanoparticles in a superlattice formation in $\text{In}_{0.53}\text{Ga}_{0.47}\text{As}$, where spacing the nanoparticles out can push the Fermi level into the band gap. Unfortunately, increasing the nanoparticles spacing increases the carrier lifetime. Note that for generation, changing the lifetime does not significantly change the bandwidth, which is likely dominated by the characteristics of the pulse laser, and THz generated with superlattices were measured to have a bandwidth up to 3.1 THz.[125] Another method to increase the dark resistance of ErAs: $\text{In}_{0.53}\text{Ga}_{0.47}\text{As}$ is to compensate the carriers with an acceptor dopant such as beryllium. Photoconductive switches made of co-deposited 0.6% ErAs and $5 \times 10^{18}\ \text{cm}^{-3}$ Be in $\text{In}_{0.53}\text{Ga}_{0.47}\text{As}$ with a square spiral antenna were able to output THz pulses with an average power of $12\ \mu\text{W}$, which is a higher power output than other reported $1.55\ \mu\text{m}$ photoconductive switches.[126] Finally, another method to make a photoconductive switch capable of being pumped with fiber coupled lasers is to use other materials. Studies of LaAs, GdAs, LuAs deposited via the growth interrupt method in $\text{In}_{0.53}\text{Ga}_{0.47}\text{As}$ show promising properties for fast photoconductive switches with further improvements in current growth conditions.[11] Alternatively, the host matrix can be changed so that ErAs pins the Fermi level within the band gap while still being able to be pumped with a fiber couple optical pump. This has recently been shown in ErAs nanoparticles co-deposited in GaBiAs where the initial films studied have a band gap capable of being pumped with a 1064 nm fiber coupled laser, short carrier lifetimes, high dark resistivities, and high carrier mobilities.[29] This is discussed in more detail in Chapter 5.

Similar to photoconductive switches, photomixers have benefited from the short

carrier lifetimes provided by the LN-V nanoparticles. Also, similar to photoconductive switches, it is desired to be able to use $1.55\ \mu\text{m}$ light for photomixing. To achieve this ErAs nanoparticles have been utilized via the growth interrupt method in $\text{In}_{0.53}\text{Ga}_{0.47}\text{As}$ with Be compensation doping, resulting in THz output powers up to $0.2\ \mu\text{W}$. This power could be increased by decreasing the spacing between the ErAs nanoparticles.[127] The ErAs: $\text{In}_{0.53}\text{Ga}_{0.47}\text{As}$ photomixer has since been improved on with the use of plasmonic contact electrodes that offer a significantly higher terahertz radiation power by reducing the average transport path length of the photocarriers.[128]

Another method of terahertz generation that has benefited from LN-V nanoparticles is large area emitters. The incorporation of ErAs nanoparticles surrounded by $\text{In}_{0.52}\text{Al}_{0.48}\text{As}$ in $\text{In}_{0.53}\text{Ga}_{0.47}\text{As}$ act as recombination centers. Note that pulsed large area emitters do not require the short carrier lifetimes that a continuous wave emitter would. Instead, the incorporation of ErAs surrounded by $\text{In}_{0.52}\text{Al}_{0.48}\text{As}$ is to reduce the resistance, by a factor of at least 45, of the $\text{In}_{0.53}\text{Ga}_{0.47}\text{As}$ matrix. This allows for higher biasing and subsequently a drastic increase in power. Pulsed large area emitters taking advantage of the ErAs nanoparticles have demonstrated operation up to $\sim 4\ \text{THz}$ with a peak field strength of $0.7\ \frac{\text{V}}{\text{cm}}$ at room temperature.[111]

Finally, terahertz modulation from ring resonators has also benefited from LN-V nanoparticles. Single ring resonator metamaterials fabricated on ErAs:GaAs improves the on/off times of the resonator due to the short carrier lifetimes in the substrate.[129] This is also seen in split ring resonators on ErAs:GaAs substrates where the resonators can be designed to modulate freely propagating THz waves or act as THz switches. The response rates of the split ring resonators are dependent upon the substrates lifetime, which can be tuned with the ErAs spacing.[130]

While the majority of the applications discussed thus far have focused on embedded LN-V nanoparticles, LN-V films have shown to be of interest as contact layers. Epitaxial ErAs and ErSb on III-V semiconductors are interesting as contact layers because of the lack of interfacial phases and the prevention of interface oxide formation due to the *in situ* growth of the semimetallic film.[32] Additionally, the barrier height

between the LN-V and the III-V film can be tuned by adjusting the III-V composition of the interface and the interfaces geometry.[131, 107, 82, 83] They are also of interest because ErAs and ErSb may make ohmic contacts to InAs and GaSb respectively.[32] Note that ErAs contacts must be capped on the top and sides to prevent oxidation and eventual degradation of the contact.[132] In addition to ErAs and ErSb, films of LuAs have shown to be interesting as a possible contact. LuAs has a similar conductivity to ErAs but has a much higher optical transmission in the near IR, making LuAs a possible choice as an IR transparent epitaxial contact.[35]

1.8 Thesis Outline

In this chapter I have summarized the majority of the recent work that has been done on the LN-V materials while indicating how the work I have done here at the University of Delaware fits into the field at large. In this dissertation I will expand upon this work. In Chapter 2 I will discuss the basics of molecular beam epitaxy as well as the characterization techniques I have used including: x-ray diffraction, Rutherford backscattering spectroscopy, Hall effect measurements, spectrophotometry, and transient absorption spectroscopy measurements. In Chapter 3 I will discuss how many of these techniques were used to determine that TbAs nanoparticles have a band gap and that TbAs forms a type I, straddled, heterojunction with GaAs and a type II, staggered, heterojunction with $\text{In}_{0.53}\text{Ga}_{0.47}\text{As}$. Chapter 4 will discuss how TbAs films were grown and characterized, leading to the discovery that TbAs is a degenerately doped semiconductor. Chapter 5 will discuss the growth and characterization of ErAs:GaBiAs as possible material for photoconductive switches. Chapter 5 will also highlight the importance of using ideal growth conditions. Finally, Chapter 6 will summarize this work and discuss possible future directions.

Chapter 2

GROWTH AND CHARACTERIZATION TECHNIQUES

The films discussed in this dissertation were grown via molecular beam epitaxy (MBE) and characterized with a variety of techniques including X-ray diffraction (XRD) $\omega - 2\theta$ scans, XRD reciprocal space mapping (RSM), Rutherford backscattering spectroscopy, Hall effect, spectrophotometry, and transient absorption spectroscopy. In this chapter, detailed descriptions of the MBE system, MBE growth techniques, and many of the characterization techniques used are presented. Specifically, Section 2.1 discusses the MBE system and growth techniques, Section 2.2 discusses XRD $\omega - 2\theta$ and RSM scans, Section 2.3 explains Rutherford backscattering spectroscopy measurements, Section 2.4 explains resistivity and Hall effect measurements, Section 2.5 discusses spectrophotometry measurements, and Section 2.6 explains the transient absorption spectroscopy techniques including optical pump terahertz probe and optical pump optical probe measurements.

2.1 Molecular Beam Epitaxy

The films studied in this dissertation were grown via molecular beam epitaxy (MBE); a schematic of a MBE growth chamber is shown in Fig. 2.1. Molecular beam epitaxy is a growth technique that allows for precise control over film composition and layer thickness with low impurity incorporation. Molecular beam epitaxy is commonly used for the thin film growth of III-V materials.[133, 134, 135, 136, 137] In this section I will highlight the basics of MBE and some of the specific techniques utilized by the OSEMI NextGEN solid source MBE here at the University of Delaware. Note that MBE is also commonly used for thin film growth of other materials including group

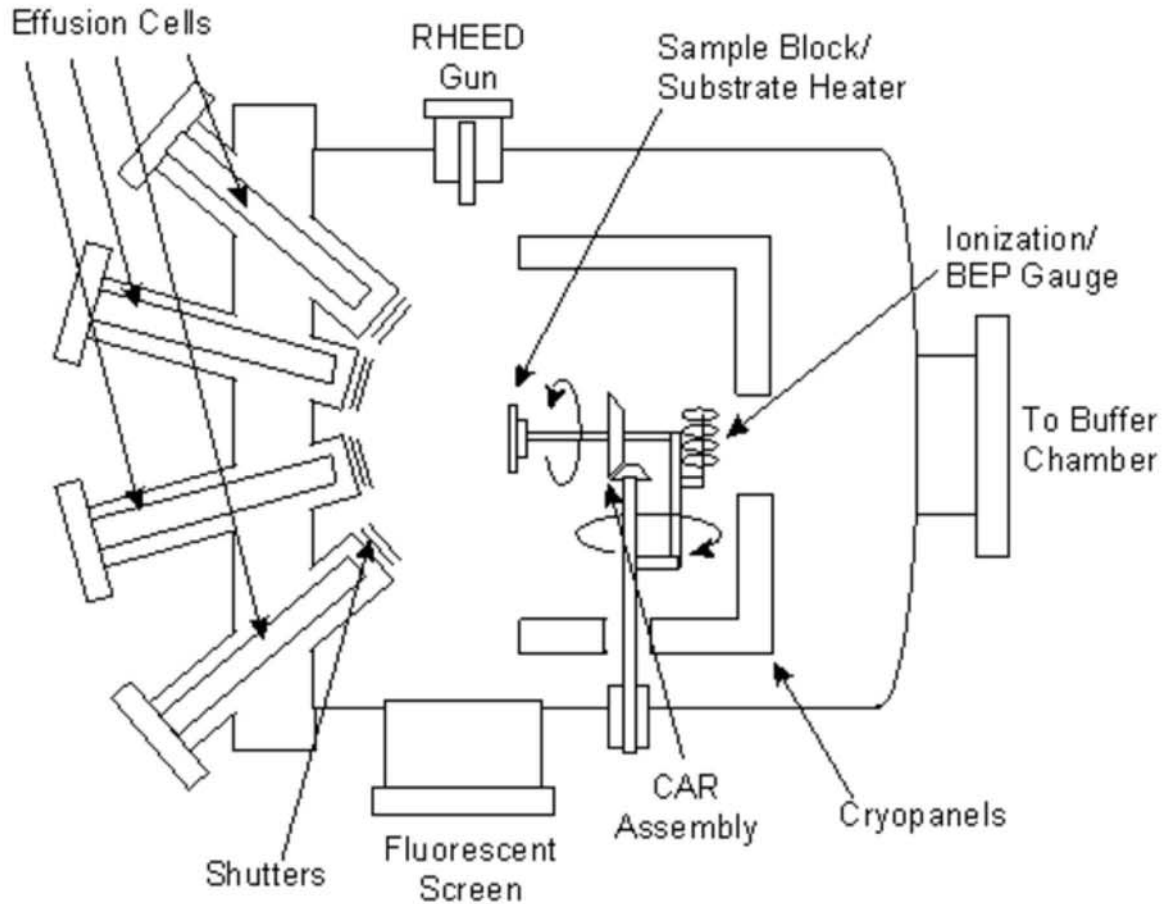


Figure 2.1: Schematic of a general molecular beam epitaxy system. Schematic from <http://lase.ece.utexas.edu/mbe.php>, reprinted with permission from Professor Seth Bank.

IV, II-VI, oxides, and topological insulators; details on those growths can be found elsewhere.[133, 136, 137, 138]

Molecular beam epitaxy is essentially a well-controlled thermal deposition method performed under ultra-high vacuum. Typically, for the growth of III-V materials, elemental sources are thermally heated to emit a beam of molecules towards a heated substrate where the molecules are deposited to form a film. The ability of each elemental source to be individually heated and shuttered provides the operator a large amount of control over the film's structure. The solid or liquid sources are typically resistively heated in crucibles within an effusion cell. Controlling the temperature of

the effusion cell provides control of the vapor pressure for each elemental source, and ultimately the flux of atoms evaporating toward the substrate. Due to the ultra-high vacuum nature of the MBE, the mean free path of the evaporated elements is larger than the distance between the effusion cells and the substrate. This results in a beam of molecules traveling to the substrate's surface and the constituents of the film only interact where the beams intersect, which is at the substrate. The individual shutter control over each effusion cell provides the ability to control which elements are interacting at the film's surface at any given time.

The ability to accurately measure and control the flux of atoms allows for excellent control over the films composition and growth rate. Instead of flux measurements, the pressure of each elemental beam is measured with an ionization gauge; known as the beam equivalent pressure (BEP) and is proportional to the molecular beam's flux. The flux, or BEP, does not relate to the same incorporation rate for all elements. Instead the incorporation rate is a function of the flux and a sticking coefficient that is specific for each element. Thus, the relationship between the BEP, growth rate and composition must be calibrated for each element. The growth rate of a film can be calibrated to the BEP of each species with *in situ* reflection high energy electron diffraction oscillations or *ex situ* characterization techniques that measure the film thickness such as X-ray diffraction, scanning electron microscopy, or transmission electron microscopy. Similarly the composition of each film can be calibrated to the BEP ratio of the films constituents with *ex situ* measurements such as X-ray diffraction and Rutherford backscattering spectroscopy. Due to the low fluxes of dopant elements, typically Si and Be in III-V materials, their incorporation rate is calibrated with the effusion cells temperature instead of a BEP. The BEP of an element scales exponentially with effusion cell temperature, and thus the dopant incorporation scales exponentially with temperature. Since we are primarily concerned with the electrically active dopant concentration, not necessarily the actual Si or Be concentration, the dopant incorporation rate is calibrated with Hall effect measurements to determine carrier concentration. Hall effect measurements are discussed below in Section 2.4. Note that while Si is an

n-type dopant for several of the III-V materials including GaAs and $\text{In}_{0.53}\text{Ga}_{0.47}\text{As}$, the incorporation of large amounts of Si can result on Si sitting on group V sites. This results in a decrease in electron concentration with increasing Si concentration at high Si concentrations.

Similar to the dopant sources, the BEP of Er used for nanoparticle growth is typically too small to measure. As discussed in Chapter 1, the rate of Er incorporation is calibrated with the Er effusion cell's temperature and *ex situ* Rutherford backscattering spectroscopy. Note that it is possible to measure the BEP of Er for high ErAs growth rates, such as those used for film growths. Similar to Er, the Tb incorporation rate is also calibrated by the Tb effusion cell's temperature with *ex situ* Rutherford backscattering spectroscopy. Due to the low vapor of Tb at the ion gauges temperature, Tb can stick to the ion gauges filament preventing the measurement of a BEP. Since it takes a significant amount of time for Tb to come off the ion gauge filaments, attempting to measure the BEP of Tb can cause errors in subsequent BEP measurements.

In addition to providing the beam like nature, the ultra-high vacuum in MBE is important for the minimization of impurities as well as *in situ* characterization techniques such as reflection high energy electron diffraction (RHEED). The ultra-high vacuum results in a very low concentration of unwanted species in the growth chamber. This results in a negligible amount of unwanted elements or contaminants impinging on the substrate surface and ultimately results in high purity film growth. The ultra-high vacuum also provides the opportunity to characterize the film growth *in situ* with RHEED. Briefly, an electron gun generates a beam of high energy electrons. This beam of high energy electrons strikes the surface of the substrate at a very low angle, and the electrons are diffracted off of the surface forming a diffraction pattern on the RHEED screen. The diffraction pattern provides key information about the surface and the growth. Specifically, the diffraction pattern is dependent upon how the surface has reconstructed to minimize the energy of the dangling bonds on the surface. This can be used to determine when the oxide on the surface of a substrate has been

desorbed, for GaAs and InP this is shown as a hazy RHEED pattern transitioning into a clear 2×4 pattern. The diffraction pattern is also dependent on the crystal structures. For example, GaAs typically displays a 2×4 RHEED reconstruction while the rock salt RE-V materials display a 2×2 pattern. The RHEED pattern also provides information about the morphology of the growth surface. For example, a streaky RHEED pattern is indicative that the films surface is smooth and growth is occurring layer by layer. A spotty RHEED pattern indicates that the surface is rough and three dimensional. The presence of chevrons indicates that the surface has facets and suggests the growth of nanoparticles on the surface.

As mentioned above, the substrate is heated during MBE growth. The temperature of the substrate can significantly alter the growth of the film. For example, the incorporation of Bi is increased at lower temperatures, and as discussed in Chapter 1 the growth temperature can significantly alter the shape and size of nanoparticles. The substrate temperature can be measured with a thermocouple, pyrometry, and band edge thermometry. Substrate temperatures measured with thermocouples are system specific because the thermocouple is typically not in direct contact with the substrate and is actually some distance away. This distance can change from system to system and thus the thermocouple reading can change between systems. Pyrometry and band edge thermometry temperatures are generally a more precise measurement. Pyrometry measures the intensity of a specific wavelength of light emitted from the substrate, which is dependent upon the emissivity and temperature of the substrate. Note the efficiency of a conventional pyrometer drops off below temperatures of $\sim 400^\circ\text{C}$. Band edge thermometry, the method used to measure the substrate temperatures in this dissertation, works by measuring the transmission of a broad band white light through the substrate. The band edge of the substrate is determined by detecting the energy, or wavelength, at which the substrate starts to absorb the light, this is essentially the band gap of the substrate. Since the band gap of the substrate decreases with increasing temperature, as determined by the Varshni parameters, the measured band edge energy can be converted into a temperature.

2.2 X-ray Diffraction

High resolution X-ray diffraction (HR-XRD) is an important tool for characterizing epitaxial films. The composition and thickness of films can be determined with ω - 2θ scans. The strain and relaxation of a film can be determined with reciprocal space mapping (RSM). Both the HR-XRD and RSM scans performed for this dissertation were performed with a Panalytical X'Pert MRD diffractometer at the University of Delaware. A 1.8 kW sealed ceramic copper X-ray tube produces an X-ray beam that is focused and passed through a four-bounce Ge (220) monochromator, providing a collimated monochromatic $\text{CuK}_{\alpha 1}$ X-ray beam. This collimated X-ray beam then diffracts off the sample. The diffracted beam is collected through a three bounce Ge(220) analyzer, which determines the angle of acceptance for the detector, and strikes the detector.

2.2.1 ω - 2θ scans

High Resolution X-ray diffraction ω - 2θ coupled scans can be used to determine both the composition and thickness of a film. During the measurement, the sample is rotated about ω while the detector is rotated about 2θ , where ω is the angle between the X-ray source and the sample and 2θ is the angle between the X-ray source and the detector, shown in Fig. 2.2. For the symmetric (004) scans used in this dissertation, $2\theta=2\times\omega$ and thus the detector moves at twice the speed as the sample. For ω - 2θ coupled scans, the intensity of the diffracted X-rays are plotted versus the 2θ angle, and this is subsequently used to determine either film composition or layer thicknesses.

The composition of a film can be determined by the 2θ position of the films peak. With the use of Bragg's law, Equation 2.1, the lattice plane spacing can be obtained and with Equation 2.2 the lattice constant can be calculated. Vegard's law, Equation 2.3 can then be used to estimate the composition of the film. In Equations 2.1, 2.2, and 2.3 d is the plane spacing, θ is half the angle between the X-ray source and the detector, n is an integral number, λ is the X-ray wavelength (1.54056 Å for $\text{CuK}_{\alpha 1}$), a is the lattice constant, and (hkl) are the Miller indices. While the method presented here provides

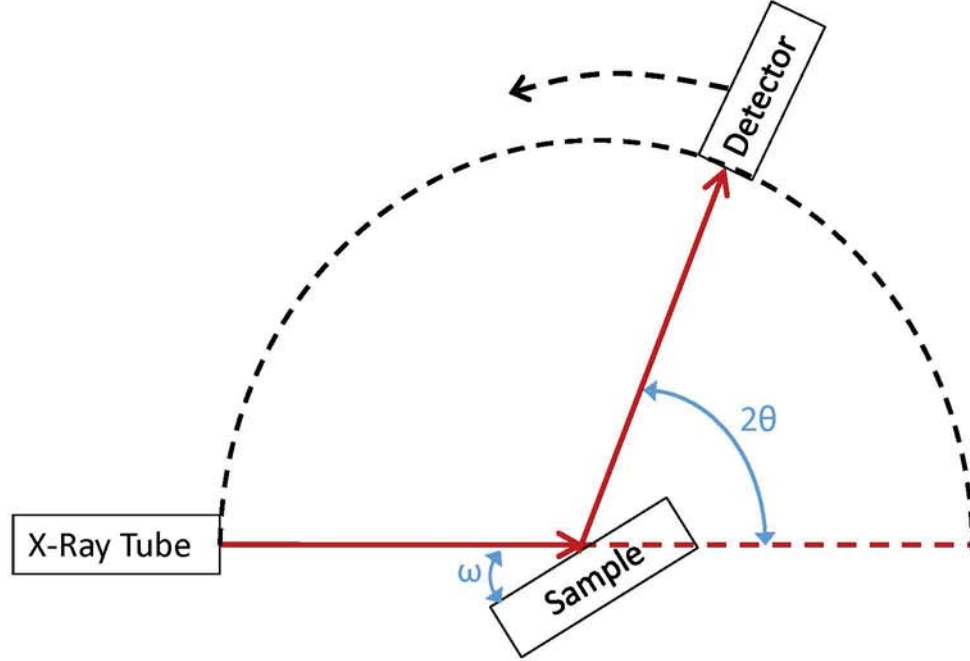


Figure 2.2: Schematic of the X-ray diffraction geometry.

a quick quantitative composition, it does not take into account Poisson's ratio which can lead to errors in the composition of strained films. Alternatively, the composition can be determined by modeling the XRD scan with software that takes into account Poisson's ratio, such as X'Pert Epitaxy.

$$2d\sin\theta = n\lambda \quad (2.1)$$

$$a = \sqrt{h^2 + k^2 + l^2}d \quad (2.2)$$

$$a_{A(1-x)Bx} = (1-x)a_A + xa_B \quad (2.3)$$

In addition to diffracting off of planes of atoms, X-rays can diffract off of interfaces between two materials. When those interfaces are smooth, the X-rays can coherently scatter, forming thickness fringes; the spacing of which is related to the film's thickness. In a superlattice structure, it is possible for each period to have

thickness fringes. Since each period of a superlattice should be identical, the thickness fringes from each period should coherently scatter causing an increase in the diffracted intensity at specific angles known as superlattice peaks. Similar to the thickness fringes, the thickness of each superlattice period is related to the separation between the superlattice peaks. The thickness of a film or superlattice period can be calculated with Equation 2.4 where t is the thickness, λ is the X-ray wavelength, n_1 and n_2 are integer number of each peak (for neighboring peaks $n_1 - n_2$ is 1), and θ_1 and θ_2 are half the angle between the X-ray source and the detector that correspond to the thickness fringe or superlattice peak. Again, modeling the XRD data with software such as X'Pert Epitaxy can also provide highly accurate thicknesses.

$$t = \frac{\lambda(n_1 - n_2)}{2 \times (\sin(\theta_1) - \sin(\theta_2))} \quad (2.4)$$

2.2.2 Reciprocal Space Mapping

Reciprocal space mapping can be used to determine if a film is perfectly lattice matched, strained, or relaxed relative to a substrate. This is important for (opto)electronic applications as strain can alter the band gap and relaxation can introduce defects that change the properties. Figure 2.3 is a 2-D schematic depicting a lattice matched film, strained film, and relaxed film on top of a substrate. In Fig. 2.3(a) it is clear that the film has the same in and out of plane lattice constant. In Fig. 2.3(b) the film is strained, shown by the in plane lattice constant of the film being the same as the substrate while the out of plane lattice constant is extended beyond the normal lattice constant of the film, as determined by Poisson's ratio. In Fig. 2.3(c) the film has relaxed, resulting in dislocations at the film/substrate interface. Each of these are depicted in various ways in a reciprocal space map (RSM). A RSM is a contour plot where the x-axis is typically the in plane reciprocal lattice constant, the y-axis is typically the out of plane reciprocal lattice constant, and color indicating diffracted X-ray intensity. A lattice matched film will have a peak directly on top of the substrate's peak, a strained film's peak will be above (tensile strained) or below (compressively

strained) the substrate's peak, and a relaxed film's peak will be along a line connecting the substrate's peak to the origin. Note that in a symmetric scan, such as an (004) scan, the line connecting the substrate's peak to the origin will be vertical, and thus it is not possible to tell from symmetric RSM alone if the film is strained or relaxed. Alternatively, an asymmetric scan, such as a (224) scan, can be used where the relaxation line and strain line will not overlap.

The RSMs discussed in this dissertation were obtained with the Panalytical X'Pert XRD diffractometer at the University of Delaware discussed above. The RSM scans on this XRD system are obtained by performing a series of coupled ω - 2θ scans over a range of different ω values. The in plane, Q_x , and out of plane, Q_y , reciprocal lattice constants in μm^{-1} can be calculated using Equations 2.5 and 2.6, respectively, where λ is the X-ray wavelength in microns, ω is the angle between the X-ray source and the substrate, 2θ is the angle between the substrate and the detector.

$$Q_x = \frac{2\pi}{\lambda}(\cos(\omega) - \cos(2\theta - \omega)) \quad (2.5)$$

$$Q_y = \frac{2\pi}{\lambda}(\sin(2\theta - \omega) + \sin(\omega)) \quad (2.6)$$

From the in plane and out of plane lattice constant, the amount the film has relaxed can be calculated. First, the relative lattice mismatch in plane (f_{\parallel}) and out of plane (f_{\perp}) needs to be calculated with Equations 2.7 and 2.8. Then the total lattice mismatch (f) can be calculated with Equation 2.9, where ν is Poisson's ratio. Finally the relaxation percentage (R) can be calculated with Equation 2.10

$$f_{\parallel} = \frac{Q_{y_{sub}} - Q_{y_{film}}}{Q_{y_{film}}} \quad (2.7)$$

$$f_{\perp} = \frac{Q_{x_{sub}} - Q_{x_{film}}}{Q_{x_{film}}} \quad (2.8)$$

$$f = f_{\perp} - f_{\parallel} \frac{1 - \nu}{1 + \nu} + f_{\parallel} \quad (2.9)$$

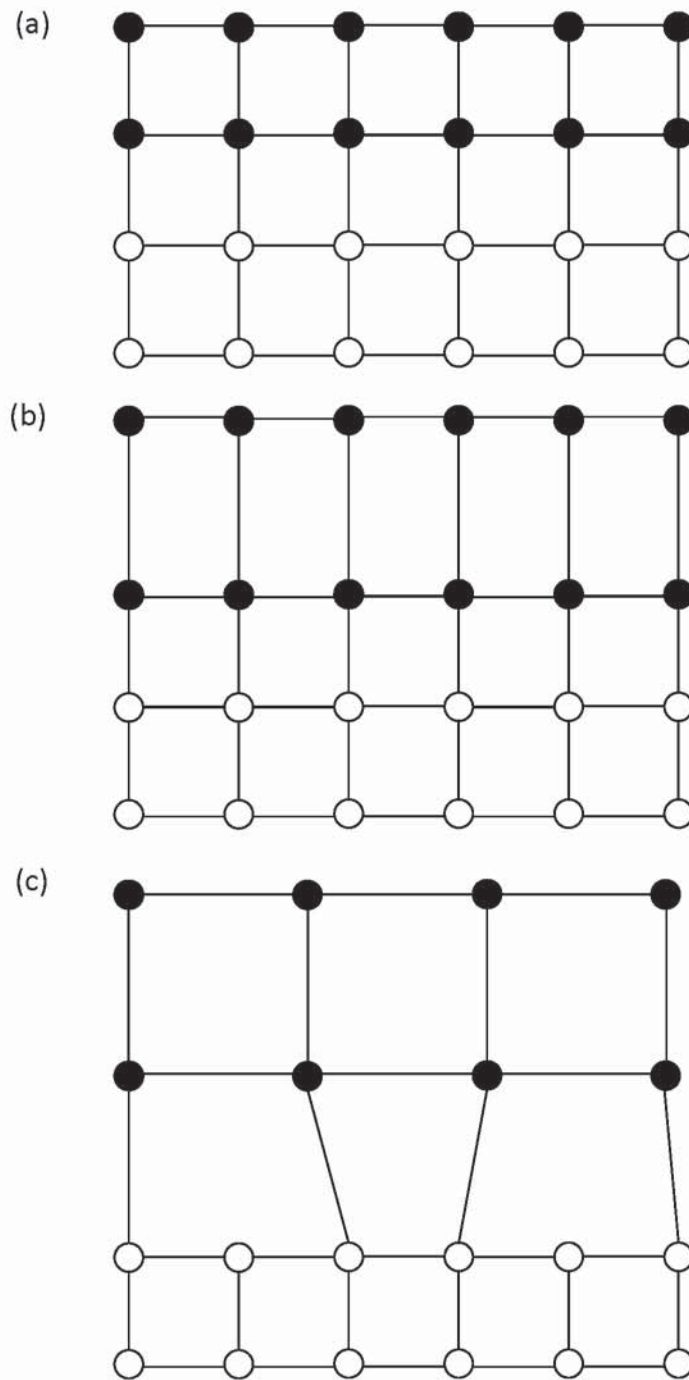


Figure 2.3: Schematic showing (a) a lattice matched film (black circles) on a substrate (open circles), (b) a compressively strained film on a substrate, and (c) a relaxed film on a substrate.

$$R = \frac{f_{\parallel}}{f} \quad (2.10)$$

2.3 Rutherford Backscattering Spectroscopy

As mentioned in Chapter 1, the incorporation of LN into III-V materials results in a superdilation of the matrix that makes determining compositions with XRD difficult. Thus, the LN compositions discussed within this dissertation were calibrated with Rutherford backscattering spectroscopy (RBS). Briefly, a beam of high energy particles, typically He^{2+} , bombards the sample. A portion of those particles are backscattered by the nucleus of the atoms in the sample where they are collected by an energy sensitive detector. The energy of the backscattered particle beam is dependent upon the mass of the element it scatters off of and the depth from where the particles scatter. The energy is reported in terms of a channel number where high channel numbers correspond to particles being backscattered off of heavier atoms and atoms closer to the surface. For composition measurements, the high energy particle beam strikes the sample at a random angle, providing a high probability for the particle beam to backscatter off of atoms in the sample. A channeling alignment can be used where the particle beam is aligned with the rows of atoms. In the channeling alignment the particle beam has the same probability of being backscattered off of the first few monolayers of the sample as the randomly aligned measurement. However, once the particle beam is past the surface the beam is primarily scattered by interstitial atoms.

Modeling the counts of backscattered particles versus the channel number allows the determination of the films composition and thickness. An example of this is shown in Fig. 2.4 for ErAs nanoparticles in GaAs. In Fig. 2.4 the black line is the randomly oriented spectrum, the red line is the simulated spectrum made from the sum of the Ga, shown as the blue line, As, shown as the pink line, and Er, shown as the green line. The RBS measurements discussed in this dissertation were measured at either Rutgers University or the University of Minnesota. Samples measured at Rutgers University used 4He atoms with an energy of 2000 keV, a 0.0 degree incident angle, 17 degree

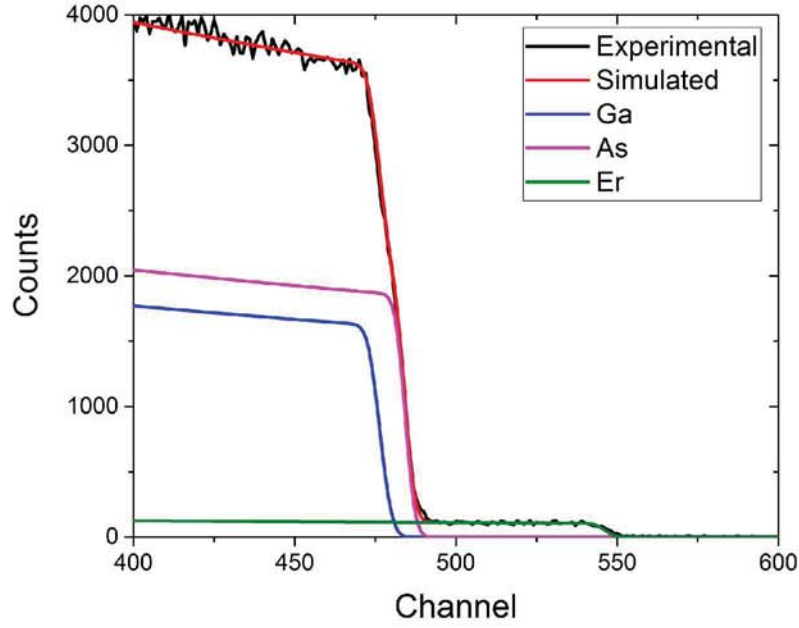


Figure 2.4: A randomly oriented and simulated RBS spectrum of ErAs:GaAs with 1.4% ErAs.

exit angle, 163 degree scattering angle, a collected charge of 10 or 20 μC , energy per channel of ~ 1.28 keV/ch, channel offset of ~ 41 keV, and a detector resolution of 13 keV. Samples measured at the University of Minnesota used 4HE atoms with an energy of 2000 keV, exit angle of 15 degrees, scattering angle of 165 degree, calibration offset of ~ 70 keV, energy per channel of ~ 3.205 keV/ch, detector resolution of 18.5 keV, and a collected charge of 10.4 μC . Modeling was done using the program SIMNRA.

2.4 Hall Effect and Resistivity Measurements

Throughout this dissertation, films are characterized via resistivity and Hall effect measurements, providing the films resistivity, carrier concentration, carrier type, and mobility. These measurements were performed with a custom built Hall effect system here at the University of Delaware capable of room temperature measurements and wide temperature, ~ 20 K to ~ 600 K, measurements. The measurements discussed in this dissertation were performed using the van der Pauw geometry, see Fig. 2.5

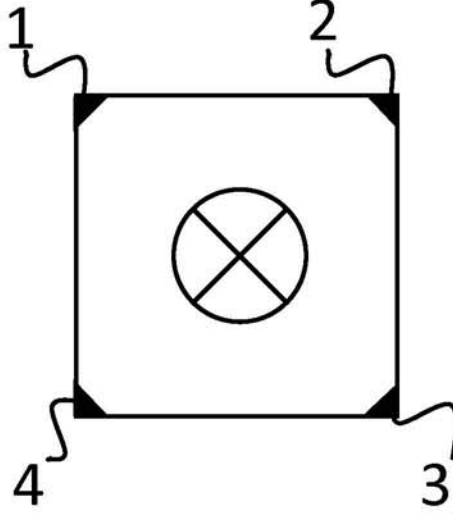


Figure 2.5: A schematic showing the van der Pauw geometry used for resistivity and Hall effect measurements. The black triangles represent the contacts, the squiggly lines represent the probes, and the circle with the X represents the direction of the magnetic field.

Resistivity measurements are performed by sourcing a current from probe 1 in Fig. 2.5 to probe 2 while measuring a voltage across probe 3 to probe 4. The slope of the current versus voltage provides the characteristic resistance R_a . The current is then sourced from probe 2 to probe 3 while the voltage is measured across probe 1 to probe 4. The slope of this current versus voltage gives the characteristic resistance R_b . The sheet resistance is then calculated numerically by iteration as follows. First the initial Z_i is calculated with Equation 2.11. The i iteration of Y_i is then calculated with Equation 2.12. Next the i iteration of Z_i is calculated with Equation 2.13. The calculation of Y_i and Z_i is repeated until $\frac{Z_i - Z_{i-1}}{Z_i}$ is less than the desired error. At that point the sheet resistance (ρ_s) is given by Equation 2.14 and the resistivity (ρ) is given by Equation 2.15, where t is the film thickness. This calculation assumes that the sample is square and nearly isotropic, if other geometries are used a shape factor must be implemented. Note, it is important that the film being measured is significantly more conductive than the substrate. If the substrate is conductive, the measurement

will be some average of the film and the substrate and it is very difficult to determine the exact effect the substrate has.[139]

$$Z_0 = \frac{2\ln(2)}{\pi(R_A + R_B)} \quad (2.11)$$

$$Y_i = \frac{1}{\exp(\pi Z_{i-1} R_A)} + \frac{1}{\exp(\pi Z_{i-1} R_B)} \quad (2.12)$$

$$Z_i = Z_{i-1} - \frac{\frac{1-Y_i}{\pi}}{\frac{R_A}{\exp(\pi Z_{i-1} R_A)} + \frac{R_B}{\exp(\pi Z_{i-1} R_B)}} \quad (2.13)$$

$$\rho_s = \frac{1}{Z_i} \quad (2.14)$$

$$\rho = \rho_s t \quad (2.15)$$

Once the resistivity measurements are complete, Hall effect measurements can be done to determine carrier type, carrier concentration, and mobility. The Hall effect measurements are performed by sourcing a current from probe 1 to probe 3 and measuring a voltage from probe 2 to probe 4, probe locations are denoted in Fig. 2.5, while applying a magnetic field perpendicular to the film. During the measurement the strength and direction of the magnetic field is swept, from a strong magnetic field going into the page, to a strong magnetic field coming out of the page, as shown in Fig. 2.5. The slope of the plot of the measured voltage versus the current times magnetic field strength is the Hall coefficient, H_A . Then, the current is sourced from probe 2 to 4 and voltage measured from probe 1 to probe 3. Again the magnetic field is applied perpendicular to the film and swept from a strong magnetic field going into the page to a strong magnetic field coming out of the page, as shown in Fig. 2.5. The slope of the measured voltage versus the current times magnetic field strength is the Hall coefficient, H_B . If the Hall coefficients are positive, electrons are the majority carrier. A negative Hall coefficient means holes are the majority carriers. The sheet

concentration (n_s), in cm^{-2} , is given by Equation 2.16 where q is the elemental charge, bulk concentration given by Equation 2.17 where t is the thickness, and mobility (μ) is given by Equation 2.18.

$$n_s = \frac{\frac{-1}{q * H_A * 100,000,000} + \frac{-1}{q * H_A * 100,000,000}}{2} \quad (2.16)$$

$$n = \frac{n_s}{t} \quad (2.17)$$

$$\mu = \frac{1}{q * n_s * \rho} \quad (2.18)$$

On highly resistive samples, to prevent the source meter from hitting the compliance voltage, low source currents for both the resistivity and Hall effect measurements are required. This results in small changes in the measured voltage with current or magnetic field and the measurement is susceptible to a low signal-to-noise ratio. Note, both the signal-to-noise ratio in the sourced current and voltage measured is decreased. To help overcome the low signal-to-noise ratio, the sample can be measured multiple times. The voltage for each sourced current can be averaged and then the electrical properties can be calculated as discussed above.

For some samples with very low carrier concentrations the Hall effect measurement can be too noisy to obtain a good measurement and averaging multiple runs has minimal effect. This occurs because there are not enough carriers in the film for the changing applied magnetic field to cause a significant change in the measured voltage. When this happens, the Hall effect measurement can be done by keeping the magnetic field constant and sweeping the sourced current.

In addition to performing resistivity and Hall effect measurements at room temperature, they can also be performed as a function of temperature. The system at the University of Delaware can measure over temperatures ranging from ~ 20 K to ~ 600 K. Indium contacts will start to melt ~ 430 K, thus higher temperatures require patterned contacts. Measuring carrier concentration, resistivity, and mobility as a function of

temperature provides a lot of information about semiconductors including determining activation energies and if a semiconductor is degenerately doped, as shown in Chapters 3 and 4.

2.5 Spectrophotometry

The spectrophotometry measurements discussed within this dissertation were performed with a Perkin-Elmer Lambda-750 UV-Visible-IR Spectrophotometer fitted with an integrating sphere located in the Institute for Energy Conversion at the University of Delaware. The samples discussed here are all films and both transmission and reflection data we obtained for them. Note that the Perkin-Elmer Lambda-750 UV-Visible-IR Spectrophotometer can measure out to 3300 nm, but the detector starts to cut out around 2500 nm.

In spectrophotometry a white light source generates light that passes through a monochromator. The light then strikes the sample, for transmission measurements the light is transmitted through the sample and collected by the detector. In reflection measurements the light is reflected off of the surface and collected by the detector. During the measurement the monochromator steps through the wavelength range desired, allowing the detector to measure the transmitted or reflected intensity of each wavelength. Prior to measuring a sample, a background scan is taken and all subsequent measurements are normalized to the absorption of air.

Once the transmission and reflection data are collected, the absorption (α) coefficient can be calculated by equation 2.19 where t is the thickness of the film, T is the transmission through the sample and R is the reflection from the sample. The band gap of the film can be extracted from a Tauc plot, plotting $(\alpha h\nu)^{1/r}$ versus energy, where r is 0.5 for a direct gap semiconductor and 2 for an indirect gap semiconductors. Fitting the linear region with a straight line of the Tauc plot and extrapolating to the x-intercept provides the band gap of the film.

$$\alpha = \left(\frac{-1}{t}\right) \ln\left(\frac{T}{1-R}\right) \quad (2.19)$$

2.6 Transient Absorption Spectroscopy

Transient absorption pump-probe spectroscopy measurements can provide information on the number of relaxation pathways, the fraction of carriers participating in each relaxation pathway, and the time it takes for carriers to relax through a particular pathway. Transient absorption measurements are performed by first exciting electrons into the conduction band and holes into the valence band with a pump laser. At a time delay τ later the probe laser is directed to the sample. A detector is used to measure the intensity of the laser's reflection or transmission and the absorption of the probe beam by the film is calculated. A difference absorption spectrum, ΔA , is then calculated by subtracting the probe beam's absorption intensity of the unexcited sample from the probe beam's absorption intensity at time τ . Note, the probe beam's absorption intensity of the unexcited sample is actually the absorption intensity of the probe before the pump laser strikes the sample, $\tau_0 < 0$, and thus can be denoted as $A(\tau_0)$. The probe beam's absorption after the pump laser strikes the sample is denoted as $A(\tau_1)$ where $\tau_1 > 0$. Thus the difference absorption spectrum can be written as $\Delta A(\tau_1) = A(\tau_1) - A(\tau_0)$. By varying the time delay between the pump laser and the probe laser, τ_1 , the ΔA as a function time can be recorded. Information on the number of relaxation pathways, the fraction of carriers participating in each relaxation pathway, and the time it takes for carriers to relax through a particular pathway can then be obtained by modeling how ΔA changes with time.

The optical pump terahertz probe transient absorption spectroscopy measurements used in Chapter 3 to characterize the TbAs nanoparticles were performed at Los Alamos National Laboratory. A regenerative amplifier laser was used to output a 800 nm laser that is split into the pump beam and the probe beam. The pump beam, kept at 800 nm, passes through a delay stage and a chopper before striking the sample, exciting electron hole pairs. The delay stage allows the path length of the pump beam to be tuned relative to the path length of the probe beam which changes the time between when the pump and probe beams strike the sample. The delay stage at Los Alamos National Laboratory is capable of producing delay times of up to 400 ps. The

pump beam passes through a chopper so that a lock-in amplifier can be utilized to improve the signal-to-noise ratio. The portion of the 800 nm laser that is split to generate the probe beam passes through a ZnTe crystal to generate terahertz radiation, resulting in a broad band 0.1-2.75 THz probe beam. The THz probe beam is then directed toward the sample, which is mounted in a He cooled cryostat capable of being cooled to 4.5 K, and the reflection of the probe beam is measured with a bolometer. Again, the signal-to-noise ratio is improved with lock-in amplification. Note that due to the low energy of the THz probe, there should be minimal absorption of the THz probe by the sample before the pump laser strikes the sample. Additionally, since the THz probe can be absorbed by either electrons in the conduction band or holes in the valence band this technique cannot provide decay times for specific types of carriers, but rather provides the overall effect of both electrons and holes decaying.[140]

The optical pump optical probe transient absorption spectroscopy measurements used in Chapter 5 were performed here at the University of Delaware. In this measurement a regenerative amplifier produced a train of 35 fs pulses centered at 800 nm. A fraction of that was then used to produce a 850 nm pump beam and a fraction to produce the 1300 nm probe beam. The pump beam passes through a motorized delay stage, providing the possibility to change the delay time between the pump and the probe, and a chopper wheel, which allows for lock-in amplifying. The probe beam is directed straight toward the sample. After striking the sample the probe beam is split in two. A portion of the probe beams is chopped and then recombines with the rest of the probe beam before being detected. The probe beam is chopped to allow for the measurement to be done with dual reference lock-in amplifier. In the optical pump optical probe measurement discussed in Chapter 5 the optical probe's wavelength was chosen to be longer than the semiconductor's cutoff wavelength. However, it is still possible that the probe can be absorbed when the sample is not pumped by exciting carriers into the band tails or shallow defect states. If the pump laser fills the band tails and shallow defect states, or completely empties the states where carriers were being excited from, the probe beam's absorption can decrease after the pump laser

strikes the sample. This is observed as a negative ΔA and is called bleaching. As the carriers relax back to their un-pumped states, the ΔA trends back toward zero.[\[141\]](#)

Chapter 3

ELECTRONIC STRUCTURE AND BAND ALIGNMENT OF TERBIUM ARSENIDE NANOPARTICLES IN GaAs AND In_{0.53}Ga_{0.47}As

In Chapter 1 I discussed the range of unique properties lanthanide monopnictide (LN-V) nanoparticles epitaxially embedded within III-V semiconductors possess and subsequently the applications for which they are of interest. To take full advantage of the unique properties provided by LN-V nanoparticles and to be able to tune their properties for specific devices and applications, a fundamental understanding of their electronic structure is needed. Most of the previous work on LN-V nanoparticles has focused on ErAs nanoparticles and studying its properties. ErAs nanoparticles pin the Fermi level within the band gap of GaAs and above the conduction band edge in InGaAs.[142, 82, 23, 109, 116] Cross-sectional scanning tunneling spectroscopy shows that ErAs nanoparticles are semi-metallic,[20] despite predictions that quantum confinement would open a band gap.[52] Models of ErAs:GaAs superlattices show that interface states from the As atoms prevent the ErAs from transitioning from a semimetal into a semiconductor, even when the ErAs layer is reduced to one monolayer.[143]

TbAs was expected to have similar properties as ErAs, which lead TbAs nanoparticles to be of interest for a variety of device applications. However, the details of TbAs nanoparticles' electronic structure in III-V are presently unknown. In this chapter we explore the fundamental electronic properties of TbAs nanoparticles in III-V films. Section 3.1 discusses the growth parameters and the basic properties of the samples used for this study. In section 3.2 we study carrier dynamics of TbAs nanoparticles in GaAs, showing TbAs nanoparticles are saturable. TbAs nanoparticles being saturable and having a band gap is in direct contrast to ErAs nanoparticles.[26] Section 3.3 uses

fluence-dependent optical-pump THz-probe measurements to study the carrier dynamics of TbAs nanoparticles in $\text{In}_{0.53}\text{Ga}_{0.47}\text{As}$, again showing that TbAs nanoparticles are saturable and likely have a band gap. Section 3.4 uses spectrophotometry to determine the energy of optical transition within the TbAs:GaAs and TbAs: $\text{In}_{0.53}\text{Ga}_{0.47}\text{As}$ systems. Section 3.5 utilizes Hall effect measurements to determine the Fermi level in each system. With the knowledge gained from each of the previously mentioned sections, Section 3.6 proposes that TbAs nanoparticles form a type I heterojunction with GaAs and a type II heterojunction with $\text{In}_{0.53}\text{Ga}_{0.47}\text{As}$. [27] Finally, a summary is provided in Section 3.7. The contents of this chapter is adapted from a manuscript that the author is a co-author on and a second paper that the author wrote, both papers have previously been published. [26, 27] Also, note that Laura Vanderhoelf's doctoral thesis also extensively discusses the optical pump terahertz probe measurements of the TbAs:GaAs sample. [140]

3.1 Growth Conditions and Sample Properties

For this work two samples were studied, a sample consisting of TbAs co-deposited in GaAs and a sample consisting of TbAs co-deposited in $\text{In}_{0.53}\text{Ga}_{0.47}\text{As}$. Both were grown in an OSEMI NextGEN solid source MBE with effusion cells for Tb, In, and Ga, and a two zoned valved cracker source for As_2 . For both samples, the growth and thermal desorption of oxides were monitored using reflection high energy electron diffraction (RHEED) and substrate temperatures were measured by band edge thermometry.

One sample is a co-deposited TbAs:GaAs film grown on a semi-insulating (100) undoped GaAs substrate and a 50 nm thick GaAs buffer layer. Growth was done using a substrate temperature of 490°C, as measured by band edge thermometry. Tb, Ga, and As were co-deposited such that the solid solubility limit of Tb in GaAs was exceeded and TbAs nanoparticles precipitated throughout the material. The GaAs growth rate used was 1 $\mu\text{m}/\text{h}$, resulting in a measured thickness of 930 nm, with an As:Ga beam equivalent pressure (BEP) ratio of $\sim 26:1$. Rutherford backscattering

spectroscopy measurements reveal a TbAs concentration of 2.12%. Using the average nanoparticle size measured from samples grown under similar growth conditions,[36] the film has a nanoparticle density of $3.2 \times 10^{19} \text{ cm}^{-3}$. [26]

The second sample is a co-deposited TbAs:In_{0.53}Ga_{0.47}As film grown on a semi-insulating (100) Fe doped InP substrate with a 100 nm In_{0.53}Ga_{0.47}As buffer layer. Growth was done at a substrate temperature of 490°C, measured by band edge thermometry. Tb, In, Ga, and As were co-deposited such that the solid solubility limit of Tb in In_{0.53}Ga_{0.47}As was exceeded and TbAs nanoparticles precipitated throughout the material. Figure 3.1 is a schematic of TbAs nanoparticles dispersed throughout a III-V matrix. An In_{0.53}Ga_{0.47}As growth rate of $\sim 1.2 \text{ } \mu\text{m/h}$ was used corresponding to a measured thickness of 1.1 μm . In to Ga and As to group III BEP ratios of about 2.65:1 and 10:1, respectively, were used to obtain a nominally lattice matched film. Note, as discussed in Chapter 2 Section 2.1, the Tb flux cannot be measured and was instead calibrated via ex-situ measurements and the terbium effusion cell's temperature. Rutherford backscattering spectroscopy measurements show a TbAs concentration of 1.3%. Based upon the average nanoparticle size measured from samples of similar growths,[37] the calculated nanoparticle density is $2.54 \times 10^{19} \text{ cm}^{-3}$. [27]

3.2 Carrier Dynamics in GaAs

Optical pump terahertz (THz) probe was used to study the carrier dynamics of TbAs:GaAs. The details of the optical pump THz probe technique was extensively covered in Chapter 2 Section 2.6. Briefly, carriers are generated by an optical pulse and subsequently relax into the TbAs nanoparticles or back across the bulk band gap. The rate of the carrier relaxation is measured by the rate of decay in the absorption of the THz probe. Note that the THz probe is only absorbed when free carriers are in the conduction or valence bands. As a reminder, this technique cannot distinguish between electrons and holes and is a convolution of the two.

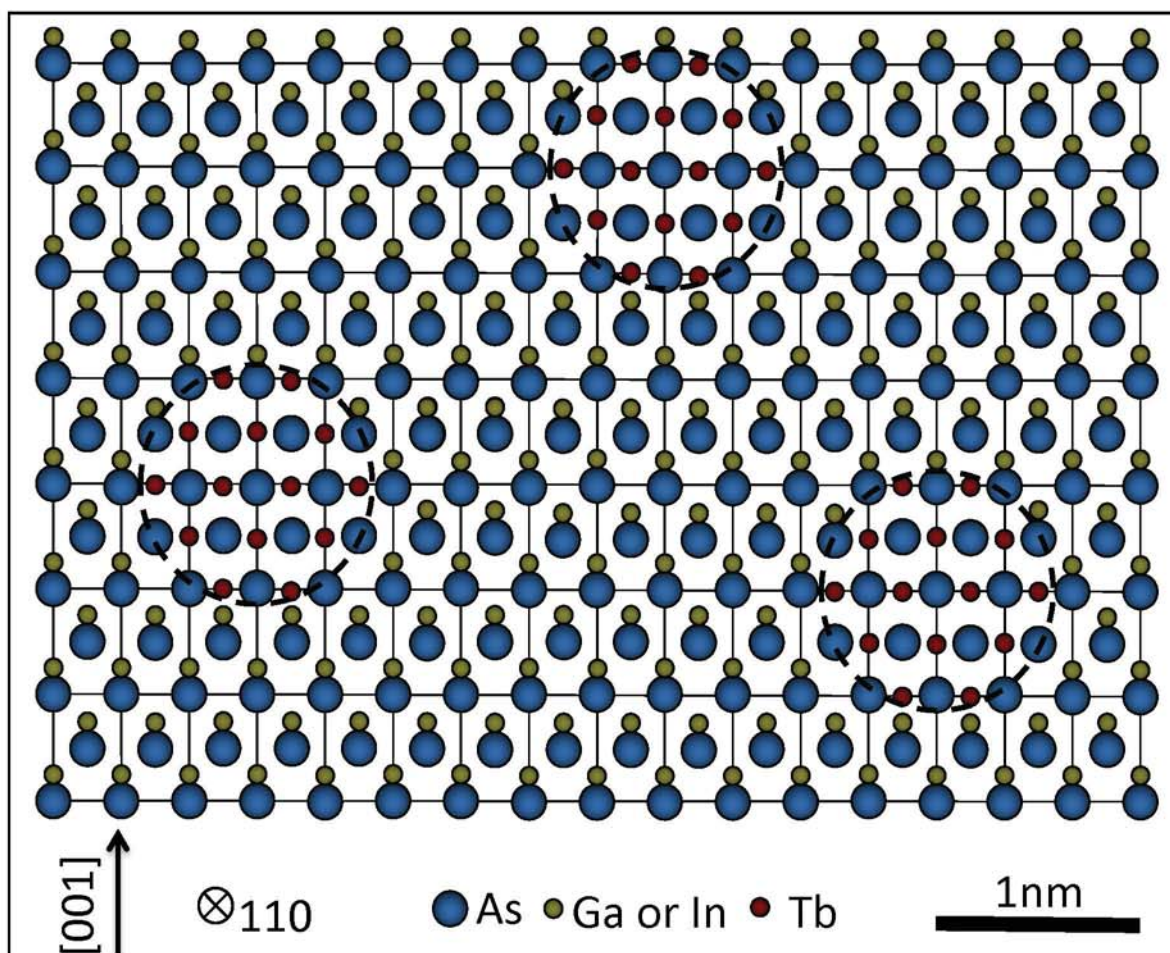


Figure 3.1: Schematic showing TbAs nanoparticles dispersed throughout a III-V matrix as a result of co-depositing Tb with the III-V materials. Reprinted figure with permission from [26]. Copyright 2014 by the American Physical Society.

3.2.1 Measurement and Data Analysis Details

For this sample, the optical pump was generated using a Ti:sapphire laser that produced 3.2 mJ, 35 fs pulses centered on 800 nm. Pump fluences ranging from 2 to 200 $\mu\text{J}/\text{cm}^2$ were used to excite the sample. A portion of the Ti:sapphire laser's output was also used to generate and detect the THz probe. The probe beam is a broad band THz pulse, generated from the Ti:sapphire laser and the electro-optic effect in ZnTe, spanning 0.1-2.75 THz. Transient absorption data was collected for delay times ranging from 0 ps to 400 ps in 0.3333 ps increments. The signal to noise ratio was improved by averaging ten complete measurements, providing the ability to determine the dynamics happening on the ps time scale. Once averaged, the data was fit to a multi-exponential decay using a linear least squares method with a Levenberg-Marquardt algorithm.[26] Note that these measurements were performed by Laura R. Vanderhoef and Abul K. Azad with the assistance of Dibakar R. Chowdhury, and Antoinette J. Taylor at Los Alamos National Laboratory.

Figure 3.2(a) shows an example of the THz absorption as a function of delay time with Fig. 3.2(b) zoomed in on the first 20 ps of the measurement, this data is the average of ten data runs measured at room temperature with a pump fluence of 6 $\mu\text{J}/\text{cm}^2$. From Fig. 3.2(a) it is clear that a single exponential decay (solid blue line) does not fit the entirety of the data. Figure 3.2(b) shows that a two exponential (dashed red line) decay does not fit the short times and a three exponential decay (dot-dashed green line) is required to fit the entirety of the measurement. Note that the use of a four exponential fit did not improve the adjusted R^2 values relative to the triple exponential fit and that the four and the triple exponential fits were indistinguishable. Thus, we fit the data with a triple exponential equation with each exponential representing a separate relaxation process. The triple exponential equation used to fit the data is shown in equation 3.1 where I is the probe absorption intensity, A , B , and C are pre-exponential factors that provide information about the fraction of carriers participating in each relaxation, and τ_0 , τ_1 , τ_2 represent the relaxation time for each process.

$$I = A \exp \frac{-t}{\tau_0} + B \exp \frac{-t}{\tau_1} + C \exp \frac{-t}{\tau_2} \quad (3.1)$$

The relaxation processes will be discussed more in section 3.2.2. Briefly, the fastest time, τ_0 , corresponds to carriers relaxing from the GaAs conduction band and valence band into the TbAs nanoparticle. The second fastest time, τ_1 , corresponds with carriers recombining or exiting the TbAs nanoparticle. The longest time, τ_2 , corresponds to carrier recombining across the bulk GaAs band gap.

3.2.2 Fluence Dependent Optical Pump Terahertz Probe Results

The time-dependent decay in THz absorption was measured for a pump fluences ranging from 2 to 200 $\mu\text{J}/\text{cm}^2$ to study the electronic structure. We consider both the relaxation times, τ_0 , τ_1 , and τ_2 , as well as the fraction of carriers participating in each relaxation pathway, $A/(A+B+C)$, $B/(A+B+C)$, and $C/(A+B+C)$, as a function of pump fluence, shown in Fig. 3.3. Note that the relaxation times and fraction of carriers participating in each relaxation pathway was obtained from equation 3.1.

Figure 3.3(a) shows that the shortest time constant, τ_0 , has an average relaxation time of 5.4 ps and does not significantly change with pump fluence. This short time constant corresponds to the time required for carriers to relax into the TbAs nanoparticles. While the time it takes for carriers to relax into the TbAs nanoparticles does not depend on pump fluence the fraction of carriers that relax into the nanoparticle does. Figure 3.3(b) shows that the fraction of carriers relaxing into the TbAs nanoparticles, $A/(A+B+C)$, decreases with increasing pump fluence. The fraction of carriers entering the TbAs nanoparticle nearly drops to zero at pump fluences of 20 $\mu\text{J}/\text{cm}^2$. To summarize, increasing the optical pump fluence, or increasing the number of generated electron hole pairs, does not change the rate of carriers relaxing into the TbAs nanoparticles but it does decrease the fraction of carriers that relax into the TbAs nanoparticle states. This suggests that the TbAs nanoparticle states are saturable and finite.

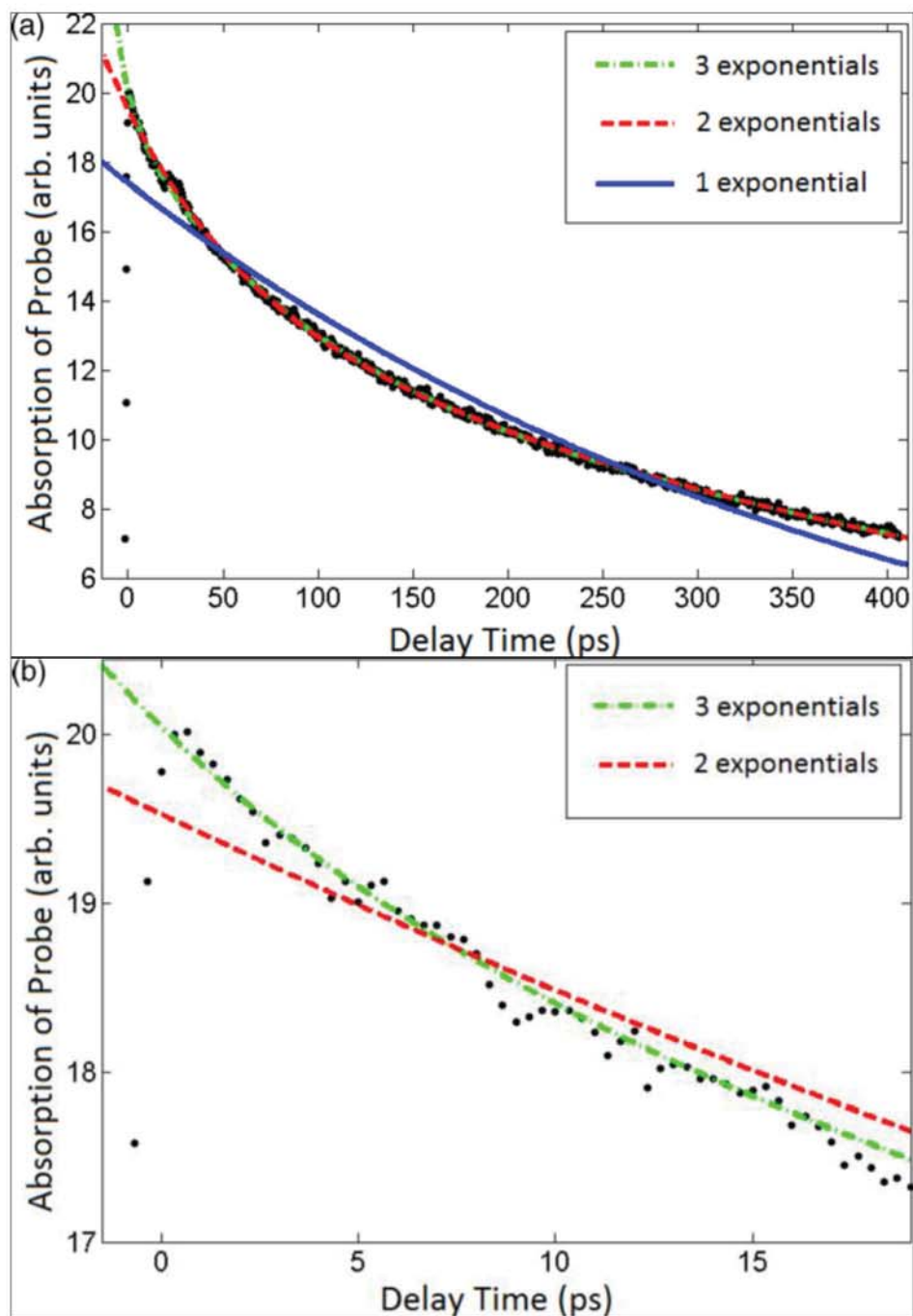


Figure 3.2: Long delay times (a) cannot be fit by a single exponential decay (solid black line) and short delay times (b) cannot be fit by a double exponential decay (red dashed lines). To fit the entirety of the data a triple exponential decay is required (green dot-dashed line).[26] Reprinted figure with permission from [26]. Copyright 2014 by the American Physical Society.

The second time constant, τ_1 , increases from 65 to 135 ps with increasing pump fluence, Fig. 3.3(c). We propose that this time constant corresponds with emptying the TbAs nanoparticle states. As the TbAs nanoparticle states empty, carriers at the GaAs band edge can now relax into the newly opened TbAs states, this relaxation time is ~ 5.6 ps as described by τ_1 above. As more carriers relax into the TbAs nanoparticle, the absorption of the THz probe decreases. As shown above, the number of states in the TbAs nanoparticle is finite, thus the carrier in the TbAs nanoparticle must recombine or empty in some manor before more carriers can relax into the TbAs from the GaAs. The time it takes for the carrier in the TbAs nanoparticle to recombine or empty in some manor must be longer than the time it takes for carriers to relax into the nanoparticle. If the time it takes for carriers to recombine in the TbAs nanoparticle, or empty out of the TbAs nanoparticle, was shorter than the time it took for carriers to enter the TbAs nanoparticle, we would not be able to see the emptying time. Thus, the second time constant must be the rate limiting step for the carrier relaxation process and corresponds with carrier recombination or emptying of carriers from the TbAs nanoparticle. Figure 3.3(d) shows that the fraction of carriers recombining within or leaving the TbAs nanoparticle decreases with increasing pump fluence. This is consistent with the TbAs nanoparticle states being saturable and finite. As the fraction of carrier entering the TbAs nanoparticle decreases, the fraction of carriers available to recombine within or empty out of the TbAs nanoparticle must also decrease.

The carriers can recombine or relax out of the TbAs nanoparticles either radiatively or nonradiatively. Spectrophotometry measurement and Fourier transform infrared (FTIR) measurements only show an absorption peak at ~ 750 meV and this absorption feature does not correspond to any photoluminescence peaks.[36] This suggests that the absorption feature at ~ 750 meV is not associated with a direct gap transition, and the TbAs carrier emptying mechanism is unlikely to be via radiative recombination. The possible nonradiative recombination mechanisms include, but are not limited to, phonon-mediated non-radiative recombination across an indirect band gap, Auger recombination, and recombination of carrier trapped in the nanoparticles

with oppositely charged carriers in the GaAs matrix. Phonon-mediated recombination is unlikely due to the lack of temperature dependence on lifetime, discussed more in Section 3.2.3. Auger recombination typically results in an decreased lifetime with increasing number of carriers, we observe the opposite, and thus Auger recombination is unlikely.[144] Instead, we propose that the dominate recombination mechanism occurs via electrons in the conduction band of TbAs recombining with holes in the GaAs valence band and holes in the TbAs valence band recombining with electrons in the conduction band. The recombination time of carrier in the TbAs nanoparticle, τ_1 , increases with increasing pump fluence well past the saturation fluence of $20 \mu\text{J}/\text{cm}^2$, shown by $A/(A+B+C)$ going to zero, see Fig. 3.3(c). Once the TbAs nanoparticle states are full, increasing the pump fluence only results in additional carriers in the GaAs conduction and valence band. The increase in carrier concentration in the GaAs matrix changing the relaxation time of carriers in the TbAs nanoparticle, suggests that recombination between carriers in the TbAs nanoparticle and those in the GaAs matrix is a significant non-radiative recombination pathway. This is further supported by the fraction of carrier relaxing out of the TbAs nanoparticle, Fig. 3.3(d), decreasing more slowly than the fraction of carriers entering the TbAs nanoparticle, Fig. 3.3(b), with increasing pump fluence.

Finally, the fraction of carriers relaxing across the bulk band gap, $C/(A+B+C)$, increases toward one with increasing pump fluence, as shown in Fig. 3.3(f), and the carrier lifetimes are approaching that of bulk TbAs, Fig. 3.3(e). This is consistent with TbAs nanoparticles saturating, shown by the decrease in the fraction of carriers both relaxing into and out of the TbAs nanoparticles. As the finite number of TbAs nanoparticles saturate, which occurs due to a finite number of states in each TbAs nanoparticle filling from an increased pump fluence, the carriers must find another way to relax, and this mechanism is via bulk radiative relaxation.

The saturation of the TbAs nanoparticles observed here, suggests that the nanoparticles are indirect gap semiconductors, and not semimetallic like ErAs.[20] A semimetallic nanoparticle has a continuous density of states that would allow for the

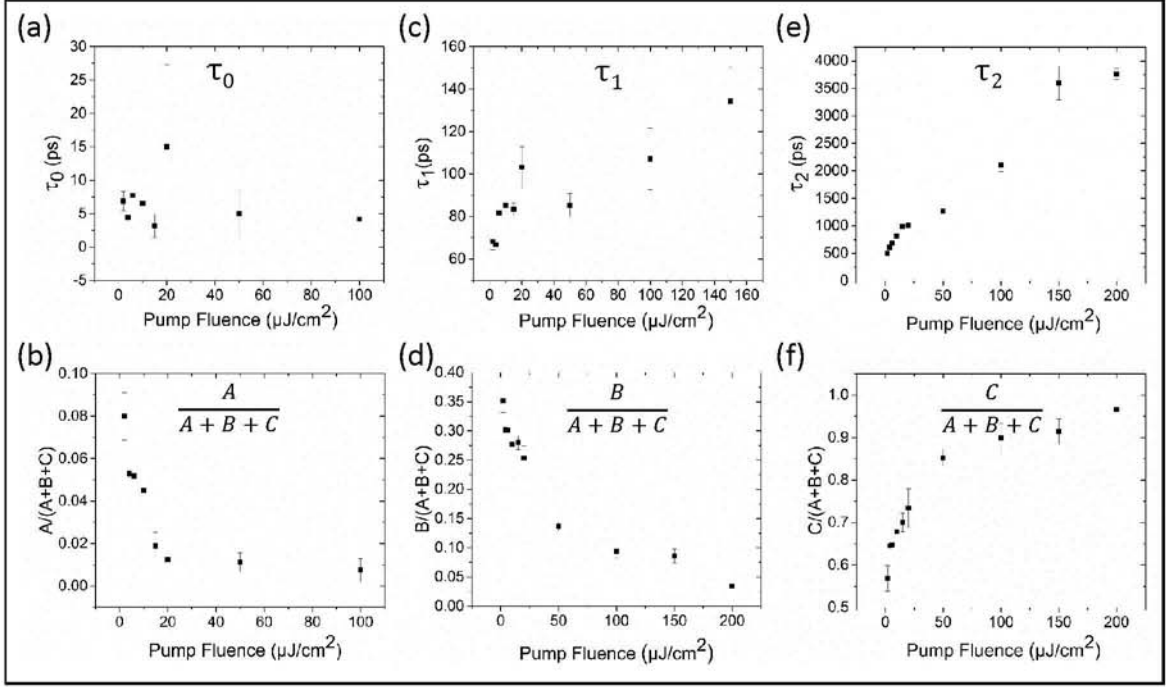


Figure 3.3: The relaxation of carriers into the TbAs nanoparticle (a) does not show a dependence on optical pump fluence while the fraction of carriers relaxing into the nanoparticles (b) decreases with increasing pump fluence. The recombination lifetime of carriers in the TbAs nanoparticle (c) increases with increasing pump fluence while the fraction of carriers recombining in or leaving the TbAs nanoparticles (d) decreases with increasing pump fluence. The relaxation time across the bulk band gap (e) approaches the lifetime of bulk GaAs and the fraction of carriers relaxing across the bulk band gap (f) approaches one with increasing pump fluence. This suggests that TbAs nanoparticles are indirect semiconductors.[26] Reprinted figure with permission from [26]. Copyright 2014 by the [American Physical Society](#).

rapid thermalization of electrons and holes. This would result in carriers quickly relaxing out of the nanoparticle and the nanoparticles would not saturate at the fluences studied here. Instead, we observe that the TbAs nanoparticles saturate which indicates a finite number of states. The saturation of the nanoparticles combined with the lack of a photoluminescence peak suggests that TbAs nanoparticles are an indirect gap semiconductor.

3.2.3 Temperature Dependent Optical Pump Terahertz Probe Results

In addition to studying the carrier relaxation dynamics as a function of pump fluence, the carrier relaxation dynamics of the TbAs:GaAs system were studied as a function of temperature from 4.5 K to 100 K. Figure 3.4 shows the fraction of carriers relaxing in to the TbAs nanoparticles, $A/(A+B+C)$, (black squares) and the fraction of carriers recombining within or leaving the TbAs nanoparticles, $B/(A+B+C)$, (red circles) as a function of temperature for a $2 \mu\text{J}/\text{cm}^2$ pump fluence. Neither the fraction of carriers entering the TbAs nanoparticles nor the fraction of carriers recombining out of the TbAs nanoparticles changes as a function of temperature. Similarly the fraction of carrier recombining across the bulk band gap and the three relaxation lifetimes, not shown, do not show a temperature dependence. The carrier recombination pathway and carrier relaxation times not depending on temperature suggests that recombination is not occurring via phonon assistance. Thus, the TbAs nanoparticle states are relatively deep within the GaAs band gap and phonon assisted relaxation across an indirect band gap is an unlikely recombination pathway.[26]

3.3 Carrier Dynamics in $\text{In}_{0.53}\text{Ga}_{0.47}\text{As}$

Optical-pump THz-probe transient absorption spectroscopy was also used to determine the carrier dynamics, including saturability, of TbAs nanoparticles epitaxially embedded in $\text{In}_{0.53}\text{Ga}_{0.47}\text{As}$. Again, the details of the optical pump THz probe technique was extensively covered in Chapter 2 Section 2.6 and a summary can be found above in section. 3.2

The time-dependent decay in THz absorption was measured for optical pump fluences ranging from $0.5 \mu\text{J}/\text{cm}^2$ to $100 \mu\text{J}/\text{cm}^2$. Data for each set of experimental conditions was taken over 10 experimental runs, averaged, and fit to an exponential decay function using the linear least squares method with a Levenberg-Marquardt algorithm. A triple exponential decay equation, equation 3.2 was used to fit the data obtained with pump fluences from $0 \mu\text{J}/\text{cm}^2$ to $12 \mu\text{J}/\text{cm}^2$ where A_0 , A_1 , and A_2 are amplitude coefficients, providing information on the percentage of carriers participating

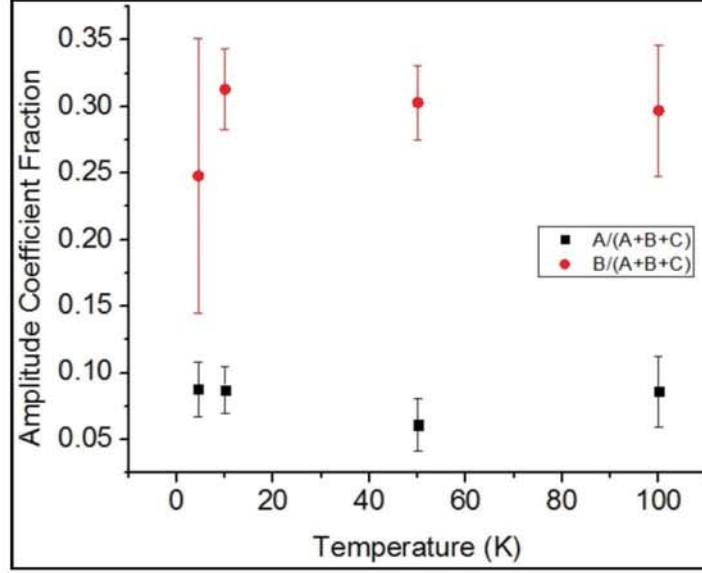


Figure 3.4: The fraction of carriers relaxing into the TbAs nanoparticle states (black squares) and the fraction of carriers recombining or leaving the TbAs nanoparticles (red circles) does not statistically depend on temperature.[26] Reprinted figure with permission from [26]. Copyright 2014 by the [American Physical Society](#).

in each relaxation process, and τ_0 , τ_1 , and τ_2 are the relaxation times for each process. Consistent with the work on TbAs:GaAs, Section 3.2,[26] τ_0 has been assigned as relaxation into the TbAs nanoparticle, τ_1 as emptying the nanoparticle, and τ_2 as recombination across the $\text{In}_{0.53}\text{Ga}_{0.47}\text{As}$ band gap. At higher fluences the saturation of states in the TbAs nanoparticles and neighboring states in the $\text{In}_{0.53}\text{Ga}_{0.47}\text{As}$ matrix reduces the fraction of carriers participating in the fastest processes (τ_0 and τ_1) to a negligible level, resulting in the use of a double (pump fluences from $20\mu\text{J}/\text{cm}^2$ to $50\mu\text{J}/\text{cm}^2$) or single (pump fluence of $100\mu\text{J}/\text{cm}^2$) exponential fit. Examples of triple, double, and single exponential decays (for different pump fluences) can be seen in Fig. 3.5. The time constants and pre-exponential factors extracted from fitting the decay in the THz probes absorption in the TbAs: $\text{In}_{0.53}\text{Ga}_{0.47}\text{As}$ sample are shown as a function of optical pump fluence in Fig. 3.6, note that the data for the TbAs:GaAs sample, discussed in Section 3.2.2 is overlaid as hollow symbols for easy comparison.

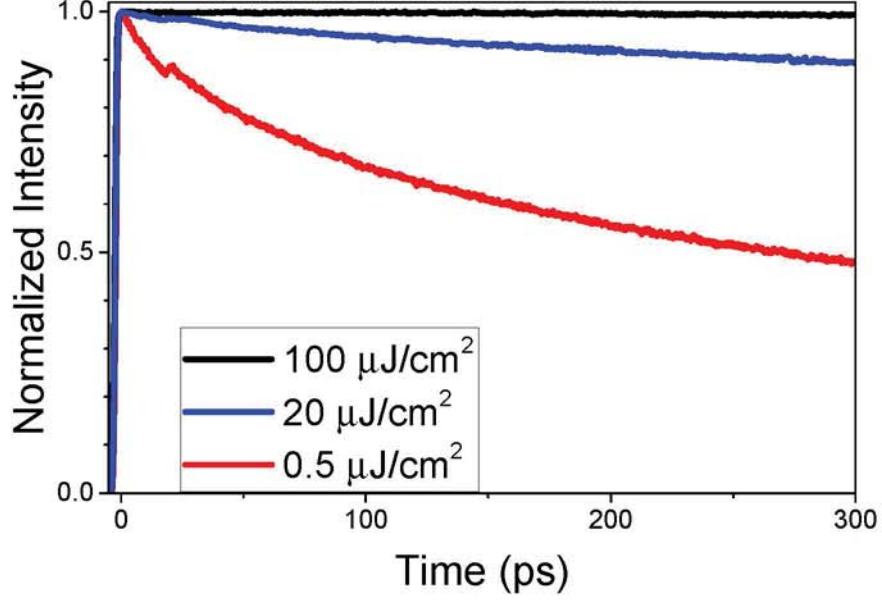


Figure 3.5: The exponential decay in THz absorption for the TbAs:In_{0.53}Ga_{0.47}As sample as a function of time, depicting the need for triple (red), double (blue), and single (black) exponential fits. Reprinted from [27], with the permission of AIP Publishing.

$$I = A_0 \exp \frac{-t}{\tau_0} + A_1 \exp \frac{-t}{\tau_1} + A_2 \exp \frac{-t}{\tau_2} \quad (3.2)$$

The average relaxation time of carriers entering the TbAs nanoparticles is 4.6 ps and is independent of pump fluence, Fig. 3.6(a) solid black squares. However, the fraction of carriers entering the TbAs nanoparticles has a dependence on pump fluence, and reaches zero by 20 $\mu\text{J}/\text{cm}^2$ pump fluence, Fig. 3.6(b) solid black squares. This indicates that the nanoparticles' carrier capture rate does not change with pump fluence and that the number of carriers that can relax into the nanoparticle is finite.

As carriers leave or recombine within the nanoparticle, additional carriers at the band edge can rapidly relax into the nanoparticle, further reducing the THz absorption. Note that the time it initially takes for carriers to relax into the nanoparticle is fast, approximately 4.6 ps, compared to the time it takes for more carriers to relax into the nanoparticle. Thus, the limiting rate for new carriers entering the nanoparticle must be the emptying of the nanoparticle which appears as a separate time constant, τ_1 ,

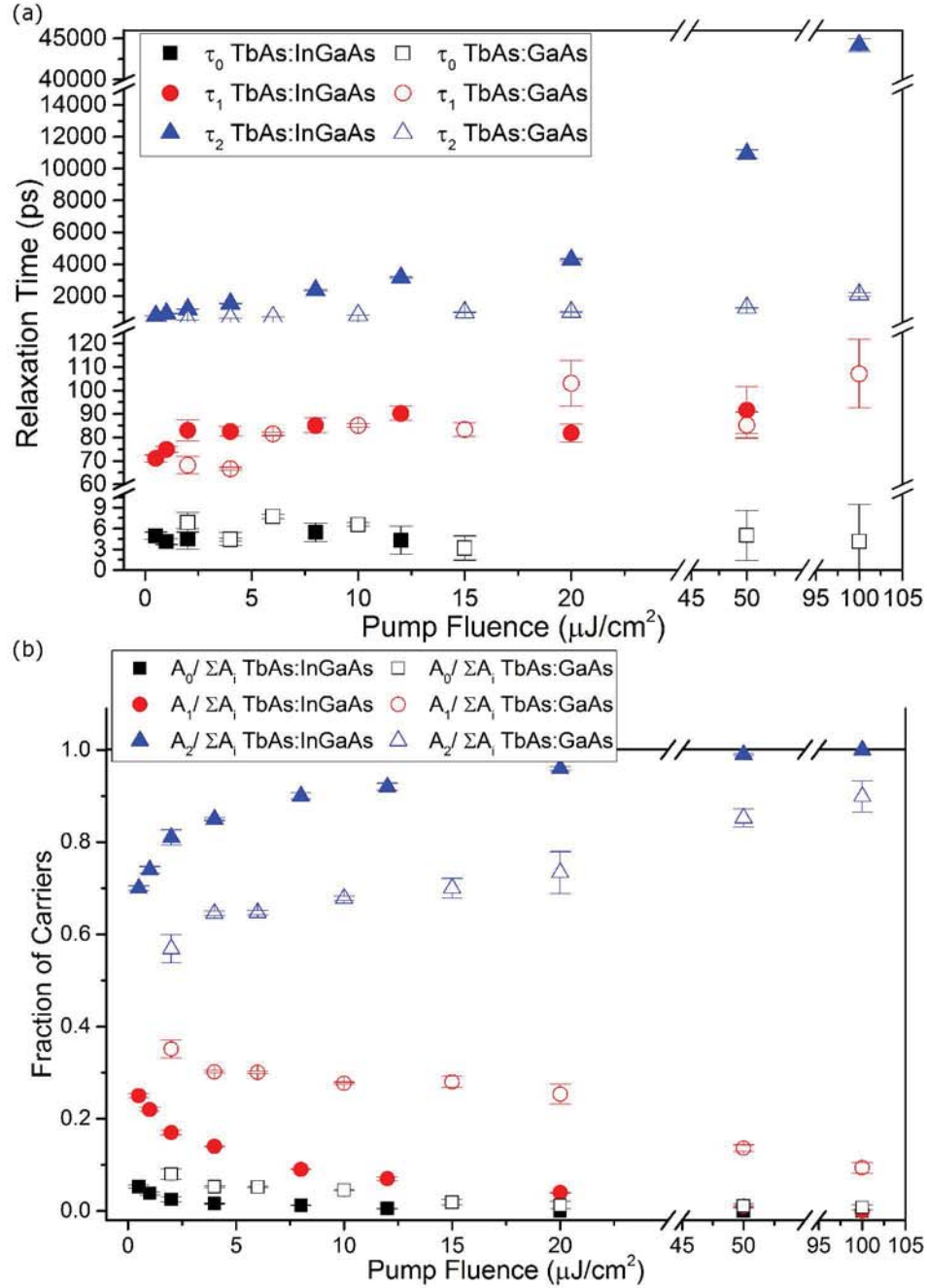


Figure 3.6: (a) The relaxation time of each of the three processes (relaxation into the nanoparticles shown as black squares, emptying or recombining in the nanoparticles shown as red circles, and relaxation across the matrix's band gap shown as blue triangles) as a function of pump fluence is shown for the TbAs:In_{0.53}Ga_{0.47}As sample (solid symbols) and the TbAs:GaAs sample (hollow symbols). (b) The fraction of carriers participating in each relaxation process as a function of pump fluence is shown for both the TbAs:In_{0.53}Ga_{0.47}As sample and the TbAs:GaAs sample. Reprinted from [27], with the permission of AIP Publishing.

and can be referred to as the nanoparticle emptying time. This nanoparticle emptying time, Fig. 3.6(a) solid red circles, initially increases from 71 ps to 92 ps as pump fluence increases, and then becomes statistically invariant. The fraction of carriers leaving the nanoparticle, Fig. 3.6(b) solid red circles, decreases with increasing pump fluence, reaching 0 at $100 \mu\text{J}/\text{cm}^2$. Notably, the fraction of carriers leaving the nanoparticle decreases at a slower rate than carriers entering the nanoparticle. This suggests that the rate and fraction of carriers leaving the nanoparticles depends on the occupation of states in the surrounding matrix, and subsequently that the recombination of electrons in the $\text{In}_{0.53}\text{Ga}_{0.47}\text{As}$ conduction band and holes in the TbAs valence band is a significant emptying process. The fraction of carriers leaving the nanoparticle diminishes to zero for high pump fluences, suggesting saturation of the states around the nanoparticle that participate in the nanoparticle emptying process.

When the nanoparticles become saturated, carriers must find another relaxation mechanism. The solid blue triangles in Fig. 3.6(a) show that the relaxation time across the bulk band gap increases with pump fluence, ranging from 766 ps to 44.2 ns, approaching the bulk lifetime of $\text{In}_{0.53}\text{Ga}_{0.47}\text{As}$.^[145] This increased lifetime can be attributed to the saturation of both TbAs and other defects in the material. The solid blue triangles in Fig. 3.6(b) show that the fraction of carriers relaxing across the $\text{In}_{0.53}\text{Ga}_{0.47}\text{As}$ band gap increases with pump fluence and is one at $100 \mu\text{J}/\text{cm}^2$. At high pump fluences the finite number of nanoparticle states and matrix to nanoparticle trap emptying states are saturated, requiring the excess carriers to relax across the bulk band gap.

There are many similarities in the carrier dynamics of the $\text{TbAs}:\text{In}_{0.53}\text{Ga}_{0.47}\text{As}$ system and the previously measured/discussed $\text{TbAs}:\text{GaAs}$ system.^[26] Both systems have similar relaxation times of carriers into the nanoparticle and emptying times of the nanoparticles. The emptying of the nanoparticles in both matrices depends on the occupation of carriers in the surrounding matrix. Finally, the percentage of carriers entering and leaving the nanoparticles decreases with increasing pump fluence, suggesting a band gap within the nanoparticle. The major difference in these two systems,

however, is that the fraction of carriers entering and leaving the TbAs nanoparticles in the TbAs:In_{0.53}Ga_{0.47}As system reached zero during this measurement, indicating complete saturation of the nanoparticles, while the nanoparticles in the TbAs:GaAs system have not completely saturated. Note that the saturation difference cannot be explained by only accounting for the difference in nanoparticle density. The TbAs:In_{0.53}Ga_{0.47}As system shows complete saturation at a pump fluence of $20 \mu\text{J}/\text{cm}^2$. If only the nanoparticle density determined the saturation rate, the TbAs:GaAs system should completely saturate at a pump fluence of $25 \mu\text{J}/\text{cm}^2$. Complete saturation of the τ_1 process in the TbAs:GaAs system is not seen for any pump fluence measured. This suggests that differences in the trapping dynamics, likely from differences in the band alignment, are causing the difference in saturation.

3.4 Optical Absorption

Sections 3.2 and 3.3 show that TbAs nanoparticles have a band gap and the band alignment affects the trapping dynamics. The next step toward proposing a band alignment for each system requires obtaining the energy of transitions within each system. The absorption energies for TbAs:GaAs and TbAs:In_{0.53}Ga_{0.47}As were obtained using spectrophotometry. The details of spectrophotometry measurements were discussed in Chapter 2 Section 2.5. Briefly, transmission and reflection spectra were collected for both the TbAs:GaAs and TbAs:In_{0.53}Ga_{0.47}As samples with a Perkin-Elmer Lambda-750 UV-Visible-IR Spectrophotometer fitted with an integrating sphere. Photoluminescence measurements,[36] consistent with theoretical predictions, suggest that a TbAs band gap would be indirect. Thus, a Tauc plot for indirect band gap materials was used to determine absorption energies, Fig. 3.7.[146] This absorption energy can be an interband transition within the nanoparticle or a transition from the nanoparticle to the matrix. The measured absorption energy is 0.63 ± 0.01 eV for the TbAs:GaAs system and 0.43 ± 0.01 eV for the TbAs:In_{0.53}Ga_{0.47}As system.

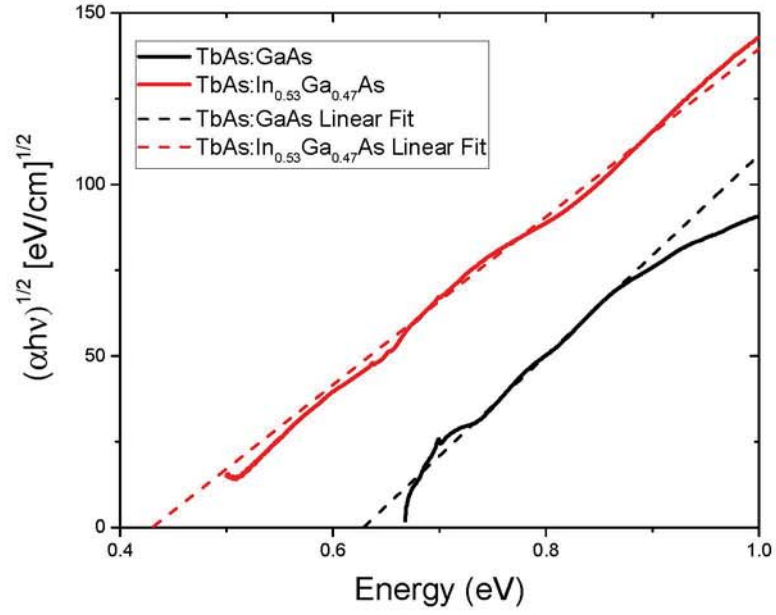


Figure 3.7: A Tauc Plot for an indirect absorption with the linear fits (dashed lines) was used to calculate an absorption energy of $0.63 \pm 0.01 \text{ eV}$ for the TbAs:GaAs system (black) and $0.43 \pm 0.01 \text{ eV}$ for the TbAs:In_{0.53}Ga_{0.47}As (red) system. Note that the detector cuts out for energies below 0.5 eV. [27] Adapted from [27], with the permission of AIP Publishing.

3.5 Determining the Fermi Level

The Fermi level position is also needed for a band alignment diagram, and is estimated using temperature dependent Hall effect. Hall effect measurements were discussed in detail in Chapter 2 Section 2.4. Measurements were performed using a custom-built Hall effect system with indium contacts in the van der Pauw geometry. Each sample was cleaved to 5 mm \times 5 mm square with indium contacts deposited on each corner. Data was collected every 5 K from 45 K to 430 K. Due to the samples being highly resistive, measurements had to be done over a small current range, $\pm 0.02 \mu\text{A}$ for the TbAs:GaAs sample and $\pm 0.1 \text{ mA}$ for the TbAs:In_{0.53}Ga_{0.47}As sample. To improve the signal to noise ratio, at each temperature the Hall effect measurement was measured multiple times (10 times for the TbAs:In_{0.53}Ga_{0.47}As sample and 20 times for the TbAs:GaAs sample), the raw data at each temperature was averaged and the carrier concentration, resistivity, and mobility were calculated. Figure 3.8 shows the free electron concentration for both films.

The free electron concentration of the TbAs:GaAs film has a clear exponential temperature dependence above 315 K. Below 315 K the free electron concentration is level at approximately $2.5 \times 10^{12} \text{ cm}^{-3}$. This is attributed to the unintentional doping of the GaAs matrix. Fitting the temperature dependent free electron concentration to the relation $n = N_c \exp(E_a/kT)$ provides an activation energy, E_a , which corresponds to the chemical potential relative to the conduction band[147], and a reasonable estimate of the Fermi level[11]. The resulting chemical potential is 0.66 eV below the conduction band edge.

The TbAs:In_{0.53}Ga_{0.47}As film, however, is degenerately doped and shows a minimal temperature dependence that may be due to band bending at the matrix nanoparticle interface. Using equation 3.3, where m is the effect mass of an electron (assumed to be that of the matrix) and μ is the Fermi level, and the Hall effect data taken at 300 K, we can estimate the Fermi level location in TbAs:In_{0.53}Ga_{0.47}As. A carrier concentration of $2.20 \times 10^{18} \text{ cm}^{-3}$ for the TbAs:In_{0.53}Ga_{0.47}As system results in a Fermi level $\sim 76 \text{ meV}$ above the conduction band edge.

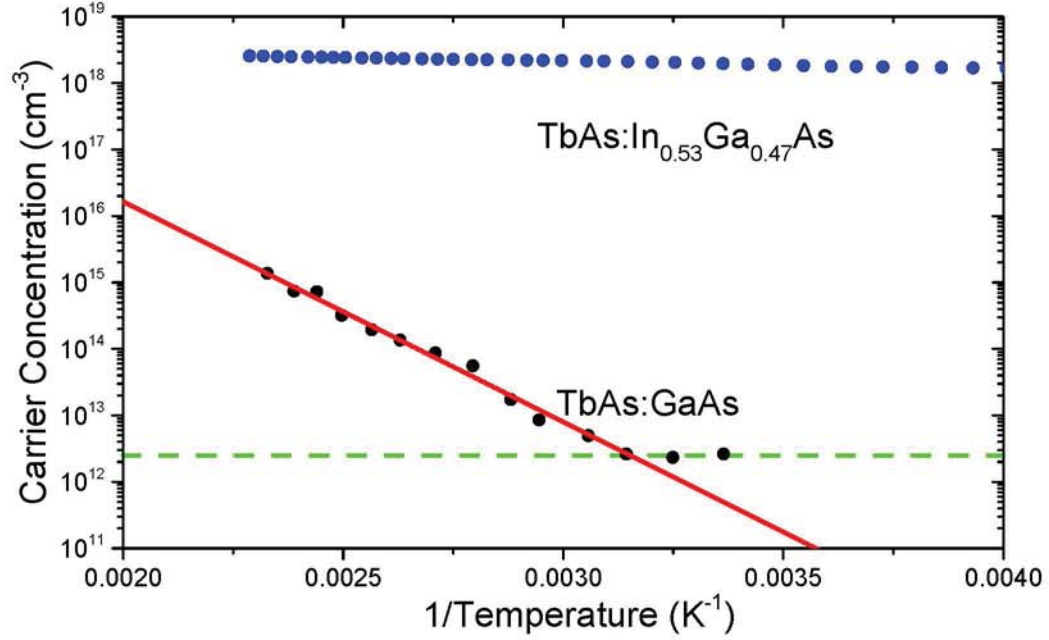


Figure 3.8: Free electron concentration of the TbAs:GaAs (black dots) strongly depends on temperature, until unintentional doping (green dashed line) dominates, allowing an exponential fit (red line) to estimate a Fermi level. The degenerate TbAs:In_{0.53}Ga_{0.47}As (blue dots) has little temperature dependence.[27] Reprinted from [27], with the permission of AIP Publishing.

$$n = \int_{E_c}^{\infty} \sqrt{2E} \frac{m^{1/2}}{\hbar^3 \pi^2} \frac{1}{\exp \frac{E-\mu}{kT} + 1} dE \quad (3.3)$$

3.6 Proposing a Band Alignment

The combination of the measurements discussed above show that a type I (straddled) heterojunction in both systems is unphysical. If both systems had a type I alignment, the absorption seen in the spectrophotometry measurement would be due to excitation of electrons from the first energy level in the TbAs valence band to the first energy level in the TbAs conduction band. Thus, the large blue shift in absorption (0.19 eV) that occurs when changing the matrix would require a change of ground state energy with a change in the height of the barrier provided by the matrix material, and

carrier effective mass in the matrix. This change in energy levels due to changing matrix material is not consistent with any reasonable combination of TbAs band gap and effective mass, as shown in the model described below.

The type I band alignment in TbAs:In_{0.53}Ga_{0.47}As and TbAs:GaAs could be modeled as a finite quantum dot with three unknowns: the native band gap of TbAs (we know the E_{1VB} to E_{1CB} transition energy in each system), the electron's effective mass in TbAs and the position of TbAs's band gap within the matrix (which effectively changes the barrier height in the model). Note that changing the matrix from In_{0.53}Ga_{0.47}As to GaAs would not change the native band gap or the effective mass of charge carriers in TbAs. This results in two systems with three unknowns. There are three limiting cases for the position of the TbAs band gap within the matrix (assuming a type I heterojunction in both systems): the TbAs nanoparticle has a flat valence band with In_{0.53}Ga_{0.47}As, the TbAs nanoparticle has a flat conduction with In_{0.53}Ga_{0.47}As, and a symmetric quantum well. For each of the limiting cases Schrödinger's equations for a 3-D finite quantum well for the TbAs:In_{0.53}Ga_{0.47}As and TbAs:GaAs systems can be simultaneously solved, determining a self-consistent band gap and electron effective mass for TbAs. All modeling attempts resulted in either a zero electron effective mass or a negative band gap. Neither of those cases can explain the results of the measurements done to date. Thus, the difference in absorption energy between the In_{0.53}Ga_{0.47}As matrix and the GaAs matrix cannot be completely explained by a shift in the nanoparticles energy levels. This suggests that the absorption is unlikely to be from a valence band to conduction band transition within the TbAs nanoparticle.

The inability of our model to explain the results from our experimental measurements suggests that the change in absorption observed with spectrophotometry cannot be explained by a change in the confinement provided by the matrix. Instead we propose that TbAs nanoparticles forms a type I (straddled) heterojunction with GaAs and a type II (staggered) heterojunction with In_{0.53}Ga_{0.47}As. A schematic of this band alignment is shown in Fig. 3.9.

The proposed band alignment is supported by the various data. Optical-pump

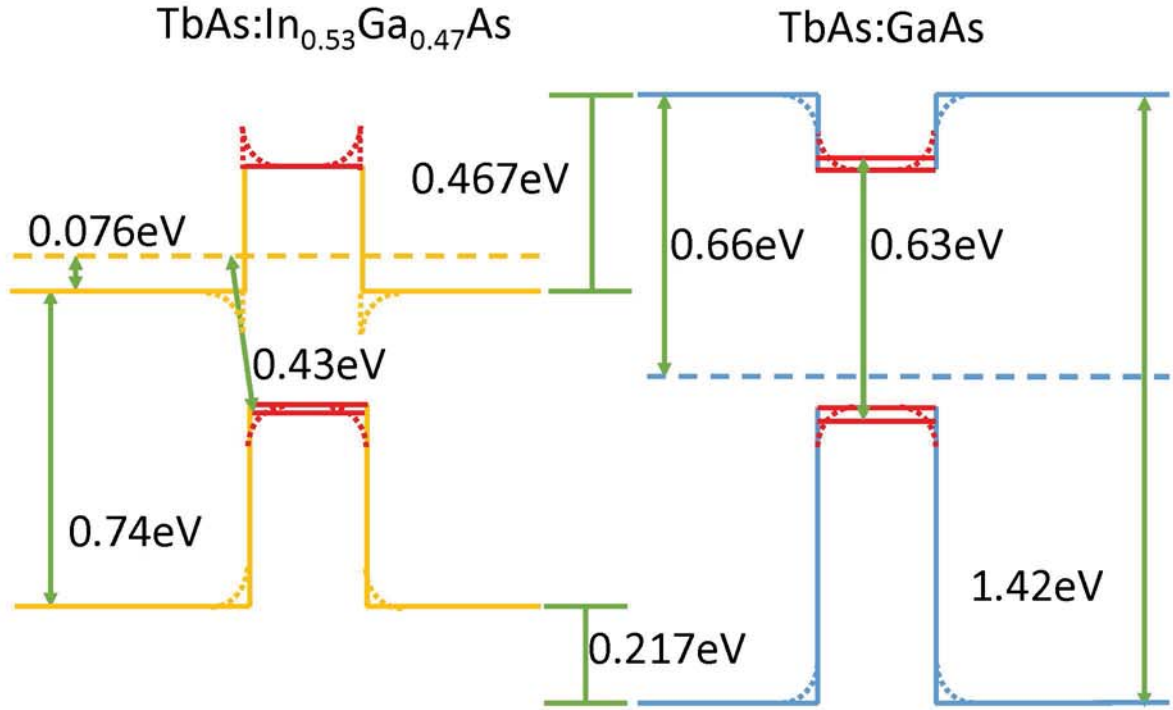


Figure 3.9: Schematic showing the proposed band alignments of TbAs nanoparticles (red) in $\text{In}_{0.53}\text{Ga}_{0.47}\text{As}$ (yellow) and GaAs (blue). Energy offsets are shown with green arrows, dashed lines represent the nanocomposites' estimated Fermi level, thin lines represent the first energy level within the nanoparticle, thick lines represent band edges, and dotted lines represent exaggerated band bending at the nanoparticle matrix interface. Note that all energies involving the TbAs nanoparticle are relative to the first energy level; the conduction and valence band edges of TbAs are only included as an estimate.[27] Adapted from [27], with the permission of AIP Publishing.

THz-probe measurements show that the TbAs nanoparticles have a band gap, which is seen in the band alignment diagram. Additionally, the optical-pump THz-probe measurements show that the two systems have different trapping dynamics. The type II heterojunction in the $\text{In}_{0.53}\text{Ga}_{0.47}\text{As}$ system causes the TbAs nanoparticle to only trap holes while TbAs nanoparticles in GaAs trap both electrons and holes. This change in trap behavior would explain the saturation of the $\text{In}_{0.53}\text{Ga}_{0.47}\text{As}$ sample at a lower fluence when compared to the GaAs sample.[26] Spectrophotometry measurements provide two different absorption energies, 0.63 eV in the TbAs:GaAs system and 0.43 eV in the TbAs: $\text{In}_{0.53}\text{Ga}_{0.47}\text{As}$ system. The type I band alignment in the TbAs:GaAs system shows that the absorption feature is within the TbAs nanoparticle, indicating that the TbAs nanoparticle has a band gap somewhat smaller than 0.63 eV. The type II band alignment in the TbAs: $\text{In}_{0.53}\text{Ga}_{0.47}\text{As}$ system means the absorption transition is due to the excitation of electrons from the TbAs valence band to the Fermi level in the $\text{In}_{0.53}\text{Ga}_{0.47}\text{As}$ matrix. Excitation of carriers must be above the Fermi level rather than the conduction band because the system is degenerately doped, as shown by the Hall effect data. The type II heterojunction would allow for band bending at the nanoparticle-matrix interface, creating a small two-dimensional electron gas in the $\text{In}_{0.53}\text{Ga}_{0.47}\text{As}$ and a small barrier for electrons entering the matrix from the TbAs conduction band. Band bending explains the small temperature dependence of the free electron concentration shown with the Hall effect measurement.

3.7 TbAs Nanoparticle Electronic Structure Conclusion

In summary, we have proposed a band alignment for TbAs nanoparticles embedded within GaAs and $\text{In}_{0.53}\text{Ga}_{0.47}\text{As}$ that is consistent with all available optical and electronic measurements. Optical-pump THz-probe measurements provide the carrier relaxation dynamics, which depend on band alignment. Optical-pump THz-probe measurements also show that the TbAs nanoparticles are saturable and likely have a band gap. Using spectrophotometry we find that the minimum energy required to generate an electron hole pair is 0.63 eV for the TbAs:GaAs system and 0.43 eV for

the TbAs:In_{0.53}Ga_{0.47}As system. Finally, Hall effect measurements estimate the Fermi level to be pinned 0.66 eV below the conduction band edge in the TbAs:GaAs system and 76 meV above the conduction band edge of the TbAs:In_{0.53}Ga_{0.47}As system. Combining all of these measurements, we propose that the TbAs nanoparticles forms a type I heterojunction with GaAs and a type II heterojunction with In_{0.53}Ga_{0.47}As.

Chapter 4

GROWTH AND CHARACTERIZATION OF TbAs FILMS

As discussed in great detail in Chapter 1, lanthanide monpnictide (Ln-V) materials are of great interest for a wide range of applications due to their crystal structure and (opto)electronic properties. Many of the LN-V systems have the rock-salt crystal structure, allowing LN-V to have an epitaxial relationship with III-V materials as either embedded nanoparticles or films. When incorporated as nanoparticles, the selection of LN-V species and III-V matrix species allows for the choice in the nanocomposites properties, including carrier lifetimes, electrical resistivity, carrier concentrations, and thermal conductivity. [148, 149, 42, 116, 11, 36, 37] This wide range of accessible properties make LN-V nanoparticles embedded in III-V matrices interesting for applications, including thermoelectrics, tunnel junctions, and photoconductive switches for terahertz detection and generation.[32, 119, 25, 124, 29] LN-V films are also of interest for a wide range of applications because of the electrical and optical properties available, which can easily be tuned by alloying multiple Ln species.[16, 35, 106, 76, 75, 39, 107]

In this chapter, we study the fundamental properties of TbAs films, expanding upon the range of known properties available with LN-V materials. Early studies on the electronic structure of bulk TbAs are contradictory, some of the literature suggests that TbAs is semimetallic with others suggesting semiconducting.[84, 91, 86, 33] In Chapter 3, which was based on our recently published work, I proposed that TbAs is a semiconductor that forms a type I, straddled, heterojunction with GaAs and a type II, staggered, heterojunction with $\text{In}_{0.53}\text{Ga}_{0.47}\text{As}$. [26, 27] To further understand the fundamental properties of TbAs, we study the morphology, optical properties, and electrical properties of MBE grown TbAs films. Section 4.1 discusses the MBE growth of the two TbAs films studied in this chapter. Section 4.2 presents a study

on the films' structural properties including morphology, thickness, and relaxation. Section 4.3 shows the spectrophotometry measurements used to obtain optical band gaps. The electronic properties of the films are presented in Section 4.4, showing the films are degenerately doped. Section 4.4 also discusses how the degenerate doping influences the optical band gap and provides information on where carriers come from. Section 4.5 discusses the study of a possible Drude edge in the TbAs films' and compares the TbAs Drude edge to that of other LN-V films. Finally, a summary of the work on TbAs films is presented in Section 4.6. The contents of this chapter are adapted from a manuscript that was written by the author is currently under review for publication.[28]

4.1 Molecular Beam Epitaxy Growth of TbAs Films

For this work, two TbAs films with different thicknesses were studied, hereafter referred to as the thick and thin samples. Both films were grown on GaAs [001] substrates using an OSEMI NextGEN solid source MBE equipped with effusion cells for Ga, Tb, and a two-zone valved cracker source for As₂. After desorbing the native oxide, a 100 nm GaAs buffer layer was grown at 530°C, as measured by band edge thermometry. Following the buffer layer growth, the substrate was allowed to cool to 430°C and the As₂ overpressure was reduced. The growth temperature of 430°C was based upon other LN-V film growths.[16, 35, 106, 76, 75, 39, 74, 77] Once cooled, the thick and thin TbAs films were grown for 210 and 45 minutes, respectively, corresponding to an $\sim 5\times$ expected thickness difference. Thicknesses were measured to be 356 ± 7 nm and 68 ± 3 nm for the thick and thin films, respectively, discussed more in Section 4.2. The films were capped with a 25 nm GaAs layer to prevent oxidation.

Note that at the time of growth, a TbAs growth rate of 0.2 Å/s was estimate based upon the Tb cell temperature, corresponding to a thick and thin film thickness of ~ 252 and ~ 54 nm, respectively. As discussed in Chapter 2 Section 2.1, the low vapor pressure of Tb at the ion gauge filament's temperature prevents measuring a Tb flux.[36] Instead, the Tb growth rate was calibrated with cell temperature and *ex situ* measurements, typically Rutherford backscattering spectroscopy. The growth rate

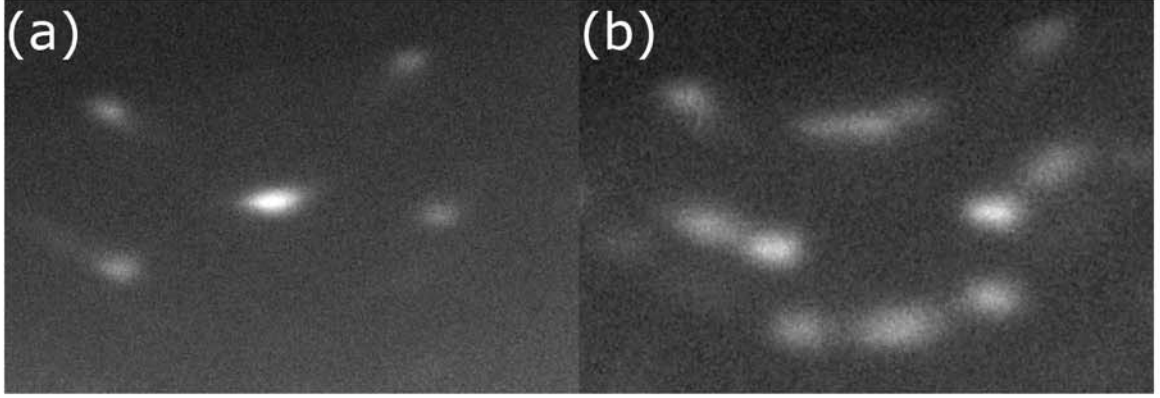


Figure 4.1: RHEED pattern observed ~ 150 nm into the thick TbAs sample (a) shows a clear, streaky 1×1 RHEED pattern with (b) rotated 90° showing a slight degradation in morphology. These represent the RHEED patterns observed throughout the growth of both samples.[28]

for these films was extrapolated from calibration curves corresponding to the amount of TbAs co-deposited in GaAs; a strict TbAs growth rate calibration study was not previously performed, and was not necessary for this study. This method required extrapolating far beyond the typical calibration curves used, and unsurprisingly resulted in an underestimation of the film thickness. Fortunately, for this study the exact thickness obtained was not important, only that the two samples had significantly different thicknesses.

4.2 Structural Properties of TbAs Films

Throughout the growth, the surface morphology was monitored with *in situ* reflection high energy electron diffraction (RHEED). RHEED was previously discussed in Chapter 2 Section 2.1. Figure 4.1(a) shows the bright and streaky 1×1 RHEED pattern observed during the growth of these films. As the sample rotated 90° a RHEED pattern indicating a slightly degraded morphology was observed, shown in Fig. 4.1(b). This degradation is likely due to exceeding the Matthews-Blakeslee critical thickness of TbAs on GaAs, ~ 20 Å.

High resolution X-ray diffraction (HRXRD) 004 ω - 2θ scans were used to confirm

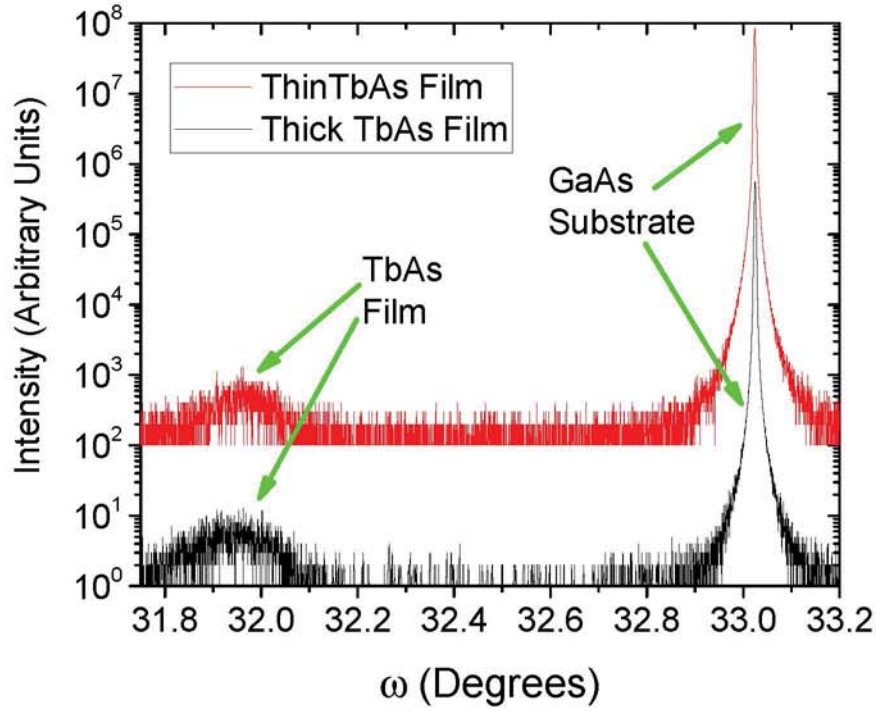


Figure 4.2: 004 ω - 2θ scan of the thick (black) and thin (red) TbAs samples. The peak corresponding to the TbAs films is broad with a low intensity, indicating defects likely introduced from exceeding the critical thickness of TbAs.[28]

the growth of TbAs films. Note that XRD ω - 2θ scans and reciprocal space mapping, presented below, were both discussed in detail in Chapter 2 Section 2.2. In both samples, the diffraction peak corresponding to TbAs is broad with low intensity, Fig. 4.2. The full width half maximum of the thick and thin films are $\sim 12\times$ and $\sim 2\times$ larger than expected from simulations respectively. This indicates that the film has some defects, possibly due to exceeding the Matthews-Blakeslee critical thickness. To further investigate the morphology and the relaxation of the TbAs film, a 224 reciprocal space map (RSM) was obtained for both samples. Figure 4.3 shows the RSM map for the thin TbAs sample, Fig 4.4 show the RSM map obtained for the thick TbAs sample. The RSMs show that in both samples the TbAs films are relaxed with the same relaxation state; the elongation of the films' peaks indicate that the films have some mosaic character.

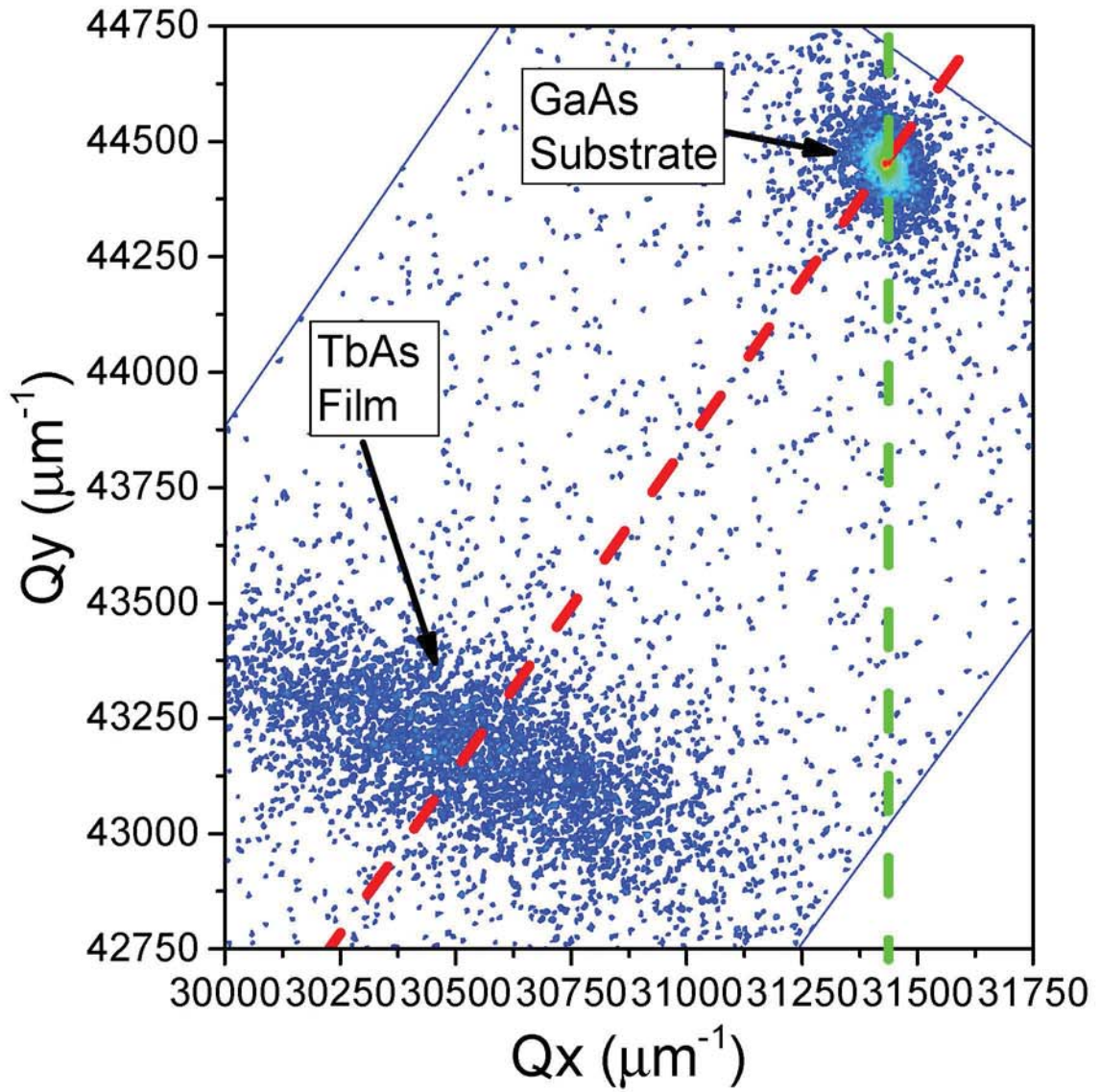


Figure 4.3: 224 RSM scan of the thin TbAs sample. The green dashed line represents the direction in which a fully strained film peak would be located and the red dashed line represents the direction in which a fully relaxed film peak would be located. The broadening of the TbAs film peak indicates that the film has some mosaic character. [28]

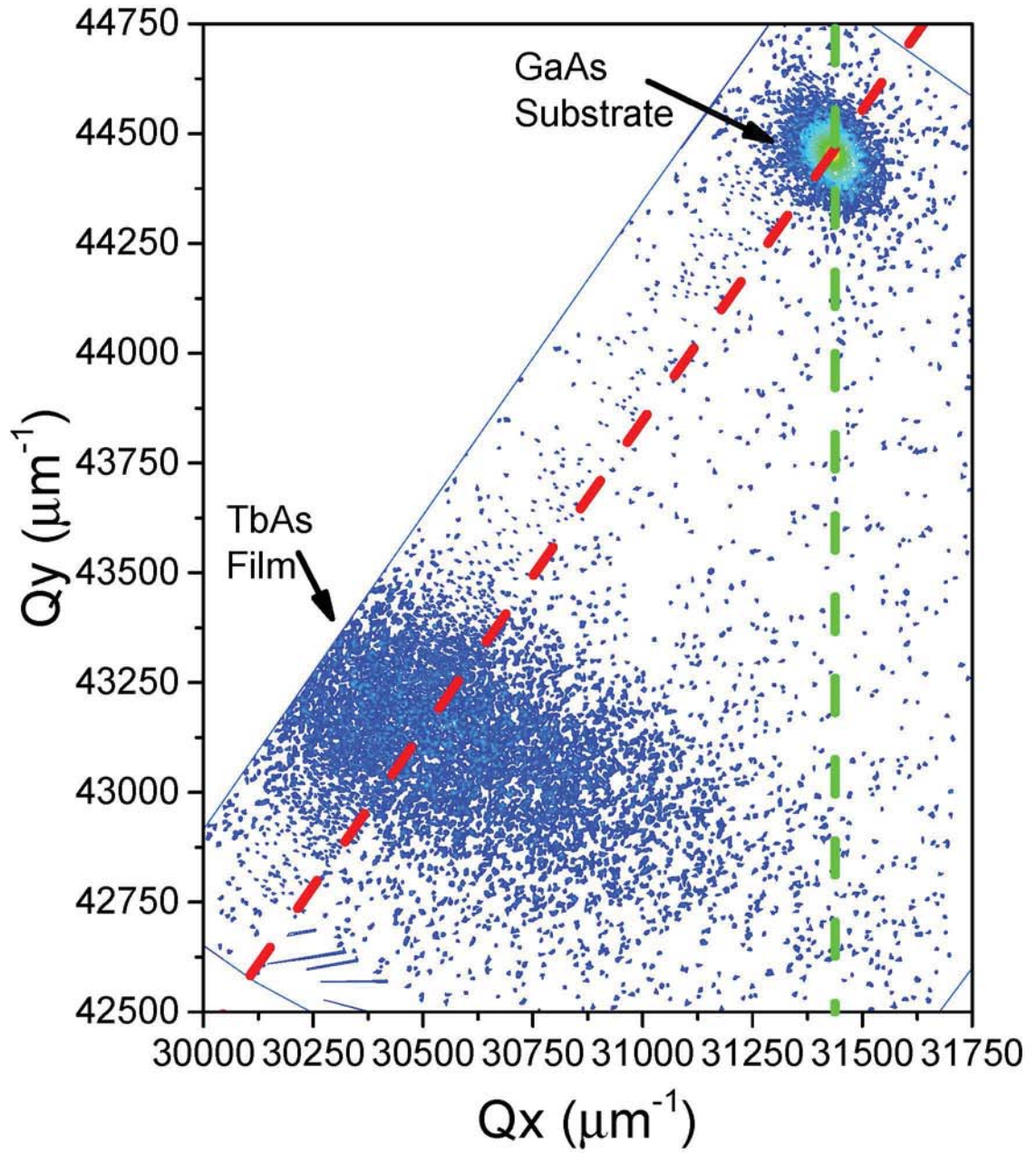


Figure 4.4: 224 RSM scan of the thick TbAs sample. Again, the green dashed line represents the direction in which a fully strained film peak would be located and the red dashed line represents the direction in which a fully relaxed film peak would be located. The broadening of the TbAs film peak indicates that the film has some mosaic character.

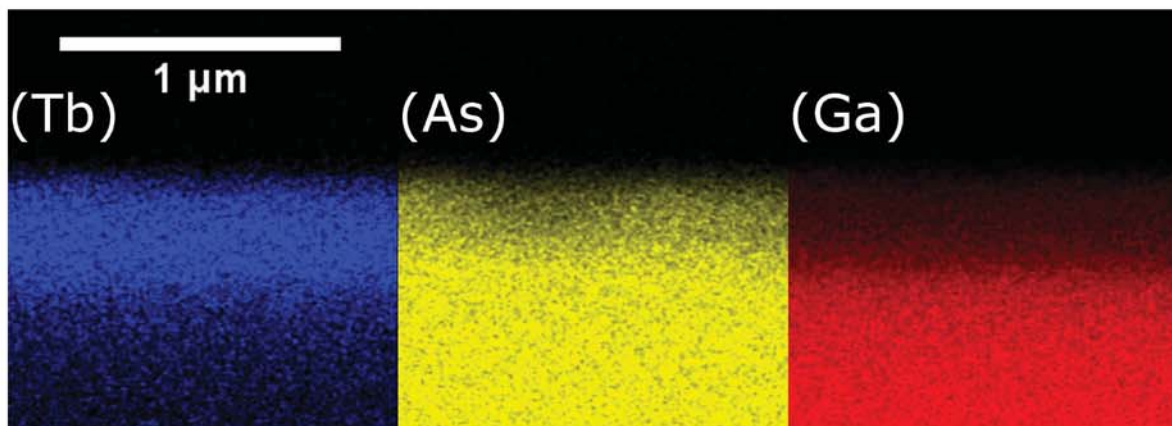


Figure 4.5: Cross-section EDS maps of Tb, Ga, and As, showing a clear TbAs layer on top of GaAs.[28]

Cross-sectional energy dispersive X-ray spectroscopy (EDS) scanning electron microscopy (SEM) images of the thick TbAs sample, Fig. 4.5, show the growth of a complete, ~ 390 nm thick, TbAs film on top of GaAs. To further study the samples' morphology and thickness, a Ga focused ion beam was used to make cross-sectional transmission electron microscopy (TEM) samples of both the thick and thin samples. Cross-sectional TEM of the thick TbAs sample is shown in Fig. 4.6(a), a zoomed-in section of the TbAs-GaAs buffer layer interface in Fig. 4.6(b), and an electron diffraction pattern in Fig 4.6(c). A cross-sectional TEM image of the thin TbAs sample is shown in Fig 4.7. From the TEM, a thickness of 356 ± 7 nm and 68 ± 3 nm was measured for the thick and thin TbAs samples, respectively. The TEM measured thickness of the thin sample matches reasonably well with the X-ray reflectivity (XRR) thickness of 65 nm (not shown); the thick sample was too thick to measure with XRR. The TEM images and the slight elongation of the electron diffraction spots also show some of the films' mosaic nature.

4.3 TbAs Film's Optical Band Gap

Recent work, Chapter 3, suggests that TbAs nanoparticles are semiconducting[26] with a band gap between 0.37 and 0.61 eV. The lower limit is set by the absorption

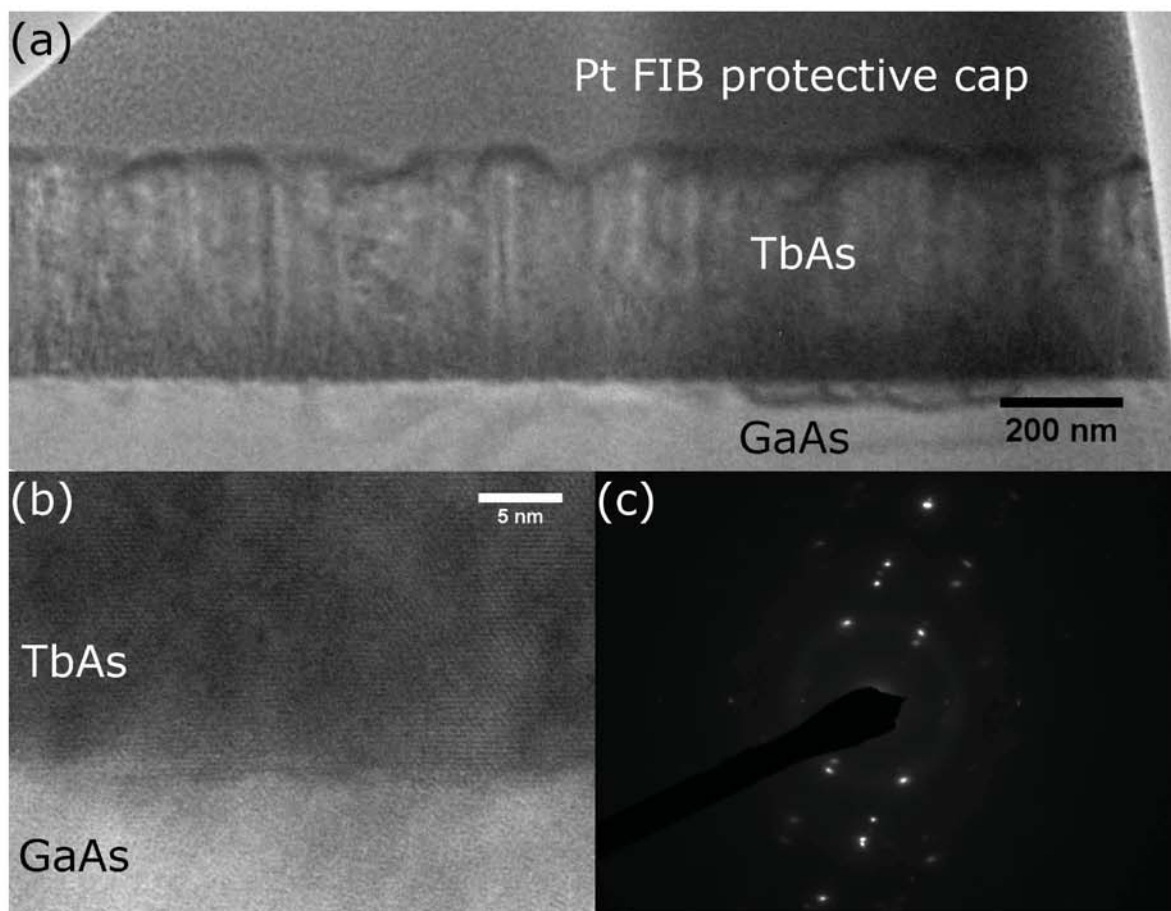


Figure 4.6: Cross-section TEM images of the (a) thicker TbAs sample, (b) zoomed-in on the TbAs-GaAs buffer layer interface, and (c) an electron diffraction pattern of the TbAs film.[28]

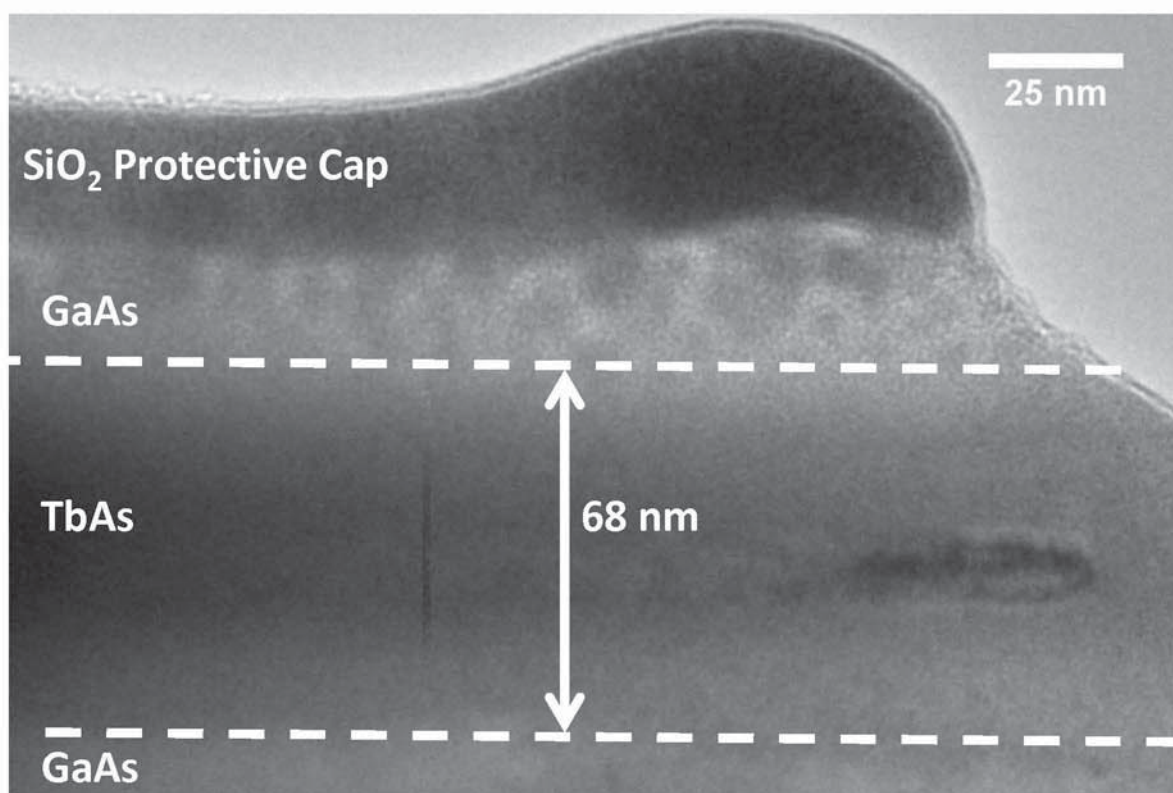


Figure 4.7: Cross-section TEM images of the thinner TbAs samples showing a film thickness of 68 nm. Note that during the FIB process, much of film was thinned too much, resulting in the film being removed.

energy measured in the type II TbAs:In_{0.53}Ga_{0.47}As system; specifically the energy between the TbAs valence band and the Fermi level within the In_{0.53}Ga_{0.47}As matrix. The upper limit is set by the observed energy absorption in the quantum confined states of TbAs nanoparticles embedded in GaAs.[27] In addition to quantum confinement altering the band gap of the TbAs nanoparticles, the strain on the nanoparticle also changes the band gap. To obtain a more accurate measure of the TbAs band gap, transmission and reflection spectra of the TbAs film samples were collected with a Perkin-Elmer Lambda-750 UV-visible-IR Spectrophotometer and used to construct a Tauc plot for an indirect semiconductor, Fig. 4.8. Note spectrophotometry and Tauc plots were discussed in detail in Chapter 2 Section 2.5. Optical band gaps of 435 meV and 517 meV for the thick and thin samples were obtained, respectively. To explain this red shift, an understanding of the electrical properties is needed, discussed in Section 4.4.

4.4 Electrical Properties of TbAs Films

A custom built wide temperature Hall effect system with indium contacts in the van der Pauw geometry was used to determine the resistivity, carrier concentration and mobility. Data was collected multiple times every 5 K from 42 K to 500 K, averaged at each temperature, and then the resistivity, carrier concentration, and mobility were calculated. Note, the details of the Hall Effect measurement technique and system was extensively discussed in Chapter 2 Section 2.4. The top graph in Fig. 4.9 shows the resistivity as a function of temperature for both the thick and the thin samples. We speculate that the resistivity observed here is lower than bulk ampule synthesized TbAs due to an improvement in purity but note that previous reports do not include carrier concentration and mobility, making comparisons inconclusive.[84, 39] Both samples have minimal variation in resistivity over the temperature range measured, indicating that the TbAs films are degenerately doped. The bottom graph in Fig. 4.9 shows that the films have large carrier concentrations that do not significantly change with temperature. This also indicates the TbAs films are degenerately doped. Note that in addition to the resistance and electron concentration having a thickness dependence,

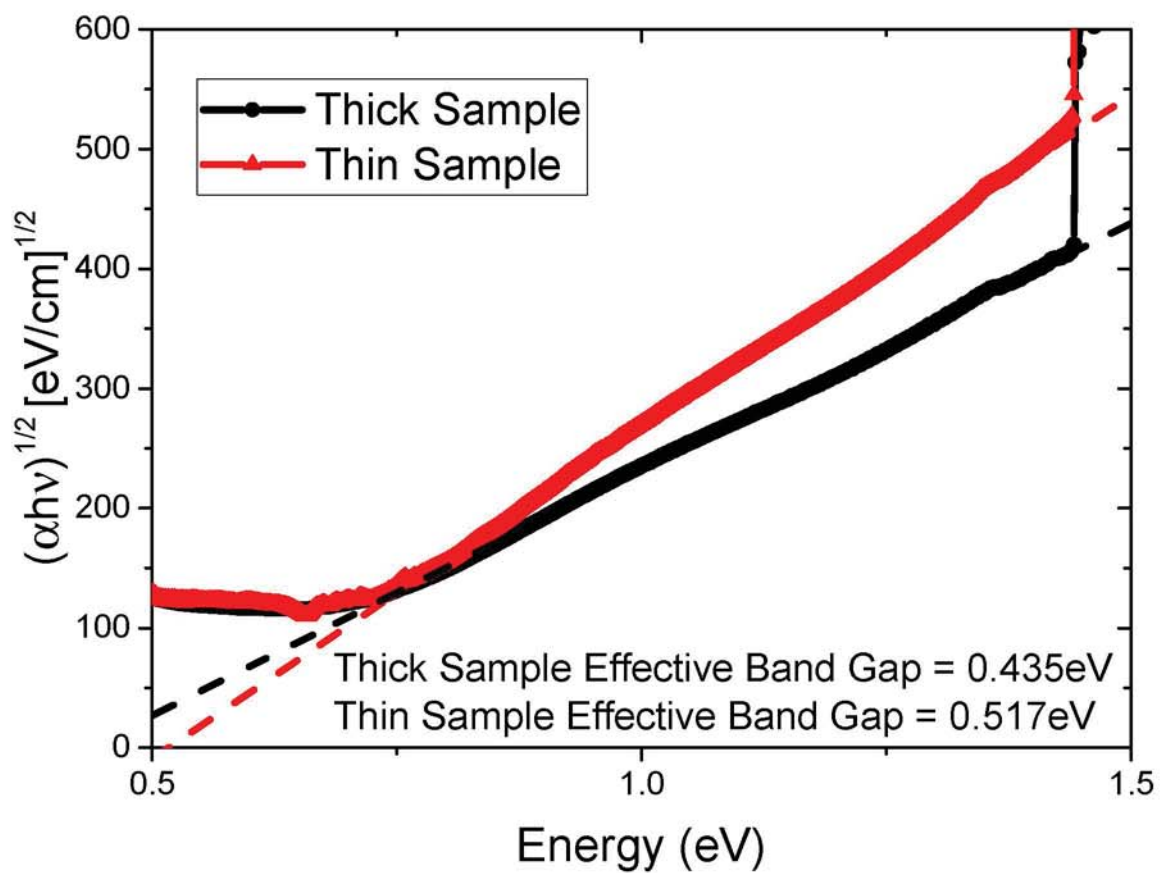


Figure 4.8: Indirect Tauc plot for the TbAs thick and thin samples, revealing an optical absorption of 435 meV and 517 meV, respectively. The solid lines show the measured data, dashed line show the linear fits used to obtain the optical band gap.

the resistivity and sheet concentration also depend on thickness, indicating that the properties measured here are of the film and not a 2-D charged interface region. Finally, both films have mobilities of ~ 25 cm²/V-s that does not significantly change with temperature, see Fig. 4.10. The low mobility is likely due to the mosaic character seen by RSM and the degraded morphology observed with RHEED. Note, as the film grows, the degraded surface morphology, observed with RHEED, would likely cause a degraded film morphology and ultimately lower mobility. Again, the mosaic character and the degraded surface morphology observed with the RSM and RHEED are likely due to lattice mismatch between the TbAs film and GaAs substrate.

The degenerate doping, and different level of doping in each sample, explains the results seen in absorption measurements. Degenerate doping causes a Burstein-Moss shift in the measured band gap; the thin sample has $\sim 4\times$ more free carriers than the thick sample, resulting in a larger Burstein-Moss shift and larger increase in the measured optical band gap. Additionally, the degenerate doping explains the constant, finite, absorption below the band gap; the presence of free carriers allows for the absorption of light with sub-band gap energy.

The higher carrier concentration in the thinner sample also suggests that carriers are coming from interface states due to the increased interface/surface to bulk state ratio in the thinner sample. This was previously proposed for ErAs nanoparticles and LuAs films.[150, 35] Additionally, in the ErAs:GaAs nanocomposite system, decreasing the nanoparticle size results in an increased carrier concentration.[142] This observation is consistent with the theory that carriers are coming from intrinsic interface states due to crystal structure changes and not only defects at the interface.

Carriers coming from interface states matches with the idea proposed by Professor Anderson Janotti based upon the chain model. The chain model states that an interface between a LN-V film and III-V film will be terminated with group III atoms, shown in Fig. 4.11. The chain model has been theoretically modeled and experimental observed.[82, 151, 18] In the III-V film, the group III layers want to give away electrons and the group V layers want to receive electrons, denoted at $+\delta$ and $-\delta$ in Fig. 4.11.

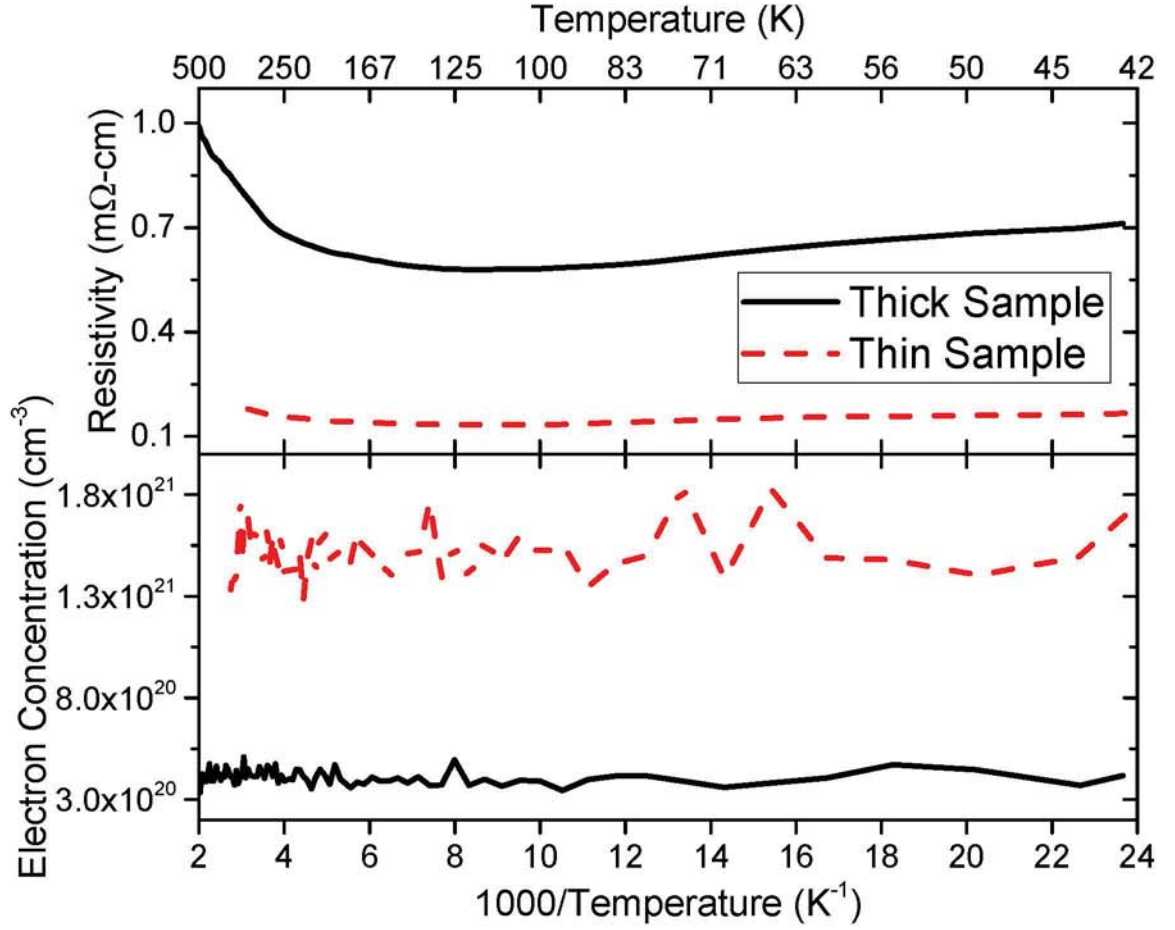


Figure 4.9: The resistivity (top) and free electron concentration (bottom) of both the thick and thin TbAs samples does not change significantly over the temperature range measured.[28]

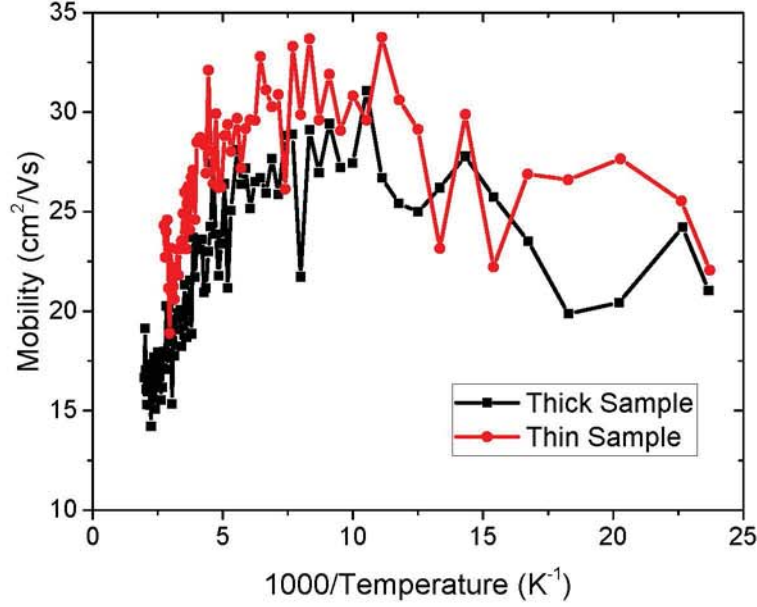


Figure 4.10: The mobility of both the thick and thin TbAs samples is ~ 25 cm²/V-s and does not change significantly over the temperature range measured.

Thus, the group III layers donate half of the electrons to the group V layer above and half of the electrons to the group V layer below, shown as $+\frac{1}{2}\delta$ in Fig. 4.11. This results in a net neutral charge in the bulk of the III-V film. In the chain model the surface of the III-V film is terminated with group III atoms, and thus wants to donate $+\frac{1}{2}\delta$ to the layer of atoms above. The LN-V film, unlike the group III-V, has charge neutral layers. Thus, the donation of $+\frac{1}{2}\delta$ from the interface group III layer adds to the carriers in the LN-V film coming from the interface states. [152]

4.5 TbAs Drude Edge

Additional optical characterization was performed with Fourier transform infrared spectroscopy (FTIR), Fig. 4.12. Note these films are optically thin and the simultaneous change in thickness and carrier concentration makes interpreting and modeling these results difficult and ultimately prevents the extraction of the TbAs optical properties. However, the reflection and transmission measurements, normalized to gold and air respectively, show a possible Drude edge at ~ 2.75 μ m where the reflection

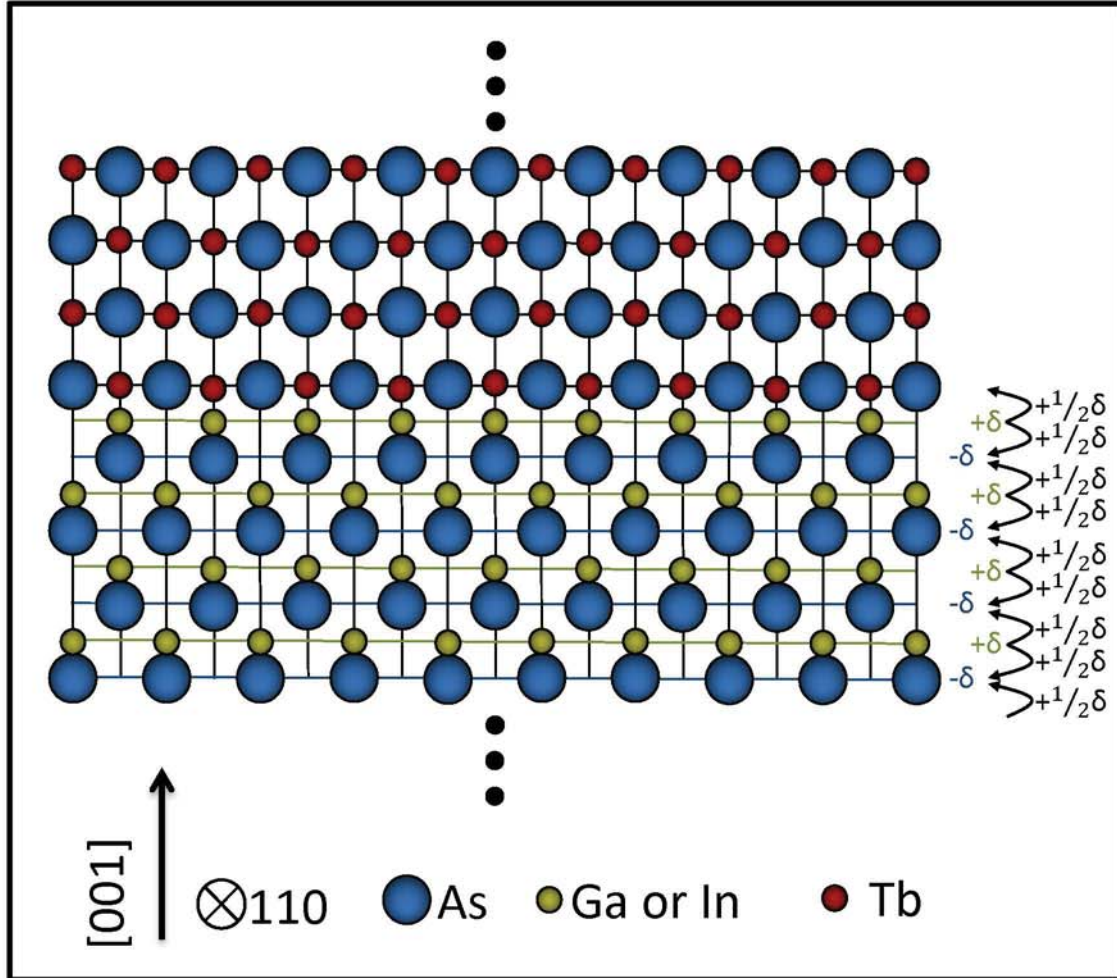


Figure 4.11: A schematic showing that group III atoms want to donate electrons while group V atoms want to accept the electrons. In the rock salt crystal structure, this results in planes of group III atoms giving electrons to the planes above and below of group V atoms. The LN-V film has mixed planes of LN and group V atoms. Thus, the extra atoms from the interfacial group III atoms adds carriers to the LN-V film.

trends toward 100% and transmission toward 0%. Note, as expected the thin sample has a higher transmission than the thick sample. The Drude edge does not significantly change with thickness or carrier concentration. Previous work on other LN-V shows a trend that films with low resistivity have a short wavelength Drude edge; TbAs does not follow this trend. The potential Drude edge observed in TbAs is similar to that of LuAs and ErAs, while having a resistivity closer to LaAs.[35, 105, 106, 75, 76, 39, 16] Note LuAs and ErAs have a lower resistivity than TbAs, and LaAs has a longer Drude edge wavelength than TbAs. We compare resistivities because LaAs, LuAs, and ErAs are semimetals and comparing carrier concentrations is limited by the challenges associated with measuring a semimetal's carrier concentration. The differences seen here could be due to multiple effects, including differences in carrier concentrations and band structure. The variety of Drude edge wavelengths and resistivities among the LN-V materials provides an opportunity to tune the optical and electrical properties of ternary LN-V alloy films.[76, 106] The unique properties of TbAs allows for a wider range of properties in future ternary and quaternary LN-V alloys.

4.6 Conclusion

Previous work shows LN-V provide a wide range of accessible material properties. This work on MBE grown TbAs films further expands upon the range of properties available. We show that TbAs, unlike many other LN-V, is a degenerately doped semiconductor with the optical band gap determined by the doping level. Thickness and temperature dependent Hall effect measurements show the films are degenerately doped and suggest that carriers are coming from interface states. Note that carrier generation at the TbAs film GaAs substrate interface cannot be distinguished from generation at the TbAs film GaAs capping layer interface. Finally, we show that TbAs has a possible Drude edge similar to other LN-Vs' that have significantly lower resistivities. The properties of TbAs discussed within this chapter are significantly different from other LN-Vs, adding to the properties available via LN-V for future applications.

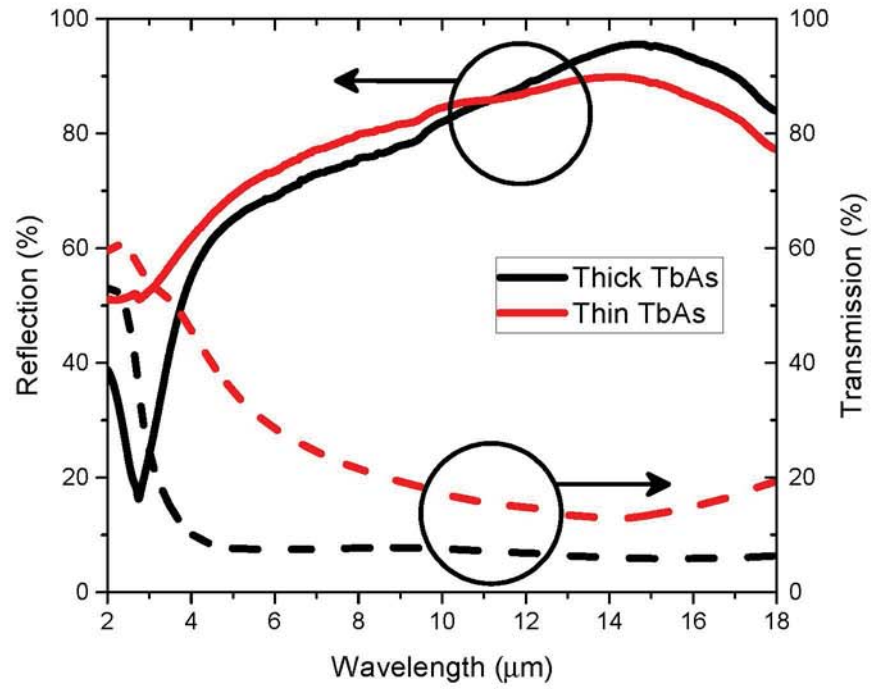


Figure 4.12: Reflection (solid lines) and transmission (dashed lines) measurements of the thick and thin TbAs samples show a possible Drude edge at $\sim 2.75 \mu m$. [28]

Chapter 5

GROWTH AND CHARACTERIZATION OF ErAs:GaBiAs

As discussed in Chapter 1, lanthanide monpnictide nanoparticles epitaxially embedded within III-V semiconductors are of great interest for a wide range of applications; one of those applications is terahertz spectroscopy and imaging. Terahertz (THz) spectroscopy and imaging is of great interest for applications including security, astronomy, medicine, and semiconductor characterization.[153, 154, 155] One method of THz generation and detection utilizes photoconductive (PC) switches.[156, 157] Photoconductive materials must possess (1) a band gap compatible with the excitation source, (2) high dark resistance, (3) high carrier mobility, and (4) short carrier lifetimes.

PC switches made from ErAs:GaAs outperform other state of the art PC switches, due in part to the short lifetimes provided by ErAs nanoparticles.[124, 68] Unfortunately, the band gap of ErAs:GaAs limits the system to being pumped with large and expensive Ti:sapphire regenerative amplifier lasers. To make robust, portable, and inexpensive THz systems, PC switches pumped with smaller fiber-coupled lasers are desired. Changing the matrix material to $\text{In}_{0.53}\text{Ga}_{0.47}\text{As}$ allows for pumping with $1.55\text{ }\mu\text{m}$ fiber-coupled lasers. However, co-doped ErAs nanoparticles pin the Fermi level above the conduction band, leading to low dark resistance.[23] ErAs nanoparticles in a superlattice structure and/or the use of compensation doping can move the Fermi level below the conduction band,[125, 42, 99, 126] but these approaches add the complexity of balancing the nanoparticle spacing for optimal performance, significantly increases the growth time, and have had limited success.[108, 142] R. Salas et al. have shown promising results of incorporating other lanthanide monpnictides (LN-V)

particles.[11] However, some LN-V materials, particularly TbAs, are semiconductors that saturate under high fluences, leading to slow recovery times.[27, 26]

To avoid the challenges faced with 1.55 μm fiber-coupled PC switches, we target a system compatible with 1064 nm fiber lasers. This is done by reducing the band gap of GaAs by adding Bi which, according to the valence band anti-crossing model, causes the valence band to split into E+ and E- valence bands, resulting in favorable ErAs:GaBiAs energy levels for PC switches.[158, 159, 160, 161]

In this chapter I will present my work towards achieving a fiber-coupled PC switch through the ErAs:GaBiAs system. Throughout this chapter I will refer to two sets of samples, samples with droplets and samples without droplets. The droplet samples refer to the first attempted growth of these materials, whereas discussed below in more detail, the arsenic flux used was too low and Ga droplets formed on the surface. The samples without droplets were the second attempt at growing these materials. The samples without droplets demonstrate properties that are promising for PC switches. The comparison of these two sets of samples demonstrates the importance in using the optimum growth conditions and how a lower film quality can drastically change the measured optoelectronic properties. In each section I will first present the results from the non-droplet samples, as these samples are the ones that possess the properties desired for a PC switch, then present the results, when applicable, for the droplet samples and compare the two sets of samples. In Section 5.1 I will discuss the growth of ErAs:GaBiAs films and determining the film compositions. Section 5.2 discusses the band gap of the materials. The films relaxation and morphology are studied in Section 5.3. Section 5.4 demonstrates that a high dark resistances and high carrier mobilities, which are desired for PC switches, are achievable with ErAs:GaBiAs. The measurement of the charge carrier lifetimes by optical pump optical probe are presented in Section 5.5. Finally, Section 5.6 summarizes this chapter. The contents of this chapter are adapted from a manuscript that was written by the author and is currently under review for publication.[29]

5.1 Growth of ErAs:GaBiAs

For this work, two sets of ErAs:GaBiAs samples were studied. The first set grown was grown under Ga rich growth conditions, resulting with Ga droplets on the surface. The second set grown was grown under near stoichiometric but slightly group V rich growth conditions, resulting in films without droplets.

The set of samples without droplets consists of eight co-deposited ErAs:GaBiAs samples with varying amounts of Er and Bi. Figure 5.1 shows the samples without droplets as a function of Bi beam equivalent pressure (BEP) and Er effusion cell output power. Note that the sample are labeled based on relative amounts of Er and Bi incorporation. All samples were grown on GaAs (001) unintentionally doped substrates in an OSEMI NextGEN solid source MBE equipped with effusion cells for Er, Ga, Bi, and a two-zone valved As cracker source. The As cell's cracking zone was cooled to 650°C to use As₄ for optimal Bi incorporation in GaBiAs.[162] Prior to growth, the BEP of Ga, Bi, and As₄ were measured using an ionization gauge. Due to the low flux of Er, the Er concentration was controlled by the effusion cell's output power and calibrated post-growth with Rutherford backscattering spectroscopy. Note that at the time these samples were grown the thermocouple in the Er effusion cell was broken and an accurate temperature reading was not possible. Thus the calibration of Er concentration was done with effusion cell output power and not effusion cell temperature. The native oxide on the GaAs substrate was desorbed under an As₄ BEP of $\sim 1.0 \times 10^{-5}$ Torr at 620°C, measured via band edge thermometry. After oxide desorption, the substrate temperature was lowered to 530°C and a 250 nm GaAs buffer layer was grown. Then, a ten minute growth interrupt was used to cool the substrate temperature to 300°C and halve the As₄ BEP. This was followed by $\sim 2 \mu\text{m}$ film growth.

The composition of the films were determined using high-resolution X-ray diffraction (XRD), Rutherford backscattering spectroscopy (RBS), and band gap measurements from spectrophotometry. High-resolution XRD (004) $\omega - 2\theta$ scans of the *No Er Low Bi* and *No Er High Bi* samples show Bi concentrations of 2.6% and 5.3%, respectively, see Fig 5.2. ErAs nanoparticles cause a superdilation of the GaAs lattice,

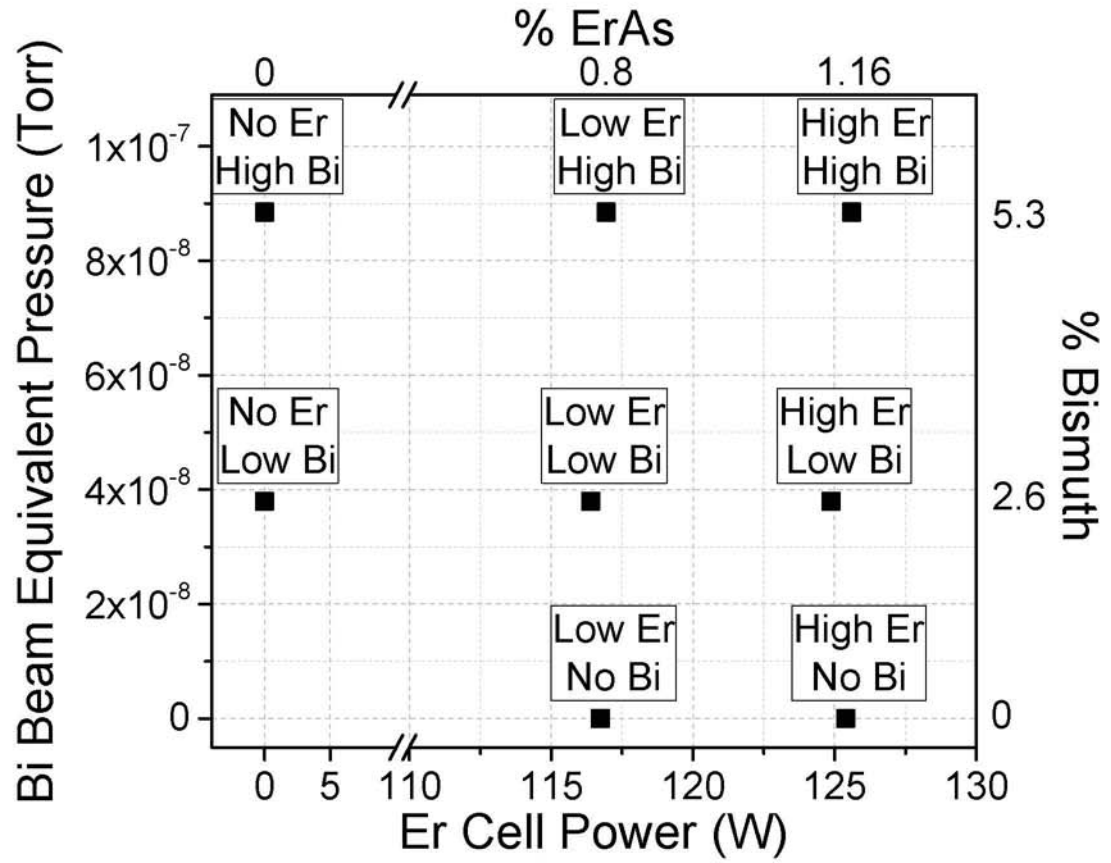


Figure 5.1: Graph showing the Bi and Er growth conditions, samples are identified by relative amounts of Er and Bi in the samples without Ga droplets. ErAs and bismuth concentrations are determined by characterization methods discussed below.[\[29\]](#)

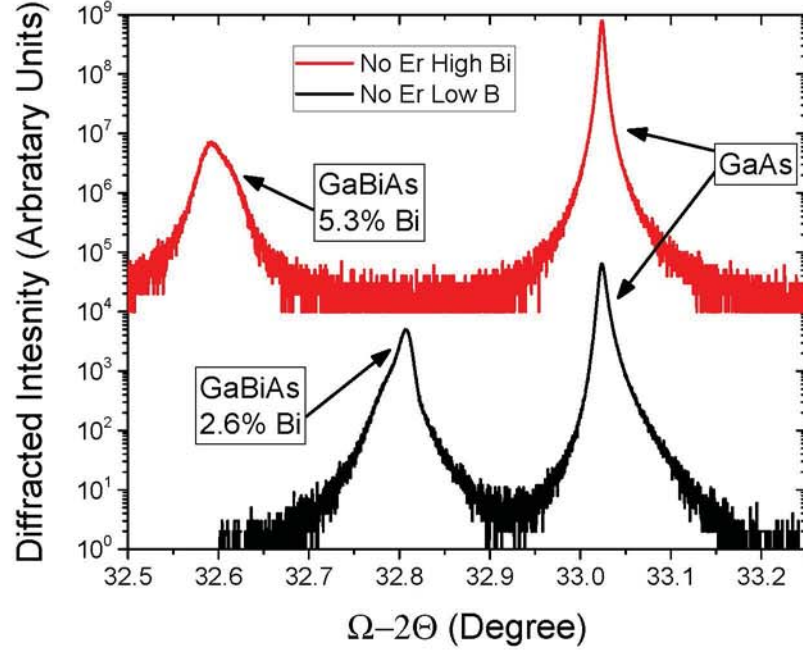


Figure 5.2: $\omega - 2\theta$ scans of the *No Er Low Bi* and *No Er High Bi* samples show Bi concentrations of 2.6% and 5.3%, respectively.

preventing the use of XRD to determine Er concentration. Instead, RBS analysis of samples *Low Er No Bi* and *High Er No Bi* determined ErAs concentrations to be 0.8% and 1.6%, respectively. The amount of Bi and Er in samples *Low Er No Bi*, *Low Er High Bi*, *High Er Low Bi*, and *High Er High Bi* could not be accurately discerned from XRD, due to superdilation; or from RBS, because Bi and Er have similar heavy atomic masses. Instead, compositions were approximated based on the similar growth conditions of samples *No Er Low Bi*, *No Er High Bi*, *Low Er No Bi*, *High Er No Bi*. To summarize, Bi BEP of 3.8×10^{-8} Torr and 8.85×10^{-8} Torr corresponds to 2.6% and 5.3% Bi incorporation, respectively; Er cell powers of 116 W and 125 W corresponds with 0.8% and 1.16% ErAs incorporation, respectively. The amount of Bi was also determined by the reduction of the band gap, discussed more in Section 5.2.

The set of samples with droplets consists of eight co-deposited ErAs:GaBiAs samples with varying amounts of Er and Bi, Fig. 5.3 shows Bi beam equivalent pressure (BEP) and ErAs concentration for each of the samples. Note that this set of

samples are also labeled based on the relative amounts of Er and Bi but have the word *droplet* at the front of the name to indicate the sample belongs to the set with droplets on them. These samples were also grown on GaAs (001) unintentionally doped substrates in an OSEMI NextGEN solid source MBE equipped with effusion cells for Er, Ga, and Bi, and a two-zone valved cracker source for As₂. For the droplet samples, the As cell's cracking zone temperature was 850°C resulting in As₂. At the time of growth of the droplet samples I did not fully understand how beneficial As₄ was for Bi growths. Again, prior to growth, the BEP of Ga, Bi, and As₂ were measured using an ionization gauge. The native oxide on the GaAs substrate was desorbed under an As₂ overpressure of 1.0×10^{-5} Torr at 620°C, measured via band edge thermometry. For the Bi containing samples, after the oxide desorption, the substrate temperature was lowered to 530°C and a 250 nm GaAs buffer layer was grown. A growth interrupt was used to further cool the substrate temperature to 300°C and the As₂ beam equivalent pressure (BEP) reduced to 1.26×10^{-6} Torr ($3.5 \times$ the Ga BEP). The growth interrupt was followed by ~ 2 μm growth; note that for the ErAs containing GaBiAs films, Er was co-deposited with Ga, Bi, and As₂. For the non Bi containing samples, after oxide desorption the substrate temperature was reduced to 530°C and a 500 nm ErAs:GaAs layer was grown. The amounts of ErAs in the droplet samples was determined using Rutherford backscattering spectrometry (RBS) measurements of the non-Bi containing samples. The Bi containing films were grown with the same deposition rate of Er as the non-Bi films. Taking into account the enthalpy of formation of ErAs and ErBi,[163, 164] it is unlikely that ErBi would form during co-deposition. Thus, it is expected that ErAs:GaBiAs films have similar amounts of ErAs to the ErAs:GaAs films: 0%, 1.14%, and 2.6%. The Bi concentration was calculated from the samples band gap, discussed in more detail below. After the growth, the Ga droplets were removed by mechanically polishing and cleaning the sample on a hot plate with acetone, methanol, and isopropanol. Most of the measurements discussed below were performed on both as-grown and polished samples; samples that were polished will have the word *polished* at the end of their name. When measurements were performed on both as-grown and

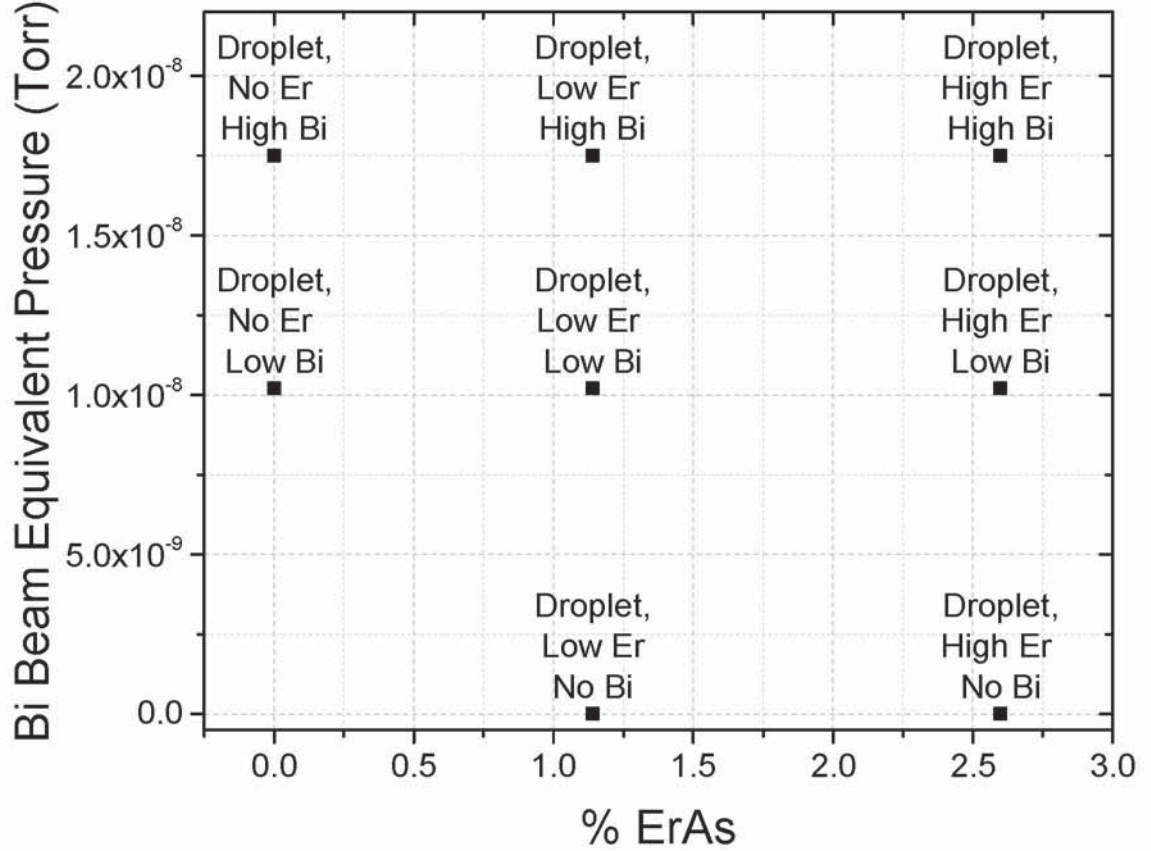


Figure 5.3: The growth conditions for each droplet sample are shown as a combination of Bi beam equivalent pressures of 0, 1.02×10^{-8} , and 1.75×10^{-8} Torr and ErAs concentrations of 0%, 1.14%, and 2.6%. Note that the ErAs:GaAs samples were measured with RBS to calibrate the amount of ErAs in all of the films.

polished samples I will present the results from both measurements to show that growing group III rich, resulting in Ga droplets, not only changes the surface properties but also the entire film's properties.

5.2 Band Gap of ErAs:GaBiAs

To determine the band gap of the non droplet samples, the first required property of PC switches, absorption measurements were done by spectrophotometry. Transmission and reflection spectra collected with a Perkin-Elmer Lambda-750 UV-Visible-IR Spectrophotometer fitted with an integrating sphere were used to create direct gap

Tauc plots, inset in Fig. 5.4. Details on spectrophotometry and band gap measurements are explained in detail in Chapter 2 Section 2.5. The amount of bismuth required to achieve the measured band gaps was calculated using a previously developed valence band anti-crossing model,[30] and closely matches the compositions measured here via XRD. The measured band gaps (in wavelength) and corresponding Bi composition are shown as a bar chart in Fig. 5.4. We have incorporated enough Bi for a PC switch to be pumped with a 1064 nm fiber-coupled laser and show tunability of band gaps from 873 nm to 1212 nm. With the incorporation of $\sim 7.5\%$ Bi, which others have exceeded, a 1330 nm laser could be used.[165, 166]

Figures 5.5 (a) and (b) show direct gap Tauc plots for the droplet ErAs:GaBiAs samples as-grown and mechanically polished, respectively. The band gaps determined from the Tauc plots are shown in Fig. 5.6(a) and (b), respectively. In Fig. 5.6(a) and (b) the right y-axis shows the Bi concentration of each sample, again calculated using the valence band anti-crossing model developed by J. P. Petropoulos et al.[30] From Fig. 5.5 (a) and (b) and Fig. 5.6(a) and (b), it is clear that the gallium droplets on the surface increased the absorption during the spectrophotometry measurement. This lead to the appearance of an increased bismuth incorporation and a reduction in band gap. Additionally, it is apparent that the Ga rich growth of GaBiAs in the presence of Er increases the bismuth incorporation.

Comparing the Tauc plots for the ErAs:GaBiAs samples without droplets, inset Fig. 5.4, and that obtained for the droplet ErAs:GaBiAs samples, Fig. 5.5, it is clear that growing Ga rich drastically changes the absorption properties of the film even after the droplets are removed. In addition to the droplets on the surface, growing Ga rich likely caused defects within the film. These defects likely caused increased absorption, below the band gap, shown as increased curvature to the Tauc plots, Fig. 5.5. This increased curvature in the Tauc plot increases the error in the estimation of the band gap. As a result, the band gaps calculated for the ErAs:GaBiAs samples are likely too small, and subsequently the calculated amounts of Bi incorporated are likely too large. This is evident when comparing the band gap and growth conditions of the two

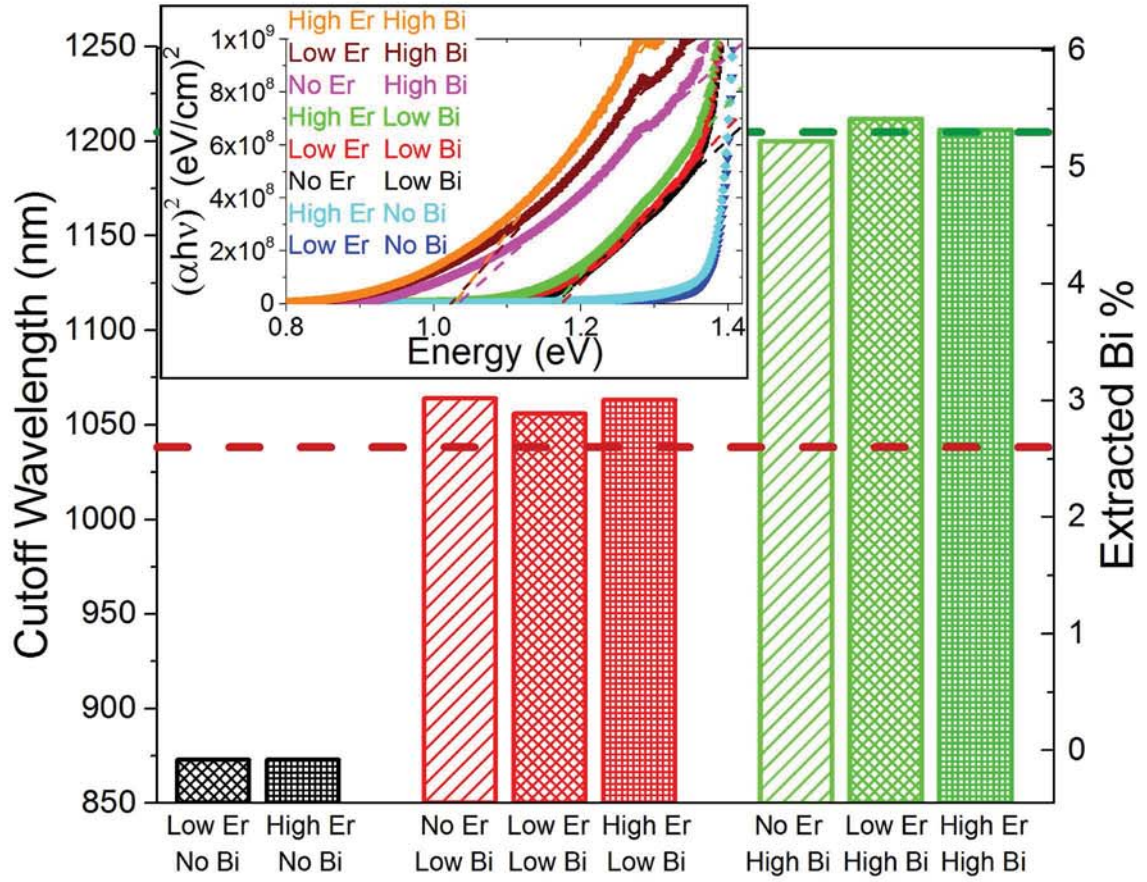


Figure 5.4: The band gap obtained from the Tauc plot (inset) and bismuth concentration (calculated using a previously developed model[30]) for the samples without droplets. The dashed lines represent Bi concentrations obtained from XRD. The inset is the direct gap Tauc plot where the symbols show the measured data and the dashed lines are the linear fits used to extrapolate the band gaps.[29]

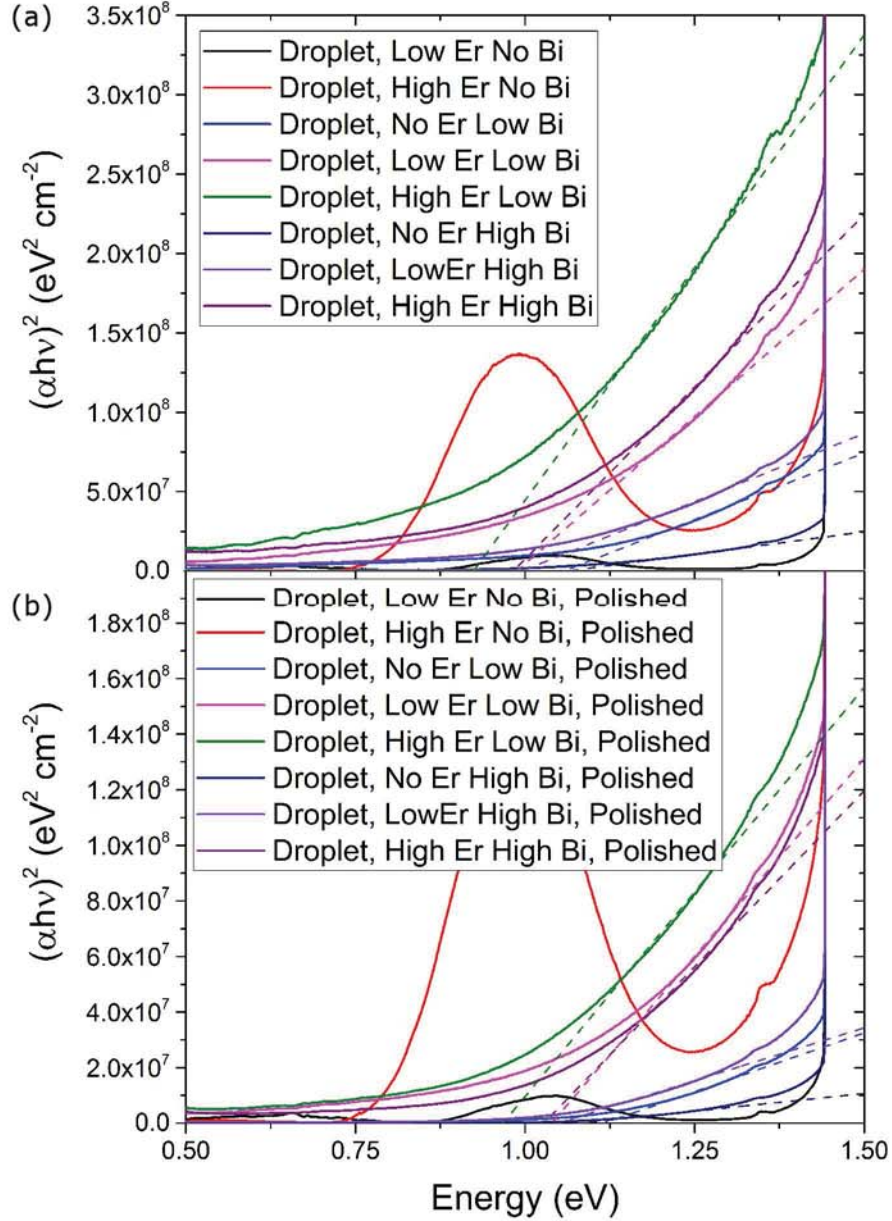


Figure 5.5: Tauc plots of the ErAs:GaBiAs samples with droplets, as-grown (a) and mechanically polished (b). The solid lines represent the measured data while the dashed lines represent the linear fit used to extrapolate the band gap. Note that samples *Droplet, Low Er No Bi* and *Droplet, High Er No Bi* did not have Ga droplets and thus were not mechanically polished. The peaks present in samples *Droplet, Low Er No Bi* and *Droplet, High Er No Bi* have previously been attributed to surface plasmon resonances from the ErAs nanoparticle.[31, 21] The samples containing Bi do not exhibit this peak as the resonance is likely to have been suppressed from absorption in the GaBiAs layer or shifted to energies outside our detection range.

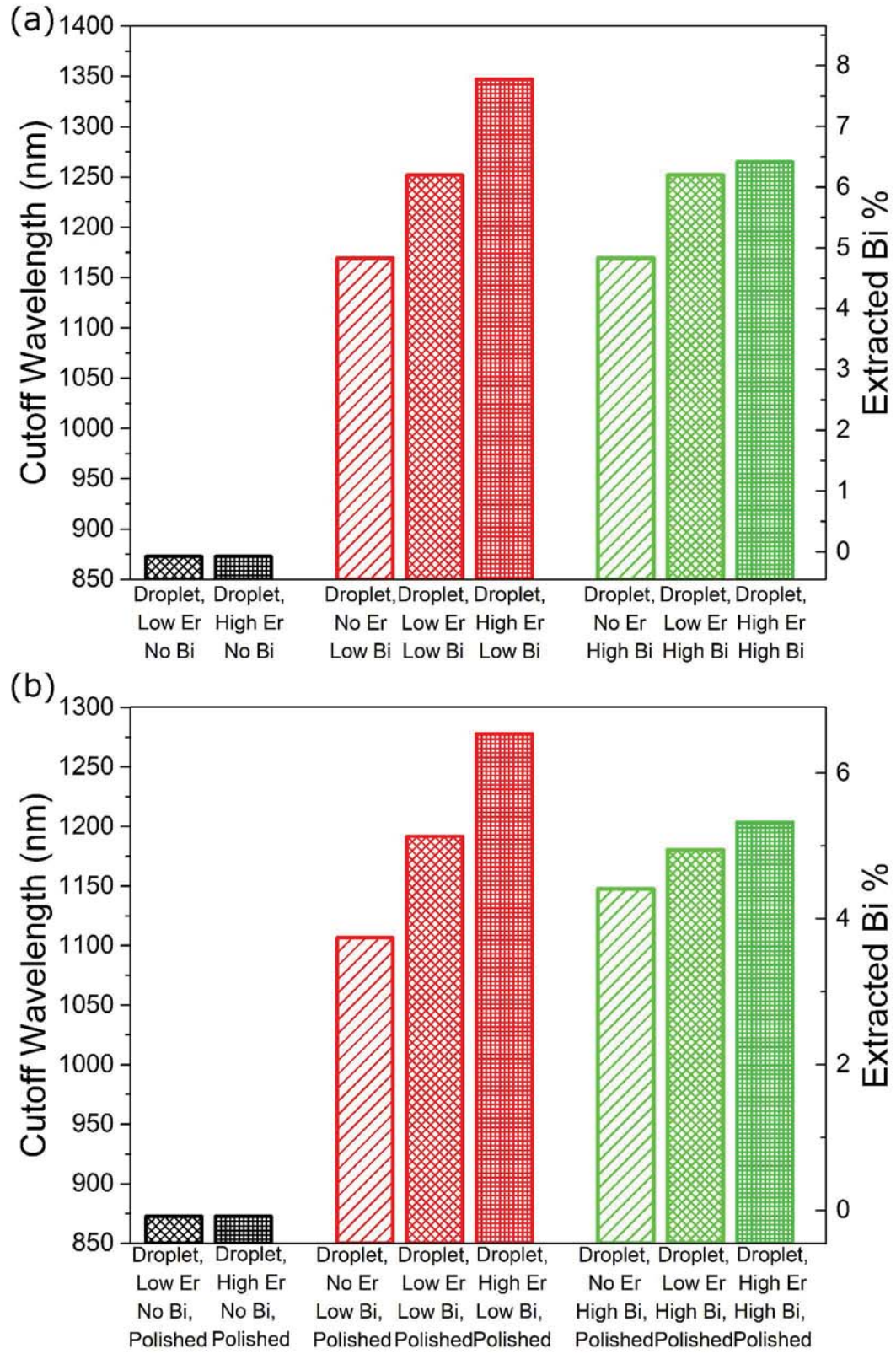


Figure 5.6: Bar chart showing the band gap of the ErAs:GABiAs samples with droplets, as-grown (a) and mechanically polished (b) samples.

samples where a significantly higher Bi flux was required to obtain a similar reduction in band gap in the non-droplet samples. The differences described here highlight how important it is to have high quality films for material property measurements, and how easily defects can alter property measurements.

It is worth noting that in the set of samples grown Ga rich, the droplet samples, the ErAs:GaAs samples were grown under normal ErAs:GaAs growth conditions: large As₂ overpressure and growth temperature of 530°C. These samples did not have droplets on the surface, and were thus not mechanically polished. The Tauc plot for these samples, *Droplet, Low Er No Bi* and *Droplet, High Er No Bi*, shows an absorption feature at $\sim 1 \mu\text{m}$. This absorption feature has previously been attributed to surface plasmon resonances from the ErAs nanoparticle.[31, 21] This absorption feature is not present in any of the Bi containing films or the ErAs:GaAs films grown with a reduced As₄ flux and at 300°C. This is likely due to changes in the nanoparticle structure and will be discussed in slightly more detail in Section 5.3.

5.3 Film Relaxation and Morphology

As discussed above, ErAs:GaAs films grown under typical growth conditions (growth temperatures of $\sim 535^\circ\text{C}$ with large As₂ over pressures) show a nanoparticle absorption feature around $2.5 \mu\text{m}$ that is not present for the Bi containing films or the ErAs:GaAs films grown with a low As₄ pressure and at a growth temperature of 300°C that are studied in this chapter.[31] This is likely due to the significantly different growth conditions. Previous reports with growth temperatures of 480 - 630°C for co-deposited ErAs:GaAs and 320 - 630°C for growth interrupt ErAs:GaAs indicate that lower growth temperatures result in smaller nanoparticles.[59, 167] Thus, the growth conditions used here can significantly alter the size of ErAs nanoparticles and change the absorption feature's energy. Cross-sectional transmission electron microscopy (TEM) used to further investigate the growth condition effects on the ErAs nanoparticle size was inconclusive. Figure 5.7 shows selected cross-sectional TEM images and diffraction patterns for the *Low Er No Bi* and *Low Er Low Bi* samples. In

Fig. 5.7 there are not clear nanoparticles, but there are areas of contrast that could be due to nanoparticles. Additionally, TEM only samples a small selection of the sample and clear nanoparticles could be located outside of the imaging area. The TEM images do show that the ErAs:GaAs samples have significant twin boundaries, likely caused by cold growth temperatures and a slight As₄ overpressure. The twin boundary density appears to decrease with increasing Bi amounts, again note that TEM only samples a small area and it is possible that we happened to image a section with a lower defect density. The lower twin boundary density is also suggested by the reduced spot elongation in the diffraction patterns, see insets in Fig. 5.7.

The incorporation of Bi into GaAs grown on GaAs can result in a significant lattice-mismatch. Previous reports show that films with large amounts of Bi can remain strained beyond the Matthews-Blakeslee critical thickness when grown at cold temperatures.[160, 168] High resolution XRD reciprocal space mapping (RSM) was used to study the strain and relaxation of the ErAs:GaBiAs films without Ga droplets, a representative selection is shown in Fig. 5.8. RSM of the ErAs:GaAs film, Fig.5.8(a), shows the film remains strained to the GaAs substrate; while the GaBiAs films, Fig. 5.8(b), are partially relaxed with significant elongation of the film peak indicating some mosaic character. Interestingly, the incorporation of Er into the GaBiAs film, Fig. 5.8(c) and (d), allows the film to remain strained to the substrate, with elongation of the peak in the relaxation direction. Sample *High Er High Bi* shows a second, partially relaxed, peak. One possible explanation is that ErAs nanoparticles act as a location for the strain energy to be reduced. In the higher bismuth containing samples, there is not enough ErAs to allow the entire film to be strained, causing localized partially relaxed sections and localized strained sections within the film.

As mentioned above, the first attempted growth of the ErAs:GaBiAs samples had droplets on the surface. This was first suspected when the samples were removed from the MBE and the surface was not specular. Scanning electron microscopy and energy dispersive spectroscopy (EDS) reveal that the surface was covered in Ga droplets. This suggests that growth occurred group V deficient. Note that the Er atoms sit on

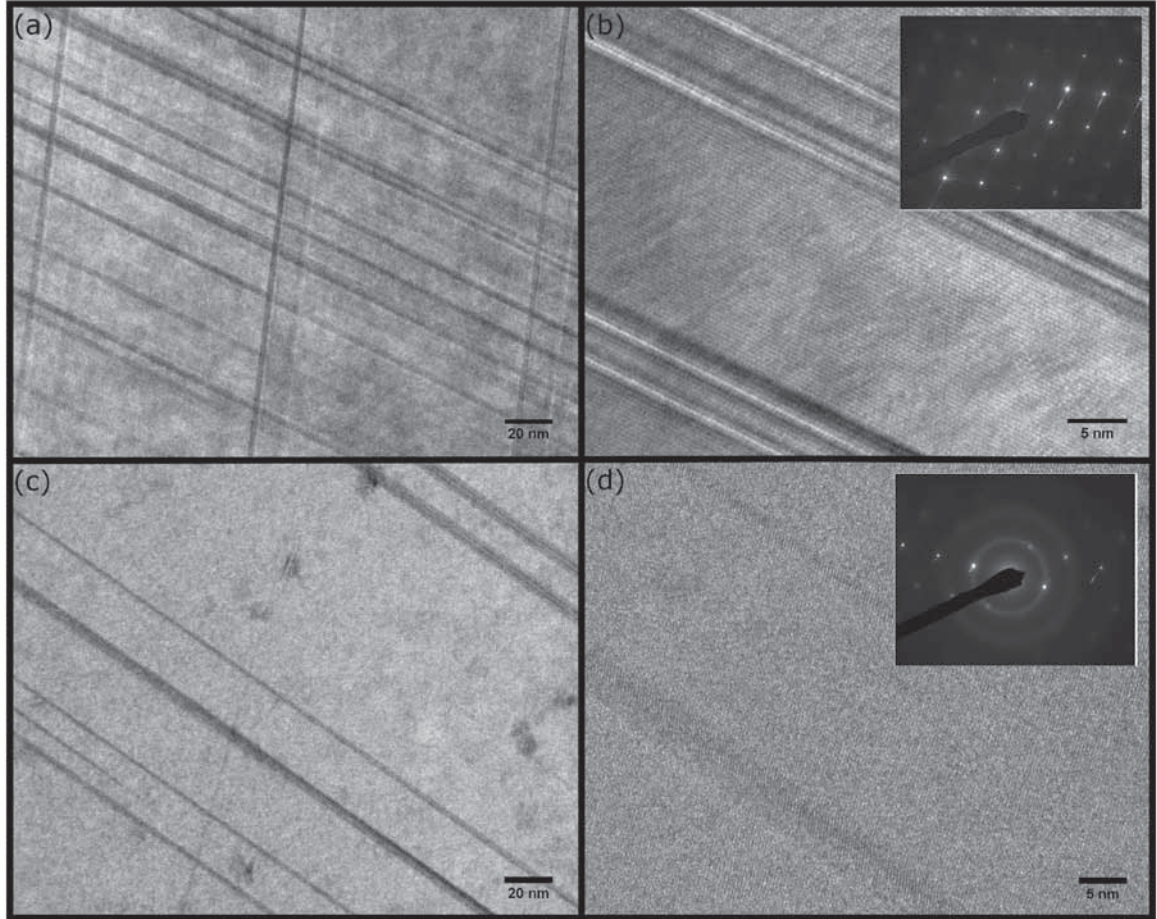


Figure 5.7: Select cross sectional transmission electron microscopy (TEM) images of the ErAs:GaBiAs samples without droplets, (a) is a selection from sample *Low Er No Bi* with (b) zoomed in, (c) shows a selection from *Low Er Low Bi* with (d) being further zoomed in. The insets in (b) and (d) are the diffraction patterns for the *Low Er No Bi* and *Low Er Low Bi* samples, respectively. It is unclear from the images whether or not ErAs nanoparticles formed, but both the micrographs and diffraction patterns suggest that the Bi containing samples have a lower density of twin boundaries.

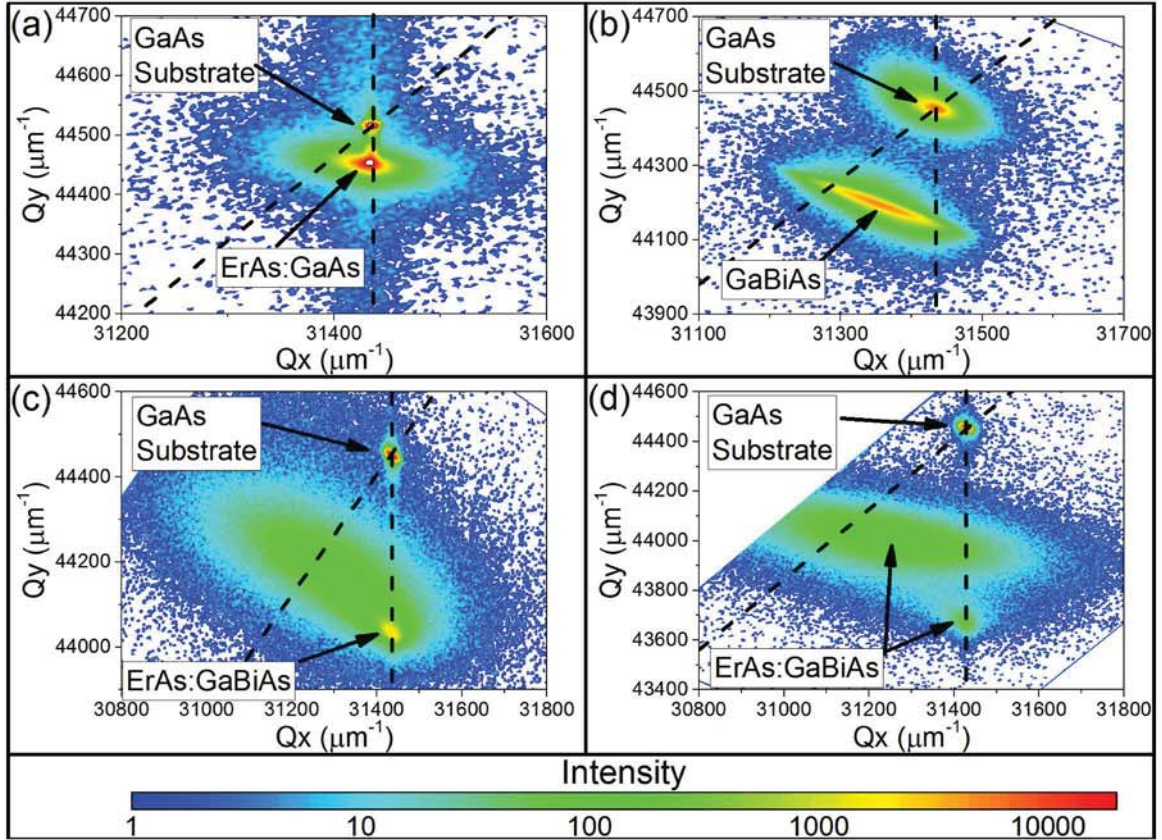


Figure 5.8: Reciprocal space maps (RSM) of samples (a) *High Er No Bi* (b) *No Er Low Bi* (c) *High Er Low Bi* and (d) *High Er High Bi* with the vertical dashed line showing the strained line and the angled dashed line showing the relaxation line.[29]

the group III sites, thus the ErAs:GaBiAs samples were grown with a larger group V deficiency than the GaBiAs samples, resulting in both larger Ga droplets and a higher Ga droplet density. The different density and sizes of droplets are shown in Fig 5.9 (a)-(c), and EDS maps of the Ga droplets are presented in Fig. 5.9 (e), (g), and (h). The Ga droplets were removed by mechanically polishing and cleaning the sample on a hot plate with acetone, methanol, and isopropanol. Figure 5.9(d) shows a SEM image of a polished sample and Fig. 5.9 (f), (i), and (j) shows energy dispersive maps of a polished sample. The rectangular pillars present on the surface after the polish are likely the start of GaAs droplet epitaxy where As₂ molecules diffused through the Ga droplet to form GaAs on the surface. Note that EDS was unable to distinguish the pillars from the surrounding surface. The start of droplet epitaxy is supported by pillar height being ~ 10 nm, measured with AFM, not shown.

Again, the incorporation of Bi into GaAs results in a lattice mismatch with the GaAs substrate. In the samples without droplets we saw that the GaBiAs film was partially relaxed but incorporating ErAs provided a location for the strain energy to be reduced. Reciprocal space mapping of the ErAs:GaBiAs droplet samples was used to study the strain and relaxation of the GaBiAs films and determine if the ErAs can still provide a location for the strain energy to be reduced. Additionally, by comparing the separation between the film peak and the substrate peak in the droplet samples to the samples without droplet also suggests that growing group III rich created defects in the film that increased the absorption of sub-band gap light. Ultimately leading to spectrophotometry overestimating the amount of Bi in the films, discussed in Section 5.2.

Figure 5.10 shows the RSM for the (a) *Droplet, No Er High Bi* and (b) *Droplet, High Er High Bi* samples. From Fig. 5.10(a) it is clear that the $2\ \mu\text{m}$ GaBiAs sample *Droplet, No Er High Bi* remains strained to the substrate. Additionally, the film peak and the substrate peak are not fully separated, indicating that only a little Bi has been incorporated, not the $\sim 5\%$ predicted by spectrophotometry. Figure 5.10(b) shows that the $2\ \mu\text{m}$ ErAs:GaBiAs sample *Droplet, High Er High Bi* also remains strained

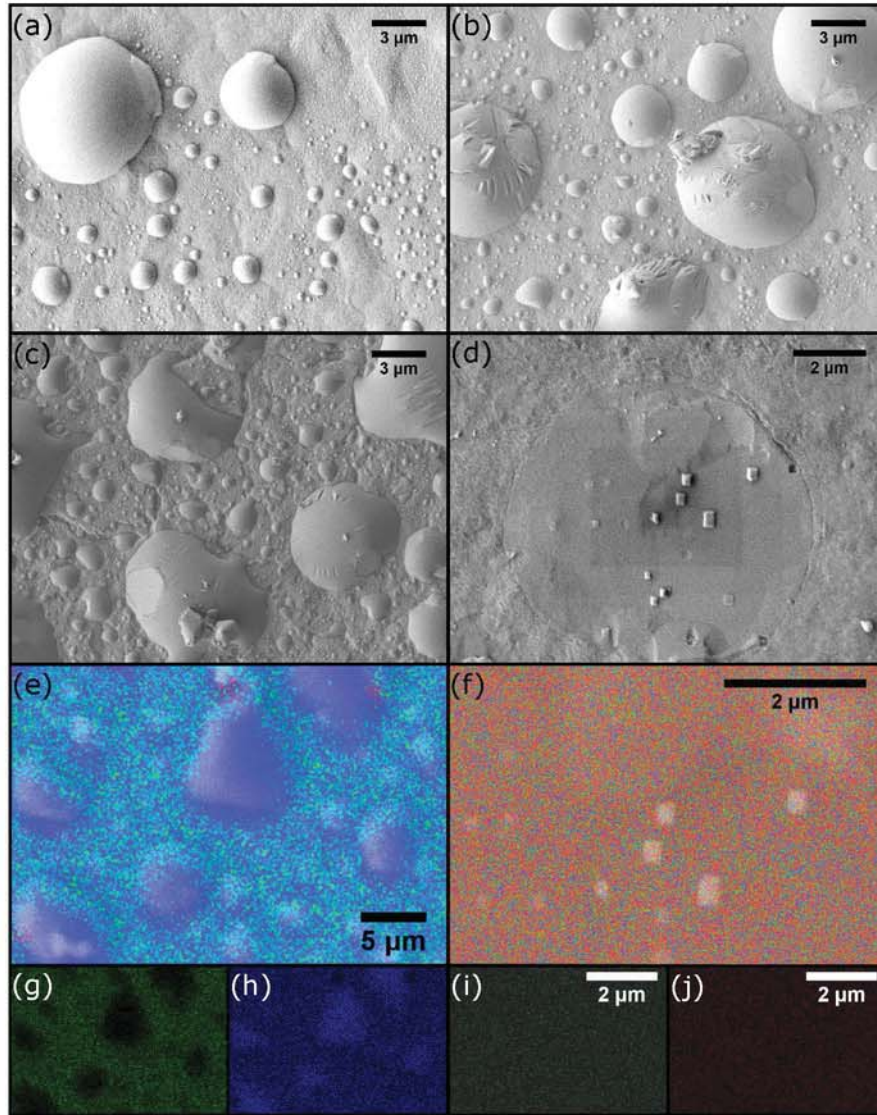


Figure 5.9: A selection of scanning electron microscope (SEM) and energy dispersive spectroscopy (EDS) maps of the ErAs:GaBiAs samples with droplets, both as grown and post polish. SEM images of the as grown (a) *Droplet, No Er High Bi*, (b) *Droplet, Low Er High Bi*, and (c) *Droplet, High Er High Bi* show that increasing the Er amount results in more and larger Ga droplets. The GaAs pillars present after droplet removal are shown for sample *Droplet, Low Er High Bi, Polished*(d). Mixed color EDS map (e) of the *Droplet, High Er High Bi* shows that the droplets are mostly (h) Ga, shown as blue, and lack (g) As, shown as green. Bi and Er are depicted as red and white, respectively. A mixed color EDS map (f) of sample *Droplet, Low Er High Bi, Polished* shows that the pillars are of the same material as the matrix. In (f) white is As, also shown in (i), red is Ga, also shown in (j), Bi is white, and Er is light blue. The inability of the EDS maps to distinguish the pillars from the matrix suggests that the pillars are the start of droplet epitaxial growth.

to the substrate and the low separation between the substrate peak and the film peak again suggests that much less than $\sim 6\%$ Bi was incorporated. The additional low intensity peak in the bottom left hand side Fig. 5.10(b) could be either due to relaxed ErAs nanoparticles or a part of the film ErAs:GaBiAs film that relaxed. The RSMs presented here, which are representative of the other droplet ErAs:GaBiAs samples, show that the films remain strained to the substrate, but only a small amount of Bi has been incorporated in the film. The amount of Bi incorporated, shown by the RSM, are much less than that predicted by spectrophotometry in Section 5.2. Again, this indicates that growing group III rich results in defects in the film that increase sub-band gap absorption in addition to Ga droplets.

5.4 ErAs:GaBiAs Electronic Properties

The next two required properties for PC switches are high dark resistance and high mobility. The dark resistance and mobility of each ErAs:GaBiAs sample without droplets was measured using a custom-built Hall effect system with indium contacts in the van der Pauw geometry, results shown in Table 5.1. The incorporation of ErAs nanoparticles into GaBiAs moves the Fermi level away from the valence band, toward the conduction band, changing the material from p-type to slightly n-type. The Fermi level pinned within the band gap causes high dark resistance and allows for a high mobility. The Bi containing films measured here have resistivities higher than and mobilities comparable to GaBiAs films previously studied for THz generation and detection.[169, 165] Note that the ErAs:GaAs samples, *Low Er No Bi* and *High Er No Bi*, have low mobilities that are likely caused by the unfavorable ErAs:GaAs growth conditions, near stoichiometric III:V flux ratio and low growth temperatures, for ErAs:GaAs.

To show the effect of Ga droplets on the surface of a film, the mobility and dark resistance of each ErAs:GaBiAs samples with droplets was measured as grown and after polishing. Again, the measurements were performed using a custom-built Hall effect system with indium contacts in the van der Pauw geometry. Table 5.2 show the

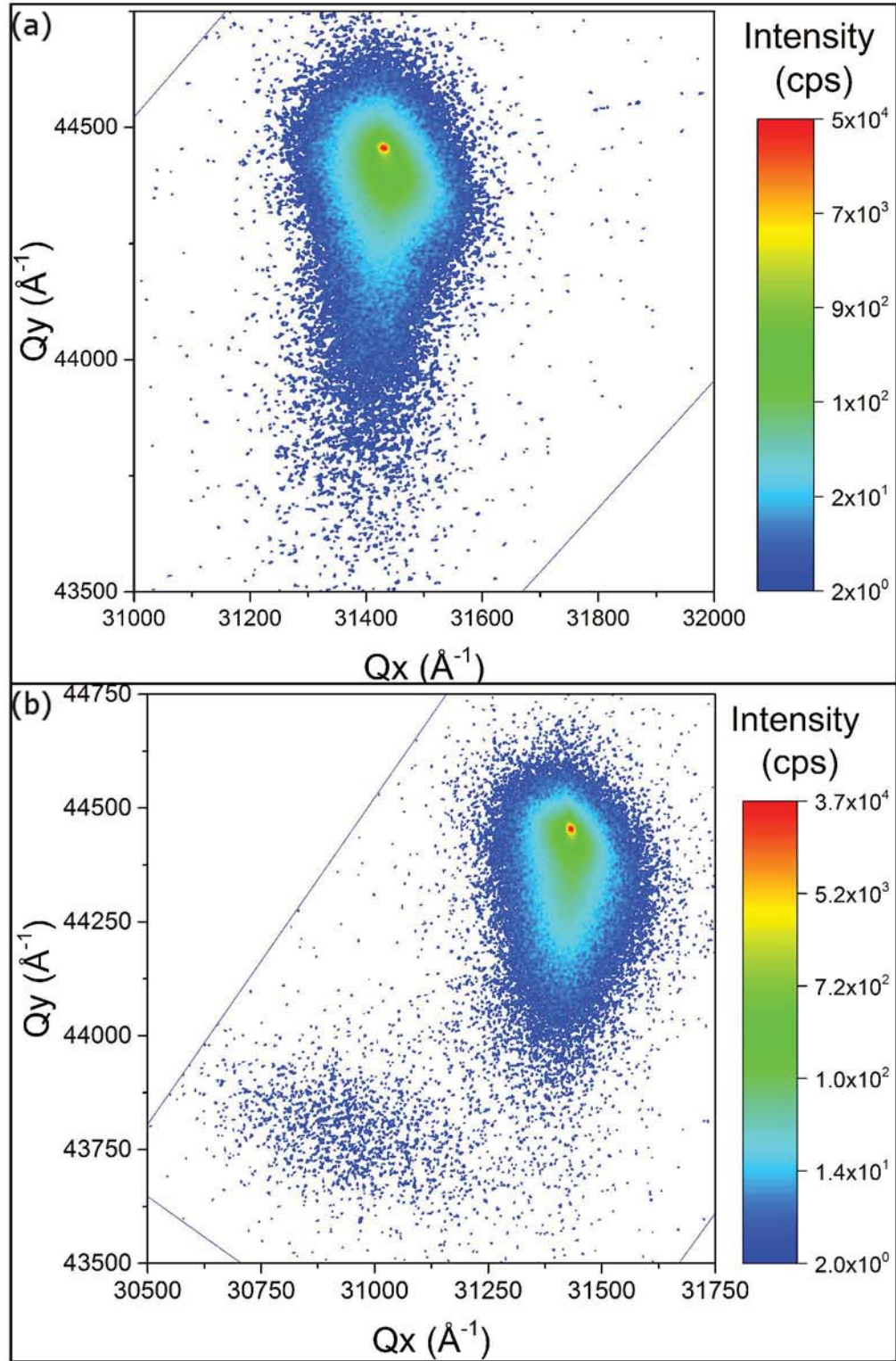


Figure 5.10: Reciprocal space maps (RSM) of samples (a) *Droplet, No Er High Bi* and (b) *Droplet, High Er High Bi* show that the ErAs:GaBiAs samples with droplets remain strained but have significantly less Bi incorporation than predicted by spectrophotometry.

Table 5.1: The majority carrier type, carrier concentration, resistivity, and mobility of the ErAs:GaBiAs samples without droplets depend on the Er and Bi incorporation.

Sample	Carrier Type	Carrier Conc. (cm^{-3})	Resistivity ($\Omega \text{ cm}$)	Mobility ($\frac{\text{cm}^2}{\text{Vs}}$)
<i>Low Er No Bi</i>	N	1.19×10^{15}	1035	5
<i>High Er No Bi</i>	N	5.92×10^{15}	1113	1
<i>No Er Low Bi</i>	P	8.08×10^{12}	2838	272
<i>Low Er Low Bi</i>	N	9.38×10^{12}	3613	184
<i>High Er Low Bi</i>	N	2.95×10^{13}	3129	68
<i>No Er High Bi</i>	P	4.23×10^{12}	2197	671
<i>Low Er High Bi</i>	N	1.13×10^{14}	201	273
<i>High Er High Bi</i>	N	1.41×10^{14}	185	239

resulting majority carrier type, mobility, and resistivity. From Table 5.2 it is clear that the removal of the Ga droplets from the surface, by polishing, increased the resistivity of the ErAs:GaBiAs films while having minimal effect on the mobility. The low mobility in these films is likely due to defects in the material caused by growing group III rich. Note that the incorporation of Er resulted in a larger As deficiency and likely caused the reduction in mobility seen when comparing the droplet GaBiAs samples to the droplet ErAs:GaBiAs samples. Note that the ErAs:GaAs films in Table 5.2 were grown under normal GaAs growth conditions, As₂ rich and at 530°C, which allows for the high resistivity and high mobility.

Comparing the films grown with droplets, Table 5.2, to those without droplets, Table 5.1 shows that growing group III rich causes defects within the film that lower the mobility and growing ErAs:GaAs at low temperatures and a near stoichiometric III:V flux ratio results in defects that increase the resistivity and lower the mobility. The GaBiAs samples without droplets have a significantly higher resistivity and comparable or higher mobility than the GaBiAs sample with droplets, both as-grown and after polishing. This suggests that growing group III rich introduced shallow defects that are trapping carriers; a reduced carrier concentration allows the mobility to remain high while decreasing the resistivity. All of the ErAs:GaBiAs samples have high resistivities, due to ErAs trapping charge carriers, however the droplet samples have a significantly lower mobility than the non-droplet samples. Since the ErAs:GaBiAs samples without droplets have high mobility, the reduced mobility in the droplet samples is likely due to defects introduced by the group III rich growth conditions. Finally, comparing the ErAs:GaAs samples, it is clear that growing cold results in a significantly increased resistivity and decreased mobility. This is likely due to defects caused by excess As incorporation, and behaves similar to low temperature grown GaAs.[170]

5.5 Charge Carrier Lifetimes

The fourth required property for PC switches is short carrier lifetimes, which ErAs provides. Carrier lifetimes of the ErAs:GaBiAs samples without droplets were

Table 5.2: The majority carrier type, mobility, and resistivity of the ErAs:GaBiAs samples with droplets all depend on the bismuth and erbium incorporation as well as the presence of droplets on the surface.

	As-grown			Polished		
Sample	Carrier Type	Resistivity ($\Omega \text{ cm}$)	Mobility ($\frac{\text{cm}^2}{\text{Vs}}$)	Carrier Type	Resistivity ($\Omega \text{ cm}$)	Mobility ($\frac{\text{cm}^2}{\text{Vs}}$)
<i>Droplets, Low Er No Bi</i>	N	596	6,380	-	-	-
<i>Droplets, High Er No Bi</i>	N	789	2,729	-	-	-
<i>Droplets, No Er Low Bi</i>	P	22	267	P	20	295
<i>Droplets, Low Er Low Bi</i>	N	506	7	N	682	8
<i>Droplets, High Er Low Bi</i>	N	1,170	6	N	2,026	13
<i>Droplets, No Er High Bi</i>	P	24	254	P	23	269
<i>Droplets, Low Er High Bi</i>	N	874	8	N	2,230	19
<i>Droplets, High Er High Bi</i>	N	540	7	N	2,040	18

determined using transient absorption optical pump optical probe spectroscopy. Note that I will not discuss the carrier lifetimes of the droplet samples. The large size of the droplets results in a high probability that the measurement would only probe the metal Ga droplet or, in the case of the polished samples, residual metal Ga smeared on the surface would distort the measurement and introduce a large uncertainty in the data analysis. The transient absorption optical pump optical probe spectroscopy measurement technique was discussed in Chapter 2 Section 2.6, the setup for this particular measurements is described in detail elsewhere.[141] Briefly, the measurement is the average of six scans, each done with the pump and probe beams set to 850 and 1300 nm, respectively. Measurements were checked to ensure linearity as a function of pump intensity.

Briefly, the measurement technique works as follows. The optical pump populates the valence band with holes and conduction band with electrons. After a time delay, a weak probe pulse with energy smaller than the band gap strikes the sample. The difference in probe absorption (the probe's absorption after the pump excitation minus the probe's absorption before the pump excitation) is measured as a function of the time delay. The carrier lifetimes are determined by using a relaxation model composed of multiple exponential decays to fit the change in probe absorption as a function of time, shown in Equation 5.1.

$$y = \sum_i A_i e^{\frac{-x}{\tau_i}} + y_0 \quad (5.1)$$

Figure 5.11 shows the change in probe absorption as a function of time after the pump laser with the relaxation models shown as dashed lines, insets are zoomed-in on the first few picoseconds of the measurements. The transient absorption measurement of the ErAs:GaBiAs films show that the system quickly returns to its pre-pump state, which is desired for PC switches. Below, we propose that a combination of up to four relaxation processes occur to return the system to the pre-perturbed state, some of these processes can be seen in the ErAs:GaAs or GaBiAs samples.

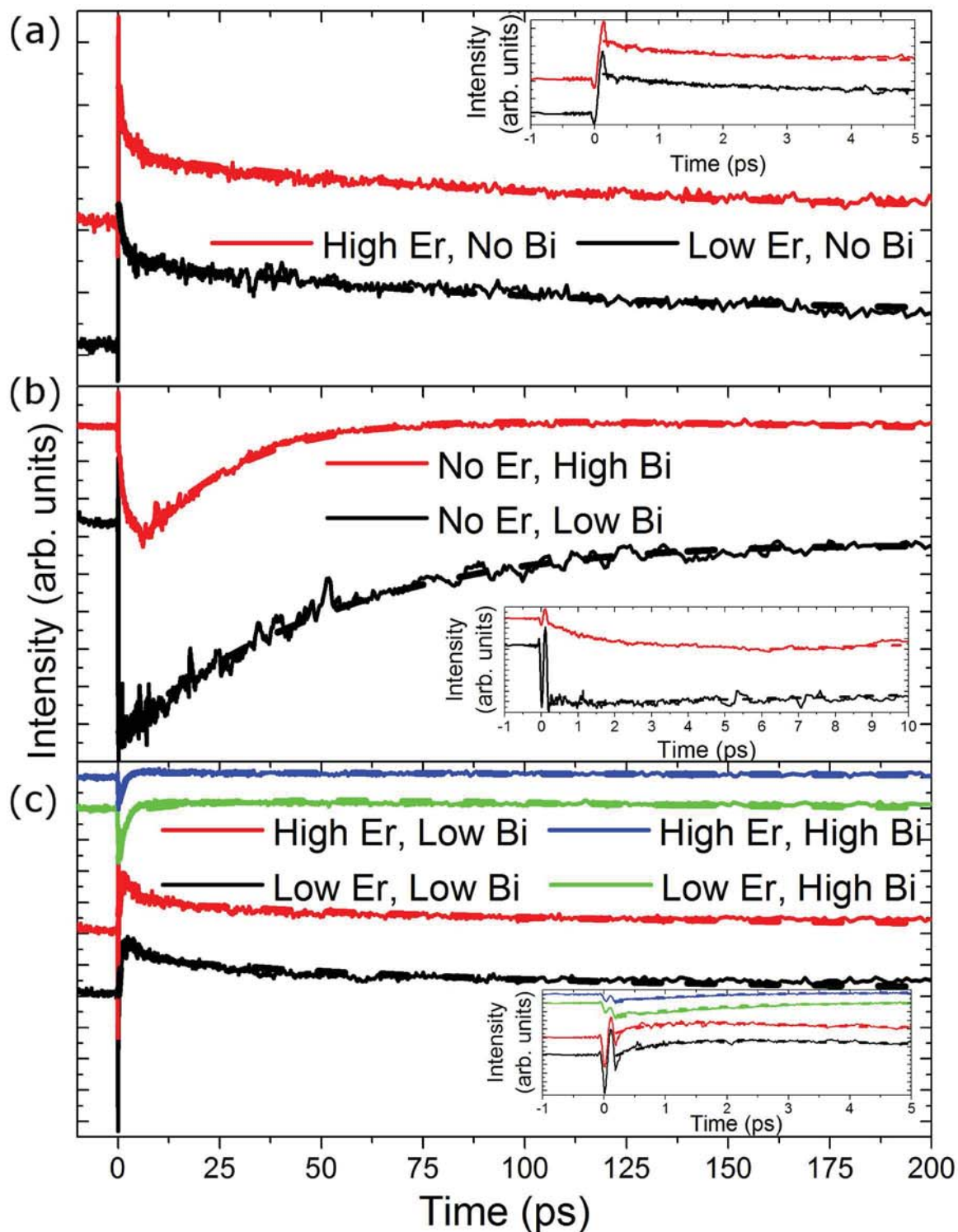


Figure 5.11: Transient absorption optical pump optical probe measurements showing the change in the probes absorption as a function of time after the pump laser. Note that transients have been vertically offset. The insets are a zoomed-in view of the first few picoseconds of each measurement. [29]

The ErAs:GaAs samples, *Low Er No Bi* and *High Er No Bi*, were modeled with a two exponential decay, Fig 5.11(a). The two lifetimes correspond with carrier trapping by the ErAs nanoparticles and recombination across the bulk band gap, see Fig. 5.12(a). [68, 98] The model determined the ErAs trapping time to be ~ 1.3 ps and the recombination time across the bulk band gap is ~ 90.0 ps. The relaxation time across the bulk band gap is lower than that of typical GaAs, likely due to defects introduced by the low growth temperatures.

Both GaBiAs samples, *No Er Low Bi* and *No Er High Bi*, become more transparent after the pump laser strikes the sample, observed as a decrease in absorption, Fig 5.11(b). The pump laser bleaches the E+ valence band states that are formed by the incorporation of Bi. Prior to the pump laser striking the sample, the probe laser was able to be absorbed by exciting electrons from the E+ valence band states into the conduction band tails or shallow defect states. When the pump laser strikes the sample, this transition is bleached. One explanation is that the E+ valence band states are emptied by the pump laser and the electrons are unavailable to absorb the probe laser because they were excited into the defect states by the pump laser. This reduces the probe laser's absorption, shown as a negative intensity. As carriers relax back into the E+ valence band, the change in absorption becomes less negative as the probe laser can be absorbed by again exciting electrons from the valence band into the defect states. This type of bleaching requires the E+ valence band states to be a limited number of states near the E+ valence band maximum and to not form a continuous band with the rest of the conduction band. Alternatively, the probe laser could bleach the E+ valence band to defect state transition by completely filling the defect states. As the electrons relax from the defect states back into the conduction band, the probe laser can again be absorbed by the E+ valence band to defect state transition. Thus, there are two relaxation processes occurring in the GaBiAs samples, shown in Fig. 5.12(b), the recovery of the bleached E+ valence band transition and normal bulk relaxation. The change in absorption was modeled with a two exponential decay. One time constant was held at 90.0 ps, corresponding with the bulk recombination determined in

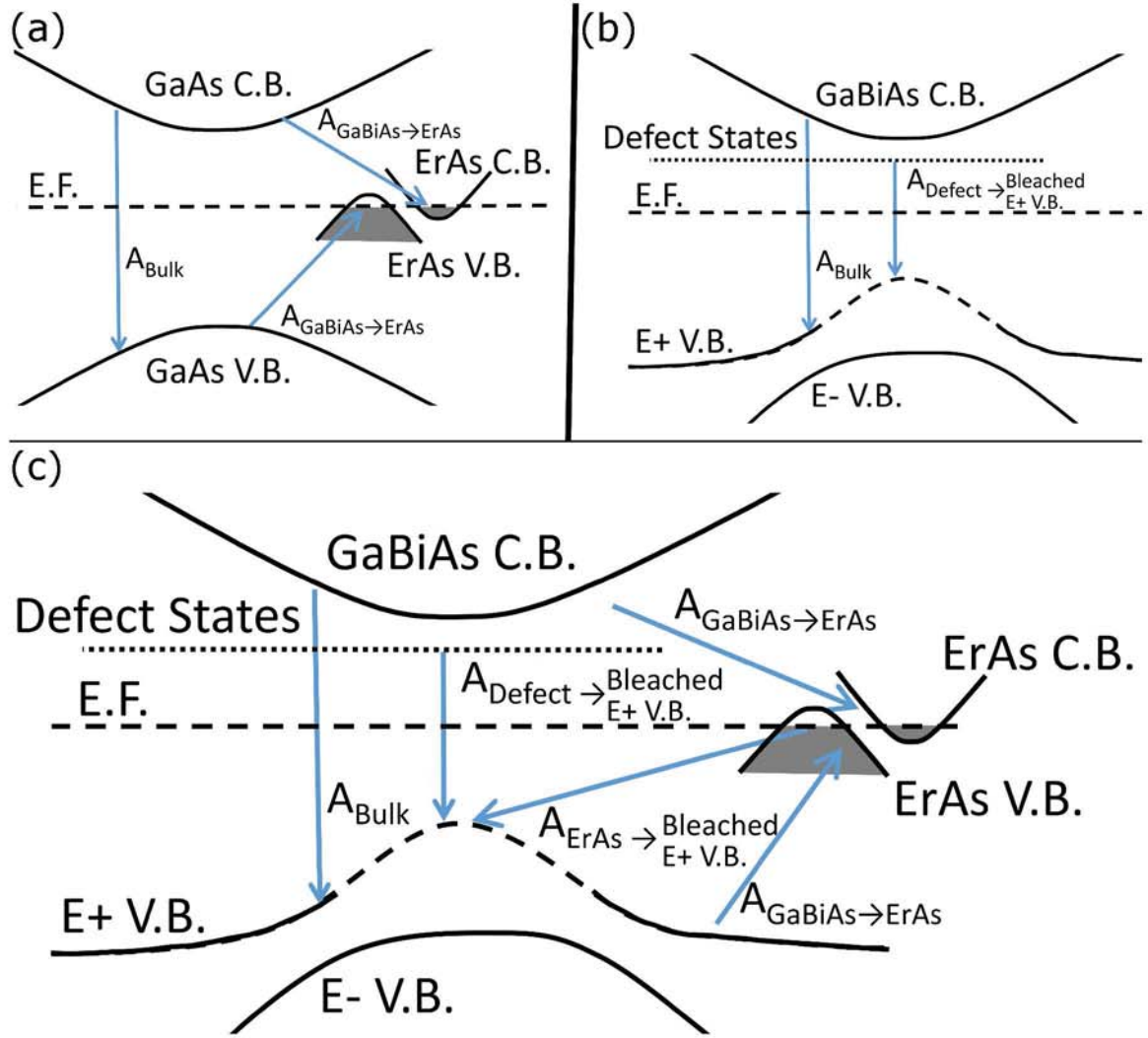


Figure 5.12: Schematic showing the proposed processes that change the change in absorption. Two relaxation processes are present in the ErAs:GaAs samples (a), relaxation across the bulk band gap (90.0 ps) and relaxation of carriers into the ErAs nanoparticles (1.3 ps). Two processes are present in the GaBiAs samples (b), relaxation across the bulk band gap (90.0 ps) and recovery of the bleached Bi E+ valence band to defect transition (89.8 and 28.6 ps). The ErAs:GaBiAs samples have up to four processes (c), relaxation across the bulk band gap (90.0 ps), relaxation of carriers into the ErAs nanoparticles (1.3 ps), recovery of the bleached Bi E+ valence band to defect transition (89.8 and 28.6 ps), and recovery of the bleached Bi E+ valence band to defect transition with the aid of semimetallic ErAs nanoparticles (1.2 ps). In this schematic the recovery of the bleached Bi E+ valence band to defect transition is shown as filling the emptied Bi E+ valence band states by carriers relaxing out of the defect states or carriers relaxing out of the ErAs nanoparticle. Alternatively, the recovery of the bleached Bi E+ valence band to defect transition could occur by filling the emptied Bi E+ valence band states from the conduction band or by emptying the electrons in the defect states within the band gap into the ErAs nanoparticle. Note that a dashed line is used for the E+ valence band in (b) and (c) to show that the E+ valence band may not form a complete band at the Bi concentrations studied here. [29]

the ErAs:GaAs samples. The second time constant corresponds with recovering the bleached E+ valence band to defect transition depends on the amount of bismuth; this was determined to be 89.8 and 28.6 ps for samples *No Er Low Bi* and *No Er High Bi*, respectively. Note that the pre-exponential factor for recovering the bleached E+ valence band transition is negative.

The ErAs:GaBiAs samples, *Low Er Low Bi*, *High Er Low Bi*, *Low Er High Bi*, and *High Er High Bi*, shown in Fig 5.11(c), can be understood by a combination of up to four relaxation processes. Three of the relaxation process come from the previously discussed control samples: relaxation across the bulk band gap, relaxation of carriers into the ErAs nanoparticle, and recovery of the bleached Bi E+ valence band to defect transtion by electrons either relaxing from the conduction band to the E+ valence band or electrons relaxing out of the defect states. The fourth process is the recovery of the bleached Bi E+ valence band to defect transtion with assistance from the semimetallic ErAs nanoparticles. Either electrons relax from the ErAs nanoparticle into the empty E+ valence band states, this does not depend on the relaxation of carriers into the ErAs nanoparticle since semimetallic ErAs nanoparticles have carriers readily available to fill the bleached states, or electrons in the defect states relax into the ErAs nanoparticle. Similar to the recovery of the bleached Bi E+ valence band to defect transtion in the GaBiAs samples, the revoery of the bleached Bi E+ valence band to defect transition with the aid of the ErAs nanoparticles causes the change in the probe's absorption to become less negative and has a negative pre-exponential coefficient. These four processes are depicted in Fig. 5.12(c). The exponential model was done using the lifetimes for the bulk recombination (90.0 ps), relaxation into the ErAs nanoparticle (1.3 ps), and recovery of the bleached Bi E+ valence band to defect transtion (89.8 and 28.6 ps) obtained from the fits of samples *Low Er No Bi*, *High Er No Bi*, *No Er Low Bi*, and *No Er High Bi*. The recovery of the bleached Bi E+ valence band to defect transtion with the aid of the ErAs nanoparticles was determined to have a time constant of 1.2 ps. While modeling the probes absorption as a function of time the pre-exponential coefficients were allowed to change and in some instances nearly

went to zero. For example, the recovery of the bleached Bi E+ valence band to defect transition without the aid of ErAs was nearly zero for samples *Low Er Low Bi* and *High Er Low Bi*. Again, note that the Bi E+ valence band to defect transition states being bleached by emptying the E+ valence band states requires a limited number of states near the E+ valence band maximum. Ultimately, the transient absorption optical pump optical probe shows that the ErAs:GaBiAs samples have fast recovery times, faster than those of previously studied GaBiAs.[169, 165]

5.6 Conclusion

In conclusion, the growth of ErAs:GaBiAs group III rich results in the formation of droplets on the surface and defects throughout the film that alter the film's properties. The growth of ErAs:GaBiAs under stoichiometric or slightly group V rich results in films that exhibit properties of interest for PC switches for THz generation and detection, among other (opto)electronic applications. Due to the valence band anticrossing, the incorporation of Bi has reduced the band gap of the nanocomposite from 1.42 eV to 1.02 eV. The incorporation of ErAs nanoparticles pins the Fermi level near the middle of the band gap, changes the material from p-type to slightly n-type, and creates high dark resistance while maintaining high mobility. Finally, the ErAs nanoparticles act as recombination centers, providing short carrier lifetimes. These properties make ErAs:GaBiAs a promising material for fiber-coupled PC switches.

Chapter 6

CONCLUSION AND FUTURE WORK

The previous chapters have focused on the growth and characterization of LN-V based materials. A review of the growth and properties of the LN-V based materials, both LN-V nanoparticles and films, and a background on the many of the techniques utilized throughout this dissertation were discussed in Chapters 1 and 2. In Chapter 3 the characterization of TbAs nanoparticles in GaAs and $\text{In}_{0.53}\text{Ga}_{0.47}\text{As}$ shows that TbAs nanoparticles have a band gap and that TbAs forms a type I heterojunction with GaAs and a type II heterojunction with $\text{In}_{0.53}\text{Ga}_{0.47}\text{As}$. This discovery can help explain the large Seebeck coefficient previously observed for TbAs: $\text{In}_{0.53}\text{Ga}_{0.47}\text{As}$, [37] and Section 6.1 will discuss this. Section 6.1 will also discuss how the techniques used to determine the band structure of TbAs nanoparticles could be applied to other materials. The growth and characterization of the TbAs films presented in Chapter 4 shows that TbAs films are degenerately doped semiconductors. This makes TbAs films interesting for possible future applications, discussed in Section 6.2. The growth and characterization of ErAs:GaBiAs presented in Chapter 5 shows that ErAs:GaBiAs is a promising material for fiber coupled photoconductive switches for THz detection and generation. Section 6.3 discusses the possibilities to move forward with this project.

6.1 Implications of the TbAs Nanoparticle Band Structure

In Chapter 1 I discussed how TbAs nanoparticles in $\text{In}_{0.53}\text{Ga}_{0.47}\text{As}$ have both a high Seebeck coefficient and a high electrical conductivity resulting in a high thermoelectric power factor [37]. This high Seebeck coefficient, electrical conductivity, and thermoelectric power factor is even more obvious as a function of temperature, Fig 6.1. Figure 6.1 also shows that both the electrical conductivity and Seebeck

coefficient increases with increasing temperature. As discussed for superlattices of $\text{ErAs:In}_{0.53}\text{Ga}_{0.47}\text{As}/\text{In}_{0.53}\text{Ga}_{0.28}\text{Al}_{0.19}\text{As}$, an increase in both electrical conductivity and Seebeck coefficient with temperature is indicative of electron filtering.[112] The discovery in Chapter 3 that TbAs nanoparticles form a type II, straddled, heterojunction with $\text{In}_{0.53}\text{Ga}_{0.47}\text{As}$ suggests that the TbAs nanoparticles may be acting as energy dependent electron filters. The results from a simple model predicting the conductivity improvement, Seebeck coefficient improvement, and thermoelectric power factor improvement provided by a barrier that perfectly scatters electrons with energy lower than the barrier's height is presented in Fig. 6.2. The improvement is the number of times the parameter is improved over $\text{Si:In}_{0.53}\text{Ga}_{0.47}\text{As}$. Additionally, this model predicts that Si doping the $\text{TbAs:In}_{0.53}\text{Ga}_{0.47}\text{As}$ films should result in an even larger improvement. To help prove this idea, a more detailed model that takes into account the possibility of low energy electron tunneling or traveling around the TbAs nanoparticle barriers should be implemented. Once a model that accurately predicts the observed thermoelectric properties is developed, the model should be used to calculate the optimum TbAs amount and doping level required to maximize the thermoelectric power factor. Finally, it would be interesting to grow the predicted $\text{TbAs:In}_{0.53}\text{Ga}_{0.47}\text{As}$ film and measure its thermoelectric properties. It is also worth mentioning that TbAs nanoparticles do not appear to scatter phonons as well as ErAs nanoparticles and the reason for this is presently unknown.

In Chapter 3, I presented a method that was used to understand the band structure of TbAs nanoparticles in both GaAs and $\text{In}_{0.53}\text{Ga}_{0.47}\text{As}$. It should be possible to extend this method to other LN-V:III-V systems such as $\text{TbErAs:In}_{0.53}\text{Ga}_{0.47}\text{As}$. TbErAs core-shell nanoparticles have recently been demonstrated in $\text{In}_{0.53}\text{Ga}_{0.47}\text{As}$ but the electronic structure of this nanocomposite system is unknown.[14] Now that the constituent systems, ErAs and TbAs nanoparticles, are better understood, the electronic structure of TbErAs nanoparticles can be investigated. Many of the measurements used to determine the $\text{TbAs:In}_{0.53}\text{Ga}_{0.47}\text{As}$ band alignment have already been performed including optical pump terahertz probe and Hall effect measurements.

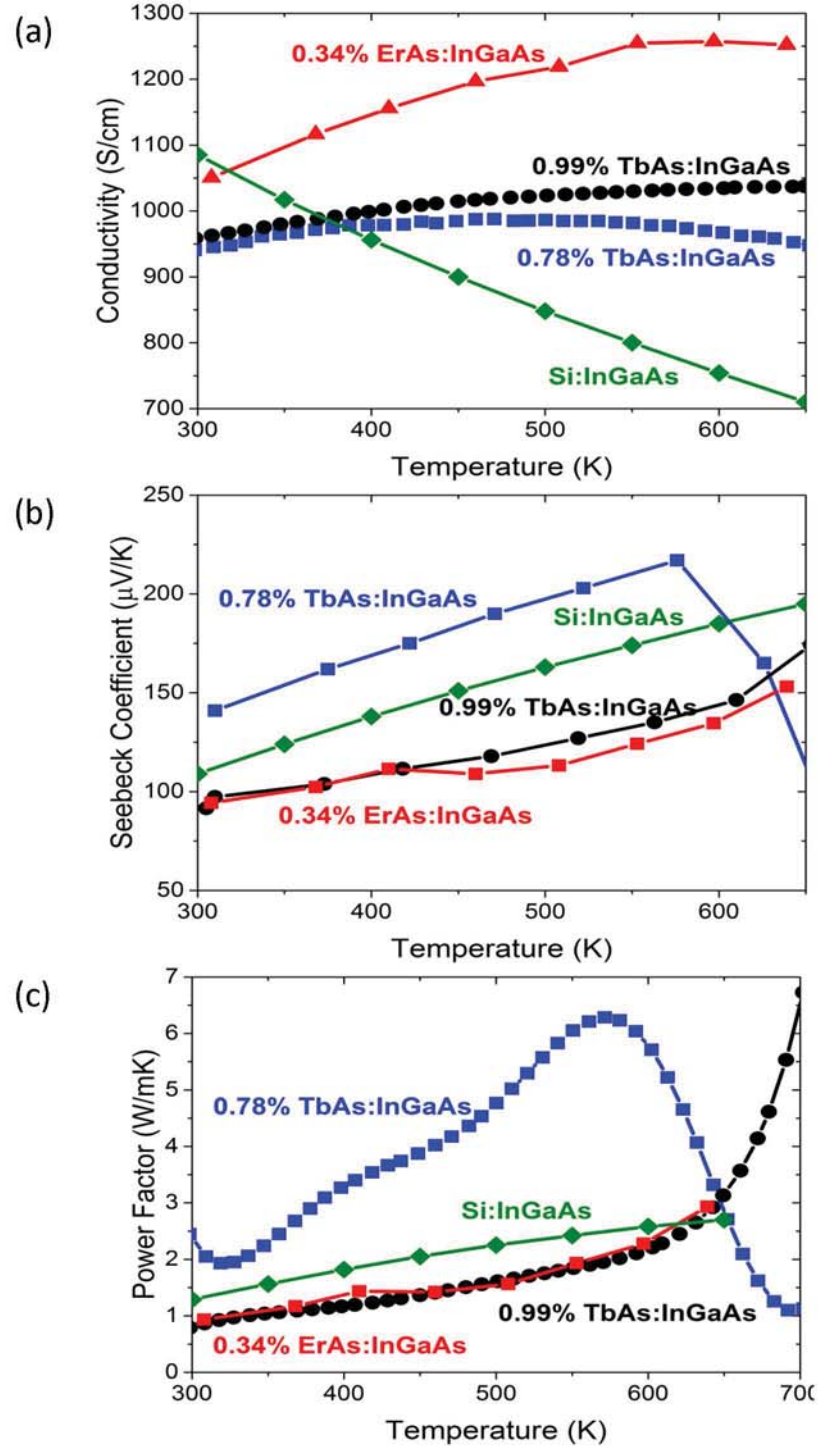


Figure 6.1: The temperature dependent (a) electrical conductivity, (b) Seebeck coefficient, and (c) thermoelectric power factor of TbAs:In_{0.53}Ga_{0.47}As compared to ErAs:In_{0.53}Ga_{0.47}As and Si:In_{0.53}Ga_{0.47}As.

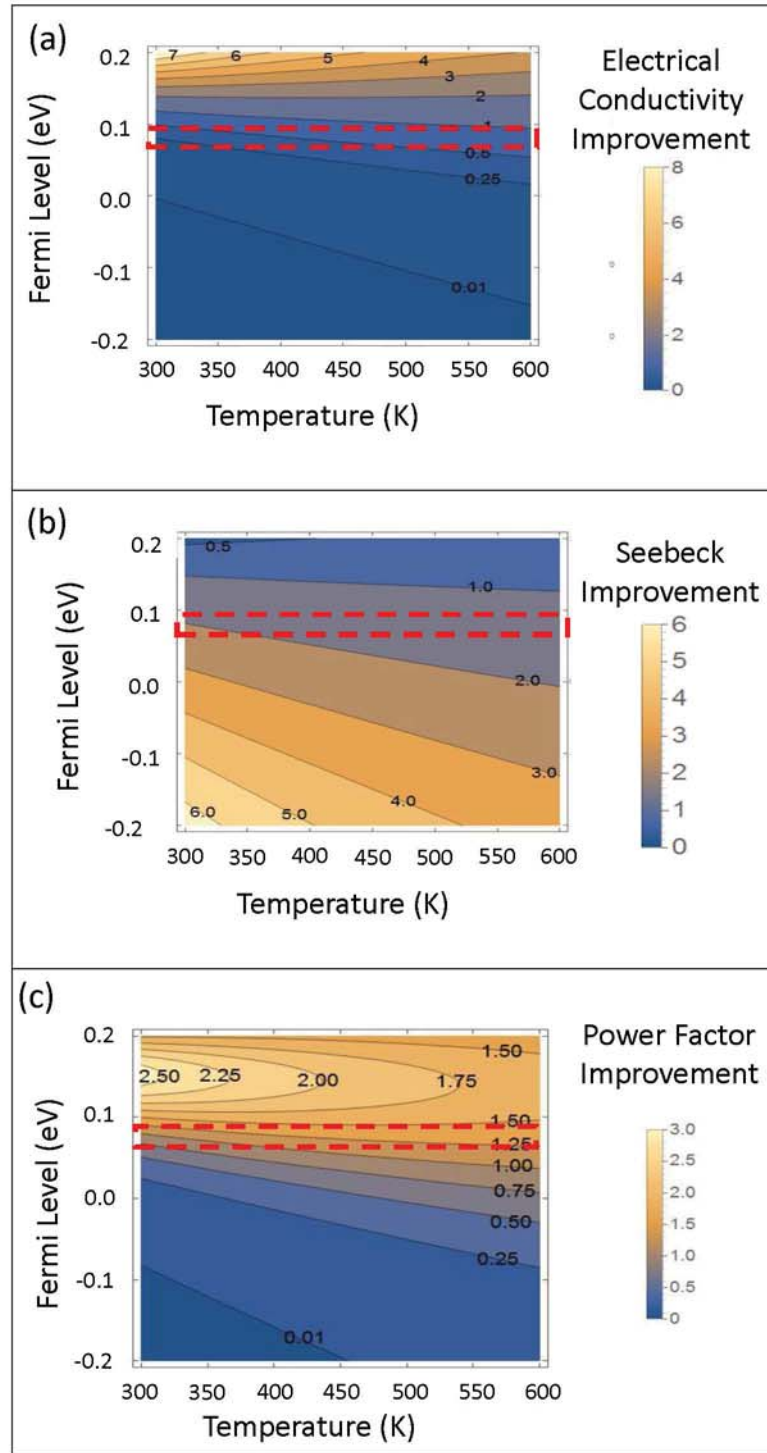


Figure 6.2: The simple model's prediction of (a) electrical conductivity, (b) Seebeck coefficient, and (c) thermoelectric power factor improvement provided by a barrier that perfectly scatters electrons with energy lower than the barrier height. The red dashed box is highlights the estimated barrier height that TbAs provides.

Additionally, Tb and Er have been co-deposited in GaAs; expecting to form TbErAs core-shell nanoparticles with a pure ErAs shell have been grown. The TbErAs:GaAs samples have also been measured, but it is currently unknown if the core shell structure expected formed. Atom probe tomography measurements of these samples are currently being performed. Once the core-shell structure is confirmed, the electronic measurements can be utilized to determine the electronic structure of the nanocomposite.

6.2 TbAs Film Applications

In Chapter 4 TbAs films were grown and studied, showing that TbAs, unlike the other Ln-V materials, is a degenerately doped semiconductor. Due to the degenerate doping, the band gap of TbAs still remains unknown. One method to determine the band gap is to grow a series of TbAs films of differing thicknesses, which should change the doping level in each sample. The optical absorption energy versus carrier concentration could then be mapped out, developing a map of the conduction band's density of states. This would allow for the calculation of a band gap and possibly the effective mass of electrons in TbAs.

Another future direction for TbAs films would be to further study where the carriers come from and the applications possible with TbAs. TbAs being a rocksalt semiconductor provides the opportunity to grow a semiconductor on top of LN-V semimetals without the defects associated with the rotation symmetry difference between the rocksalt and zincblend crystal structures. If the carriers of the degenerately doped TbAs film are coming from the interface, as expected, growing on a rocksalt structure such as ErAs may reduce the carrier concentration of the film. The growth of a rocksalt semiconductor on a rocksalt semimetal could be extended to growing an all rocksalt semimetal-semiconductor superlattice. These types of structures could have applications for thermoelectrics and metamaterials.

6.3 Future Work on ErAs:GaBiAs

Chapter 5 demonstrated the growth and characterization of ErAs:GaBiAs films that are capable of being pumped with a 1064 nm laser and show electrical properties that are promising for photoconductive switches. We are currently working with Dr. Etienne Gagnon at Franklin and Marshall College to develop a model to predict THz detection with LN-V:III-V based detectors. Currently, the model is being developed to predict the performance of the ErAs:GaAs photoconductive switch already characterized.[124] Once the model can accurately predict the performance of ErAs:GaAs, it should be extended to predicting the performance of a device made from ErAs:GaBiAs. It would also be worthwhile to make a device from the ErAs:GaBiAs samples compatible with the 1064 nm fiber coupled lasers presented here and demonstrate THz detection and generation. Additionally, while a photoconductive switch capable of being pumped with a 1064 nm fiber coupled laser is a technologically important step, it would be ideal to develop a switch capable of being pumped with a 1330 nm, or better yet, a 1550 nm, fiber coupled laser. It should be possible to achieve 1330 nm with the incorporation of slightly more Bi than presented here. It might also be possible to achieve 1550 nm with even more Bi, however incorporating this much Bi could be challenging and might introduce a significant amount of defects. Alternatively, a 1550 nm compatible photoconductive switch could be achieved with the proper amount of indium and aluminum incorporated into the GaBiAs matrix.

BIBLIOGRAPHY

- [1] David R Gaskell. *Introduction to the Thermodynamics of Materials*. CRC Press, 2008.
- [2] Momentive Performance Materials Quartz Inc. <http://www.quartz.com/gedata.html#thermal>, March 2007.
- [3] John R Howell, M Pinar Menguc, and Robert Siegel. *Thermal radiation heat transfer*. CRC press, 2010.
- [4] The Engineering ToolBox. http://www.engineeringtoolbox.com/thermal-conductivity-d_429.html, n.d. n.d.
- [5] Cory C Bomberger, Peter M Attia, Ajay K Prasad, and Joshua MO Zide. Modeling passive power generation in a temporally-varying temperature environment via thermoelectrics. *Applied Thermal Engineering*, 56(1):152–158, 2013.
- [6] The Engineering ToolBox. http://www.engineeringtoolbox.com/dry-air-properties-d_973.html, n.d. n.d.
- [7] W.A. Gray and R. Muller. *Engineering Calculations in Radiative Heat Transfer*. Pergamon Press, New York, 1 edition, 1974.
- [8] Omar Reis. <http://www.tecepe.com.br/scripts/AlmanacPagesISAPI.dll>, 2004.
- [9] Peter M Attia, Matthew R Lewis, Cory C Bomberger, Ajay K Prasad, and Joshua MO Zide. Experimental studies of thermoelectric power generation in dynamic temperature environments. *Energy*, 60:453–456, 2013.
- [10] Woonchul Kim, Suzanne L Singer, Arun Majumdar, Joshua MO Zide, Dmitri Klenov, Arthur C Gossard, and Susanne Stemmer. Reducing thermal conductivity of crystalline solids at high temperature using embedded nanostructures. *Nano Letters*, 8(7):2097–2099, 2008.
- [11] R Salas, S Guchhait, SD Sifferman, KM McNicholas, VD Dasika, EM Krivoy, D Jung, ML Lee, and SR Bank. Growth and properties of rare-earth arsenide ingaas nanocomposites for terahertz generation. *Applied Physics Letters*, 106(8):081103, 2015.

- [12] Peter G Burke, Hong Lu, Nicholas G Rudawski, Susanne Stemmer, Arthur C Gossard, Je-Hyeong Bahk, and John E Bowers. Electrical properties of er-doped in_{0.53}ga_{0.47}as. *Journal of Vacuum Science & Technology B*, 29(3):03C117, 2011.
- [13] Jason K Kawasaki, Brian D Schultz, Hong Lu, Arthur C Gossard, and Chris J Palmstrøm. Surface-mediated tunable self-assembly of single crystal semimetallic ersb/gasb nanocomposite structures. *Nano Letters*, 13(6):2895–2901, 2013.
- [14] Pernell Dongmo, Matthew Hartshorne, Thomas Cristiani, Michael L Jablonski, Cory Bomberger, Dieter Isheim, David N Seidman, Mitra L Taheri, and Joshua Zide. Observation of self-assembled core-shell structures in epitaxially embedded tberas nanoparticles. *small*, 10(23):4920–4925, 2014.
- [15] BD Schultz, SG Choi, and CJ Palmstrøm. Embedded growth mode of thermodynamically stable metallic nanoparticles on iii-v semiconductors. *Applied Physics Letters*, 88(24):243117, 2006.
- [16] EM Krivoy, S Rahimi, HP Nair, R Salas, SJ Maddox, DJ Ironside, Y Jiang, VD Dasika, DA Ferrer, G Kelp, et al. Growth and characterization of single crystal rocksalt laas using luas barrier layers. *Applied Physics Letters*, 101(22):221908, 2012.
- [17] Adam M Crook, Hari P Nair, Domingo A Ferrer, and Seth R Bank. Suppression of planar defects in the molecular beam epitaxy of gaas/eras/gaas heterostructures. *Applied Physics Letters*, 99(7):072120, 2011.
- [18] Dmitri O Klenov, Joshua M Zide, Jeremy D Zimmerman, Arthur C Gossard, and Susanne Stemmer. Interface atomic structure of epitaxial eras layers on (001) in_{0.53}ga_{0.47}as and gaas. *Applied Physics Letters*, 86(24):241901, 2005.
- [19] Leonid V Pourovskii, Kris T Delaney, Chris G Van de Walle, Nicola A Spaldin, and Antoine Georges. Role of atomic multiplets in the electronic structure of rare-earth semiconductors and semimetals. *Physical Review Letters*, 102(9):096401, 2009.
- [20] Jason K Kawasaki, Rainer Timm, Kris T Delaney, Edvin Lundgren, Anders Mikkelsen, and Chris J Palmstrøm. Local density of states and interface effects in semimetallic eras nanoparticles embedded in gaas. *Physical Review Letters*, 107(3):036806, 2011.
- [21] MP Hanson, AC Gossard, and ER Brown. Infrared surface plasmon resonances due to er-v semimetallic nanoparticles in iii-v semiconductor matrices. *Journal of Applied Physics*, 102(4):3112, 2007.
- [22] X Liu, AT Ramu, John E Bowers, CJ Palmstrøm, Peter G Burke, Hong Lu, and Arthur C Gossard. Properties of molecular beam epitaxially grown scas:

- Ingaas and eras: Ingaas nanocomposites for thermoelectric applications. *Journal of Crystal Growth*, 316(1):56–59, 2011.
- [23] JMO Zide, J-H Bahk, R Singh, M Zebarjadi, G Zeng, H Lu, JP Feser, D Xu, SL Singer, ZX Bian, et al. High efficiency semimetal/semiconductor nanocomposite thermoelectric materials. *Journal of Applied Physics*, 108(12):123702, 2010.
 - [24] Gehong Zeng, Je-Hyeong Bahk, John E Bowers, Hong Lu, Arthur C Gossard, Suzanne L Singer, Arun Majumdar, Zhixi Bian, Mona Zebarjadi, and Ali Shakouri. Thermoelectric power generator module of 16x16 bi₂te₃ and 0.6% eras:ingaas in a laser segmented elements. *Applied Physics Letters*, 95:083503, 2009.
 - [25] JMO Zide, A Kleiman-Shwarscstein, NC Strandwitz, JD Zimmerman, T Steenblock-Smith, AC Gossard, A Forman, A Ivanovskaya, and GD Stucky. Increased efficiency in multijunction solar cells through the incorporation of semimetallic eras nanoparticles into the tunnel junction. *Applied Physics Letters*, 88(16):162103, 2006.
 - [26] Laura R Vanderhoef, Abul K Azad, Cory C Bomberger, Dibakar Roy Chowdhury, D Bruce Chase, Antoinette J Taylor, Joshua MO Zide, and Matthew F Doty. Charge carrier relaxation processes in tbas nanoinclusions in gaas measured by optical-pump thz-probe transient absorption spectroscopy. *Physical Review B*, 89(4):045418, 2014.
 - [27] Cory C Bomberger, Laura R Vanderhoef, Abdur Rahman, Deesha Shah, D Bruce Chase, Antoinette J Taylor, Abul K Azad, Matthew F Doty, and Joshua MO Zide. Determining the band alignment of tbas:gaas and tbas:in_{0.53}ga_{0.47}as. *Applied Physics Letters*, 107(10):102103, 2015.
 - [28] Cory C Bomberger, Bo E. Tew, Matthew R. Lewis, and Joshua MO Zide. Growth and characterization of tbas films. (Under Review), 2016.
 - [29] Cory C Bomberger, Jesus Nieto-Pescador, Matthew R Lewis, Bo E Tew, Yuejing Wang, D Bruce Chase, Lars Gundlach, and Joshua MO Zide. Growth and characterization of eras:gabi_xas_{1-x}. (Under Review), 2016.
 - [30] JP Petropoulos, Y Zhong, and JMO Zide. Optical and electrical characterization of ingabias for use as a mid-infrared optoelectronic material. *Applied Physics Letters*, 99(3):031110, 2011.
 - [31] ER Brown, A Bacher, D Driscoll, M Hanson, C Kadow, and AC Gossard. Evidence for a strong surface-plasmon resonance on eras nanoparticles in gaas. *Physical Review Letters*, 90(7):077403, 2003.
 - [32] MP Hanson, SR Bank, JMO Zide, JD Zimmerman, and AC Gossard. Controlling electronic properties of epitaxial nanocomposites of dissimilar materials. *Journal of Crystal Growth*, 301:4–9, 2007.

- [33] Chun-Gang Duan, Renat F Sabirianov, WN Mei, Peter A Dowben, SS Jaswal, and Evgeny Y Tsymbal. Electronic, magnetic and transport properties of rare-earth mononictides. *Journal of Physics: Condensed Matter*, 19(31):315220, 2007.
- [34] Franck Natali, Ben J Ruck, Natalie OV Plank, H Joe Trodahl, Simon Granville, Claire Meyer, and Walter RL Lambrecht. Rare-earth mononitrides. *Progress in Materials Science*, 58(8):1316–1360, 2013.
- [35] EM Krivoy, HP Nair, AM Crook, S Rahimi, SJ Maddox, R Salas, DA Ferrer, VD Dasika, D Akinwande, and SR Bank. Growth and characterization of luas films and nanostructures. *Applied Physics Letters*, 101(14):141910, 2012.
- [36] Laura E Cassels, Trevor E Buehl, Peter G Burke, Chris J Palmstrøm, Art C Gossard, Gilles Pernot, Ali Shakouri, Chelsea R Haughn, Matthew F Doty, and Joshua MO Zide. Growth and characterization of tbas:gaas nanocomposites. *Journal of Vacuum Science & Technology B*, 29(3):03C114, 2011.
- [37] Laura E Clinger, Gilles Pernot, Trevor E Buehl, Peter G Burke, Arthur C Gossard, Christopher J Palmstrøm, Ali Shakouri, and Joshua MO Zide. Thermoelectric properties of epitaxial tbas:ingaas nanocomposites. *Journal of Applied Physics*, 111(9):094312, 2012.
- [38] KA Gschneidner and FW Calderwood. The arsenic-rare earth systems. *Bulletin of Alloy Phase Diagrams*, 7(3):274–276, 1986.
- [39] T Sands, CJ Palmstrøm, JP Harbison, VG Keramidas, N Tabatabaie, TL Cheeks, R Ramesh, and Y Silberberg. Stable and epitaxial metal/iii-v semiconductor heterostructures. *Materials Science Reports*, 5(3):99–170, 1990.
- [40] Michael A Scarpulla, CS Gallinat, S Mack, JS Speck, and AC Gossard. Gdn (111) heteroepitaxy on gan (0001) by n₂ plasma and nh₃ molecular beam epitaxy. *Journal of Crystal Growth*, 311(5):1239–1244, 2009.
- [41] Matthew Lewis, Kevin Bichoupan, S Ismat Shah, and Joshua MO Zide. Growth of eras nanoparticles by pulsed laser ablation in an inert environment. *Journal of Electronic Materials*, pages 1–4, 2016.
- [42] Abul K Azad, Rohit P Prasankumar, Diyar Talbayev, Antoinette J Taylor, Richard D Averitt, Joshua MO Zide, Hong Lu, Arthur C Gossard, and John F O’Hara. Carrier dynamics in ingaas with embedded eras nanoislands. *Applied Physics Letters*, 93(12):121108, 2008.
- [43] Axel Svane, Niels Egede Christensen, L Petit, Z Szotek, and WM Temmerman. Electronic structure of rare-earth impurities in gaas and gan. *Physical Review B*, 74(16):165204, 2006.

- [44] Peter G Burke, Trevor E Buehl, Pernot Gilles, Hong Lu, Ali Shakouri, Chris J Palmstøm, John E Bowers, and Arthur C Gossard. Controlling n-type carrier density from er doping of ingaas with mbe growth temperature. *Journal of Electronic Materials*, 41(5):948–953, 2012.
- [45] Peter G Burke, Lars Ismer, Hong Lu, Elan Frantz, Anderson Janotti, Chris G Van de Walle, John E Bowers, and Arthur C Gossard. Electrically active er doping in inas, in_{0.53}ga_{0.47}as, and gaas. *Applied Physics Letters*, 101(23):232103, 2012.
- [46] Joseph P Feser, Dongyan Xu, Hong Lu, Yang Zhao, Ali Shakouri, Arthur C Gossard, and Arun Majumdar. Reduced thermal conductivity in er-doped epitaxial inxga_{1-x}sb alloys. *Applied Physics Letters*, 103(10):103102, 2013.
- [47] R Wang and AJ Steckl. Effect of growth conditions on eu³⁺ luminescence in gan. *Journal of Crystal Growth*, 312(5):680–684, 2010.
- [48] JH Park and AJ Steckl. Laser action in eu-doped gan thin-film cavity at room temperature. *Applied Physics Letters*, 85(20):4588–4590, 2004.
- [49] Hong Lu, Daniel G Ouellette, Sascha Preu, Justin D Watts, Benjamin Zaks, Peter G Burke, Mark S Sherwin, and Arthur C Gossard. Self-assembled ersb nanostructures with optical applications in infrared and terahertz. *Nano Letters*, 14(3):1107–1112, 2013.
- [50] Dmitri O Klenov, Joshua MO Zide, James M LeBeau, Arthur C Gossard, and Susanne Stemmer. Ordering of eras nanoparticles embedded in epitaxial ingaas layers. *Applied Physics Letters*, 90(12):1917, 2007.
- [51] JK Kawasaki, BD Schultz, and CJ Palmstrøm. Size effects on the electronic structure of ersb nanoparticles embedded in the gasb (001) surface. *Physical Review B*, 87(3):035419, 2013.
- [52] Michael A Scarpulla, Joshua MO Zide, James M LeBeau, Chris G Van de Walle, Arthur C Gossard, and Kris T Delaney. Near-infrared absorption and semimetal-semiconductor transition in 2nm eras nanoparticles embedded in gaas and alas. *Applied Physics Letters*, 92(17):173116, 2008.
- [53] Jason K Kawasaki, Rainer Timm, Trevor E Buehl, Edvin Lundgren, Anders Mikkelsen, Arthur C Gossard, and Chris J Palmstrøm. Cross-sectional scanning tunneling microscopy and spectroscopy of semimetallic eras nanostructures embedded in gaas. *Journal of Vacuum Science & Technology B*, 29(3):03C104, 2011.
- [54] Trevor E Buehl, Christopher J Palmstrøm, and Arthur C Gossard. Embedded eras nanorods on gaas (n11) substrates by molecular beam epitaxy. *Journal of Vacuum Science & Technology B*, 29(3):03C108, 2011.

- [55] Trevor E Buehl, James M LeBeau, Susanne Stemmer, Michael A Scarpulla, Christopher J Palmstrøm, and Arthur C Gossard. Growth of embedded eras nanorods on (411)a and (411)b gaas by molecular beam epitaxy. *Journal of Crystal Growth*, 312(14):2089–2092, 2010.
- [56] Rachel Koltun, Jacqueline L Hall, Thomas E Mates, John E Bowers, Brian D Schultz, and Christopher J Palmstrøm. Thermoelectric properties of single crystal sc1-xerxas:ingaas nanocomposites. *Journal of Vacuum Science & Technology B*, 31(4):041401, 2013.
- [57] AJ Young, BD Schultz, and CJ Palmstrøm. Lattice distortion in single crystal rare-earth arsenide/gaas nanocomposites. *Applied Physics Letters*, 104(7):073114, 2014.
- [58] Ashok T Ramu, Laura E Clinger, Pernell B Dongmo, Jeffrey T Imamura, Joshua MO Zide, and John E Bowers. Incompatibility of standard iii-v compound semiconductor processing techniques with terbium-doped ingaas of high terbium concentration. *Journal of Vacuum Science & Technology A*, 30(3):031508, 2012.
- [59] C Kadow, JA Johnson, K Kolstad, and AC Gossard. Growth-temperature dependence of the microstructure of eras islands in gaas. *Journal of Vacuum Science & Technology B*, 21(1):29–32, 2003.
- [60] I Poole, KE Singer, AR Peaker, and AC Wright. Growth and structural characterization of molecular beam epitaxial erbium-doped gaas. *Journal of crystal growth*, 121(1-2):121–131, 1992.
- [61] C Kadow, JA Johnson, K Kolstad, JP Ibbetson, and AC Gossard. Growth and microstructure of self-assembled eras islands in gaas. *Journal of Vacuum Science & Technology B*, 18(4):2197–2203, 2000.
- [62] BD Schultz and CJ Palmstrøm. Embedded assembly mechanism of stable metal nanocrystals on semiconductor surfaces. *Physical Review B*, 73(24):241407, 2006.
- [63] KW Park, VD Dasika, HP Nair, AM Crook, SR Bank, and ET Yu. Conductivity and structure of eras nanoparticles embedded in gaas pn junctions analyzed via conductive atomic force microscopy. *Applied Physics Letters*, 100(23):233117, 2012.
- [64] KW Park, HP Nair, AM Crook, SR Bank, and ET Yu. Quantitative scanning thermal microscopy of eras/gaas superlattice structures grown by molecular beam epitaxy. *Applied Physics Letters*, 102(6):061912, 2013.
- [65] KW Park, HP Nair, AM Crook, SR Bank, and ET Yu. Scanning capacitance microscopy of eras nanoparticles embedded in gaas pn junctions. *Applied Physics Letters*, 99(13):133114, 2011.

- [66] Chao-Yu Hung, Tomah Sogabe, Naoya Miyashita, and Yoshitaka Okada. Growth of eras nanodots by molecular beam epitaxy for application to tunneling junctions in multijunction solar cells. *Japanese Journal of Applied Physics*, 55(2):021201, 2016.
- [67] TF Kent, J Yang, L Yang, MJ Mills, and RC Myers. Epitaxial ferromagnetic nanoislands of cubic gdn in hexagonal gan. *Applied Physics Letters*, 100(15):152111, 2012.
- [68] C Kadow, SB Fleischer, JP Ibbetson, JE Bowers, AC Gossard, JW Dong, and CJ Palmstrøm. Self-assembled eras islands in gaas: Growth and subpicosecond carrier dynamics. *Applied Physics Letters*, 75(22):3548–3550, 1999.
- [69] Yuanchang Zhang, Kurt G Eyink, Joseph Peoples, Krishnamurthy Mahalingam, Madelyn Hill, and Larry Grazulis. Erassb nanoparticle growth on gaas surface by molecular beam epitaxy. *Journal of Crystal Growth*, 435:62–67, 2016.
- [70] Adam M Crook, Hari P Nair, and Seth R Bank. High-performance nanoparticle-enhanced tunnel junctions for photonic devices. *Physica Status Solidi. C: Current Topics in Solid State Physics*, 7(10):2544–2547, 2010.
- [71] Adam M Crook, Hari P Nair, and Seth R Bank. Surface segregation effects of erbium in gaas growth and their implications for optical devices containing eras nanostructures. *Applied Physics Letters*, 98(12):121108, 2011.
- [72] Daniel J. Ironside, adam M. Crook, Alec M. Skipper, and Seth R. Bank. Optimal integration of rare-earth mononpnictide nanostructures in iii-v for high optical quality applications. In *58th Electronic Materials Conference*, 2016.
- [73] Kurt G Eyink, Luke J Bissell, Jodie Shoaf, David H Tomich, Daniel Esposito, Madelyn Hill, Larry Grazulis, Andrew Aronow, and Krishnamurthy Mahalingam. Growth and spectroscopic ellipsometry evaluation of composite layers of eras and inas nanoparticles. *Journal of Vacuum Science & Technology B*, 31(3):03C131, 2013.
- [74] CJ Palmstro, N Tabatabaie, and SJ Allen Jr. Epitaxial growth of eras on (100) gaas. *Applied Physics Letters*, 53(26):2608–2610, 1988.
- [75] CJ Palmstro, KC Garrison, S Mounier, T Sands, CL Schwartz, N Tabatabaie, SJ Allen Jr, HL Gilchrist, and PF Miceli. Growth of epitaxial rare-earth arsenide/(100) gaas and gaas/rare-earth arsenide/(100) gaas structures. *Journal of Vacuum Science & Technology B*, 7(4):747–752, 1989.
- [76] S Rahimi, EM Krivoy, J Lee, ME Michael, SR Bank, and D Akinwande. Temperature dependence of the electrical resistivity of laxlul-xas. *AIP Advances*, 3(8):082102, 2013.

- [77] CJ Palmstro, S Mounier, TG Finstad, and PF Miceli. Lattice-matched scl-xerxas/gaas heterostructures: A demonstration of new systems for fabricating lattice-matched metallic compounds to semiconductors. *Applied Physics Letters*, 56(4):382–384, 1990.
- [78] A Guivarc’h, A Le Corre, P Auvray, B Guenais, J Caulet, Y Ballini, R Gúcrin, S Deputier, MC Le Clanche, G Jezequel, et al. Growth by molecular beam epitaxy of (rare-earth group v element)/iii-v semiconductor heterostructures. *Journal of materials research*, 10(08):1942–1952, 1995.
- [79] A Le Corre, J Caulet, and A Guivarch. Growth of matched metallic erp0.6as0.4 layers on gaas in a molecular beam epitaxy system. *Applied Physics Letters*, 55(22):2298–2300, 1989.
- [80] Sahil J Patel, Jason K Kawasaki, John Logan, Brian D Schultz, Johan Adell, Balasubramanian Thiagarajan, Anders Mikkelsen, and Chris J Palmstrøm. Surface and electronic structure of epitaxial ptusb (001) thin films. *Applied Physics Letters*, 104(20):201603, 2014.
- [81] F Natali, NOV Plank, J Galipaud, BJ Ruck, HJ Trodahl, F Semond, S Sorieul, and L Hirsch. Epitaxial growth of gdn on silicon substrate using an aln buffer layer. *Journal of Crystal Growth*, 312(24):3583–3587, 2010.
- [82] Kris T Delaney, Nicola A Spaldin, and Chris G Van de Walle. Theoretical study of schottky-barrier formation at epitaxial rare-earth-metal/semiconductor interfaces. *Physical Review B*, 81(16):165312, 2010.
- [83] Jeramy D Zimmerman, Arthur C Gossard, Adam C Young, Merritt P Miller, and Elliott R Brown. Eras island-stacking growth technique for engineering textured schottky interfaces. *Journal of Vacuum Science & Technology B*, 24(3):1483–1487, 2006.
- [84] LH Brixner. Structure and electrical properties of some new rare earth arsenides, antimonides and tellurides. *Journal of Inorganic and Nuclear Chemistry*, 15(1):199–201, 1960.
- [85] SER Hiscocks and JB Mullin. An investigation of the preparation and properties of some iia-vb compounds. *Journal of Materials Science*, 4(11):962–973, 1969.
- [86] F Hulliger. Rare earth pnictides. *Handbook on the physics and chemistry of rare earths*, 4:153–236, 1979.
- [87] JB Taylor, LD Calvert, JG Despault, EJ Gabe, and JJ Murray. The rare-earth arsenides: Non-stoichiometry in the rocksalt phases. *Journal of the Less Common Metals*, 37(2):217–232, 1974.

- [88] Yoshikazu Takeda, Keiji Fujita, Naoteru Matsubara, Naoki Yamada, Satofumi Ichiki, Masao Tabuchi, and Yasufumi Fujiwara. Layer structure analysis of δ -doped inp by x-ray crystal truncation rod scattering. *Journal of Applied Physics*, 82(2):635–638, 1997.
- [89] Leonid Bolotov, Junji Tsuchiya, Yasufumi Fujiwara, Yoshikazu Takeda, and Arao Nakamura. Formation of erp islands on inp (001) surface by organometallic vapor phase epitaxy. *Japanese Journal of Applied Physics*, 36(11B):L1534, 1997.
- [90] Hiroaki Yoshitomi, Shinya Kitayama, Takashi Kita, Osamu Wada, M Fujisawa, Hitoshi Ohta, and T Sakurai. Optical and magnetic properties in epitaxial gdn thin films. *Physical Review B*, 83(15):155202, 2011.
- [91] N Sclar. Energy gaps of the iii–v and the (rare earth)-v semiconductors. *Journal of Applied Physics*, 33(10):2999–3002, 1962.
- [92] A Guivarc’h, J Caulet, and A Le Corre. Epitaxial growth of metallic erp, ersb and lattice-matched erp/sub x/sb/sub (1-x)/layers on (001)inp and (001)gaas. *Electronics Letters*, 16(25):1050–1052, 1989.
- [93] L Ilver, J Kanski, C Wigren, Ulf O Karlsson, and PR Varekamp. Quantum size effects in epitaxial eras on gaas (001). *Physical Review Letters*, 77(24):4946, 1996.
- [94] Takashi Komesu, Hae-Kyung Jeong, Jaewu Choi, CN Borca, Peter A Dowben, AG Petukhov, BD Schultz, and CJ Palmstrøm. Electronic structure of eras (100). *Physical Review B*, 67(3):035104, 2003.
- [95] Kris T Delaney, Nicola A Spaldin, and Chris G Van de Walle. Theoretical study of the structural and electronic properties of strained eras. *Physical Review B*, 77(23):235117, 2008.
- [96] L Bolotov, T Tsuchiya, A Nakamura, T Ito, Y Fujiwara, and Y Takeda. Semimetal to semiconductor transition in erp islands grown on inp (001) due to quantum-size effects. *Physical Review B*, 59(19):12236, 1999.
- [97] CR Haughn, EH Steenbergen, LJ Bissell, EY Chen, KG Eyink, JMO Zide, and MF Doty. Carrier transfer from inas quantum dots to eras metal nanoparticles. *Applied Physics Letters*, 105(10):103108, 2014.
- [98] JY Suen, PR Kroger, S Preu, H Lu, AC Gossard, DC Driscoll, and PM Lubin. Measurement and modeling of eras: In_{0.53}Ga_{0.47}As nanocomposite photoconductivity for thz generation at 1.55 μm pump wavelength. *Journal of Applied Physics*, 116(1):013703, 2014.
- [99] F Ospald, D Maryenko, K von Klitzing, DC Driscoll, MP Hanson, H Lu, AC Gossard, and JH Smet. 1.55 μm ultrafast photoconductive switches based on eras:ingaas. *Applied Physics Letters*, 92:131117, 2008.

- [100] AJ Kenyon. Recent developments in rare-earth doped materials for optoelectronics. *Progress in Quantum Electronics*, 26(4):225–284, 2002.
- [101] Thomas F Kent, Santino D Carnevale, and Roberto C Myers. Atomically sharp 318 nm gd: Algan ultraviolet light emitting diodes on si with low threshold voltage. *Applied Physics Letters*, 102(20):201114, 2013.
- [102] Takashi Kita, Shinya Kitayama, Masashi Kawamura, Osamu Wada, Yoshitaka Chigi, Yoshihiro Kasai, Tetsuro Nishimoto, Hiroyuki Tanaka, and Mikihiro Kobayashi. Narrow-band deep-ultraviolet light emitting device using algdxn. *Applied Physics Letters*, 93:211901, 2008.
- [103] DS Lee and AJ Steckl. Enhanced blue and green emission in rare-earth-doped gan electroluminescent devices by optical photopumping. *Applied Physics Letters*, 81(13):2331–2333, 2002.
- [104] Akihiro Wakahara, Hiroto Sekiguchi, Hiroshi Okada, and Yasufumi Takagi. Current status for light-emitting diode with eu-doped gan active layer grown by mbe. *Journal of Luminescence*, 132(12):3113–3117, 2012.
- [105] MP Hanson, AC Gossard, and ER Brown. Eras as a transparent contact at 1.55 μ m. *Applied Physics Letters*, 89(11), 2006.
- [106] Erica Michelle Krivoy. PhD thesis, The University of Texas at Austin, 2013.
- [107] CJ Palmstro, TL Cheeks, HL Gilchrist, JG Zhu, CB Carter, BJ Wilkens, and R Martin. Effect of orientation on the schottky barrier height of thermodynamically stable epitaxial metal/gaas structures. *Journal of Vacuum Science & Technology A*, 10(4):1946–1953, 1992.
- [108] DC Driscoll, MP Hanson, AC Gossard, and ER Brown. Ultrafast photoresponse at 1.55 μ m in ingaas with embedded semimetallic eras nanoparticles. *Applied Physics Letters*, 86(5):051908, 2005.
- [109] JM Zide, DO Klenov, S Stemmer, AC Gossard, G Zeng, JE Bowers, D Vashaee, and A Shakouri. Thermoelectric power factor in semiconductors with buried epitaxial semimetallic nanoparticles. *Applied Physics Letters*, 87(11):112102–112102, 2005.
- [110] Ekaterina Selezneva, Laura E Clinger, Ashok T Ramu, Gilles Pernot, Trevor E Buehl, Tela Favaloro, Je-Hyeong Bahk, Zhixi Bian, John E Bowers, Joshua MO Zide, et al. Thermoelectric transport in ingaas with high concentration of rare-earth tbas embedded nanoparticles. *Journal of Electronic Materials*, 41(6):1820–1825, 2012.

- [111] Sascha Preu, M Mittendorff, H Lu, Heiko B Weber, S Winnerl, and AC Gossard. 1550 nm eras:in(al)gaas large area photoconductive emitters. *Applied Physics Letters*, 101(10):101105, 2012.
- [112] JMO Zide, D Vashaee, ZX Bian, G Zeng, JE Bowers, A Shakouri, and AC Gossard. Demonstration of electron filtering to increase the seebeck coefficient in in_{0.53}ga_{0.47}as/in_{0.53}ga_{0.28}al_{0.19}as superlattices. *Physical Review B*, 74(20):205335, 2006.
- [113] GH Zeng, John E Bowers, Joshua MO Zide, Arthur C Gossard, Woochul Kim, Suzanne Singer, Arun Majumdar, Rajeev Singh, Zhixi Bian, Yan Zhang, et al. Eras:ingaas/ingaalas superlattice thin-film power generator array. *Applied Physics Letters*, 88(11), 2006.
- [114] Gehong Zeng, Joshua MO Zide, Woochul Kim, John E Bowers, Arthur C Gossard, Zhixi Bian, Yan Zhang, Ali Shakouri, Suzanne L Singer, and Arun Majumdar. Cross-plane seebeck coefficient of eras:ingaas/ingaalas superlattices. *Journal of Applied Physics*, 101(3):034502, 2007.
- [115] Gehong Zeng, Je-Hyeong Bahk, John E Bowers, Hong Lu, Joshua MO Zide, Arthur C Gossard, Rajeev Singh, Zhixi Bian, Ali Shakouri, Suzanne L Singer, et al. Power generator modules of segmented bi₂te₃ and eras:(ingaas)_{1-x}(inalas)_x. *Journal of Electronic Materials*, 37(12):1786–1792, 2008.
- [116] Woochul Kim, Joshua Zide, Arthur Gossard, Dmitri Klenov, Susanne Stemmer, Ali Shakouri, and Arun Majumdar. Thermal conductivity reduction and thermoelectric figure of merit increase by embedding nanoparticles in crystalline semiconductors. *Physical Review Letters*, 96(4):045901, 2006.
- [117] KW Park, EM Krivoy, HP Nair, SR Bank, and ET Yu. Cross-sectional scanning thermal microscopy of eras/gaas superlattices grown by molecular beam epitaxy. *Nanotechnology*, 26(26):265701, 2015.
- [118] Hong Lu, Peter G Burke, Arthur C Gossard, Gehong Zeng, Ashok T Ramu, Je-Hyeong Bahk, and John E Bowers. Semimetal/semiconductor nanocomposites for thermoelectrics. *Advanced Materials*, 23(20):2377–2383, 2011.
- [119] Gehong Zeng, Je-Hyeong Bahk, John E Bowers, Joshua MO Zide, Arthur C Gossard, Zhixi Bian, Rajeev Singh, Ali Shakouri, Woochul Kim, Suzanne L Singer, et al. Eras:(ingaas)_{1-x}(inalas)_x alloy power generator modules. *Applied Physics Letters*, 91(26):3510, 2007.
- [120] Mona Zebarjadi, Keivan Esfarjani, Ali Shakouri, Je-Hyeong Bahk, Zhixi Bian, Gehong Zeng, John Bowers, Hong Lu, Joshua Zide, and Art Gossard. Effect of nanoparticle scattering on thermoelectric power factor. *Applied Physics Letters*, 94(20):202105, 2009.

- [121] Hari P Nair, Adam M Crook, and Seth R Bank. Enhanced conductivity of tunnel junctions employing semimetallic nanoparticles through variation in growth temperature and deposition. *Applied Physics Letters*, 96(22):222104, 2010.
- [122] S Preu, S Malzer, GH Döhler, H Lu, AC Gossard, and LJ Wang. Efficient iii-v tunneling diodes with eras recombination centers. *Semiconductor Science and Technology*, 25(11):115004, 2010.
- [123] Sriram Krishnamoorthy, Thomas F Kent, Jing Yang, Pil Sung Park, Roberto C Myers, and Siddharth Rajan. Gdn nanoisland-based gan tunnel junctions. *Nano Letters*, 13(6):2570–2575, 2013.
- [124] John F OHara, JMO Zide, AC Gossard, AJ Taylor, and RD Averitt. Enhanced terahertz detection via eras:gaas nanoisland superlattices. *Applied Physics Letters*, 88(25):251119, 2006.
- [125] A Schwagmann, Z-Y Zhao, F Ospald, H Lu, DC Driscoll, MP Hanson, AC Gossard, and JH Smet. Terahertz emission characteristics of eras:ingaas-based photoconductive antennas excited at $1.55\text{ }\mu\text{m}$. *Applied Physics Letters*, 96(14):141108, 2010.
- [126] Kimani K Williams, ZD Taylor, JY Suen, Hong Lu, RS Singh, AC Gossard, and ER Brown. Toward a 1550 nm ingaas photoconductive switch for terahertz generation. *Optics Letters*, 34(20):3068–3070, 2009.
- [127] M Sukhotin, ER Brown, AC Gossard, D Driscoll, M Hanson, P Maker, and R Muller. Photomixing and photoconductor measurements on eras/ingaas at $1.55\text{ }\mu\text{m}$. *Applied Physics Letters*, 82(18):3116–3118, 2003.
- [128] Christopher W Berry, Mohammad R Hashemi, Sascha Preu, Hong Lu, Arthur C Gossard, and Mona Jarrahi. High power terahertz generation using 1550 nm plasmonic photomixers. *Applied Physics Letters*, 105(1):011121, 2014.
- [129] RD Averitt, Willie John Padilla, HT Chen, JF O’Hara, AJ Taylor, C Highstrete, M Lee, JMO Zide, SR Bank, and AC Gossard. Terahertz metamaterial devices. In *Optics East 2007*, pages 677209–677209. International Society for Optics and Photonics, 2007.
- [130] Hou-Tong Chen, Willie J Padilla, Joshua MO Zide, Seth R Bank, Arthur C Gossard, Antoinette J Taylor, and Richard D Averitt. Ultrafast optical switching of terahertz metamaterials fabricated on eras/gaas nanoisland superlattices. *Optics Letters*, 32(12):1620–1622, 2007.
- [131] Jeramy D Zimmerman, Elliott R Brown, and Arthur C Gossard. Tunable all epitaxial semimetal-semiconductor schottky diode system: Eras on inalaas. *Journal of Vacuum Science & Technology B*, 23(5):1929–1935, 2005.

- [132] Uttam Singiseti, Jeramy D Zimmerman, Mark A Wistey, Joël Cagnon, Brian J Thibeault, Mark JW Rodwell, Arthur C Gossard, Susanne Stemmer, and Seth R Bank. Eras epitaxial ohmic contacts to ingaas/inp. *Applied Physics Letters*, 94(8):83505, 2009.
- [133] Mohamed Henini. *Molecular beam epitaxy: from research to mass production*. Newnes, 2012.
- [134] Alfred Y Cho. Film deposition by molecular-beam techniques. *Journal of Vacuum Science & Technology*, 8(5):S31–S38, 1971.
- [135] AY Cho and JR Arthur. Molecular beam epitaxy. *Progress in solid state chemistry*, 10:157–191, 1975.
- [136] J W Orton and Tom Foxon. *Molecular beam epitaxy : a short history*. Oxford University Press, Oxford, 2015.
- [137] Alfred Cho. *Molecular beam epitaxy*. American Institute of Physics.
- [138] John C Bean, Subramanian S Iyer, and Kang L Wang. *Silicon Molecular Beam Epitaxy*. Materials Research Society, Pittsburgh, 1991.
- [139] W. Robert Thurber. http://www.nist.gov/pml/div683/hall_algorithm.cfm, April 2015.
- [140] Laura R Vanderhoef. *Understanding Charge Carrier Relaxation Processes in Terbium Arsenide Nanoparticles Using Transient Absorption Spectroscopy*. PhD thesis, University of Delaware, 2015.
- [141] Jesus Nieto-Pescador, Baxter Abraham, Allen J Pistner, Joel Rosenthal, and Lars Gundlach. Electronic state dependence of heterogeneous electron transfer: injection from the s1 and s2 state of phlorin into tio2. *Physical Chemistry Chemical Physics*, 17(12):7914–7923, 2015.
- [142] DC Driscoll, M Hanson, C Kadow, and AC Gossard. Electronic structure and conduction in a metal-semiconductor digital composite: Eras: Ingaas. *Applied Physics Letters*, 78(12):1703–1705, 2001.
- [143] M Said, CM Bertoni, A Fasolino, and Stefano Ossicini. Electronic structure of rare earth arsenide/gallium arsenide superlattices. *Solid State Communications*, 100(7):477–480, 1996.
- [144] Trevor W Roberti, Nerine J Cherepy, and Jin Z Zhang. Nature of the power-dependent ultrafast relaxation process of photoexcited charge carriers in ii-vi semiconductor quantum dots: Effects of particle size, surface, and electronic structure. *The Journal of Chemical Physics*, 108(5):2143–2151, 1998.

- [145] RK Ahrenkiel, RI Ellingson, S Johnston, and M Wanlass. Recombination lifetime of $\text{In}_0.53\text{Ga}_{0.47}\text{As}$ as a function of doping density. *Applied Physics Letters*, 72(26):3470–3472, 1998.
- [146] Jacques I. Pankove. *Optical Processes In Semiconductors*. Prentice-Hall, INC., Englewood Cliffs, N.J., 1971.
- [147] Neil W. Ashcroft and N. David Mermin. *Solid State Physics*. Holt, Rinehart and Winston, New York, 1976.
- [148] S Sethi and PK Bhattacharya. Characteristics and device applications of erbium doped iii-v semiconductors grown by molecular beam epitaxy. *Journal of Electronic Materials*, 25(3):467–477, 1996.
- [149] RP Prasankumar, A Scopatz, DJ Hilton, AJ Taylor, RD Averitt, JM Zide, and AC Gossard. Carrier dynamics in self-assembled eras nanoislands embedded in gaas measured by optical-pump terahertz-probe spectroscopy. *Applied Physics Letters*, 86(20):201107, 2005.
- [150] Joshua Michael Olney Zide. PhD thesis, University of California, Santa Barbara, 2007.
- [151] WRL Lambrecht, AG Petukhov, and BT Hemmelman. Schottky barrier formation at eras/gaas interfaces: a case of fermi level pinning by surface states. *Solid State Communications*, 108(6):361–365, 1998.
- [152] Anderson Janotti. "Private Communication", n.d. 2016.
- [153] John F Federici, Brian Schulkin, Feng Huang, Dale Gary, Robert Barat, Filipe Oliveira, and David Zimdars. Thz imaging and sensing for security applicationexplosives, weapons and drugs. *Semiconductor Science and Technology*, 20(7):S266, 2005.
- [154] Peter H Siegel et al. Terahertz technology. *IEEE Transactions on Microwave Theory and Techniques*, 50(3):910–928, 2002.
- [155] Masayoshi Tonouchi. Cutting-edge terahertz technology. *Nature Photonics*, 1(2):97–105, 2007.
- [156] P Uhd Jepsen, David G Cooke, and Martin Koch. Terahertz spectroscopy and imaging—modern techniques and applications. *Laser & Photonics Reviews*, 5(1):124–166, 2011.
- [157] Bradley Ferguson and Xi-Cheng Zhang. Materials for terahertz science and technology. *Nature Materials*, 1(1):26–33, 2002.

- [158] K Alberi, J Wu, W Walukiewicz, KM Yu, OD Dubon, SP Watkins, CX Wang, X Liu, Y-J Cho, and J Furdyna. Valence-band anticrossing in mismatched iii-v semiconductor alloys. *Physical Review B*, 75(4):045203, 2007.
- [159] Kirstin Alberi, OD Dubon, W Walukiewicz, KM Yu, K Bertulis, and A Krotkus. Valence band anticrossing in gabixas1- x. *Applied Physics Letters*, 91(5):051909, 2007.
- [160] Z Batool, K Hild, Thomas Jeffrey Cockburn Hosea, X Lu, T Tiedje, and SJ Sweeney. The electronic band structure of gabias/gaas layers: influence of strain and band anti-crossing. *Journal of Applied Physics*, 111(11):113108, 2012.
- [161] IP Marko, P Ludewig, ZL Bushell, SR Jin, K Hild, Z Batool, S Reinhard, L Nattermann, W Stolz, K Volz, et al. Physical properties and optimization of gabias/(al) gaas based near-infrared laser diodes grown by movpe with up to 4.4% bi. *Journal of Physics D: Applied Physics*, 47(34):345103, 2014.
- [162] Robert D Richards, Faebian Bastiman, Christopher J Hunter, Danuta F Mendes, Abdul R Mohmad, John S Roberts, and John PR David. Molecular beam epitaxy growth of gaasbi using as2 and as4. *Journal of Crystal Growth*, 390:120–124, 2014.
- [163] Adolf M Mulokozi. An alloying theory of transition metals with p-block elements ii: A theoretical treatment of the heats of formation and other properties of rare earth arsenides and bismuthides. *Journal of the Less Common Metals*, 75(1):125–132, 1980.
- [164] C Colinet, A Pasturel, A Percheron-Guegan, and JC Achard. Enthalpies of formation of liquid and solid binary alloys of lead, antimony and bismuth with rare earth elements. *Journal of the Less Common Metals*, 102(2):239–249, 1984.
- [165] V Pačebutas, K Bertulis, G Aleksejenko, and A Krotkus. Molecular-beam-epitaxy grown gabias for terahertz optoelectronic applications. *Journal of Materials Science: Materials in Electronics*, 20(1):363–366, 2009.
- [166] Xianfeng Lu, DA Beaton, RB Lewis, T Tiedje, and Yong Zhang. Composition dependence of photoluminescence of gaas1-xbix alloys. *Applied Physics Letters*, 95(4):041903, 2009.
- [167] Nicolas Jourdan, Hiroshi Yamaguchi, and Yoshiji Horikoshi. Dependence of eras clustering and er segregation in eras/gaas heterostructures on growth temperature. *Japanese Journal of Applied Physics*, 32(12B):L1784, 1993.
- [168] Y Zhong, PB Dongmo, JP Petropoulos, and JMO Zide. Effects of molecular beam epitaxy growth conditions on composition and optical properties of inxgal-xbiyas1-y. *Applied Physics Letters*, 100(11):112110, 2012.

- [169] V Pačebutas, K Bertulis, L Dapkus, G Aleksejenko, A Krotkus, KM Yu, and W Walukiewicz. Characterization of low-temperature molecular-beam-epitaxy grown gabis layers. *Semiconductor Science and Technology*, 22(7):819, 2007.
- [170] Shantanu Gupta, John F Whitaker, Gerard Mourou, et al. Ultrafast carrier dynamics in iii-v semiconductors grown by molecular-beam epitaxy at very low substrate temperatures. *Quantum Electronics, IEEE Journal of*, 28(10):2464–2472, 1992.
- [171] Y Meydbray, R Singh, and Ali Shakouri. Thermoelectric module construction for low temperature gradient power generation. In *Proceedings of the International Conference on Thermoelectrics*, pages 348–351, 2005.
- [172] Kazuaki Yazawa and Ali Shakouri. Cost-efficiency trade-off and the design of thermoelectric power generators. *Environmental Science & Technology*, 45(17):7548–7553, 2011.
- [173] DK Benson and CE Tracy. Design and fabrication of thin film thermoelectric generators. In *Power Sources Symposium. 30*, pages 238–240, 1982.
- [174] Ryosuke O Suzuki and Daisuke Tanaka. Mathematic simulation on thermoelectric power generation with cylindrical multi-tubes. *Journal of Power Sources*, 124(1):293–298, 2003.
- [175] H Scherrer and S Scherrer. Handbook of thermoelectrics edited by dm rowe, 1994.
- [176] R Byron Bird, Warren E Stewart, and Edwin N Lightfoot. *Transport Phenomena*. John Wile & Sons, Inc., New York, 2 edition, 2006.
- [177] D.R. Poirier and G.H. Geiger. *Transport Phenomena in Materials Processing*. The Minerals, Metals & Materials Society, Warrendale, 1994.
- [178] Jon Henderson. Thermoelectric generator system to be presented at the 14th intersociety energy conversion. In *Intersociety Energy Conversion Engineering Conference Vol. 2*, pages 1835–1840, 1979.
- [179] Fankai Meng, Lingen Chen, and Fengrui Sun. A numerical model and comparative investigation of a thermoelectric generator with multi-irreversibilities. *Energy*, 36(5):3513–3522, 2011.
- [180] James W Stevens. Optimal design of small δt thermoelectric generation systems. *Energy Conversion and Management*, 42(6):709–720, 2001.
- [181] M.N. Ozisik. *Basic Heat Trnsfer*. McGraw-Hill, 1977.
- [182] TWF Russell, AS Robinson, and NJ Wagner. *Mass and Heat Transfer*. Cambridge University Press, New York, 1 edition, 2008.

- [183] H Glosch, M Ashauer, U Pfeiffer, and W Lang. A thermoelectric converter for energy supply. *Sensors and Actuators A: Physical*, 74(1):246–250, 1999.
- [184] John C Bass and Daniel T Allen. Milliwatt radioisotope power supply for space applications. In *Thermoelectrics, 1999. Eighteenth International Conference on*, pages 521–524. IEEE, 1999.

Appendix A

PASSIVE POWER GENERATION IN A TEMPORALLY-VARYING TEMPERATURE ENVIRONMENT VIA THERMOELECTRICS

While attending the University of Delaware, I was fortunate enough to have the opportunity to work on a project exploring a novel way to generate power with thermoelectric devices. Typically, thermoelectrics convert thermal energy into electrical energy when a temperature difference is applied across the thermoelectric device. Instead of using a thermoelectric to transform temperature differences in space to electrical energy, our goal was to transform temperature differences in time into thermal energy with a thermoelectric. Our hypothesis was that by placing a thermoelectric plate between two heat exchangers that change temperatures at different rates, the temperature changing with time could be transformed into a spatial temperature difference and ultimately into electrical energy. I focused on the initial modeling of this concept, demonstrating power generation with a thermoelectric in a temporally-varying temperature environment. Once the model was complete, I oversaw the work of two students experimentally verifying the model. Since the experimental verification, our group has had four undergraduate researches work on optimizing this device for maximum power output and explore the use of this device for a specific application.

While this work does not completely fit in with the rest of my dissertation, it has been an important part of my career here at the University of Delaware and I seem to keep coming back to this project. Thus I will present much of this work here. The contents of this chapter is adapted from a manuscript on the modeling that the author wrote and a second manuscript on experimental verification on which the author is a co-author of, both papers have previously been published.[5, 9] Section A.1 will describe the device and environment being modeled as well as details into the numerical model.

Section A.2 shows the result of the numerical model. Section A.3 will highlight some of the work done to experimentally verify this work. Some of the work to optimize the device is presented in Section A.4. Finally, the exploration of this device for a specific application is presented and a summary of this work is presented in Section A.5.

A.1 Model Description

In this numerical analysis, a thermoelectric plate is sandwiched between two different heat exchangers, shown in Fig. A.1. The heat exchangers are designed such that one has a large thermal mass (HE1) and the other a small thermal mass (HE2), allowing the temperature of HE1 to remain relatively constant while the temperature of HE2 responds quickly to fluctuations in the environments temperature. With these design constraints considered, HE1 is chosen to be a truncated quartz sphere, allowing a flat top for good thermal contact with the thermoelectric device. The thermoelectric device consists of 254 elements in a 16×16 array, with two elements removed to allow for electrical contacts. Each element has a length of 3.11 mm, corresponding to the thickness of the thermoelectric (see the inset in Fig. A.1). The thickness of the thermoelectric was determined based on a fill factor of 1 and the optimization of the power output.[171, 172]

Thermoelectric elements are generally sandwiched between two ceramic plates for mechanical stability; in this model, we neglect the ceramic plates. The ceramic plates lie at the interface between the heat exchangers and the thermoelectric module. Thus, at any given instance in time, they would reduce the temperature differential across the thermoelectric and reduce the output power at that time. However, by introducing additional thermal resistance, the ceramic plates would help to insulate the two heat exchangers from each other and maintain their temperature differential, extending the time period over which power is produced. Thus, neglecting the ceramic plates causes a slight overestimation of the power output at any given time, but the time period over which power is produced is somewhat conservative. Since the ceramic

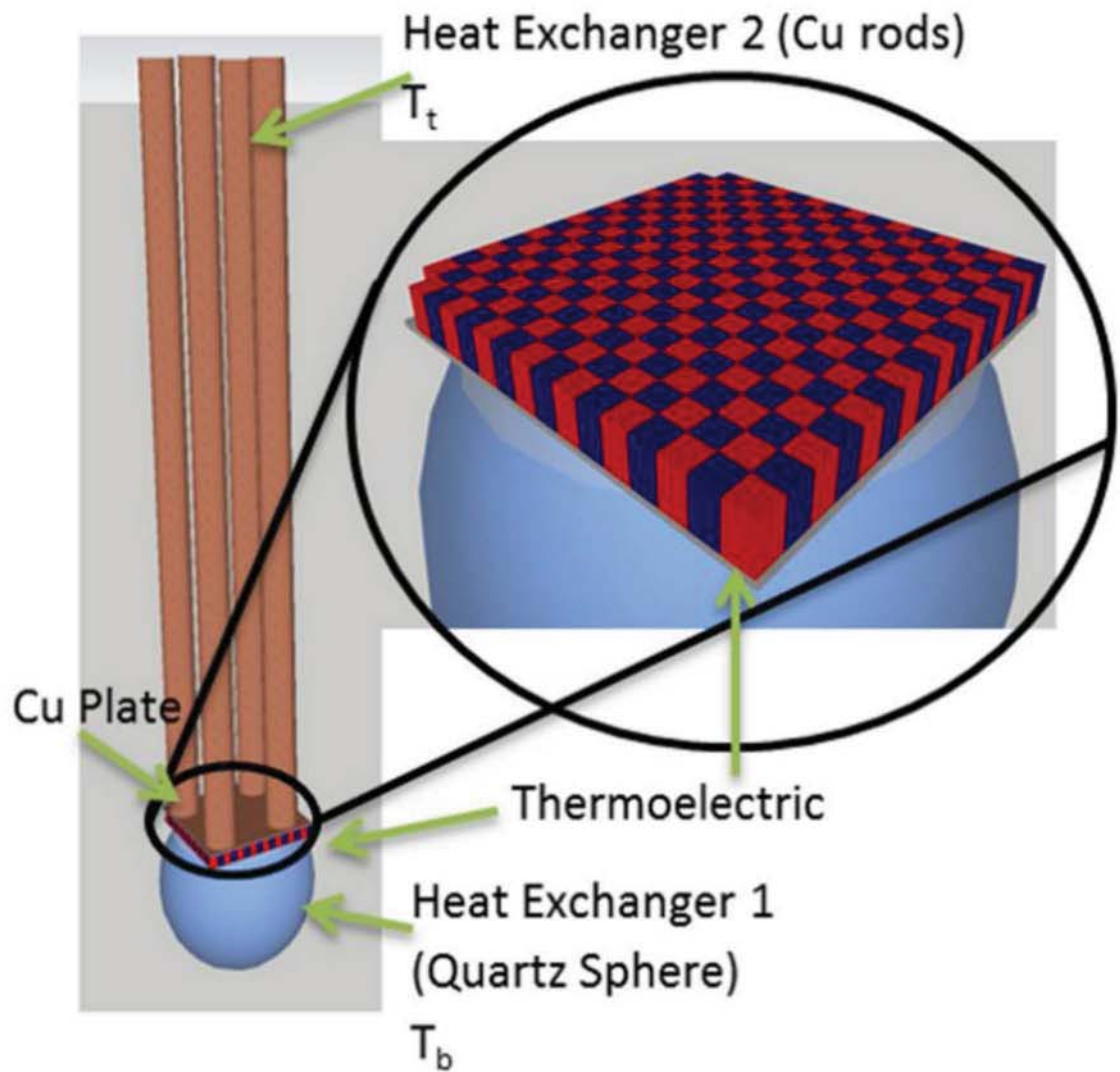


Figure A.1: A schematic of the device setup. Heat exchanger 1 is the sphere below the thermoelectric plate, with a temperature of T_b . Heat exchanger 2 is the rod array and copper plate assembly mounted to the top of the thermoelectric plate, with a temperature of T_t . The inset shows the array of thermoelectric elements that make up the thermoelectric module. [5] Reprinted from [5] with permission from Elsevier.

Table A.1: Material properties of HE1 and HE2. [1, 2, 3, 4] Reprinted from [5] with permission from Elsevier.

	Material	Thermal Conductivity $\kappa (\frac{W}{m-K})$	Specific Heat $C_p (\frac{J}{mol-k})$	Density $\rho (\frac{g}{cm^3})$	Absorptivity α	Emissivity ϵ
HE1	Quartz	1.4	44.2	2.635	-	-
HE2	Copper	401	24.6	8.96	0.7	0.78

plates have much higher thermal conductivity compared to the thermoelectric elements, we believe these effects to be relatively small.

The other side of the thermoelectric device is thermally bonded to HE2. HE2 consists of an array of copper rods, configured to maximize heat transfer with the surrounding environment, mounted on a copper plate that spreads the heat from the copper rods, laterally over the surface of the thermoelectric, and vice versa. In this setup, HE1 is on the bottom and HE2 is on the top. The material properties for HE1 and HE2 are shown in Table A.1.[1, 2, 3, 4] The performance of the thermoelectric power generation is limited by one of the semiconductors, the n- or p-type.[173] This model uses the materials properties of the p-type Bi_2Te_3 because it performs slightly worse than n-type Bi_2Te_3 , resulting in a conservative power output estimate. P-type Bi_2Te_3 has a thermal conductivity of $2.06 \frac{W}{m-K}$, Seebeck coefficient of $162 \frac{\mu V}{K}$, and electrical resistivity of $5.5 \mu\Omega m$. [174, 175]

In this simulation, the device is assumed to be operating during the summer in an environment similar to that of Death Valley, CA. Based on this location, the temperature of the air fluctuates sinusoidally with a maximum of 321 K occurring at 2 p.m. and a minimum of 293 K occurring at 2 a.m. The fluid surrounding the device is assumed to be dry air with constant properties given in Table A.2.[6] It is assumed that the air is moving at a constant velocity of $0.894 \frac{m}{s}$, there is no temperature gradient within the fluid, and any heat transferred from the device to the fluid has a negligible effect on the fluids temperature. Due to the small temperature range, it is assumed that the properties of HE1, HE2, the thermoelectric device, and the air do not change

Table A.2: Material properties of the air. [6] Reprinted from [5] with permission from Elsevier.

Material	Thermal Conductivity $\kappa \left(\frac{W}{m-K} \right)$	Prandtl Number Pr	Kinematic Viscosity ν $\left(\frac{m^2}{s} \right)$	Velocity V $\left(\frac{m}{s} \right)$
Dry Air	0.03003	0.697	2.056×10^{-5}	0.894

with time.

This model considers three modes of heat transfer: convection between the air and HE1 and HE2, heat flow between HE1 and HE2 (across the thermoelectric), and radiation between HE2 and the sun or night sky. Conduction between the device and the earth is neglected by assuming a thermally isolating stand to hold the device above the earth; this stand would make minimal contact with the device resulting in a negligible amount of heat transfer between the stand and the device. Additionally, due to the small contact area, the stand would not inhibit the devices ability to exchange heat with the air. In some plausible applications, the contact between the device and the environment can be minimized as in the current implementation. In other situations, any physical contact between the device and surrounding material will affect the heat transfer process. Such an effect can be estimated only after the specific material and the exact nature of the contact are known. Our goal here is to present the simplest situation where such contact is minimized.

A lumped-parameter analysis is implemented such that thermal gradients within the solid bodies may be neglected. The Biot number is used to assess the validity of the lumped-parameter analysis. The Biot number is given as $Bi = \frac{hR}{\kappa}$ where h is the heat transfer coefficient between the body and the surroundings, R is the characteristic length scale of the body, and κ is its thermal conductivity. For true lumped-parameter behavior, Bi must be much less than 1. The Biot number is reported for each simulation in Section A.2.

The rate of heat flow is calculated assuming the temperature difference between two time steps (dT) is insignificant. The time step was selected to be less than τ ,

where τ is given by Equation A.1. Here, R is a characteristic length, ρ is the density, C_p is the molar heat capacity at constant pressure, κ is the thermal conductivity, and MW is the molecular weight.

$$\tau = \frac{R^2 \rho C_p}{\kappa MW} \quad (\text{A.1})$$

The governing equations of the rate of convective heat transfer between the fluid and the bottom and top heat exchangers, are given in Equations A.2 and A.3 respectively. In Equations A.2 and A.3 A_{fb} and A_{ft} are the surface areas of HE1 and each rod in HE2 that is exposed to the fluid, respectively,[176, 177] and n is the number of rods in HE2. The heat transfer coefficients for the bottom and top heat exchangers are given by Equations A.4 and A.5, respectively. In Equations A.4 and A.5 κ_f is the thermal conductivity of the air, and R_b and R_t are the radii of the sphere and one rod, respectively. The Nusselt numbers are calculated with Equations A.6 and A.7 and the Reynolds numbers are calculated using Equations A.8 and A.9. In Equations A.8 and A.9 V_f is the air velocity, and ν_f is the air's kinematic viscosity.[176, 177]

$$\dot{Q}_{fb} = h_b A_{fb} (T_f - T_b) \quad (\text{A.2})$$

$$\dot{Q}_{ft} = n h_t A_{ft} (T_f - T_t) \quad (\text{A.3})$$

$$h_b = \frac{Nu_b \kappa_f}{R_b} \quad (\text{A.4})$$

$$h_t = \frac{Nu_t \kappa_f}{R_t} \quad (\text{A.5})$$

$$Nu_b = 2 + 0.6 Re_b^{0.5} Pr^{\frac{1}{3}} \quad (\text{A.6})$$

$$Nu_t = (0.376 Re_t^{0.5} + 0.057 Re_t^{\frac{2}{3}}) Pr^{1/3} + 0.93 \left(\log \left(\frac{7.4055}{Re_t} \right) + 4.18 Re_t \right)^{-\frac{1}{3}} Re_t^{\frac{1}{3}} Pr^{\frac{1}{3}} \quad (\text{A.7})$$

$$Re_b = \frac{V_f R_b}{\nu_f} \quad (\text{A.8})$$

$$Re_t = \frac{V_f R_t}{\nu_f} \quad (\text{A.9})$$

Radiative heat transfer between the device and its surroundings was considered only for the case of radiative heat transfer from the sun and space to HE2. The rods in HE2 are arranged so they do not shade each other, allowing maximum radiative heat transfer with HE2. Due to the geometry of the device, it was assumed that HE2 shades the thermoelectric module and HE1 from exposure to the sun and the sky preventing radiative interactions. Additional shading can also be provided to eliminate radiative heat transfer between the sun or sky and the thermoelectric module or HE1. It was also assumed that the temperatures of the earth and any nearby objects were close enough to the temperature of the heat exchangers such that radiative heat transfer can be neglected. Sun angle data for Death Valley from a Nautical Almanac during the summer were fitted to a sinusoidal function to determine the radiation between the sun, sky, and HE2 as a function of time.[3, 177, 7, 8] The radiative flux between the sun and HE2 during the day in kilowatts is given by Equation A.10 where α_t and A_{st} are absorptivity and the area seen by the sun of each rod in HE2 respectively, t is time measured in seconds from 9:00 am and C_0 , C_1 , C_2 , and C_3 are fitting parameters given in Table A.3 based on the angle of the sun as a function of time. A_{st} is given by Equation A.11 where R_t and H_t are the radius and height, respectively, of each rod in HE2. The radiative flux between HE2 and the sky is given by Equation A.12 where A_{nt} is the area of each rod seen by the night sky, and ϵ_t is the emissivity of HE2. A_{nt} is given by Equation A.13 where R_t and H_t are the radius and height, respectively, of each rod in HE2. A_{st} and A_{nt} differ because at any instance the sun only sees one side and the top of the rod while all sides and the top of a rod are viewable by the night sky.

Table A.3: Fitting parameters for radiative exchange between HE2 and the sun, based on the angle of the sun as a function of time on July 10th, 11th, and 12th.[7, 8]Reprinted from [5] with permission from Elsevier.

C_0	C_1	C_2	C_3
0.0060	1.12537	10836.19437	43206.60646

$$\dot{Q}_{st} = n\alpha_t A_{st} (C_0 + C_1 \sin \frac{\pi(t + C_2)}{C_3}) \quad (\text{A.10})$$

$$A_{st} = 2R_t H_t + \pi R_t^2 \quad (\text{A.11})$$

$$\dot{Q}_{nt} = nA_{nt}\sigma\epsilon_t(T_n^4 - T_t^4) \quad (\text{A.12})$$

$$A_{nt} = 2\pi R_t H_t + \pi R_t^2 \quad (\text{A.13})$$

The foregoing discussion pertained to heat exchange between the two bodies and their surroundings. Next, we focus on heat transfer from HE1 to HE2. There are two modes of heat transfer between HE1 and HE2: heat flow by conduction across the thermoelectric plate and direct heat flow via radiation. Because the view factor between the two heat exchangers is approximately zero, radiation between HE1 and HE2 is neglected. The rate of heat flow between the heat exchangers and the thermoelectric module is given by summing the rate of heat flows due to conduction, Peltier heat transfer, Joule heating, and the Thomson effect. The rate of heat transfer across the thermoelectric by conduction is given by Equation A.14 where A_e , κ_e , and L_e are the area, thermal conductivity, and thickness of one thermoelectric element, respectively, and A_m is the area of the entire thermoelectric plate (which is equal to $(N + 2)A_e$ for a fill factor of 1). The Peltier heat flux into and out of HE1 and HE2 are given by Equations A.15 and A.16, respectively, where S is the Seebeck coefficient, and T is the temperature of the heat exchanger in question at the time of interest. When the

external resistance is load-matched to the internal resistance, the current is given by Equation A.17 where $T_t - T_b$ is the temperature differential across the thermoelectric plate, and ρ is the electrical resistivity of the thermoelectric element. Note that when HE2 is warmer than HE1, the current is positive, resulting in the Peltier effect adding heat to HE1 and removing heat from HE2; the reverse is also true. Joule heating within the module is assumed to distribute the heat equally into each heat exchanger. The rate of resistive heating in each heat exchanger is given by Equation A.18. It is important to note that both the Peltier effect and Joule heating are far smaller in magnitude when compared with conduction, convection or radiative heat flow. Thus, these two modes of heat transfer could have been neglected with minimal effect on the power production. The Thomson effect can be neglected because the temperature fluctuations within the device are on the order of only a few degrees, resulting in a negligible change in the Seebeck coefficient.[178, 179, 171]

$$\dot{Q}_{cond} = \frac{(\kappa_e A_e N + \kappa_f (A_m - N A_e))(T_t - T_b)}{L_e} \quad (\text{A.14})$$

$$\dot{Q}_{PeltierHE1} = N S T_b I \quad (\text{A.15})$$

$$\dot{Q}_{PeltierHE2} = -N S T_t I \quad (\text{A.16})$$

$$I = \frac{S(T_t - T_b)A_e}{2\rho L_e} \quad (\text{A.17})$$

$$\dot{Q}_{resistive} = \frac{1}{2} N \frac{I^2 L_e \rho}{A_e} \quad (\text{A.18})$$

Assuming that the thermoelectric plate does not store heat, is isolated from the environment, and that the energy removed from the system by electricity is negligible relative to the total energy flow,[180] the change in temperature for HE1 is given by Equation A.19. The change in temperature for HE2 during the day and the night,

respectively, are given by Equations A.20 and A.21 where M_b and M_t are the masses of HE1 and HE2, respectively. The temperature differential across the thermoelectric plate is equal to $T_t - T_b$, assuming that the thermal resistance of the interface between the thermoelectric plate and the heat exchangers is insignificant.[178] Thus, the instantaneous electrical power output is given by Equation A.22. The power density is obtained by dividing the instantaneous power output by the area of the thermoelectric plate.

$$\Delta T_b = \frac{\dot{Q}_{fb} + \dot{Q}_{cond} + \dot{Q}_{peltierHE1} + \dot{Q}_{resistive}}{\frac{M_b}{MW_b} C p_b} \Delta t \quad (\text{A.19})$$

$$\Delta T_t = \frac{\dot{Q}_{ft} + \dot{Q}_{st} - \dot{Q}_{cond} + \dot{Q}_{peltierHE2} + \dot{Q}_{resistive}}{\frac{M_t}{MW_t} C p_t} \Delta t \quad (\text{A.20})$$

$$\Delta T_t = \frac{\dot{Q}_{ft} + \dot{Q}_{nt} - \dot{Q}_{cond} + \dot{Q}_{peltierHE2} + \dot{Q}_{resistive}}{\frac{M_t}{MW_t} C p_t} \Delta t \quad (\text{A.21})$$

$$P = \frac{S^2 (T_t - T_b)^2 N A_e}{4 \rho_e L_e} \quad (\text{A.22})$$

A.2 Simulation Results and Discussion

In the lumped-parameter analysis, $Bi \ll 1$ corresponds to a body whose internal temperature is essentially uniform and therefore internal temperature gradients may be ignored. For a spherical body, $Bi \approx 0.1$ corresponds to a surface temperature that is within 5% of the center temperature. At larger Biot numbers, the surface of the sphere equilibrates more quickly with the surroundings than the center, resulting in a larger difference between the center and the surface temperatures and the lumped-parameter analysis is no longer valid. HE1 is designed to have a large thermal mass, which implies a large size, in order to suppress its rate of response to temporal variations in the temperature of the environment. Bi increases with length scale, hence it is not possible to simultaneously satisfy the requirements for both a large thermal mass and the lumped-parameter limit. In the current design, it is expected that the surface of

HE1 equilibrates more rapidly with the surroundings than its center. However, the use of the lumped-parameter analysis in this work forces the center of the sphere to equilibrate with the surroundings as quickly as the surface.

The sizes of HE1, HE2 and the thermoelectric module were selected to obtain the smallest possible Biot number while maintaining a reasonable time step. HE1, the quartz sphere, has a diameter of 22 mm and is truncated at 17.6 mm from the bottom. Each of the four copper rods of HE2 has a diameter of 4.4 mm and a height of 88 mm. Each element of the thermoelectric has a cross-sectional area of 0.96 mm^2 resulting in a total module area of 245.2 mm^2 . From their characteristic lengths, thermal conductivities, and heat transfer coefficients (Equations A.4 and A.5), the Biot numbers for HE1 and HE2 are 0.29 and 0.00036, respectively. A Biot number of 0.29 results in a temperature difference between the center of a sphere and the surface of the sphere of about 15%.[181]

Temperature and power output profiles for this geometry are shown in Fig.A.2. It is shown in Fig. A.2(a) that the air temperature experiences lower excursions than both HE1 and HE2 due to the radiative heat transfer HE2 experiences, and the consequent heat flow from HE2 to HE1 and vice versa. The temperature difference between HE1 and HE2 in Fig. A.2(b) is just a few degrees. In Fig. A.2(b), the overshoot in the temperature differential when the temperature gradient is reversed arises from the radiation model used. When the sun sets below the horizon, HE2 instantaneously switches from receiving radiation from the sun to radiating to the night sky; similarly, when the sun rises above the horizon, HE2 instantaneously begins receiving solar radiation instead of emitting radiation. This temperature difference results in a fluctuating power density with a maximum of $1.16 \frac{\text{W}}{\text{m}^2}$, an average of $0.164 \frac{\text{W}}{\text{m}^2}$, and a minimum of $0 \frac{\text{W}}{\text{m}^2}$. This corresponds to a maximum power output of 0.285 mW and an average power output of 0.04 mW, for the size of the thermoelectric selected (245.2 mm^2).

Because the hot and cold sides switch once during the diurnal cycle, the temperature differential ($T_t - T_b$) where T_t and T_b are the temperatures of HE2 and HE1, respectively, experiences two zero-crossings during each 24-hour period, and so the

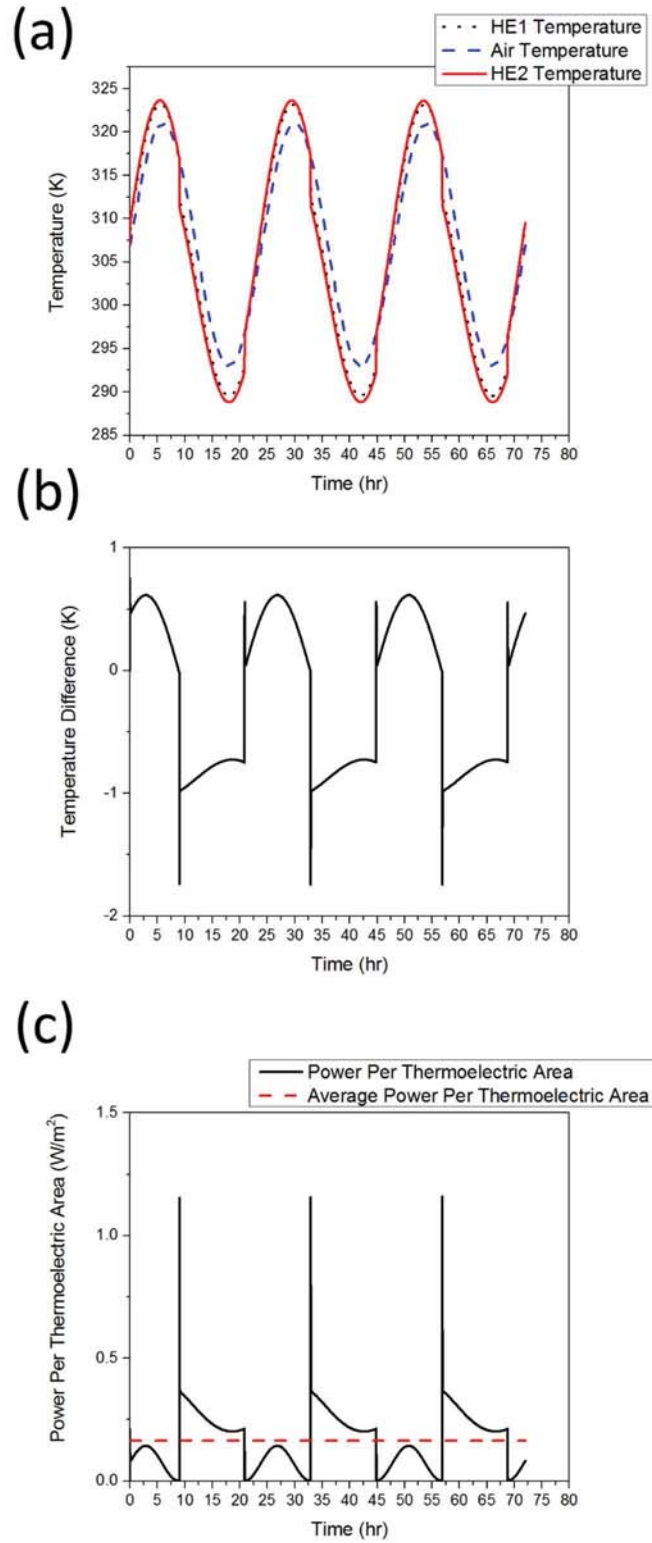


Figure A.2: (a) Temperature profiles for HE1, HE2, and the surrounding fluid; (b) resulting temperature difference ($T_t - T_b$) across the thermoelectric; (c) instantaneous and time-averaged power density generated by the thermoelectric device. [5] Reprinted from [5] with permission from Elsevier.

power production drops to zero at those two time instants. This diurnal cycle can be seen in Fig. A.2(b), where $(T_t - T_b)$ is positive for half of the day and negative for the other half of the day. During the daylight hours, HE2 receives heat from the sun via radiation, such that $(T_t - T_b) > 0$. During the night, HE2 emits heat to the night sky via radiation, such that $(T_t - T_b) < 0$. The temperature differential between the clear night sky in the desert and HE2 is greater than the temperature differential between the sun and HE2 during daylight hours. As a result, $(T_t - T_b)$ experiences a negative temperature excursion at night that is much larger in magnitude than its positive excursion during the day. The corresponding radiative heat flux scales as the fourth power of the temperature differential between the source and the sink. It is also seen in Fig. A.2(c) that the frequency of the power curve is exactly equal that of the diurnal temperature variation.

Figure A.3 shows the effect of scaling up the size of the device on the average power density, and the inset shows the effect of size scaling on the average and maximum power. Device size is changed by proportionately changing all length scales including the sphere radius, the size of the thermoelectric module, the radius of the rods, and the lengths of the rods. The thermoelectric modules surface area is chosen as a representative dimension to indicate device size as this approximates the area the device would occupy on the ground. It is seen that the average power density increases rapidly with device size, reaches a maximum for a size of 2.03 m^2 , and declines thereafter. The inset shows that an increase in size results in an increase in the temperature difference across the thermoelectric module and subsequently a larger power. As the device size increases further the thermal mass of HE2 also increases, reducing the temperature variation that the rods experience in response to the changing environment temperature. This effectively restricts the temperature difference across the thermoelectric module, and thus restricts the amount of power generated. As a result, the power out plateaus beyond 2 m^2 , and the power density peaks at 2.03 m^2 . It should be noted that although the lumped-parameter analysis may not be valid for larger device sizes, this only creates a temperature variation within HE1. This slightly

affects the magnitude of the change in average power density with size, but the trend in the variation still holds. Additional optimization such as scaling the sizes of HE1 and HE2 independently, changing material type, and considering other thermoelectric module and heat exchanger geometries could result in a higher power density.

From these simulations, it is clear that using thermoelectrics in a thermally time-dependent environment produces relatively small amounts of power. Moreover, the power output is not steady. However, both shortcomings can be overcome by wiring several of these devices together and using recent advancements in power switching and electrical storage systems, leading to devices that could prove useful for remote power applications such as sensors and communication devices.

Initial estimates suggest that the cost of materials to build these devices is less than \$10. While other technologies certainly exist for larger-scale and less-expensive power generation for many applications, we believe that this approach is particularly useful when other power sources are not possible or reliable. In the proposed desert application, this approach offers the advantage over solar photovoltaics of greater mechanical robustness, immunity to coverage by dust storms, and night-time generation. Miniaturized, portable versions of these devices could be designed to power sensors on passive robots probing remote environments and tracking beacons for shore birds, fish, and other wildlife whose movements cause temporal temperature changes. While A.3 shows that smaller sizes produce less power, we can optimize other design features to generate more power for small devices. For example, increasing either the surface area-to-volume ratio of HE2 via surface roughening, or adding thermal insulation to HE1 would increase the amount of power generated for a fixed device size. In addition to optimizing for the geometry and materials for a given size, one must also consider the rate at which the fluid changes temperature. A device operating on the concepts presented here could be designed to exploit the temperature fluctuations in the human bloodstream to power sensors for health monitoring or mechanisms for targeted drug delivery by considering exotic materials and suitable geometries that generate an adequate temperature gradient from thermal variations occurring on a faster time

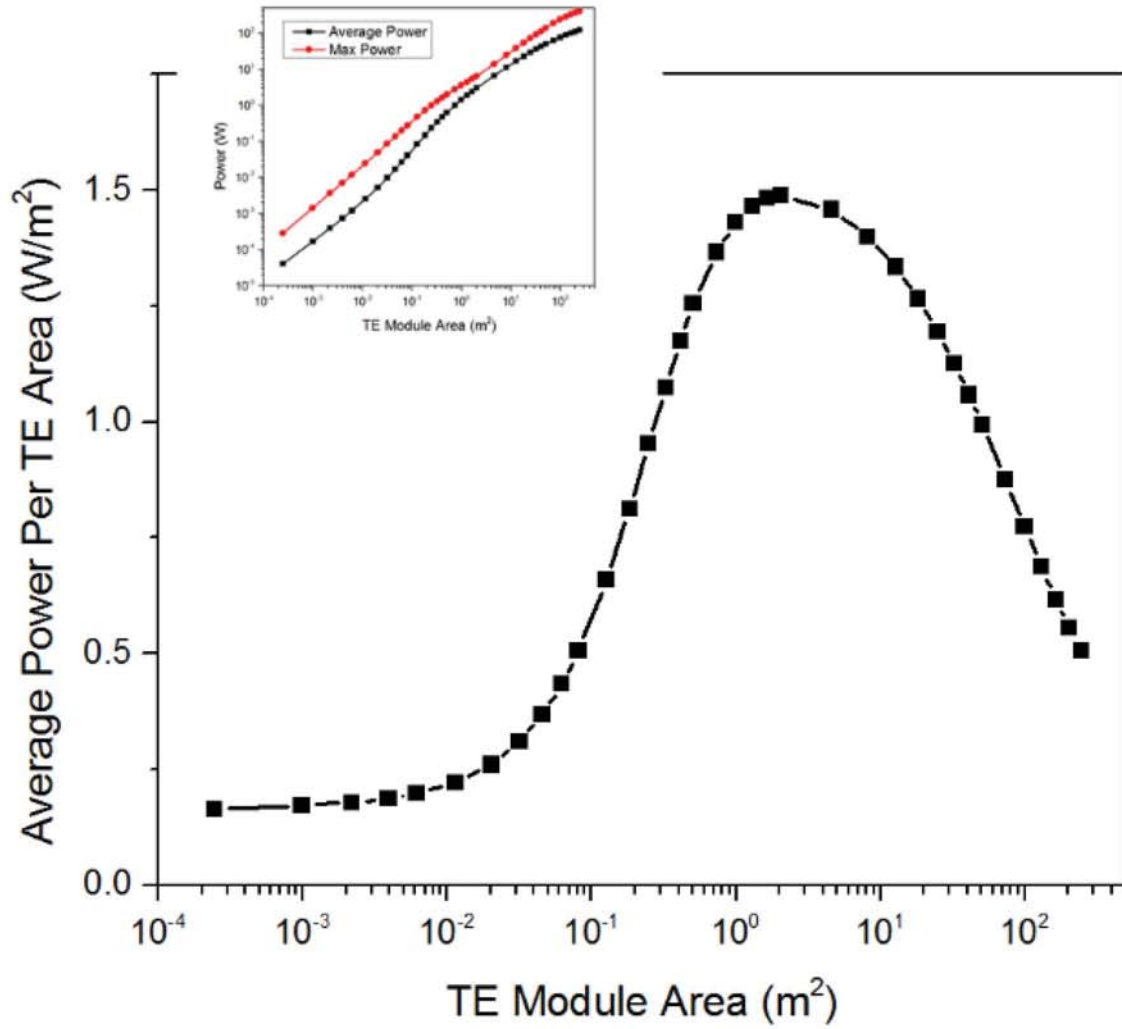


Figure A.3: Average power density produced by the thermoelectric module as a function of the thermoelectric modules surface area. Inset shows that power increases with size at small sizes. [5] Reprinted from [5] with permission from Elsevier.

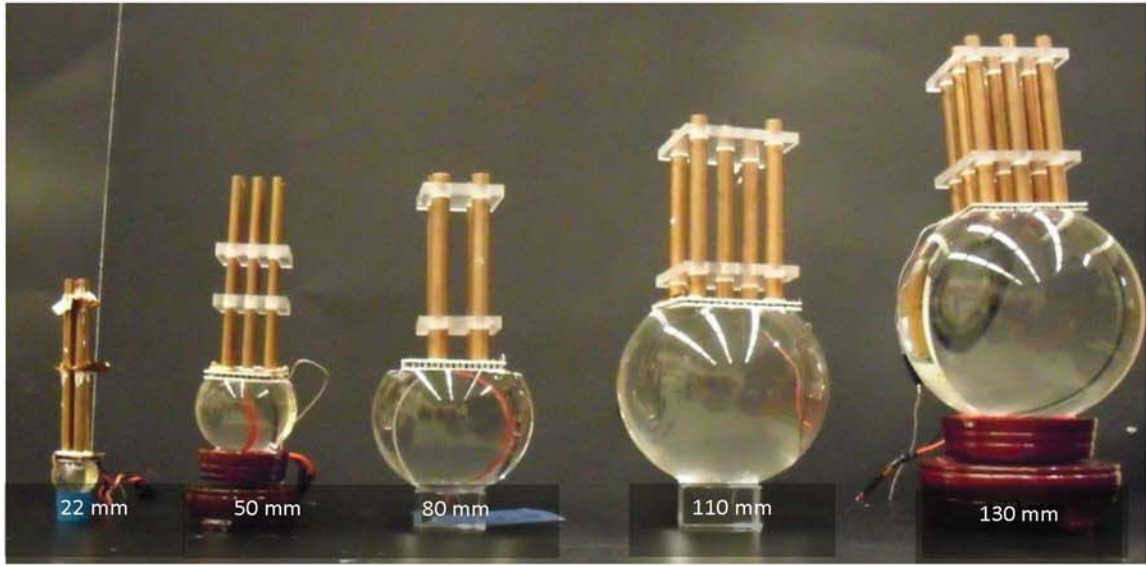


Figure A.4: Picture of the devices tested, labels indicate the quartz sphere's diameter. [9] Reprinted from [9] with permission from Elsevier.

scale.

A.3 Experimental Verification

In an attempt to verify the theoretical model described above, five devices with varying heat exchanger sizes and configurations were built, as shown in Fig. A.4. The devices consist of a series of 10 cm long copper rods attached to a heat-spreading copper plate, a thermoelectric device with elements composed of bismuth telluride, and a truncated quartz sphere. The copper rods are the rapid heat exchanger and the quartz sphere is the slow heat exchanger. The heat exchangers were bonded to the thermoelectric plate using thermally conductive silver epoxy. Acrylic support plates were used to secure the vertically upright copper rods and are assumed to have a negligible effect on the heat transfer to and from the rods. The devices were supported by stands that made minimal contact with the quartz spheres, shown in Fig. A.4. The specifications for each device is presented in Table A.4; throughout this chapter the devices are referred to by the diameter of the sphere.[9]

To measure the power output of each device as a function of the temperature

Table A.4: Device specifications. Reprinted from [9] with permission from Elsevier.

Sphere Diameter (mm)	Sphere Truncation Distance (mm)	Number of Copper Rods	Copper Rod Diameter (mm)	Thermoelectric Area (mm ²)	Number of Thermoelectric Element Pairs
22	4	4	4.76	15×15	31
50	11	9	4.76	36×36	49
80	13	4	9.53	50×50	127
110	15	5	9.53	62×62	127
130	13	9	9.53	62×62	127

change over time, each devices was placed in an Espec ECT temperature-controllable chamber and connected to an external resistor that is approximately load-matched to the internal resistance of the thermoelectrics. The devices were allowed to equilibrate at 34°C. Once equilibrated, the temperature of the chamber was sinusoidally varied from 20°C to 48°C. The voltage across the resistor and the environmental temperatures were logged during the measurement and the power was calculated using $P = \frac{V^2}{R}$. [9]

The measured voltage and power output was modeled using the method described above. [5] The device properties including: heat exchanger mass, thermoelectric Seebeck coefficients, and resistances were all measured experimentally. The heat transfer coefficients of the heat exchangers were found experimentally, rather than theoretically, using the procedure provided by Russell et al. [182] Additionally, the experiment was performed without a radiation source, and thus this was removed from the model. With these modifications, the model was found to be in reasonably good agreement with the experiment and did not require the use of a fitting parameter. Figure A.5 shows the comparison of an experimental and theoretical power profile for the 110 mm devices for a temperature oscillation period of 1 hour. As the model predicted, the power profile exhibits a frequency double that of the environment temperature. Note the device generally takes about three cycles to reach a dynamic equilibrium with the environmental temperature profile. Thus, the first three power peaks differ from those of the subsequent peaks; the shape of the power profile approximately repeats after the

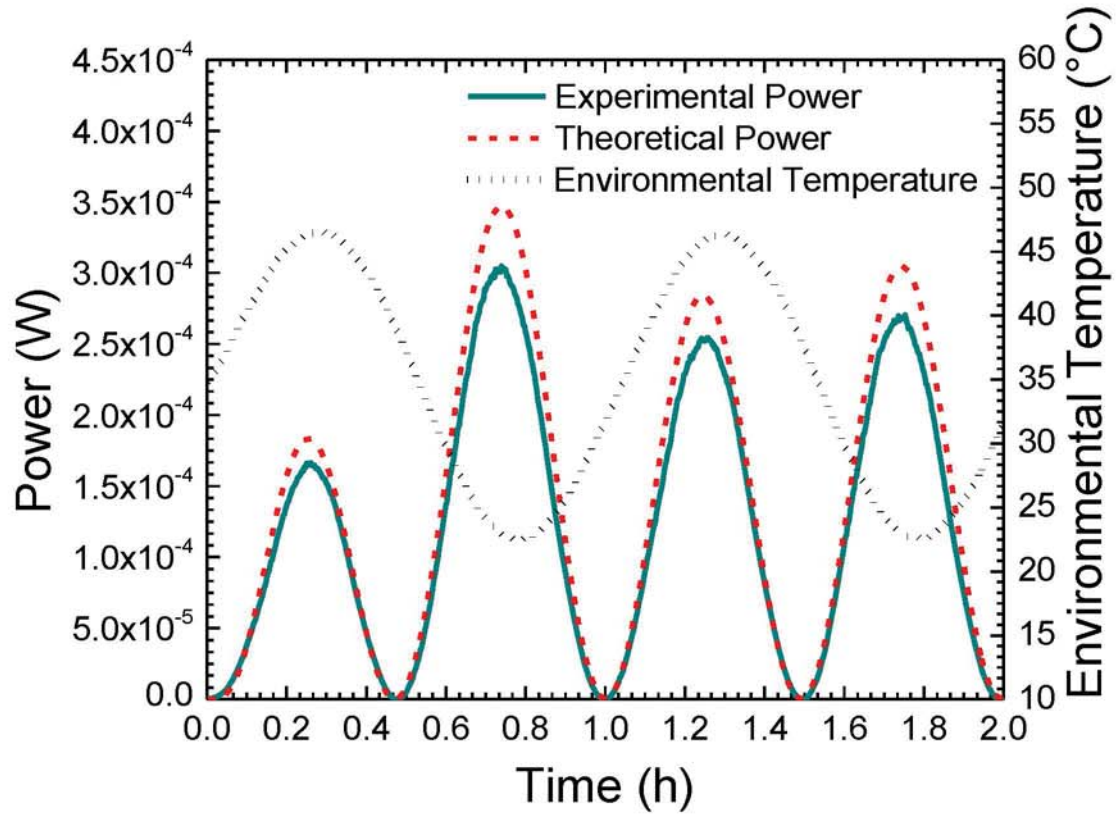


Figure A.5: Experimental and theoretical power profiles for the 110 mm device and the corresponding environments temperature profile, indicating good agreement between theory and experiment.[9] Reprinted from [9] with permission from Elsevier.

first three peaks. [9]

A.4 Optimization

In an attempt to optimize the device's power output, the effect of heat exchanger size and geometry was tested using the five devices configurations presented in Table A.4. To aid in the comparison geometries, we defined a proportionality constant K termed the thermal response rate coefficient. The derivation of the thermal response rate coefficient is shown in Equation A.23 where T is temperature of the heat exchanger, h is the convective heat transfer coefficient, ρ is the density of the heat exchanger, C_p is the specific heat capacity of the heat exchanger, $\frac{A}{V}$ is the surface

area to volume ratio of the heat exchanger, and T_a is the ambient temperature. All devices use the same heat exchanger materials, and thus the heat transfer coefficient h is roughly constant. This results in the ratio of heat exchanger thermal response rate coefficients reducing to the ratio of heat exchanger surface area to volume ratios. Thus the ratio K_{rapid}/K_{slow} increases for a given K_{rapid} with increasing sizes for the slow heat exchanger, resulting in an increase in the power generation. The effect of increasing the ratio of K_{rapid}/K_{slow} by increasing the device size is shown in Fig. A.6 where increasing K_{rapid}/K_{slow} increases the power output. Note the power output eventually levels off with increasing devices size for $K_{rapid}/K_{slow} > 3.5$. [9]

$$\frac{dT}{dt} = \frac{h}{\rho C_p} \frac{A}{V} (T_a - T) = K(T_a - T) \quad (\text{A.23})$$

A second method to increase power output by increasing the ratio of heat exchanger thermal response rate coefficients is to insulate the slow heat exchanger. Adding insulation to the slow heat exchanger reduces the thermal response rate coefficient by reducing the effective heat transfer coefficient. The effect of adding insulation is shown in Fig. A.7(a) where the theoretical average power output is plotted against the slow heat exchanger's heat transfer coefficient for three values of the rapid heat exchangers heat transfer coefficient. Note the average output power rapidly decreases for the slow heat exchangers heat transfer coefficient that corresponds to $K_{rapid}/K_{slow}=1$. This corresponds to the rate of temperature change for each heat exchanger being equal and no power is generated. The effect of insulating the slow heat exchanger was experimentally tested by adding layers of 3.175 mm thick polyester insulation to the slow heat exchanger, shown in Fig A.7 for the 22 mm device and temperature oscillation period of 1 hour. Adding three layers of insulation resulted in the average power output increasing from $5.9 \pm 0.8 \times 10^{-7}$ W to $7.45 \pm 0.04 \times 10^{-6}$ W. Adding one layer of insulation to the 130 mm device results in a power increase from 0.124 ± 0.004 mW to 0.160 ± 0.002 mW. Thus, insulating the slow heat exchanger is an effective means of improving the device power output. [9]

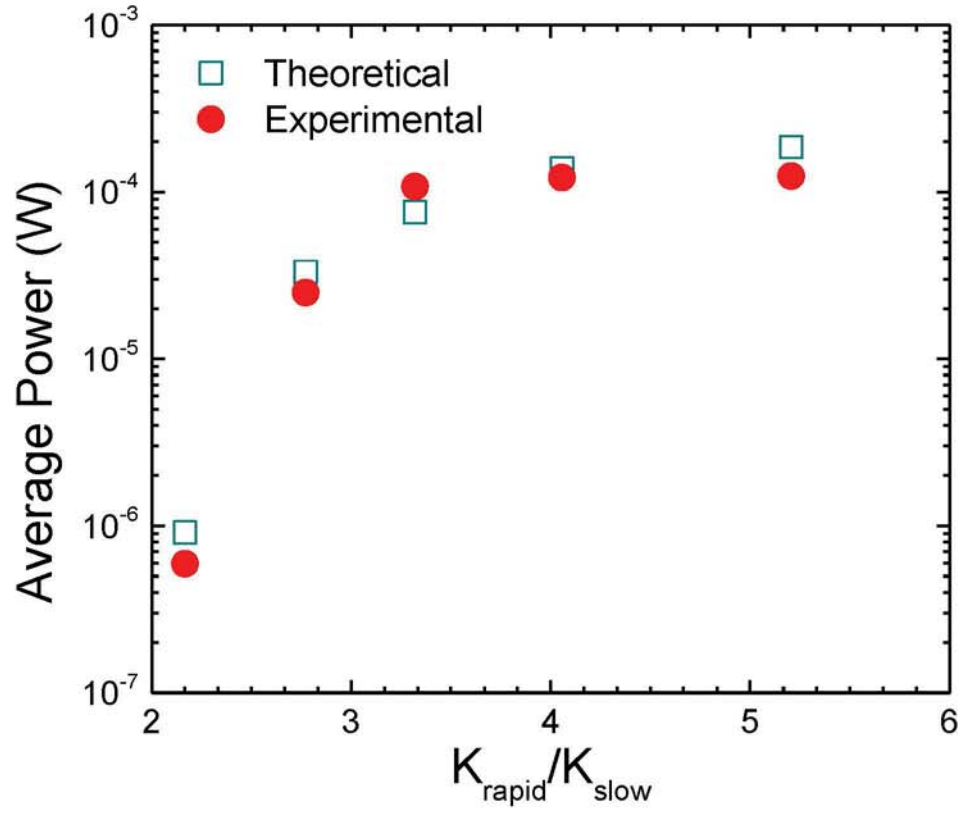


Figure A.6: Experimental and theoretical average power output as a function of $K_{\text{rapid}}/K_{\text{slow}}$ indicating increased device sizes result in increased power output.[9] Reprinted from [9] with permission from Elsevier.

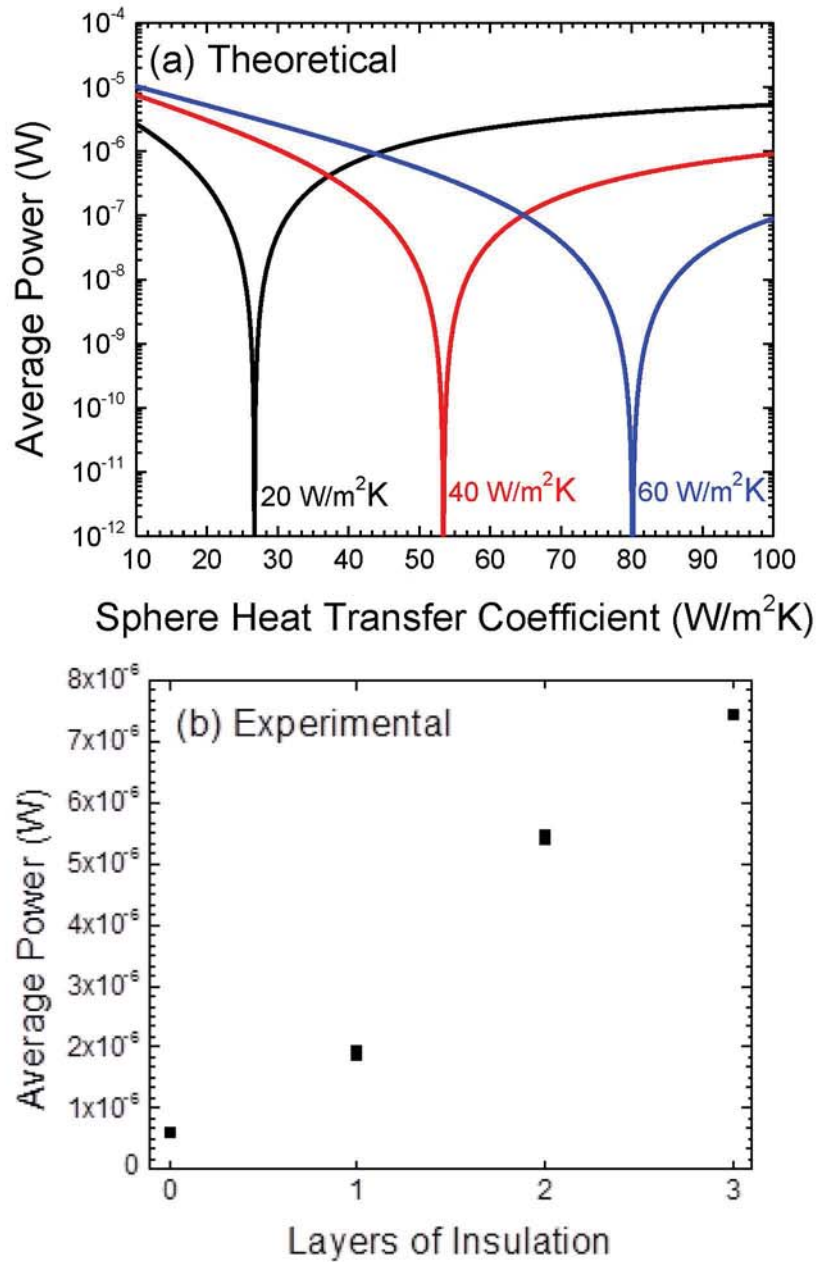


Figure A.7: (a) Theoretical prediction of the average power as a function of the heat exchangers' heat transfer coefficients for the 22 mm device with a 1 hour period of temperature oscillation. (b) Experimental average power as a function of layer of insulation of the 22 mm devices, effectively decreasing the heat transfer coefficient of the slow heat exchanger. Measurements were performed with a 1 hour period of temperature oscillation.[9] Reprinted from [9] with permission from Elsevier.

With the knowledge that the slow heat exchanger can be optimized with added insulation, we recently theoretically explored the possibility of optimizing the rapid heat exchanger. The theoretical model suggests that increasing the number of rods from one to nine and increasing the rod length increase the power output. Both of these changes effectively increases the surface area to volume ratio of the rapid heat exchanger, which increases the rate at which the top heat exchanger can change temperature with the environment. Similarly, increasing the radius of the rods generally decreases the power output. Finally, attempts to change the orientation of the rods was not conclusive and is an area worth further exploration. Note the theoretical calculations do suggest that spacing the rods further apart increases the power output, but alignment of the rods with respect to air flow direction is inconclusive.

A.5 Summary and Applications

In this chapter I have shown both theoretically and experimentally that a thermoelectric power generator placed between two different heat exchanges in a dynamic temperature environment can produce small amounts of power. Experimentally we were able to output power on the order of 10^{-4} W, which is comparable to low-power thermoelectric applications for preamplifiers and sensor control systems and radioisotope-power probes for space exploration.[183, 184] I have also explained our effort to optimize the power output of such a device, demonstrating the effects of adding insulation to the slow heat exchanger and optimizing the geometry of the rapid heat exchanger. The power output could be further increased with increased thermoelectric efficiency. Additionally, the device materials and geometry can be optimized for maximum power output.

We recently explored the use of this device to power a Global Positioning System (GPS) attached to sperm whales. As the whale periodically dives through the ocean thermals, the device would experience an environment that changes temperature periodically and the two heat exchanges could convert the temporal temperature profile into a spatial temperature gradient across the thermoelectric. The goal would be for

the thermoelectric device to produce enough power to recharge the AA batteries that power the GPS, allowing the GPS system to run indefinitely. Preliminary results show that a device made with an acrylic block for the slow heat exchanger and aluminum fins as the fast heat exchange can produce small amounts of power when submerged in a tank of water that changes temperature with time simulating a whale diving through ocean thermals. Unfortunately, this device did not produce enough power to completely recharge the batteries. However, this device is far from optimized and future optimization could allow for more power output.


Appendix B

FIGURE REPRINT PERMISSIONS

Figure B.1: Reprint permission for Fig. 1.1(a) and Fig. 1.17.

8/16/2016

Rightslink® by Copyright Clearance Center



Copyright Clearance Center


Most Trusted. Most Cited. Most Read.

RightsLink®


Home

Create Account

Help



Live Chat



ACS Publications

Most Trusted. Most Cited. Most Read.

Title:

Reducing Thermal Conductivity of Crystalline Solids at High Temperature Using Embedded Nanostructures

Author:

Woochul Kim, Suzanne L. Singer, Arun Majumdar, et al

Publication:

Nano Letters

Publisher:

American Chemical Society

Date:

Jul 1, 2008

Copyright © 2008, American Chemical Society

LOGIN

If you're a copyright.com user, you can login to RightsLink using your copyright.com credentials. Already a RightsLink user or want to learn more?

PERMISSION/LICENSE IS GRANTED FOR YOUR ORDER AT NO CHARGE

This type of permission/license, instead of the standard Terms & Conditions, is sent to you because no fee is being charged for your order. Please note the following:

- Permission is granted for your request in both print and electronic formats, and translations.
- If figures and/or tables were requested, they may be adapted or used in part.
- Please print this page for your records and send a copy of it to your publisher/graduate school.
- Appropriate credit for the requested material should be given as follows: "Reprinted (adapted) with permission from (COMPLETE REFERENCE CITATION). Copyright (YEAR) American Chemical Society." Insert appropriate information in place of the capitalized words.
- One-time permission is granted only for the use specified in your request. No additional uses are granted (such as derivative works or other editions). For any other uses, please submit a new request.

If credit is given to another source for the material you requested, permission must be obtained from that source.

BACK

CLOSE WINDOW

Copyright © 2016 Copyright Clearance Center, Inc. All Rights Reserved. [Privacy statement](#). [Terms and Conditions](#). Comments? We would like to hear from you. E-mail us at customer@copyright.com

<https://s100.copyright.com/AppDispatchServlet#formTop>

1/1

191

Figure B.2: Reprint permission for Fig. 1.1(b) and Fig. 1.15.

RightsLink Printable License

AIP PUBLISHING LLC LICENSE TERMS AND CONDITIONS

Aug 16, 2016

This Agreement between Cory C Bomberger ("You") and AIP Publishing LLC ("AIP Publishing LLC") consists of your license details and the terms and conditions provided by AIP Publishing LLC and Copyright Clearance Center.

License Number	3930600054951
License date	Aug 16, 2016
Licensed Content Publisher	AIP Publishing LLC
Licensed Content Publication	Applied Physics Letters
Licensed Content Title	Growth and properties of rare-earth arsenide InGaAs nanocomposites for terahertz generation
Licensed Content Author	R. Salas,S. Guchhait,S. D. Sifferman, et al.
Licensed Content Date	Feb 24, 2015
Licensed Content Volume Number	106
Licensed Content Issue Number	8
Type of Use	Thesis/Dissertation
Requestor type	Student
Format	Print and electronic
Portion	Figure/Table
Number of figures/tables	2
Title of your thesis / dissertation	Growth, Characterization, and Applications of Lanthanide Monopnictide Nanoparticles and Films in and on III-Semiconductors
Expected completion date	Sep 2016
Estimated size (number of pages)	185
Requestor Location	Cory C Bomberger 201 DuPont Hall NEWARK, DE 19716 United States Attn: Cory C Bomberger
Billing Type	Invoice
Billing Address	Cory C Bomberger 201 DuPont Hall NEWARK, DE 19716 United States Attn: Cory C Bomberger
Total	0.00 USD
Terms and Conditions	

<https://s100.copyright.com/AppDispatchServlet>

 $\frac{1}{2}$

Figure B.3: Reprint permission for Fig. 1.2.

8/16/2016

RightsLink Printable License

**AIP PUBLISHING LLC LICENSE
TERMS AND CONDITIONS**

Aug 16, 2016

This Agreement between Cory C Bomberger ("You") and AIP Publishing LLC ("AIP Publishing LLC") consists of your license details and the terms and conditions provided by AIP Publishing LLC and Copyright Clearance Center.

License Number	3930600704179
License date	Aug 16, 2016
Licensed Content Publisher	AIP Publishing LLC
Licensed Content Publication	Journal of Vacuum Science & Technology B
Licensed Content Title	Electrical properties of Er-doped In _{0.53} Ga _{0.47} As
Licensed Content Author	Peter G. Burke,Hong Lu,Nicholas G. Rudawski, et al.
Licensed Content Date	Mar 3, 2011
Licensed Content Volume Number	29
Licensed Content Issue Number	3
Type of Use	Thesis/Dissertation
Requestor type	Student
Format	Print and electronic
Portion	Figure/Table
Number of figures/tables	1
Title of your thesis / dissertation	Growth, Characterization, and Applications of Lanthanide Monopnictide Nanoparticles and Films in and on III-Semiconductors
Expected completion date	Sep 2016
Estimated size (number of pages)	185
Requestor Location	Cory C Bomberger 201 DuPont Hall NEWARK, DE 19716 United States Attn: Cory C Bomberger
Billing Type	Invoice
Billing Address	Cory C Bomberger 201 DuPont Hall NEWARK, DE 19716 United States Attn: Cory C Bomberger
Total	0.00 USD
Terms and Conditions	


<https://s100.copyright.com/AppDispatchServlet>

1/2

Figure B.4: Reprint permission for Fig. 1.3.


8/16/2016

Rightslink® by Copyright Clearance Center



Copyright Clearance Center


Most Trusted. Most Cited. Most Read.




Home

Account Info

Help



Live Chat



ACS Publications

Most Trusted. Most Cited. Most Read.

Title:

Surface-Mediated Tunable Self-Assembly of Single Crystal Semimetallic ErSb/GaSb Nanocomposite Structures

Author:

Jason K. Kawasaki, Brian D. Schultz, Hong Lu, et al

Publication:

Nano Letters

Publisher:

American Chemical Society

Date:

Jun 1, 2013

Copyright © 2013, American Chemical Society

Logged in as:

Cory Bomberger

LOGOUT

PERMISSION/LICENSE IS GRANTED FOR YOUR ORDER AT NO CHARGE

This type of permission/license, instead of the standard Terms & Conditions, is sent to you because no fee is being charged for your order. Please note the following:

- Permission is granted for your request in both print and electronic formats, and translations.
- If figures and/or tables were requested, they may be adapted or used in part.
- Please print this page for your records and send a copy of it to your publisher/graduate school.
- Appropriate credit for the requested material should be given as follows: "Reprinted (adapted) with permission from (COMPLETE REFERENCE CITATION). Copyright (YEAR) American Chemical Society." Insert appropriate information in place of the capitalized words.
- One-time permission is granted only for the use specified in your request. No additional uses are granted (such as derivative works or other editions). For any other uses, please submit a new request.

If credit is given to another source for the material you requested, permission must be obtained from that source.

BACK

CLOSE WINDOW

Copyright © 2016 Copyright Clearance Center, Inc. All Rights Reserved. [Privacy statement](#). [Terms and Conditions](#). Comments? We would like to hear from you. E-mail us at customer@copyright.com

Figure B.5: Reprint permission for Fig. 1.4.

8/16/2016

RightsLink Printable License

**JOHN WILEY AND SONS LICENSE
TERMS AND CONDITIONS**

Aug 16, 2016

This Agreement between Cory C Bomberger ("You") and John Wiley and Sons ("John Wiley and Sons") consists of your license details and the terms and conditions provided by John Wiley and Sons and Copyright Clearance Center.

table { border-collapse: collapse; width: 100%; }
tr { border-bottom: 1px solid black; }
tr:last-child { border-bottom: none; }
tr td { padding-bottom: 10px; }
tr td { padding-bottom: 10px; }

License Number	3930601400411
License date	Aug 16, 2016
Licensed Content Publisher	John Wiley and Sons
Licensed Content Publication	Small
Licensed Content Title	Observation of Self-Assembled Core-Shell Structures in Epitaxially Embedded TbErAs Nanoparticles
Licensed Content Author	Pernell Dongmo,Matthew Hartshome,Thomas Cristiani,Michael L. Jablonski,Cory Bomberger,Dieter Isheim,David N. Seidman,Mitra L. Taheri,Joshua Zide
Licensed Content Date	Aug 8, 2014
Licensed Content Pages	6
Type of use	Dissertation/Thesis
Requestor type	University/Academic
Format	Print and electronic
Portion	Figure/table
Number of figures/tables	1
Original Wiley figure/table number(s)	Figure 2
Will you be translating?	No
Title of your thesis / dissertation	Growth, Characterization, and Applications of Lanthanide Monopnictide Nanoparticles and Films in and on III-Semiconductors
Expected completion date	Sep 2016
Expected size (number of pages)	185
Requestor Location	Cory C Bomberger 201 DuPont Hall NEWARK, DE 19716 United States Attn: Cory C Bomberger
Publisher Tax ID	EU826007151
Billing Type	Invoice
Billing Address	Cory C Bomberger 201 DuPont Hall NEWARK, DE 19716 United States Attn: Cory C Bomberger

<https://s100.copyright.com/AppDispatchServlet>

1/5

Figure B.6: Reprint permission for Fig. 1.5.

8/16/2016

RightsLink Printable License

**AIP PUBLISHING LLC LICENSE
TERMS AND CONDITIONS**

Aug 16, 2016

This Agreement between Cory C Bomberger ("You") and AIP Publishing LLC ("AIP Publishing LLC") consists of your license details and the terms and conditions provided by AIP Publishing LLC and Copyright Clearance Center.

table { border-collapse: collapse; width: 100%; }
tr { border-bottom: 1px solid black; }
tr:last-child { border-bottom: none; }
tr td { padding-bottom: 10px; }
tr td { padding-bottom: 10px; }

License Number	3930610223914
License date	Aug 16, 2016
Licensed Content Publisher	AIP Publishing LLC
Licensed Content Publication	Applied Physics Letters
Licensed Content Title	Embedded growth mode of thermodynamically stable metallic nanoparticles on III-V semiconductors
Licensed Content Author	B. D. Schultz, S. G. Choi, C. J. Palmström
Licensed Content Date	Jun 15, 2006
Licensed Content Volume Number	88
Licensed Content Issue Number	24
Type of Use	Thesis/Dissertation
Requestor type	Student
Format	Print and electronic
Portion	Figure/Table
Number of figures/tables	1
Title of your thesis / dissertation	Growth, Characterization, and Applications of Lanthanide Monopnictide Nanoparticles and Films in and on III-Semiconductors
Expected completion date	Sep 2016
Estimated size (number of pages)	185
Requestor Location	Cory C Bomberger 201 DuPont Hall NEWARK, DE 19716 United States Attn: Cory C Bomberger
Billing Type	Invoice
Billing Address	Cory C Bomberger 201 DuPont Hall NEWARK, DE 19716 United States Attn: Cory C Bomberger
Total	0.00 USD
Terms and Conditions	

<https://s100.copyright.com/AppDispatchServlet>

1/2

Figure B.7: Reprint permission for Fig. 1.6 and Fig. 1.12.

8/16/2016

RightsLink Printable License

**AIP PUBLISHING LLC LICENSE
TERMS AND CONDITIONS**

Aug 16, 2016

This Agreement between Cory C Bomberger ("You") and AIP Publishing LLC ("AIP Publishing LLC") consists of your license details and the terms and conditions provided by AIP Publishing LLC and Copyright Clearance Center.

License Number	3930610466776
License date	Aug 16, 2016
Licensed Content Publisher	AIP Publishing LLC
Licensed Content Publication	Applied Physics Letters
Licensed Content Title	Growth and characterization of single crystal rocksalt LaAs using LuAs barrier layers
Licensed Content Author	E. M. Krivoy, S. Rahimi, H. P. Nair, et al.
Licensed Content Date	Nov 26, 2012
Licensed Content Volume Number	101
Licensed Content Issue Number	22
Type of Use	Thesis/Dissertation
Requestor type	Student
Format	Print and electronic
Portion	Figure/Table
Number of figures/tables	2
Title of your thesis / dissertation	Growth, Characterization, and Applications of Lanthanide Monopnictide Nanoparticles and Films in and on III-Semiconductors
Expected completion date	Sep 2016
Estimated size (number of pages)	185
Requestor Location	Cory C Bomberger 201 DuPont Hall NEWARK, DE 19716 United States Attn: Cory C Bomberger
Billing Type	Invoice
Billing Address	Cory C Bomberger 201 DuPont Hall NEWARK, DE 19716 United States Attn: Cory C Bomberger
Total	0.00 USD
Terms and Conditions	

<https://s100.copyright.com/AppDispatchServlet>

1/2

Figure B.8: Reprint permission for Fig. 1.7.

8/16/2016

RightsLink Printable License

**AIP PUBLISHING LLC LICENSE
TERMS AND CONDITIONS**

Aug 16, 2016

This Agreement between Cory C Bomberger ("You") and AIP Publishing LLC ("AIP Publishing LLC") consists of your license details and the terms and conditions provided by AIP Publishing LLC and Copyright Clearance Center.

table { border-collapse: collapse; width: 100%; }
tr { border-bottom: 1px solid black; }
tr:last-child { border-bottom: none; }
tr td { padding-bottom: 10px; }
tr td { padding-bottom: 10px; }

License Number	3930610754506
License date	Aug 16, 2016
Licensed Content Publisher	AIP Publishing LLC
Licensed Content Publication	Applied Physics Letters
Licensed Content Title	Suppression of planar defects in the molecular beam epitaxy of GaAs/ErAs/GaAs heterostructures
Licensed Content Author	Adam M. Crook,Hari P. Nair,Domingo A. Ferrer, et al.
Licensed Content Date	Aug 19, 2011
Licensed Content Volume Number	99
Licensed Content Issue Number	7
Type of Use	Thesis/Dissertation
Requestor type	Student
Format	Print and electronic
Portion	Figure/Table
Number of figures/tables	1
Title of your thesis / dissertation	Growth, Characterization, and Applications of Lanthanide Monopnictide Nanoparticles and Films in and on III-Semiconductors
Expected completion date	Sep 2016
Estimated size (number of pages)	185
Requestor Location	Cory C Bomberger 201 DuPont Hall NEWARK, DE 19716 United States Attn: Cory C Bomberger
Billing Type	Invoice
Billing Address	Cory C Bomberger 201 DuPont Hall NEWARK, DE 19716 United States Attn: Cory C Bomberger
Total	0.00 USD
Terms and Conditions	

<https://s100.copyright.com/AppDispatchServlet>

1/2

Figure B.9: Reprint permission for Fig. 1.8.

8/16/2016

RightsLink Printable License

**AIP PUBLISHING LLC LICENSE
TERMS AND CONDITIONS**

Aug 16, 2016

This Agreement between Cory C Bomberger ("You") and AIP Publishing LLC ("AIP Publishing LLC") consists of your license details and the terms and conditions provided by AIP Publishing LLC and Copyright Clearance Center.

License Number	3930610929228
License date	Aug 16, 2016
Licensed Content Publisher	AIP Publishing LLC
Licensed Content Publication	Applied Physics Letters
Licensed Content Title	Interface atomic structure of epitaxial ErAs layers on (001) In _{0.53} Ga _{0.47} As and GaAs
Licensed Content Author	Dmitri O. Klenov, Joshua M. Zide, Jeremy D. Zimmerman, et al.
Licensed Content Date	Jun 6, 2005
Licensed Content Volume Number	86
Licensed Content Issue Number	24
Type of Use	Thesis/Dissertation
Requestor type	Student
Format	Print and electronic
Portion	Figure/Table
Number of figures/tables	1
Title of your thesis / dissertation	Growth, Characterization, and Applications of Lanthanide Monopnictide Nanoparticles and Films in and on III-Semiconductors
Expected completion date	Sep 2016
Estimated size (number of pages)	185
Requestor Location	Cory C Bomberger 201 DuPont Hall NEWARK, DE 19716 United States Attn: Cory C Bomberger
Billing Type	Invoice
Billing Address	Cory C Bomberger 201 DuPont Hall NEWARK, DE 19716 United States Attn: Cory C Bomberger
Total	0.00 USD
Terms and Conditions	

<https://s100.copyright.com/AppDispatchServlet>

1/2

Figure B.10: Reprint permission for Fig. 1.9.

8/16/2016

RightsLink Printable License

**AMERICAN PHYSICAL SOCIETY LICENSE
TERMS AND CONDITIONS**

Aug 16, 2016

This Agreement between Cory C Bomberger ("You") and American Physical Society ("American Physical Society") consists of your license details and the terms and conditions provided by American Physical Society and Copyright Clearance Center.

License Number	3930611234357
License date	Aug 16, 2016
Licensed Content Publisher	American Physical Society
Licensed Content Publication	Physical Review Letters
Licensed Content Title	Role of Atomic Multiplets in the Electronic Structure of Rare-Earth Semiconductors and Semimetals
Licensed Content Author	Leonid V. Pourovskii et al.
Licensed Content Date	Mar 2, 2009
Licensed Content Volume Number	102
Type of Use	Thesis/Dissertation
Requestor type	Student
Format	Print, Electronic
Portion	chart/graph/table/figure
Number of charts/graphs/tables/figures	1
Portion description	Figure 2
Rights for	Main product
Duration of use	Life of Current Edition
Creation of copies for the disabled	no
With minor editing privileges	no
For distribution to	Worldwide
In the following language(s)	Original language of publication
With incidental promotional use	no
The lifetime unit quantity of new product	0 to 499
The requesting person/organization is:	Cory Bomberger / University of Delaware
Order reference number	
Title of your thesis / dissertation	Growth, Characterization, and Applications of Lanthanide Monopnictide Nanoparticles and Films in and on III-Semiconductors
Expected completion date	Sep 2016
Expected size (number of pages)	185

<https://s100.copyright.com/AppDispatchServlet>

1/3

Figure B.11: Reprint permission for Fig. 1.10.

8/16/2016

RightsLink Printable License

**AMERICAN PHYSICAL SOCIETY LICENSE
TERMS AND CONDITIONS**

Aug 16, 2016

This Agreement between Cory C Bomberger ("You") and American Physical Society ("American Physical Society") consists of your license details and the terms and conditions provided by American Physical Society and Copyright Clearance Center.

License Number	3930620119835
License date	Aug 16, 2016
Licensed Content Publisher	American Physical Society
Licensed Content Publication	Physical Review Letters
Licensed Content Title	Local Density of States and Interface Effects in Semimetallic ErAs Nanoparticles Embedded in GaAs
Licensed Content Author	Jason K. Kawasaki et al.
Licensed Content Date	Jul 14, 2011
Licensed Content Volume Number	107
Type of Use	Thesis/Dissertation
Requestor type	Student
Format	Print, Electronic
Portion	chart/graph/table/figure
Number of charts/graphs/tables/figures	1
Portion description	Figure 2
Rights for	Main product
Duration of use	Life of Current Edition
Creation of copies for the disabled	no
With minor editing privileges	no
For distribution to	Worldwide
In the following language(s)	Original language of publication
With incidental promotional use	no
The lifetime unit quantity of new product	0 to 499
The requesting person/organization is:	Cory Bomberger / The University of Delaware
Order reference number	
Title of your thesis / dissertation	Growth, Characterization, and Applications of Lanthanide Monopnictide Nanoparticles and Films in and on III-Semiconductors
Expected completion date	Sep 2016
Expected size (number of pages)	185

<https://s100.copyright.com/AppDispatchServlet>

1/3

Figure B.12: Reprint permission for Fig. 1.11.

8/16/2016

RightsLink Printable License

AIP PUBLISHING LLC LICENSE TERMS AND CONDITIONS

Aug 16, 2016

This Agreement between Cory C Bomberger ("You") and AIP Publishing LLC ("AIP Publishing LLC") consists of your license details and the terms and conditions provided by AIP Publishing LLC and Copyright Clearance Center.

License Number	3930620369618
License date	Aug 16, 2016
Licensed Content Publisher	AIP Publishing LLC
Licensed Content Publication	Journal of Applied Physics
Licensed Content Title	Infrared surface plasmon resonances due to Er-V semimetallic nanoparticles in III-V semiconductor matrices
Licensed Content Author	M. P. Hanson,A. C. Gossard,E. R. Brown
Licensed Content Date	Aug 30, 2007
Licensed Content Volume Number	102
Licensed Content Issue Number	4
Type of Use	Thesis/Dissertation
Requestor type	Student
Format	Print and electronic
Portion	Figure/Table
Number of figures/tables	1
Title of your thesis / dissertation	Growth, Characterization, and Applications of Lanthanide Monopnictide Nanoparticles and Films in and on III-Semiconductors
Expected completion date	Sep 2016
Estimated size (number of pages)	185
Requestor Location	Cory C Bomberger 201 DuPont Hall NEWARK, DE 19716 United States Attn: Cory C Bomberger
Billing Type	Invoice
Billing Address	Cory C Bomberger 201 DuPont Hall NEWARK, DE 19716 United States Attn: Cory C Bomberger
Total	0.00 USD
Terms and Conditions	

<https://s100.copyright.com/AppDispatchServlet>

1/2

Figure B.13: Reprint permission for Fig. 1.13.

8/16/2016

RightsLink Printable License

**ELSEVIER LICENSE
TERMS AND CONDITIONS**

Aug 16, 2016

This Agreement between Cory C Bomberger ("You") and Elsevier ("Elsevier") consists of your license details and the terms and conditions provided by Elsevier and Copyright Clearance Center.

License Number	3930620727591
License date	Aug 16, 2016
Licensed Content Publisher	Elsevier
Licensed Content Publication	Journal of Crystal Growth
Licensed Content Title	Properties of molecular beam epitaxially grown ScAs:InGaAs and ErAs:InGaAs nanocomposites for thermoelectric applications
Licensed Content Author	X. Liu, A.T. Ramu, J.E. Bowers, C.J. Palmström, P.G. Burke, H. Lu, A.C. Gossard
Licensed Content Date	1 February 2011
Licensed Content Volume Number	316
Licensed Content Issue Number	1
Licensed Content Pages	4
Start Page	56
End Page	59
Type of Use	reuse in a thesis/dissertation
Intended publisher of new work	other
Portion	figures/tables/illustrations
Number of figures/tables/illustrations	1
Format	both print and electronic
Are you the author of this Elsevier article?	No
Will you be translating?	No
Order reference number	
Original figure numbers	Figure 1
Title of your thesis/dissertation	Growth, Characterization, and Applications of Lanthanide Monopnictide Nanoparticles and Films in and on III-Semiconductors
Expected completion date	Sep 2016
Estimated size (number of pages)	185
Elsevier VAT number	GB 494 6272 12
Requestor Location	Cory C Bomberger 201 DuPont Hall

<https://s100.copyright.com/AppDispatchServlet>

1/6

Figure B.14: Reprint permission for Fig. 1.14 and Fig. 1.19.

RightsLink Printable License

AIP PUBLISHING LLC LICENSE TERMS AND CONDITIONS

Aug 16, 2016

This Agreement between Cory C Bomberger ("You") and AIP Publishing LLC ("AIP Publishing LLC") consists of your license details and the terms and conditions provided by AIP Publishing LLC and Copyright Clearance Center.

License Number	3930621101960
License date	Aug 16, 2016
Licensed Content Publisher	AIP Publishing LLC
Licensed Content Publication	Journal of Applied Physics
Licensed Content Title	High efficiency semimetal/semiconductor nanocomposite thermoelectric materials
Licensed Content Author	J. M. O. Zide,J.-H. Bahk,R. Singh, et al.
Licensed Content Date	Dec 20, 2010
Licensed Content Volume Number	108
Licensed Content Issue Number	12
Type of Use	Thesis/Dissertation
Requestor type	Student
Format	Print and electronic
Portion	Figure/Table
Number of figures/tables	2
Title of your thesis / dissertation	Growth, Characterization, and Applications of Lanthanide Monopnictide Nanoparticles and Films in and on III-Semiconductors
Expected completion date	Sep 2016
Estimated size (number of pages)	185
Requestor Location	Cory C Bomberger 201 DuPont Hall NEWARK, DE 19716 United States Attn: Cory C Bomberger
Billing Type	Invoice
Billing Address	Cory C Bomberger 201 DuPont Hall NEWARK, DE 19716 United States Attn: Cory C Bomberger
Total	0.00 USD
Terms and Conditions	

<https://s100.copyright.com/AppDispatchServlet>

1/2

Figure B.15: Reprint permission for Fig. 1.16 and Fig. 1.18.

8/16/2016

RightsLink Printable License

**AIP PUBLISHING LLC LICENSE
TERMS AND CONDITIONS**

Aug 16, 2016

This Agreement between Cory C Bomberger ("You") and AIP Publishing LLC ("AIP Publishing LLC") consists of your license details and the terms and conditions provided by AIP Publishing LLC and Copyright Clearance Center.

License Number	3930621378484
License date	Aug 16, 2016
Licensed Content Publisher	AIP Publishing LLC
Licensed Content Publication	Applied Physics Letters
Licensed Content Title	Thermoelectric power generator module of $16 \times 16 \text{Bi}_2\text{Te}_3$ and 0.6% $\text{ErAs}:(\text{InGaAs})_{1-x}(\text{InAlAs})_x$ segmented elements
Licensed Content Author	Gehong Zeng, Je-Hyeong Bahk, John E. Bowers, et al.
Licensed Content Date	Aug 26, 2009
Licensed Content Volume Number	95
Licensed Content Issue Number	8
Type of Use	Thesis/Dissertation
Requestor type	Student
Format	Print and electronic
Portion	Figure/Table
Number of figures/tables	2
Title of your thesis / dissertation	Growth, Characterization, and Applications of Lanthanide Monopnictide Nanoparticles and Films in and on III-Semiconductors
Expected completion date	Sep 2016
Estimated size (number of pages)	185
Requestor Location	Cory C Bomberger 201 DuPont Hall NEWARK, DE 19716 United States Attn: Cory C Bomberger
Billing Type	Invoice
Billing Address	Cory C Bomberger 201 DuPont Hall NEWARK, DE 19716 United States Attn: Cory C Bomberger
Total	0.00 USD
Terms and Conditions	

<https://s100.copyright.com/AppDispatchServlet>

1/2

Figure B.16: Reprint permission for Fig. 1.20.

8/16/2016

RightsLink Printable License

**AIP PUBLISHING LLC LICENSE
TERMS AND CONDITIONS**

Aug 16, 2016

This Agreement between Cory C Bomberger ("You") and AIP Publishing LLC ("AIP Publishing LLC") consists of your license details and the terms and conditions provided by AIP Publishing LLC and Copyright Clearance Center.

table { border-collapse: collapse; width: 100%; }
tr { border-bottom: 1px solid black; }
tr:last-child { border-bottom: none; }
tr td { padding-bottom: 10px; }
tr td { padding-bottom: 10px; }

License Number	3930630059982
License date	Aug 16, 2016
Licensed Content Publisher	AIP Publishing LLC
Licensed Content Publication	Applied Physics Letters
Licensed Content Title	Increased efficiency in multijunction solar cells through the incorporation of semimetallic ErAs nanoparticles into the tunnel junction
Licensed Content Author	J. M. O. Zide,A. Kleiman-Shwarscstein,N. C. Strandwitz, et al.
Licensed Content Date	Apr 17, 2006
Licensed Content Volume Number	88
Licensed Content Issue Number	16
Type of Use	Thesis/Dissertation
Requestor type	Student
Format	Print and electronic
Portion	Figure/Table
Number of figures/tables	1
Title of your thesis / dissertation	Growth, Characterization, and Applications of Lanthanide Monopnictide Nanoparticles and Films in and on III-Semiconductors
Expected completion date	Sep 2016
Estimated size (number of pages)	185
Requestor Location	Cory C Bomberger 201 DuPont Hall NEWARK, DE 19716 United States Attn: Cory C Bomberger
Billing Type	Invoice
Billing Address	Cory C Bomberger 201 DuPont Hall NEWARK, DE 19716 United States Attn: Cory C Bomberger
Total	0.00 USD
Terms and Conditions	

<https://s100.copyright.com/AppDispatchServlet>

1/2

Figure B.17: Reprint permission for Fig. 2.1.

8/15/2016

Gmail - Figure Reprint Permission



Cory Bomberger <cory.bomberger@gmail.com>

Figure Reprint Permission

Seth R Bank <sbank@utexas.edu>
To: Cory Bomberger <cbomberg@udel.edu>

Mon, Aug 15, 2016 at 10:21 AM

Sure!

Seth R. Bank
Associate Professor
Temple Foundation Faculty Fellowship No. 5
Electrical and Computer Engineering
The University of Texas at Austin
phone: (512) 471-9669
email: sbank@ece.utexas.edu
web: <http://lase.ece.utexas.edu/>

On Aug 15, 2016, at 9:20 AM, Cory Bomberger <cbomberg@udel.edu> wrote:

Hello Dr. Bank,

I would like to request permission to use the MBE schematic, Figure 2.1, located on your website (<http://lase.ece.utexas.edu/mbe.php>) within my dissertation. Please let me know if this would be okay.

Thank you,
Cory Bomberger

—
Cory Bomberger
Doctoral Student
Material Science and Engineering
University of Delaware

email: cbomberg@udel.edu

Figure B.18: Reprint permission for Fig. 3.1, Fig. 3.2, Fig. 3.3, and Fig. 3.4.

8/16/2016

RightsLink Printable License

**AMERICAN PHYSICAL SOCIETY LICENSE
TERMS AND CONDITIONS**

Aug 16, 2016

This Agreement between Cory C Bomberger ("You") and American Physical Society ("American Physical Society") consists of your license details and the terms and conditions provided by American Physical Society and Copyright Clearance Center.

License Number	3930940478972
License date	Aug 16, 2016
Licensed Content Publisher	American Physical Society
Licensed Content Publication	Physical Review B
Licensed Content Title	Charge carrier relaxation processes in TbAs nanoinclusions in GaAs measured by optical-pump THz-probe transient absorption spectroscopy
Licensed Content Author	Laura R. Vanderhoef et al.
Licensed Content Date	Jan 21, 2014
Licensed Content Volume Number	89
Type of Use	Thesis/Dissertation
Requestor type	Student
Format	Print, Electronic
Portion	chart/graph/table/figure
Number of charts/graphs/tables/figures	4
Portion description	Figure 1, Figure 3, Figure 5, Figure 6
Rights for	Main product
Duration of use	Life of Current Edition
Creation of copies for the disabled	no
With minor editing privileges	no
For distribution to	Worldwide
In the following language(s)	Original language of publication
With incidental promotional use	no
The lifetime unit quantity of new product	0 to 499
The requesting person/organization is:	Cory Bomberger / University of Delaware
Order reference number	
Title of your thesis / dissertation	Growth, Characterization, and Applications of Lanthanide Monophenyl Nanoparticles and Films in and on III-Semiconductors
Expected completion date	Sep 2016
Expected size (number of pages)	185

<https://s100.copyright.com/AppDispatchServlet>

1/3

Figure B.19: Reprint permission for Fig. 3.5, Fig. 3.6, Fig. 3.7, Fig. 3.8, and Fig. 3.9.

8/16/2016

RightsLink Printable License

**AIP PUBLISHING LLC LICENSE
TERMS AND CONDITIONS**

Aug 16, 2016

This Agreement between Cory C Bomberger ("You") and AIP Publishing LLC ("AIP Publishing LLC") consists of your license details and the terms and conditions provided by AIP Publishing LLC and Copyright Clearance Center.

License Number	3930941150165
License date	Aug 16, 2016
Licensed Content Publisher	AIP Publishing LLC
Licensed Content Publication	Applied Physics Letters
Licensed Content Title	Determining the band alignment of TbAs:GaAs and TbAs:In _{0.53} Ga _{0.47} As
Licensed Content Author	Cory C. Bomberger, Laura R. Vanderhoef, Abdur Rahman, et al.
Licensed Content Date	Sep 10, 2015
Licensed Content Volume Number	107
Licensed Content Issue Number	10
Type of Use	Thesis/Dissertation
Requestor type	Author (original article)
Format	Print and electronic
Portion	Figure/Table
Number of figures/tables	5
Title of your thesis / dissertation	Growth, Characterization, and Applications of Lanthanide Monopnictide Nanoparticles and Films in and on III-Semiconductors
Expected completion date	Sep 2016
Estimated size (number of pages)	185
Requestor Location	Cory C Bomberger 201 DuPont Hall NEWARK, DE 19716 United States Attn: Cory C Bomberger
Billing Type	Invoice
Billing Address	Cory C Bomberger 201 DuPont Hall NEWARK, DE 19716 United States Attn: Cory C Bomberger
Total	0.00 USD
Terms and Conditions	

<https://s100.copyright.com/AppDispatchServlet>

1/2

Figure B.20: Reprint permission for Fig. A.1, Fig. A.2, Fig. A.3, and Tab. A.1, Tab. A.2, Tab. A.3.

8/16/2016

RightsLink Printable License

**ELSEVIER LICENSE
TERMS AND CONDITIONS**

Aug 16, 2016

This Agreement between Cory C Bomberger ("You") and Elsevier ("Elsevier") consists of your license details and the terms and conditions provided by Elsevier and Copyright Clearance Center.

License Number	3930950687106
License date	Aug 16, 2016
Licensed Content Publisher	Elsevier
Licensed Content Publication	Applied Thermal Engineering
Licensed Content Title	Modeling passive power generation in a temporally-varying temperature environment via thermoelectrics
Licensed Content Author	Cory C. Bomberger, Peter M. Attia, Ajay K. Prasad, Joshua M.O. Zide
Licensed Content Date	July 2013
Licensed Content Volume Number	56
Licensed Content Issue Number	1-2
Licensed Content Pages	7
Start Page	152
End Page	158
Type of Use	reuse in a thesis/dissertation
Intended publisher of new work	other
Portion	figures/tables/illustrations
Number of figures/tables/illustrations	6
Format	both print and electronic
Are you the author of this Elsevier article?	Yes
Will you be translating?	No
Order reference number	
Original figure numbers	Figure 1, Table 1, Table 2, Table 3, Figure 2, Figure 3
Title of your thesis/dissertation	Growth, Characterization, and Applications of Lanthanide Monopnictide Nanoparticles and Films in and on III-Semiconductors
Expected completion date	Sep 2016
Estimated size (number of pages)	185
Elsevier VAT number	GB 494 6272 12
Requestor Location	Cory C Bomberger 201 DuPont Hall

NEWARK, DE 19716

<https://s100.copyright.com/AppDispatchServlet>

1/6

Figure B.21: Reprint permission for Fig. A.4, Fig. A.5, Fig. A.6, Fig. A.7, and Tab. A.4.

8/16/2016

RightsLink Printable License

**ELSEVIER LICENSE
TERMS AND CONDITIONS**

Aug 16, 2016

This Agreement between Cory C Bomberger ("You") and Elsevier ("Elsevier") consists of your license details and the terms and conditions provided by Elsevier and Copyright Clearance Center.

License Number	3930960276893
License date	Aug 16, 2016
Licensed Content Publisher	Elsevier
Licensed Content Publication	Energy
Licensed Content Title	Experimental studies of thermoelectric power generation in dynamic temperature environments
Licensed Content Author	Peter M. Attia,Matthew R. Lewis,Cory C. Bomberger,Ajay K. Prasad,Joshua M.O. Zide
Licensed Content Date	1 October 2013
Licensed Content Volume Number	60
Licensed Content Issue Number	n/a
Licensed Content Pages	4
Start Page	453
End Page	456
Type of Use	reuse in a thesis/dissertation
Intended publisher of new work	other
Portion	figures/tables/illustrations
Number of figures/tables/illustrations	5
Format	both print and electronic
Are you the author of this Elsevier article?	No
Will you be translating?	No
Order reference number	
Original figure numbers	Figure 1, Table 1, Figure 2, Figure 3, Figure 4
Title of your thesis/dissertation	Growth, Characterization, and Applications of Lanthanide Monopnictide Nanoparticles and Films in and on III-Semiconductors
Expected completion date	Sep 2016
Estimated size (number of pages)	185
Elsevier VAT number	GB 494 6272 12
Requestor Location	Cory C Bomberger 201 DuPont Hall

<https://s100.copyright.com/AppDispatchServlet>

1/6

Figure B.22: Reprint permission for article [27].

8/16/2016

RightsLink Printable License

**AIP PUBLISHING LLC LICENSE
TERMS AND CONDITIONS**

Aug 16, 2016

This Agreement between Cory C Bomberger ("You") and AIP Publishing LLC ("AIP Publishing LLC") consists of your license details and the terms and conditions provided by AIP Publishing LLC and Copyright Clearance Center.

License Number	3930951509117
License date	Aug 16, 2016
Licensed Content Publisher	AIP Publishing LLC
Licensed Content Publication	Applied Physics Letters
Licensed Content Title	Determining the band alignment of TbAs:GaAs and TbAs:In _{0.53} Ga _{0.47} As
Licensed Content Author	Cory C. Bomberger, Laura R. Vanderhoef, Abdur Rahman, et al.
Licensed Content Date	Sep 10, 2015
Licensed Content Volume Number	107
Licensed Content Issue Number	10
Type of Use	Thesis/Dissertation
Requestor type	Author (original article)
Format	Print and electronic
Portion	Excerpt (> 800 words)
Will you be translating?	No
Title of your thesis / dissertation	Growth, Characterization, and Applications of Lanthanide Monopnictide Nanoparticles and Films in and on III-Semiconductors
Expected completion date	Sep 2016
Estimated size (number of pages)	185
Requestor Location	Cory C Bomberger 201 DuPont Hall NEWARK, DE 19716 United States Attn: Cory C Bomberger
Billing Type	Invoice
Billing Address	Cory C Bomberger 201 DuPont Hall NEWARK, DE 19716 United States Attn: Cory C Bomberger
Total	0.00 USD
Terms and Conditions	

<https://s100.copyright.com/AppDispatchServlet>

1/2

Figure B.23: Reprint permission for article [5].

8/16/2016

RightsLink Printable License

**ELSEVIER LICENSE
TERMS AND CONDITIONS**

Aug 16, 2016

This Agreement between Cory C Bomberger ("You") and Elsevier ("Elsevier") consists of your license details and the terms and conditions provided by Elsevier and Copyright Clearance Center.

table { border-collapse: collapse; width: 100%; }
tr { border-bottom: 1px solid black; }
tr:last-child { border-bottom: none; }
tr td { padding-bottom: 5px; }
tr td { padding-bottom: 5px; }
License Number	3930951314105
License date	Aug 16, 2016
Licensed Content Publisher	Elsevier
Licensed Content Publication	Applied Thermal Engineering
Licensed Content Title	Modeling passive power generation in a temporally-varying temperature environment via thermoelectrics
Licensed Content Author	Cory C. Bomberger, Peter M. Attia, Ajay K. Prasad, Joshua M.O. Zide
Licensed Content Date	July 2013
Licensed Content Volume Number	56
Licensed Content Issue Number	1-2
Licensed Content Pages	7
Start Page	152
End Page	158
Type of Use	reuse in a thesis/dissertation
Intended publisher of new work	other
Portion	full article
Format	both print and electronic
Are you the author of this Elsevier article?	Yes
Will you be translating?	No
Order reference number	
Title of your thesis/dissertation	Growth, Characterization, and Applications of Lanthanide Monopnictide Nanoparticles and Films in and on III-Semiconductors
Expected completion date	Sep 2016
Estimated size (number of pages)	185
Elsevier VAT number	GB 494 6272 12
Requestor Location	Cory C Bomberger 201 DuPont Hall NEWARK, DE 19716 United States Attn: Cory C Bomberger
Total	0.00 USD

<https://s100.copyright.com/AppDispatchServlet>

1/6